

## Abstract

## Measurement of ( $\pi^-$ -Ar) and ( $K^+$ -Ar) total hadronic cross sections in the LArIAT experiment

Elena Gramellini

2018

**6 Abstract** goes here. Limit 750 words.

7                   **Measurement of ( $\pi^-$ -Ar) and ( $K^+$ -Ar)**

8                   **total hadronic cross sections in the**

9                   **LArIAT experiment**

10                   A Dissertation  
11                   Presented to the Faculty of the Graduate School  
12                   of  
13                   Yale University  
14                   in Candidacy for the Degree of  
15                   Doctor of Philosophy

16                   by  
17                   Elena Gramellini

18                   Dissertation Director: Bonnie T. Fleming

19                   Date you'll receive your degree

<sup>20</sup>

Copyright © 2018 by Elena Gramellini

<sup>21</sup>

All rights reserved.

22

*A mia mamma e mio babbo,*

23

*grazie per le radici e grazie per le ali.*

24

*To my mom and dad,*

25

*thank you for the roots and thank you for the wings.*

# <sup>26</sup> Contents

<sup>27</sup>	<b>Acknowledgements</b>	viii
<sup>28</sup>	<b>Introduction</b>	ix
<sup>29</sup>	<b>1 The theoretical framework</b>	1
<sup>30</sup>	1.1 The Standard Model . . . . .	1
<sup>31</sup>	1.2 Neutrinos: tiny cracks in the Standard Model . . . . .	4
<sup>32</sup>	1.2.1 Neutrinos in the Standard Model . . . . .	4
<sup>33</sup>	1.2.2 Neutrino Oscillations . . . . .	6
<sup>34</sup>	1.2.3 Make up of Neutrino Interactions . . . . .	7
<sup>35</sup>	1.3 Beyond the Standard Model . . . . .	9
<sup>36</sup>	1.3.1 Open Questions in Neutrino Physics . . . . .	11
<sup>37</sup>	1.3.2 Towards a more fundamental theory: GUTs . . . . .	15
<sup>38</sup>	1.4 Motivations for Hadronic Cross Sections in Argon . . . . .	18
<sup>39</sup>	1.4.1 Pion-Argon Total Hadronic Cross Section . . . . .	18
<sup>40</sup>	1.4.2 Kaon-Argon Total Hadronic Cross Section . . . . .	29
<sup>41</sup>	<b>2 Liquid Argon Detectors at the Intensity Frontier</b>	34
<sup>42</sup>	2.1 The Liquid Argon Time Projection Chamber Technology . . . . .	34
<sup>43</sup>	2.1.1 TPCs, Neutrinos & Argon . . . . .	35
<sup>44</sup>	2.1.2 LArTPC: Principles of Operation . . . . .	37

45	2.1.3	Liquid Argon: Ionization Charge . . . . .	40
46	2.1.4	Liquid Argon: Scintillation Light . . . . .	45
47	2.1.5	Signal Processing and Event Reconstruction . . . . .	49
48	2.2	The Intensity Frontier Program . . . . .	53
49	2.2.1	Prospects for LArTPCs in Neutrino Physics: SBN and DUNE	54
50	2.2.2	Prospects for LArTPCs in GUT Physics: DUNE . . . . .	55
51	2.2.3	Enabling the next generation of discoveries: LArIAT . . . . .	57
52	<b>3</b>	<b>LArIAT: Liquid Argon In A Testbeam</b>	<b>60</b>
53	3.1	The Particles' Path to LArIAT . . . . .	60
54	3.2	LArIAT Tertiary Beam Instrumentation . . . . .	62
55	3.2.1	Bending Magnets . . . . .	63
56	3.2.2	Multi-Wire Proportional Chambers . . . . .	65
57	3.2.3	Time-of-Flight System . . . . .	67
58	3.2.4	Punch-Through and Muon Range Stack Instruments . . . . .	68
59	3.2.5	LArIAT Cosmic Ray Paddle Detectors . . . . .	70
60	3.3	In the Cryostat . . . . .	71
61	3.3.1	Cryogenics and Argon Purity . . . . .	71
62	3.3.2	LArTPC: Charge Collection . . . . .	74
63	3.3.3	LArTPC: Light Collection System . . . . .	77
64	3.4	Trigger and DAQ . . . . .	80
65	3.5	Control Systems . . . . .	81
66	<b>4</b>	<b>Total Hadronic Cross Section Measurement Methodology</b>	<b>87</b>
67	4.1	Event Selection . . . . .	88
68	4.1.1	Selection of Beamline Events . . . . .	88
69	4.1.2	Particle Identification in the Beamline . . . . .	89
70	4.1.3	TPC Selection: Halo Mitigation . . . . .	89

71	4.1.4	TPC Selection: Shower Removal . . . . .	90
72	4.2	Beamline and TPC Handshake: the Wire Chamber to TPC Match . .	91
73	4.3	The Thin Slice Method . . . . .	93
74	4.3.1	Cross Sections on Thin Target . . . . .	93
75	4.3.2	Not-so-Thin Target: Slicing the Argon . . . . .	94
76	4.3.3	Corrections to the Raw Cross Section . . . . .	96
77	4.4	Procedure testing with truth quantities . . . . .	97
78	<b>5</b>	<b>Data and MC preparation for the Cross Section Measurements</b>	<b>100</b>
79	5.1	Cross Section Analyses Data Sets . . . . .	100
80	5.2	Construction of a Monte Carlo Simulation for LArIAT . . . . .	102
81	5.2.1	G4Beamline . . . . .	102
82	5.2.2	Data Driven MC . . . . .	107
83	5.3	Estimate of Backgrounds in the Pion Cross Section . . . . .	110
84	5.3.1	Background from Pion Capture and Decay . . . . .	110
85	5.3.2	Contributions from the Beamline Background . . . . .	113
86	5.4	Estimate of Energy Loss before the TPC . . . . .	116
87	5.5	Tracking Studies . . . . .	120
88	5.5.1	Angular Resolution . . . . .	120
89	5.6	Calorimetry Studies . . . . .	126
90	5.6.1	Kinetic Energy Measurement . . . . .	126
91	<b>6</b>	<b>Negative Pion Cross Section Measurement</b>	<b>129</b>
92	6.1	Raw Cross Section . . . . .	129
93	6.1.1	Statistical Uncertainty . . . . .	131
94	6.1.2	Treatment of Systematics . . . . .	133
95	6.2	Corrections to the Raw Cross Section . . . . .	134
96	6.2.1	Background subtraction . . . . .	134

97	6.2.2 Efficiency Correction . . . . .	137
98	6.3 Results . . . . .	141
99	<b>7 Positive Kaon Cross Section Measurement</b>	<b>143</b>
100	7.1 Raw Cross Section . . . . .	143
101	7.2 Corrections to the Raw Cross Section . . . . .	145
102	7.3 Results . . . . .	147
103	<b>8 Conclusions</b>	<b>150</b>
104	<b>A Measurement of LArIAT Electric Field</b>	<b>151</b>
105	<b>B Additional Tracking Studies for LArIAT Cross Section Analyses</b>	<b>159</b>
106	B.0.1 Study of WC to TPC Match . . . . .	160
107	B.0.2 Tracking Optimization . . . . .	162
108	<b>C Energy Calibration</b>	<b>163</b>

# <sup>109</sup> Acknowledgements

<sup>110</sup> “*Dunque io ringrazio tutti quanti.*

<sup>111</sup> *Specie la mia mamma che mi ha fatto così funky.”*

<sup>112</sup> – Articolo 31, Tanqi Funky, 1996 –

<sup>113</sup> “*At last, I thank everyone.*

<sup>114</sup> *Especially my mom who made me so funky.”*

<sup>115</sup> – Articolo 31, Tanqi Funky, 1996 –

<sup>116</sup> “

# <sup>117</sup> Introduction

<sup>118</sup> This thesis work concerns the first measurement of the ( $\pi^-$ -Ar) total hadronic cross  
<sup>119</sup> section in the 100-1000 MeV kinetic energy range and the first measurement of the  
<sup>120</sup> ( $K^+$ -Ar) total hadronic cross section in the 100-650 MeV kinetic energy range. We  
<sup>121</sup> performed these measurements at the LArIAT experiment, a small (0.25 ton) Liquid  
<sup>122</sup> Argon Time Projection Chamber (LArTPC) on a beam of charged particles at the  
<sup>123</sup> Fermilab Test Beam Facility. Albeit particle and nuclear physics have a long history  
<sup>124</sup> of hadronic cross section measurements, the work outlined in this thesis presents a  
<sup>125</sup> new methodology – the “thin slice method” – for cross section measurements in argon,  
<sup>126</sup> possible only thanks to the detection capabilities of the LArTPC technology. The  
<sup>127</sup> combination of fine-grained tracking and excellent calorimetric information provided  
<sup>128</sup> by the LArTPC technology allows to see unprecedented details of particle interactions  
<sup>129</sup> in argon and, in LArIAT, to measure the kinetic energy of a hadron at each step  
<sup>130</sup> of the tracking. A renewed interest for precision measurements of hadronic cross  
<sup>131</sup> sections, particularly in argon, arises from the current panorama of experimental  
<sup>132</sup> particle physics at the intensity frontier.

<sup>133</sup> The discovery of the Higgs boson in 2012 marked the triumph of the Standard  
<sup>134</sup> Model of Particle Physics; exploring what lays beyond is the real challenge in our field  
<sup>135</sup> today. Since their formulation in 1930, neutrinos have been a source of surprises (and  
<sup>136</sup> Nobel Prizes) for particle physicists, tiny cracks in our understanding of Nature. In  
<sup>137</sup> particular, the discovery of neutrino oscillation represents the first evidence of physics

138 Beyond the Standard Model (BSM). From a theoretical point of view, the field is  
139 developing new theories to account for the small but non-zero mass of neutrinos,  
140 while trying to remain consistent with the rest of the Standard Model. From an  
141 experimental point of view, we are developing technologies and huge collaborations  
142 to probe these theories. As we enter the era of precision measurements of neutrino  
143 interaction, neutrinos might hold the key to the next generation of discoveries in  
144 particle physics.

145 Experimentally, precision measurements can be achieved only if the detector tech-  
146 nology is able to resolve the fine details of a neutrino interaction and to record a  
147 statistically relevant number of neutrinos. With “fine details” here we mean the abil-  
148 ity to distinguish the many products of the neutrino interaction, such as protons,  
149 pions, muons and electrons, and to measure their energy. Historically, bubble cham-  
150 ber neutrino detectors were the first revolution in neutrino detection: for example,  
151 the spatial resolution of Gargamelle allowed the discovery of neutrino neutral current  
152 interaction. Despite the high precision of bubble chambers images, this technology  
153 is hard to scale to massive size, making statistical analyses on neutrino interactions  
154 almost impossible to perform. To make up for the small neutrino interaction cross  
155 section, neutrino experiments moved to very large size, at the expenses of spatial  
156 precision. This is the case for the detectors which discovered neutrino oscillation:  
157 both Super-Kamiokande and SNO are massive Cherenkov detectors. With LArT-  
158 PCs, the field is gaining again bubble-chamber like precision but at massive scales.  
159 Following the recommendations of the latest Particle Physics Project Prioritization  
160 Panel [107], the US particle physics panorama is directing a substantial effort to-  
161 wards the exploration of the intensity frontier through the construction of massive  
162 LArTPCs. In particular, the near future will see the development of a Short Baseline  
163 Neutrino Program (SBN) and long baseline neutrino program (DUNE), both based  
164 on the LArTPC detector technology. The US liquid argon program has the potential

165 to answer many of the fundamental open questions in particle physics today, such  
166 as: is there a fourth generation neutrino? is CP violated in the lepton sector? are  
167 there any additional symmetries? and, can we find an indication of Grand Unified  
168 Theories?

169 The SBN program at Fermilab is tasked with conclusively addressing the existence  
170 of a fourth neutrino generation in the  $\Delta m^2 = \Delta m_{14}^2 \sim [0.1 - 10] \text{ eV}^2$  parameter space.  
171 The SBN program entails three surface LArTPCs positioned on the Booster Neutrino  
172 Beam at different distances from the neutrino production in oder to fully exploit the  
173 L/E dependence of the oscillation pattern: SBND (100 m from the decay pipe),  
174 MicroBooNE (450 m), and ICARUS (600 m). SBN will also perform an extensive  
175 program of neutrino cross section measurements, fundamental to abate systematics  
176 in the oscillation analyses in both SBN and DUNE.

177 DUNE has a vast neutrino and non-accelerator physics reach. For what it concerns  
178 neutrino physics, oscillation analyses in DUNE have the capability of solving the mass  
179 hierarchy and octant problem, and discovering CP violation in the neutrino sector.  
180 Besides its neutrino program, DUNE can open an experimental window on Grand  
181 Unified Theories (GUTs). GUTs could potentially answer fundamental questions  
182 such as the existence of non-zero neutrino masses and matter-antimatter asymmetry,  
183 explaining some “accidents” in the Standard Models, such as the exact cancellation of  
184 the proton and the electron charge. Directly probing GUTs at the unification energy  
185 scale is impossible by any foreseeable collider experiment. We then need an indirect  
186 proof such as baryon number violation, which is predicted by almost every GUT in the  
187 form of proton decay, bounded nucleon decay or  $n - \bar{n}$  oscillations on long time-scales.  
188 Historically, the main technology used in these searches has been water Cherenkov  
189 detectors, with Super-Kamiokande setting all the current experimental limits on the  
190 decay lifetimes at the order of  $\sim 10^{34}$  years. The DUNE far detector and its non-  
191 accelerator physics program is a interesting new actor on this stage. LArTPCs can in

192 fact complement nucleon decay searches in modes where water Cherenkov detectors  
193 are less sensitive, especially  $p \rightarrow K^+ \bar{\nu}$  [11].

194 Such a diverse physics program speaks to the versatility of the LArTPC technol-  
195 ogy. LArTPCs provide excellent electron/photon separation [9] lacking in Cherenkov  
196 detectors which can be leveraged to abate the photon background from neutral cur-  
197 rent interactions in  $\nu_e$  searches. LArTPCs also share superb tracking capability with  
198 bubble chamber detectors, with several additional benefits. They are electronically  
199 read out and self triggered detectors; they provide full 3D-imaging with millimeter  
200 resolution, precise calorimetric reconstruction and excellent particle identification.

201 The amount of information a LArTPC can provide makes these detectors rather  
202 complex: a series of dedicated measurements is necessary to obtain meaningful physics  
203 results from a LArTPC. The complexity of the LArTPC technology for neutrino  
204 detection is due to several reasons. Argon is a fairly heavy element, which means that  
205 nuclear effects play an important role in the looks of the interaction topology. For  
206 example, pions are one of the main products of neutrino interactions; yet, since data  
207 on charged particle interaction in argon is scarce, neutrino event generators have big  
208 uncertainties in the re-scattering simulation of pion in argon. The amount of details  
209 in an LArTPC event is easily parsed by human eye, but can make automatic event  
210 reconstruction rather challenging. Thus, reconstruction algorithms in LArTPC need  
211 to be tune to recognize the different topologies of the neutrino interaction products in  
212 argon. This is particularly true for pions, since they are an abundant product of the  
213 neutrino interactions: the occurrence of a pion interaction in argon can modify the  
214 topology of the neutrino event, causing a misidentification of the neutrino interaction.

215 The LArIAT [38] experiment is performing precise cross section measurements of  
216 charged particles in argon to bridge this gap of knowledge. The LArIAT LArTPC sits  
217 on a beam of charged particles at the Fermilab Test Beam Facility which provides  
218 charge particles of the type and energy range relevant for neutrino interaction of

219 both SBN and DUNE. The ( $\pi^-$ -Ar) hadronic cross section is a fundamental input for  
220 neutrino detectors in liquid argon, as pion interactions can modify the topology and  
221 energy reconstruction of neutrino events in the GeV range, where pion production  
222 is abundant. The ( $K^+$ -Ar) total hadronic differential cross section in LArIAT is  
223 particularly relevant for a high identification efficiency in the context of proton decay  
224 searches in DUNE in the  $p \rightarrow K^+ \bar{\nu}$  channel. In fact, the kaon-argon cross section  
225 affects the kaon topology by modifying the kaon tracking and energy reconstruction,  
226 impacting the basis for kaon identification in a LArTPC.

227 The cross section analyses exploit the totality of LArIAT’s experimental handles;  
228 they rely on beam line detector information as well as both calorimetry and tracking  
229 in the TPC. These analyses are LArIAT’s first physics results. In order to measure  
230 total hadronic argon cross sections, several steps are necessary. The analyses start by  
231 identifying a sample of the hadron of interest in the beam line and assessing the beam  
232 line contaminations. It proceeds with tracking the hadron candidates in the TPC and  
233 measuring their kinetic energy at each point in the tracking: the fine sampling of an  
234 hadron in the TPC forms the set of “incident” hadrons. Then, the hadronic interac-  
235 tion point is identified and the raw cross section is calculated. Two corrections are  
236 then applied to the raw cross section – a background subtractions and a correction  
237 for detector effects – to obtain the true cross section measurement.

238

239 This body of work is organized in 8 chapters. We provide a description of the  
240 theoretical framework for the measurements in Chapter 1. Chapter 2 outlines the  
241 LArTPC detector technology, while Chapter 3 describes LArIAT experimental setup.  
242 We present the event selection for both the pion and kaon analyses, as well as the  
243 “thin slice method” in Chapter 4. Chapter 5 describes the work done on the data  
244 and Monte Carlo samples in preparation of the cross section analyses. Chapter 6  
245 shows the results for the ( $\pi^-$ -Ar) total hadronic cross section measurement. Chapter

<sup>246</sup> 7 shows the results for the ( $K^+$ -Ar) total hadronic cross section measurement. We  
<sup>247</sup> draw the final remarks on this work in Chapter 8

<sup>248</sup> A series of additional studies and calibrations were necessary to perform the cross  
<sup>249</sup> section analyses. Appendix A shows a measurement of the LArIAT LArTPC electric  
<sup>250</sup> field using cosmic data. Appendix B shows an optimization of the tracking algorithms  
<sup>251</sup> geared towards maximizing the efficiency of finding the hadronic interaction point.  
<sup>252</sup> Appendix C shows the calorimetry calibration of the LArIAT LArTPC, which is a  
<sup>253</sup> pivotal measurement to enable any physics analysis with TPC data.

254 **Chapter 1**

255 **The theoretical framework**



256

– J. S. Bach, 1720 ca. –

257 In this chapter, we set the ( $\pi^-$ - Ar) and ( $K^+$ - Ar) total hadronic cross section  
258 measurements into the greater theoretical and phenomenological framework. We start  
259 by briefly describing the Standard Model (Section 1.1), with particular attention to  
260 neutrinos and neutrino interactions (Section 1.2). We then describe some of the  
261 open questions in neutrino physics today and Beyond Standard Model theories (1.3)  
262 setting the stage for the measurements reported in this work (Section 1.4).

263 **1.1 The Standard Model**

264 The Standard Model (SM) of particle physics is the most accurate theoretical descrip-  
265 tion of the subatomic world and, in general, one of the most precisely tested theories  
266 in the history of physics. The SM describes the strong, electromagnetic and weak  
267 interactions among elementary particles in the framework of quantum field theory,

268 accounting for the unification of electromagnetic and weak interactions for energies  
269 above the vacuum expectation value (VEV) of the Higgs field. The SM does not  
270 describe gravity or general relativity.

271 The Standard Model is a gauge theory based on the local symmetry group

$$G_{SM} = SU(3)_C \otimes SU(2)_L \otimes U(1)_Y \quad (1.1)$$

272 where the subscripts C indicates the conserved strong charge (color), and the  
273 subscripts Y indicates the conserved hypercharge. If we indicated with T the weak  
274 isospin T and with T3 its third component, hypercharge can be related to the electric  
275 charge Q through the Gell-Mann-Nishijima relation:

$$Q = \frac{Y}{2} + T_3. \quad (1.2)$$

276 In the quantum field framework, the SM fields correspond to the irreducible rep-  
277 resentations of the  $G_{SM}$  symmetry group. In particular, the particles are divided in  
278 two categories, fermions and bosons, according to their spin-statistics. Described by  
279 the Fermi-Dirac statistics, fermions have half-integer spin and are sometimes called  
280 “matter-particles”. Bosons or “force carriers” have integer spin, follow the Bose-  
281 Einstein statistics and mediate the interaction between fermions. The fundamental  
282 fermions and their quantum numbers are listed in Tab 1.1.

283 Quarks can interact via all three the fundamental forces; they are triplets of  
284  $SU(3)_C$ , that is they can exist in three different colors. If one chooses a base where  
285  $u$ ,  $c$  and  $t$  quarks are simultaneously eigenstates of both the strong and the weak  
286 interactions, the remaining eigenstates are usually written as  $d$ ,  $s$  and  $b$  for the strong  
287 interaction and  $d'$ ,  $s'$  and  $b'$  for the weak interaction, because the latter ones are  
288 the result of a CKM rotation on the first ones. Charged leptons interact via the  
289 weak and the electromagnetic forces, while neutrinos only interact via the weak force.

Generation	I	II	III	T	Y	Q
Leptons	$\begin{pmatrix} \nu_e \\ e \end{pmatrix}_L$	$\begin{pmatrix} \nu_\mu \\ \mu \end{pmatrix}_L$	$\begin{pmatrix} \nu_\tau \\ \tau \end{pmatrix}_L$	$1/2$ $-1/2$	$-1$ $-1$	$0$ $-1$
	$e_R$	$\mu_R$	$\tau_R$	$0$	$-2$	$1$
Quarks	$\begin{pmatrix} u \\ d' \end{pmatrix}_L$	$\begin{pmatrix} c \\ s' \end{pmatrix}_L$	$\begin{pmatrix} t \\ b' \end{pmatrix}_L$	$1/2$ $-1/2$	$1/3$ $1/3$	$2/3$ $-1/3$
	$u_R$ $d'_R$	$c_R$ $s'_R$	$t_R$ $b'_R$	$0$ $0$	$4/3$ $-2/3$	$2/3$ $-1/3$

Table 1.1: SM elementary fermionic fields. The subscripts L and R indicate respectively the negative chirality (left-handed) and the positive chirality (right-handed).

- 290 The gauge group univocally determines the number of gauge bosons that carry the  
 291 interaction; the gauge bosons correspond to the generators of the group: eight gluons  
 292 (g) for the strong interaction, one photon ( $\gamma$ ) and three bosons ( $W^\pm$ ,  $Z^0$ ) for the  
 293 electroweak interaction. A gauge theory by itself cannot provide a description of  
 294 massive particles, but it is experimentally well known that most of the elementary  
 295 particles have non-zero masses. The introduction of massive fields in the Standard  
 296 Model lagrangian would make the theory not gauge invariant, resulting ill-defined.  
 297 This problem is solved in the SM by the introduction of a scalar iso-doublet  $\Phi(x)$ , the  
 298 Higgs field, which gives mass to  $W^\pm$  and  $Z^0$  gauge bosons through the electroweak  
 299 symmetry breaking mechanism and to the fermions through Yukawa coupling [76, 77].  
 300 The discovery of the Higgs boson in 2012 by the LHC experiments [41, 42] marked  
 301 the ultimate confirmation of a long history of successful predictions by the SM.

302 **1.2 Neutrinos: tiny cracks in the Standard Model**

303 To our current knowledge, neutrinos are the most abundant fermion in the Universe.  
304 And yet, they are maybe the most mysterious particle in the SM: they generate  
305 theoretical puzzles and experimental challenges. In this section, we treat neutrinos  
306 within and beyond the SM and describe the make up of their interaction with matter.

307 **1.2.1 Neutrinos in the Standard Model**

308 Neutrino can be introduced in the SM as left-handed massless Weyl spinors. The  
309 Dirac equation of motion for a free field

$$(i\gamma^\mu \partial_\mu - m)\psi = 0 \quad (1.3)$$

310 for a fermionic field

$$\psi = \psi_L + \psi_R \quad (1.4)$$

311 is equivalent to the equations

$$i\gamma^\mu \partial_\mu \psi_L = m\psi_R \quad (1.5)$$

312

$$i\gamma^\mu \partial_\mu \psi_R = m\psi_L \quad (1.6)$$

313 for the chiral fields  $\psi_R$  and  $\psi_L$ , whose evolution in space and time is coupled  
314 through the mass  $m$ . If the fermion is massless, the chiral fields decouple and the  
315 fermion can be described by a single Weyl spinor with two independent compo-  
316 nents [116]. Pauli initially rejected the description of a physical particle through  
317 a single Weyl spinor because of its implication of parity violation. In fact, since  
318 the spatial inversion operator throws  $\psi_R \leftrightarrow \psi_L$ , parity is conserved only if both chi-  
319 ral components exist at the same time. For the neutrino introduction in the SM,  
320 experiments came in help of the theoretical description. The constraint of parity

<sup>321</sup> conservation weakened after Wu's experiment in 1957 [119]. Additionally, there was  
<sup>322</sup> no experimental indication for massive neutrinos, nor evidence of interaction via the  
<sup>323</sup> neutrino right-handed component.

<sup>324</sup> The symmetry group  $SU(2)_L \otimes U(1)_Y$  is the only group relevant for neutrino  
<sup>325</sup> interactions. The SM electroweak lagrangian is the most general renormalizable la-  
<sup>326</sup> grangian invariant under the local symmetry group  $SU(2)_L \otimes U(1)_Y$ . The lagrangian  
<sup>327</sup> couples the weak isotopic spin doublets and singlets described in Table 1.1 with the  
<sup>328</sup> gauge bosons  $A_a^\mu$  ( $a = 1, 2, 3$ ) and  $B^\mu$ , and Higgs doublet  $\Phi(x)$ :

$$\begin{aligned} \mathcal{L} = & i \sum_{\alpha=e,\mu,\tau} \bar{L}'_{\alpha L} \not{D} L'_{\alpha L} + i \sum_{\alpha=1,2,3} \bar{Q}'_{\alpha L} \not{D} Q'_{\alpha L} \\ & + i \sum_{\alpha=e,\mu,\tau} \bar{l}'_{\alpha R} \not{D} l'_{\alpha R} + i \sum_{\alpha=d,s,b} \bar{q}'^D_{\alpha R} \not{D} q'^D_{\alpha R} + i \sum_{\alpha=u,c,t} \bar{q}'^U_{\alpha R} \not{D} q'^U_{\alpha R} \\ & - \frac{1}{4} A_{\mu\nu} A^{\mu\nu} - \frac{1}{4} B_{\mu\nu} B^{\mu\nu} \\ & + (D_\rho \Phi)^\dagger (D^\rho \Phi) - \mu^2 \Phi^\dagger \Phi - \lambda (\Phi^\dagger \Phi)^2 \\ & - \sum_{\alpha,\beta=e,\mu,\tau} \left( Y_{\alpha\beta}^l \bar{L}'_{\alpha L} \Phi l'_{\beta R} + Y_{\alpha\beta}^{l*} \bar{l}'_{\beta R} \Phi^\dagger L'_{\alpha L} \right) \\ & - \sum_{\alpha=1,2,3} \sum_{\beta=d,s,b} \left( Y_{\alpha\beta}^D \bar{Q}'_{\alpha L} \Phi q'^D_{\beta R} + Y_{\alpha\beta}^{D*} \bar{q}'^D_{\beta R} \Phi^\dagger Q'_{\alpha L} \right) \\ & - \sum_{\alpha=1,2,3} \sum_{\beta=u,c,t} \left( Y_{\alpha\beta}^U \bar{Q}'_{\alpha L} \tilde{\Phi} q'^U_{\beta R} + Y_{\alpha\beta}^{U*} \bar{q}'^U_{\beta R} \tilde{\Phi}^\dagger Q'_{\alpha L} \right). \end{aligned} \quad (1.7)$$

<sup>329</sup> The first two lines of the lagrangian summarize the kinetic terms for the fermionic  
<sup>330</sup> fields and their coupling to the gauge bosons  $A_a^{\mu\nu}$ ,  $B^{\mu\nu}$ <sup>1</sup>. The third line describes  
<sup>331</sup> the kinetic terms and the self-coupling terms of the gauge bosons. The forth line is  
<sup>332</sup> the Higgs lagrangian, which results in the spontaneous symmetry breaking. The last  
<sup>333</sup> three lines describe the Yukawa coupling between fermions and the Higgs field, origin  
<sup>334</sup> of the fermions' mass.

---

1. In gauge theories the ordinary derivative  $\partial_\mu$  is substituted with the covariant derivative  $D_\mu$ . Here  $D_\mu = \partial_\mu + igA_\mu \cdot I + ig'B_\mu \frac{Y}{2}$ , where  $I$  and  $Y$  are the  $SU(2)_L$  and  $U(1)_Y$  generators, respectively.

335      The coupling between left-handed and right-handed field generates the mass term  
336 for fermions. The SM assumes only left-handed components for neutrinos, thus im-  
337 plying zero neutrino mass. Since any linear combination of massless fields results in a  
338 massless field, the flavor eigenstates are identical to the mass eigenstates in the SM.

### 339 1.2.2 Neutrino Oscillations

340      The determination of the flavor of a neutrino dynamically arises from the correspond-  
341 ing charged lepton associated in a change current interaction; for example, a  $\nu_e$  is a  
342 neutrino which produces an  $e^-$ , a  $\bar{\nu}_\mu$  is a neutrino which produces a  $\mu^+$ , *etc.* The  
343 neutrino flavor eigenstates  $|\nu_\alpha\rangle$ , with  $\alpha = e, \mu, \tau$ , are orthogonal to each other and  
344 form a base for the weak interaction matrix.

345      Overwhelming experimental data show that neutrinos change flavor during their  
346 propagation [102]. This phenomenon, called “neutrino oscillations”, was predicted  
347 first by Bruno Pontecorvo in 1957 [103]. Neutrino oscillations are possible only if  
348 the neutrino flavor eigenstate are not identical to the mass eigenstates. Thus, the  
349 observation of neutrino oscillation results in the first evidence of physics beyond the  
350 Standard Model. A minimal extension of the SM introduces three mass eigenstates,  
351  $|\nu_i\rangle$  ( $i = 1, 2, 3$ ), whose mass  $m_i$  is well defined. The unitary Pontecorvo-Maki-  
352 Nakagawa-Sakata matrix transforms the mass base into the flavor base as follows

$$|\nu_\alpha\rangle = U_{PMNS} |\nu_i\rangle, \quad (1.8)$$

353      with

$$U_{PMNS} = \begin{bmatrix} c_{12} & s_{12} & 0 \\ -s_{12} & c_{12} & 0 \\ 0 & 0 & 1 \end{bmatrix} \begin{bmatrix} c_{13} & 0 & s_{13}e^{-i\delta} \\ 0 & 1 & 0 \\ -s_{13}e^{-i\delta} & 0 & c_{13} \end{bmatrix} \begin{bmatrix} 1 & 0 & 0 \\ 0 & c_{23} & s_{23} \\ 0 & -s_{23} & c_{23} \end{bmatrix} \begin{bmatrix} e^{i\alpha_1} & 0 & 0 \\ 0 & e^{i\alpha_2} & 0 \\ 0 & 0 & 1 \end{bmatrix} \quad (1.9)$$

354 where  $c$  e  $s$  stand respectively for cosine and sine of the corresponding mixing  
 355 angles ( $\theta_{12}$ ,  $\theta_{23}$  and  $\theta_{13}$ ),  $\delta$  is the Dirac CP violation phase,  $\alpha_1$  and  $\alpha_2$  are the eventual  
 356 Majorana CP violation phases. Experimental results on neutrino oscillations are  
 357 generally reported in terms of the mixing angles and of the squared mass splitting  
 358  $\Delta m_{ab}^2 = m_a^2 - m_b^2$ , where  $a$  and  $b$  represent the mass eigenstates. A summary of the  
 359 current status of experimental results, albeit partial, is given in table 1.2.

Table 1.2: Summary of experimental results on neutrino oscillation parameters. **ADD CITATIONS**

	Value	Precision	Experiment
$\theta_{23}$	$45^\circ$	9.0%	Super Kamiokande, MINOS,
$-\Delta m_{32}^2$	$2.5 \cdot 10^{-3} \text{ eV}^2$	1.8%	Nova, MACRO
$\theta_{12}$	$34^\circ$	5.8%	SNO, Gallex,
$-\Delta m_{12}^2$	$7.4 \cdot 10^{-5} \text{ eV}^2$	2.8%	SAGE, KamLAND
$\theta_{13}$	$9^\circ$	4.7%	DAYA Bay,
$-\Delta m_{32}^2$	$2.5 \cdot 10^{-3} \text{ eV}^2$	1.8%	RENO

### 360 1.2.3 Make up of Neutrino Interactions

361 All neutrino experiments involving the detection of single neutrinos are concerned  
 362 with neutrino interactions (and neutrino cross sections) on nuclei. Given the invis-  
 363 ible nature of the neutrino, characterizing the products of its interaction is the only  
 364 method to a) assess the neutrino presence, b) detect its flavor in case of a charge  
 365 current interaction and c) eventually reconstruct its energy.

366 Historically, neutrino interactions with the nucleus in the GeV region are divided  
 367 into three categories into three categories whose contributions change as a function

368 of increasing neutrino energy:: quasi elastic (QE), resonant (RES), and deep inelastic  
369 (DIS) scattering. All current and forthcoming oscillation experiments on neutrino  
370 beams live in the 0.1-10 GeV transition region, which encompasses the energy where  
371 the QE neutrino-nucleus interaction transitions into RES and then into DIS. For  
372 scattering off free nucleons, neutrino and antineutrino QE charge current scattering  
373 refers to the process  $\nu_l n \rightarrow l^- p$  and  $\bar{\nu}_l p \rightarrow l^+ n$  where a charged lepton and single  
374 nucleon are ejected in the elastic interaction. Resonant scattering refers to an inelas-  
375 tic collision producing a nucleon excited state ( $\Delta, N^*$ ) – the resonance – which then  
376 quickly decays, most often to a nucleon and single-pion final state. DIS refers to the  
377 head-on collision between the neutrino and a parton inside the nucleon, producing  
378 hadronization and subsequent abundant production of mesons and nucleons. In addi-  
379 tion to such interactions between the neutrino and a single component of the nucleus,  
380 neutrinos can also interact with the nucleus as a whole, albeit more rarely, a well  
381 documented process called coherent meson production scattering [58]; the signature  
382 of such process is the production of a distinctly forward-scattered single meson final  
383 state, most often a pion. This simple picture of neutrino interactions works rather  
384 well for scattering off of light nuclear targets, such as the H<sub>2</sub> and D<sub>2</sub> of bubble cham-  
385 ber experiments [64], but the complexity of the nuclear structure for heavier nuclei  
386 such as argon complicates this model.

387 As we will discuss in Chapter 2, the properties of argon make it a good candidate  
388 for an interacting medium in neutrino experiments; in particular the density of its  
389 interaction centers increases the yield of neutrino interactions and allows for relatively  
390 compact detectors. Though, the choice of a relatively heavy nuclear target comes at  
391 the cost of enhancing nuclear effects which modify the kinematic and final state of  
392 the neutrino interaction products.

393 Nuclear effects can potentially affect neutrino event rates, final state particle emis-  
394 sion, neutrino energy reconstruction, and the neutrino/antineutrino ratios, carrying

395 deep implications for oscillation experiments. Even in the case of “simple” QE scattering,  
396 intra-nuclear hadron rescattering and correlation effects between the target  
397 nucleons can cause the ejection of additional nucleons in the final state, modifying  
398 the final state kinematics and topology. In the case of resonant and DIS scattering,  
399 the hadronic interactions of meson and nucleons produced in the decay of the res-  
400 onance or during hadronization complicate this picture even more. A large source  
401 of uncertainty in modeling nuclear effects in neutrino interactions come from mesons  
402 interactions (and re-interactions) in the nucleus, e.g., pion re-scattering, charge ex-  
403 change, and absorption.

404 A renewed interest for neutrino cross section measurements surged in recent years,  
405 along with a lively discussion on the data reporting; the historical method of reporting  
406 the neutrino cross section as a function of the neutrino energy or momentum trans-  
407 fered shakes under the weight of its dependency on the chosen nuclear model. On one  
408 hand, correcting for nuclear effects in neutrino interaction can introduce unwanted  
409 sources of uncertainty and model dependency especially due to the mis-modeling of  
410 the meson interactions. On the other, avoiding this correction makes a comparison  
411 between neutrino interactions on different target nuclei extremely difficult.

412 Data on neutrino scattering off many different nuclei are available for both charged  
413 current (CC) and neutral current (NC) channels, as summarized in [64]. A summary  
414 of the results on QE, resonant and DIS scattering for neutrinos and antineutrinos from  
415 accelerators on different target is reported in Figure 1.1, where the (NUANCE) [37]  
416 event generator is used as comparison with the theory.

### 417 1.3 Beyond the Standard Model

418 The discovery of neutrino oscillation and its implication of non-zero neutrino mass  
419 mark the beginning of a new, exciting era in neutrino physics: the era of physics Be-

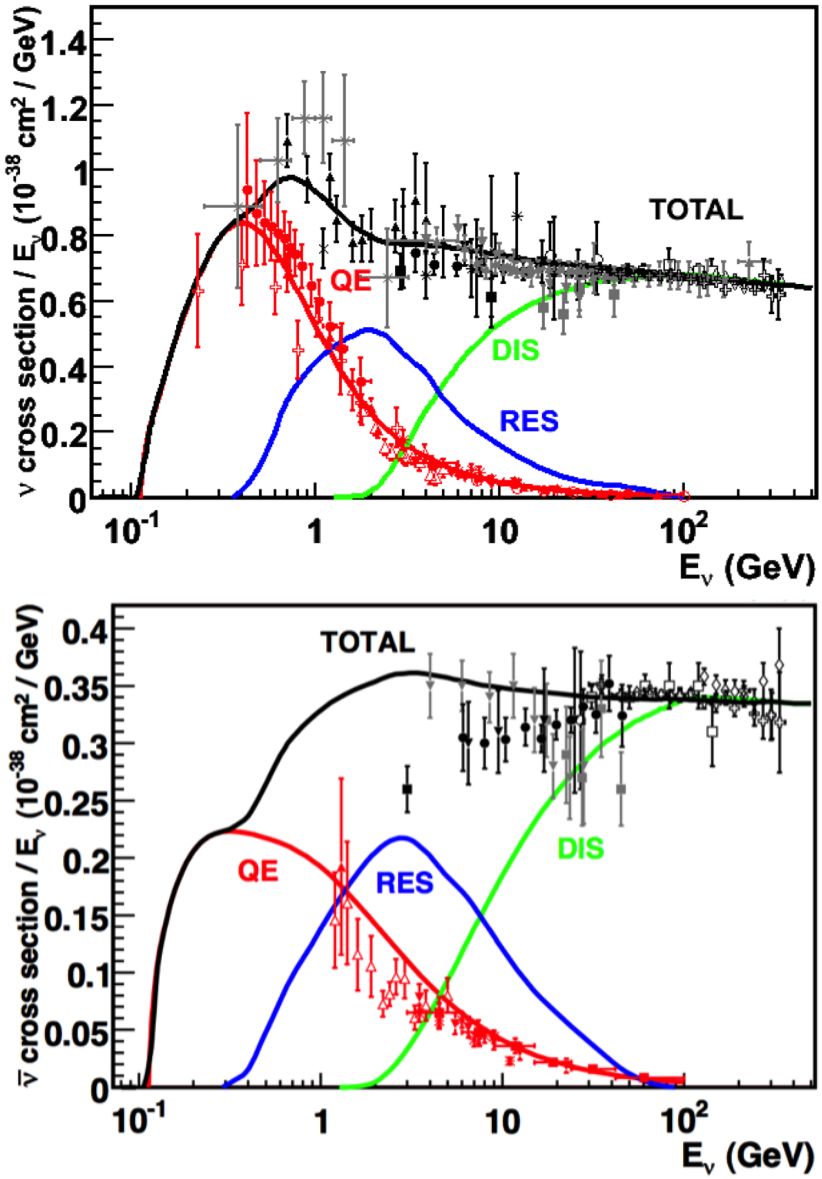


Figure 1.1: Total neutrino (top) and antineutrino (bottom) CC cross sections per nucleon divided by neutrino energy as a function of energy as reported in [64]. Predictions for the total (black), the QE (red), resonant (blue) and DIS (green) are provided by the NUANCE generator. The quasi-elastic scattering data and predictions have been averaged over neutron and proton targets (isoscalar target).

420 yond the Standard Model (BSM) at the intensity frontier. We are currently searching  
421 for new, deeper theories that can accommodate neutrinos with tiny but non-zero  
422 masses, while remaining consistent with the rest of the Standard Model.

423 **1.3.1 Open Questions in Neutrino Physics**

424 On one hand, the last three decades of experiments in neutrino oscillations brought  
425 spectacular advancements in the understanding of the oscillations pattern, measuring  
426 the neutrino mixing angles and mass splitting with a precision of less than 10%. On  
427 the other, they opened the field for a series of questions needing experimental answers.

428 **Sterile neutrinos.** Hints to the existence of at least one additional neutrino,  
429 in the form of various anomalies, have been puzzling physicists almost from the be-  
430 ginning of neutrino oscillation searches. Originally designed to look for evidence of  
431 neutrino oscillation, the Liquid Scintillator Neutrino Detector (LSND) [54] provided  
432 a first conflicting result with the Standard Model expectation of only three neutrinos.  
433 A second conflicting result has also been provided by the MiniBooNE experiment [50].

434 The LSND and MiniBooNE  $\nu_e$  and  $\bar{\nu}_e$  appearance results, known as the “LSND and  
435 MiniBooNE anomalies” [14, 15, 23], may be interpreted under the assumption of a new  
436 right-handed neutrino. The additional neutrino needs to be “sterile”, i.e needs not  
437 to couple with the electroweak force carriers, in order to meet the constraint imposed  
438 by the measurement of the width of the Z boson [2]. The new sterile neutrino would  
439 mainly be composed of a heavy neutrino  $\nu_4$  with mass  $m_4$  such that  $m_1, m_2, m_3 \ll m_4$   
440 and  $\Delta m^2 = \Delta m_{14}^2 \sim [0.1 - 10] \text{ eV}^2$ . The introduction of sterile neutrinos is an ap-  
441 pealing line of thinking, since this renormalizable generalization of the SM has the  
442 potential to impact long standing questions in high energy physics and cosmology:  
443 light sterile neutrinos are candidates for dark matter particles and there are ideas  
444 that the theory could be adjusted to explain the baryon asymmetry of the Universe  
445 via leptogenesis [72].

446       **CP Violation In Lepton Sector.** The measurement of non-zero value for the  
 447       oscillation parameter  $\theta_{13}$  allows the exploration of low-energy CP violation in the lep-  
 448       ton sector at neutrino long baseline oscillation experiments, enabling the possibility  
 449       to measure the Dirac CP-violating phase  $\delta$ . Exciting theoretical results tie  $\delta$  directly  
 450       to the generation of the baryon asymmetry of the Universe at the Grand Unified  
 451       Theory scale **a couple of cit would be nice**. According to the theoretical model de-  
 452       scribed in [101], for example, leptogenesis can be achieved if  $|\sin \theta_{13} \sin \delta| > 0.11$ , i.e.  
 453        $\sin \delta > 0.7$ .  
 454       The asymmetry in the oscillation probability of neutrinos and antineutrinos is the ob-  
 455       servable sensitive to the Dirac CP-violating phase  $\delta$  leveraged in neutrino oscillation  
 456       experiments. Using the parameterization of the PMNS matrix shown in Equation  
 457       1.9, the difference between the probability of  $\nu_e \rightarrow \nu_\mu$  oscillation and the probability  
 458       of  $\bar{\nu}_e \rightarrow \bar{\nu}_\mu$  oscillation can be parametrized as follows [39],

$$P_{\nu_e \rightarrow \nu_\mu} - P_{\bar{\nu}_e \rightarrow \bar{\nu}_\mu} = J \cos \left( \pm \delta - \frac{\Delta_{31} L}{2} \right) \sin \left( \frac{\Delta_{21} L}{2} \right) \sin \left( \frac{\Delta_{31} L}{2} \right) \quad (1.10)$$

459       where

$$J = \cos \theta_{13} \sin 2\theta_{13} \sin 2\theta_{12} \sin 2\theta_{23} \quad (1.11)$$

460       is the Jarlskog invariant [82],  $L$  the neutrino baseline, i.e. the distance between  
 461       the neutrino production and detection points, and  $\Delta_{ab}$  a factor proportional to the  
 462       sign and magnitude of the mass splitting. From these equations, it is clear how the  
 463       relative large value of  $\theta_{13}$  is a happy accident necessary not to completely suppress  
 464       the sensitivity to CP violation. The equations also show how the sensitivity to  $\delta$  is  
 465       tied to the measurement of the least precisely measured mixing angle,  $\theta_{23}$  (via the  
 466        $\sin 2\theta_{23}$  term) and to an other unknown quantity, the neutrino “mass hierarchy” (via  
 467       the  $\Delta_{ab}$  terms). The precise determination of  $\theta_{23}$  is often referred as to “the octant  
 468       problem”. Current experimental results [3, 12] are consistent with  $\theta_{23} = 45^\circ$ , which

469 would imply maximal mixing between  $\nu_\mu$  -  $\nu_\tau$ , hinting to an intriguing new symmetry.  
470 Therefore, a precise measurement of  $\theta_{23}$  is of great interest for theoretical models of  
471 quark-lepton universality [75, 93, 106], whose quark and lepton mixing matrices are  
472 proportional to the deviation of  $\theta_{23}$  from 45°.

473 **Neutrino mass hierarchy.** The “mass hierarchy” problem refers to the unknown  
474 ordering of the value of absolute mass of the neutrino mass eigenstates. Current  
475 oscillation experiments are sensitive only to the magnitude of the mass splitting, and  
476 not directly to its sign. In a framework where the lightest neutrino mass (arbitrarily)  
477 corresponds to the first eigenstate  $m_1$ , it is unknown whether  $m_2 - m_1 < m_3 - m_1$   
478 (Normal Hierarchy) or  $m_2 - m_1 > m_3 - m_1$  (Inverted Hierarchy). The mass hierarchy  
479 affects not only the sensitivity to CP violation searches in long baseline oscillation  
480 experiments, but also the sensitivity to determine whether neutrinos are Majorana  
481 particles in neutrinoless double beta decay experiments.

482 **Majorana or Dirac?** Evidence of neutrino oscillations demands the introduction  
483 of a mechanism which can give mass to the neutrinos. This mechanism should possibly  
484 also explain why neutrino masses are at least six orders of magnitude lower than the  
485 electron mass (the second lightest SM fermion). In a description of neutrinos as Dirac  
486 4-component spinors, the neutrino field acquires mass via the Higgs mechanism as  
487 any other fermion of the SM. In this case, the neutrino mass is given by  $m_a = \frac{y_a^\nu v}{\sqrt{2}}$ ,  
488 where  $v$  is the Higgs VEV and  $y_a^\nu$  is the Yukawa coupling between the Higgs and the  
489 neutrino. The smallness of neutrino masses can only be pinned on a tiny Yukawa  
490 coupling which is not justified by the theory.

491 In 1937, Majorana demonstrated that the introduction of a two components spinor is  
492 sufficient to describe a massive fermion [92]. The Dirac equations of motion for the  
493 chiral fields (equations 1.5 and 1.6) hold true in the case of two components spinor  
494 under the assumption that the chiral components  $\psi_R$  and  $\psi_L$  are correlated through  
495 the charge conjugation matrix  $\mathcal{C}$ ,  $\psi_R = \mathcal{C}\bar{\psi}_L$ . Therefore the theory is applicable only

496 to neutral fermions. Neutrinos are the only neutral elementary particles in the SM  
497 – the only possible Majorana particle candidate. This theory constructs a neutrino  
498 Majorana mass term  $\mathcal{L}_5$  of the following form in the Higgs unitary gauge

$$\mathcal{L}_5 = \frac{1}{2} \frac{gv^2}{\mathcal{M}} \nu_L^T \mathcal{C}^\dagger \nu_L, \quad (1.12)$$

499 where  $g$  is the coupling coefficient,  $v$  the Higgs VEV and  $\mathcal{M}$  a constant with the  
500 dimension of the mass proportional to the scale of new physics. The  $\mathcal{L}_5$  term would  
501 introduce a non-renormalizable term in the lagrangian, since it has dimensions of  
502 energy to the fifth power. This is not allowed in the SM lagrangian; however, the  
503 existence of such terms is plausible if we consider the SM as an effective theory  
504 at low energy, manifestation of the symmetry breaking of a more general theory at  
505 higher energy, e.g. a Grand Unified Theory (GUT), and not the definitive theory.  
506 The mass term in eq 1.12 implies the neutrino mass to be  $m = \frac{gv^2}{\mathcal{M}}$ . The coupling  
507 coefficient can be of the order of any other fermion's coupling coefficient, since the  
508 smallness of neutrino masses is achieved by the big value of the new physics mass  
509 scale alone. This vanilla formulation is the conceptual basis for many flavors of *see-*  
510 *saw mechanism* [121], which we will not discuss here in any detail. However, it is  
511 fascinating how the puzzle of the neutrino mass hints to the existence of a deeper and  
512 more complete theory.

513 From a kinematic point of view, Dirac and Majorana neutrinos satisfy the same  
514 energy-momentum dispersion relationship. Thus, it is impossible to discern the neu-  
515 trino nature through kinematic effects such as neutrino oscillations. Neutrinoless  
516 double beta decay searches are the most promising way to understand the nature of  
517 the neutrino and are therefore subject of great theoretical and experimental interest.  
518 Observation of the lepton number violating process  $0\nu\beta\beta$  would imply neutrinos have  
519 a Majorana component. Depending on the mass hierarchy, the theory also predicts

520  $0\nu\beta\beta$  exclusion regions and confirmation of the sole Dirac component for neutrinos [44].

522

### 523 1.3.2 Towards a more fundamental theory: GUTs

524 Despite its highly predictive power, a number of conceptual issues arise in the SM  
525 which disfavor it to be a good candidate for a fundamental theory.

526 The SM does not include a suitable dark matter candidate and a mechanisms  
527 that accounts for the baryon asymmetry of the universe. Additionally, up to a total  
528 of 25 parameters remain seemingly arbitrary and need to be fitted to data: 3 gauge  
529 couplings, 9 charged fermion masses, 3 mixing angles and one CP phase in the CKM  
530 matrix, the Higgs mass and quartic coupling,  $\theta_{QCD}$ , 3 neutrino mixing angles, 1 Dirac  
531 phase and, eventually, 2 Majorana phases.

532 From a group theory perspective, the SM has a rather complex group structure,  
533 where a gauge group is formed with the direct product of other three groups as shown  
534 in eq. 1.1. Drawing a parallel with the electroweak symmetry breaking mechanism,  
535 where the  $SU(2)_L \otimes U(1)_Y$  is recovered from  $U(1)_{EM}$ , an interesting line of simplification  
536 for the SM group structure would be to devise a similar mechanism where  
537  $SU(3)_C \otimes SU(2)_L \otimes U(1)_Y$  is recovered from an hypothetical larger group. IS THIS  
538 CORRECT? Just as the electroweak unification becomes evident at energies higher  
539 than the Higgs VEV, a direct manifestation of Grand Unification Theories (GUTs)  
540 would occur at even higher energies.

541 As the smallness of neutrino masses suggests the existence of a higher mass scale,  
542 an other, even stronger, hint to Grand Unification comes from the slope of running  
543 of the coupling constants. The coupling constants for the electromagnetic, weak and  
544 strong interactions in the SM vary as a function of the interaction energy as shown  
545 in figure 1.2; they do not exactly meet under the current experimental constraints,

<sup>546</sup> but their trend is interesting enough to push for the construction of theories where  
<sup>547</sup> perfect unification is achieved through the addition of new particles.

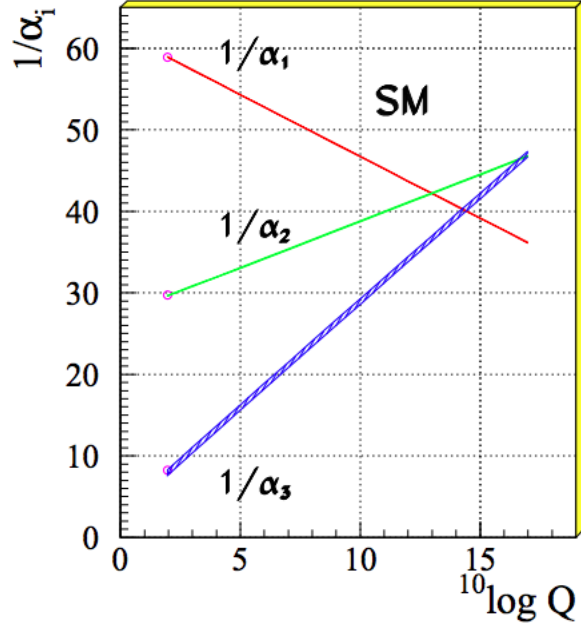


Figure 1.2: Evolution of the inverse of the three coupling constants in the Standard Model as a function of the momentum transferred, [86].

**SU(5).** The smallest simple group containing  $SU(3)_C \otimes SU(2)_L \otimes U(1)_Y$  is  $SU(5)$ , as shown first by Georgi and Glashow in [68]. Quarks and leptons in this group fit the  $\bar{5}$  and  $10$  representations. The representation for left-handed fermions are the following

$$\bar{5} = (\nu_e, e^-)_L + \bar{d}_L \quad (1.13)$$

$$10 = e_L^+ + \bar{u}_L + (u, d)_L, \quad (1.14)$$

<sup>548</sup> while the boson structure gains a new couple of super heavy bosons (X,Y)

$$24 = \underbrace{(8, 1)}_{\text{gluons}} + \underbrace{(1, 3) + (1, 1)}_{W^\pm, Z, \gamma} + \underbrace{(3, 2) + (\bar{3}, 2)}_{X, Y \text{ bosons}}. \quad (1.15)$$

<sup>549</sup> Nice features such as charge quantization and the identity between the positron

and proton charge value come directly from the group structure. The new super heavy bosons are colored and form a weak doublet. Their are the mediator of the interaction that turns quarks into leptons, leading to predict the existence of processes that violate baryon number, such as  $p \rightarrow \pi^0 + e^+$  (see fig 1.8, right). The prediction for proton decay lifetime,  $\tau_p \sim \frac{M_X^4}{m_p^5} \sim 10^{30 \pm 1.5}$  years, is unfortunately experimentally disproved by IMB and Super-Kamiokande [4, 28].

**SO(10).** More complicated group structures, such as SO(10) are still viable candidates for GUT. SO(10) includes the same type of  $X$  and  $Y$  bosons as SU(5). Right-handed massive neutrinos are embedded in the construction of the irreducible representation of SO(10). Different patterns of SO(10) symmetry breaking to recover the SM are possible and lead to different predictions for the proton decay lifetime; some of these predictions are not excluded by the experiments [87].

**SUSY GUTs.** Supersymmetry theories allow for another family of GUTs. In SUSY, every fundamental particle in the SM has a “superpartner”, identical in each quantum number except for the spin-statistics: the fermion supersymmetric partners are bosons and vice versa. Collider experiments (mainly LHC) constrain the mass of the supersymmetric partners to be very heavy [?]. The SU(5), SU(10) groups with a SUSY twist are the basic groups for SUSY GUTs. From the phenomenology point of view, SUSY models tend to push the proton decay life time higher by a factor of four, they solve the “hierarchy problem”, and they also predict new channels for the proton decay. In particular they predict the presence of kaons in the final product, with a dominant mode of  $p \rightarrow K^+ \bar{\nu}$ . Predictions on the proton decay lifetime depend on the chosen SUSY model; again, some of the predictions are not excluded by the experiments [90, 91, 110].

574 **1.4 Motivations for Hadronic Cross Sections in Ar-**

575 **gon**

576 Critical challenges await the next decade of high energy physics at the intensity  
577 frontier. Following the recommendation of the latest Particle Physics Project Priori-  
578 tization Panel [107], the US is dedicating substantial resources to the development of  
579 a short- and long- baseline neutrino program to address many of open questions in  
580 neutrino physics today. This program pivots on the Liquid Argon Time Projection  
581 Chamber (LArTPC) detector technology which will be described in Chapter 2.

582 The main goals of these research programs include:

- 583 - the assessment of the existence of right-handed sterile neutrinos via the study  
584 of accelerator neutrinos on a short baseline (SBN),
- 585 - the determination of the sign of  $\Delta m_{13}^2$  (or  $\Delta m_{23}^2$ ), i.e., the neutrino mass hier-  
586 archy via the study of accelerator neutrinos on a long baseline (DUNE),
- 587 - the determination of the octant, i.e. whether  $\theta_{23}$  is maximal, via the study of  
588 accelerator neutrinos on a long baseline (DUNE),
- 589 - the determination the status of CP symmetry in the lepton sector, via the study  
590 of accelerator neutrinos on a long baseline (DUNE),
- 591 - the search for observables predicted by GUTs, such as proton decay via the  
592 study of non accelerator physics in massive underground detectors (DUNE).

593 **1.4.1 Pion-Argon Total Hadronic Cross Section**

594 This section outlines the importance of the pion-argon total hadronic cross section in  
595 the context of the current and upcoming liquid argon neutrino experiments, SBN and  
596 DUNE. We describe the signal signature and historic measurements of pion-nucleus

597 cross section, as well as the implementation of these cross sections in the current  
598 version of the simulation package used by LArIAT.

599  **$\pi^-$ Ar Cross Section in the Context of Neutrino Searches**

600 As outlined in 1.2.3, neutrino experiments use the products of neutrino interactions  
601 to identify the energy and flavor of the incoming neutrino. Pions are a common  
602 product of neutrino interaction, especially in resonant scattering, DIS and coherent  
603 pion production. For neutrino experiments in argon, there are two main reasons  
604 why understanding pion hadronic interactions with argon is important: to model the  
605 behavior of the pion inside the target nucleus and to model the behavior of the pion  
606 during its propagation inside the detector medium.

607 Assumptions on the nuclear modeling and on the interaction of hadrons inside the  
608 nucleus performed at the level of the neutrino event generator bridge the measure-  
609 ment of the products of a neutrino interaction to the reconstruction of the neutrino  
610 energy and flavor. Thus, understanding pion hadronic interactions with the nucleus is  
611 particularly important to model correctly resonant, DIS and coherent pion production  
612 in neutrino interactions. For example, in case of resonant scattering,

$$\nu_l + N \rightarrow l + \Delta/N^* \rightarrow l + \pi + N', \quad (1.16)$$

613 the  $\Delta$  and  $N^*$  and excited states will decay hadronically in matters of  $\sim 10^{-24}$  s  
614 inside the nucleus producing pions which will have many chances to re-interact  
615 as they exit the target medium. The decay modes for the lower mass  $\Delta$  (1232) and  
616  $N^*(1440)$  are listed in table 1.3.

617 The key elements of a neutrino event generators for resonance and DIS events  
618 are the nuclear model and the hadron treatment (both production and transporta-  
619 tion). We illustrate here the conceptual basis of the GENIE Neutrino Generator [18]

620 as an example, since GENIE is one the most popular event generators for liquid ar-  
621 gon experiments. For example, the nuclear model used by GENIE for all processes  
622 is a Relativistic Fermi Gas (RFG) model modified to incorporate nucleon-nucleon  
623 correlations [30]. This means that the initial momentum and binding energy of the  
624 struck nucleon is determined by assuming nucleons inside the nucleus are quasi-free,  
625 acting independently in the mean field of the nucleus. For  $A > 20$  such as argon, the  
626 2-parameter Woods-Saxon shell model for density function is used. The GENIE mod-  
627 ule INTRANUKE [85] is used to simulate final-state interactions (FSI) which model  
628 hadron re-interactions inside the nucleus. This module places the outgoing parti-  
629 cles in the nucleus and propagates them using the “hA model”. In the INTRANUKE  
630 hA model, hadrons can undergo at most one FSI per event. When possible, external  
631 hadron-nucleus scattering data are used to tune INTRANUKE. Since no data is avail-  
632 able for Argon, GENIE uses an interpolation of data from heavier and lighter nuclei  
633 for the pion-argon cross section leading to large (10?s of %) resultant uncertainties in  
634 the INTRANUKE module.

635 Once the pion has left the target nucleus, the pion-argon hadronic cross section also  
636 plays an important role in the pion transportation inside the argon medium: processes  
637 such as pion absorption or pion charge exchange can greatly modify the topology of  
638 a neutrino interactions in the detector and lead to significant modifications in the  
639 event classification. Being able to reconstruct the details of pions inside the detector  
640 is an imperative for modern liquid argon neutrino experiment to achieve the design  
641 resolution for their key physics measurements.

## 642 $\pi^-$ -Ar Hadronic Interaction: Signal Signatures

643 Strong hadronic interaction models [49, 70] predict the pion interaction processes with  
644 argon in the [100 - 1200] MeV energy range. The total hadronic  $\pi^-$ -Ar interaction  
645 cross section is defined as the one related to the single process driven only by the

646 strong interaction which is dominant in the considered energy range. In measuring  
647 the “total” cross section, we include both the elastic and reaction channels, regardless  
648 of the final state,

$$\sigma_{Tot} = \sigma_{Elastic} + \sigma_{Reaction}; \quad (1.17)$$

649 the reaction channel is further characterized by several exclusive channels with defined  
650 topologies,

$$\sigma_{Reaction} = \sigma_{Inelastic} + \sigma_{abs} + \sigma_{chex} + \sigma_{\pi prod}. \quad (1.18)$$

651 A summary of the pion final states in order of pion multiplicity for the reaction  
652 channel is given in table 1.4. Pion capture and pion decay at rest dominate the  
653 cross section under 100 MeV. We define pion capture as the process determining the  
654 formation of a pionic atom and the subsequent pion’s end of life. Stopping negative  
655 pions can form pionic argon, where the negative pion plays the role of an orbital  
656 electron. Since the pion mass is two orders of magnitude greater than the electron  
657 mass, the spatial wave form of the pion will overlap more with the nucleus compared  
658 to the electron case. After the electromagnetic formation of the pionic atom, the  
659 pion will get quickly absorbed by the nucleus, which is put in an excited state. The  
660 nucleus then de-excites with the emission of low energy nucleons and photons. Pion  
661 capture is dominant compared to pion decay, the other important process for very  
662 low energy pions. The decay of a pion is governed by the weak force; the pion decay  
663 life time is  $\tau_\pi = 2.6 \times 10^{-8}$  s and the main decay mode is  $\pi^- \rightarrow \mu^- + \bar{\nu}_\mu$  (BR 99.98%).  
664 Since pion capture can be considered an electromagnetic process and pion decay is a  
665 weak process, this energy region is purposely excluded from the hadronic cross section  
666 measurement.

667 **Previous measurements: Lighter and Heavier Nuclei**

668 Many experiments with pion beams have studied the hadronic interaction of pions on  
669 light and heavy materials, such as He, Li, C, Fe, Pb [36]. However, data on argon are  
670 rare: the total differential hadronic cross section has never been measured before on  
671 argon. Simulation packages such as Geant4 base their pion transportation for argon  
672 on data from lighter and heavier nuclei: the goal of LArIAT’s dedicated measurement  
673 on argon is to bridge this gap in data, thus reducing the uncertainties related to pion  
674 interactions in argon in both neutrino event generators and in simulation packages of  
675 pion transportation.

676 The shape of the pion-nucleus interaction cross section in the energy range con-  
677 sidered shows the distinct features indicating the presence of a resonance. In fact, the  
678 mean free path of a pion of kinetic energy between 100 and 400 MeV is much shorter  
679 than the average distance between nucleons (which is of the order of 1 fm). There-  
680 fore, the pion interacts with surface nucleons. A  $\Delta$  resonance is often produced in  
681 the interaction, which subsequently decays inside the nucleus. Experimental results  
682 on several nuclei as reported in [36] are shown in Figure 1.3; it is interesting to notice  
683 here how the shape of the  $\Delta$  resonance becomes less pronounced as a function of the  
684 mass number of the target nucleus. Pion interactions with heavier nuclei also shift the  
685 peak of the resonance at lower energy; this effect is due to kinematic considerations  
686 and to the difference in propagation of the  $\Delta$  inside the nucleus. Multiple scattering  
687 effect modify the resonance width, which is larger than the natural-decay width. As  
688 an example of a fairly well studied target, Figure 1.4 reports the negative pion cross  
689 section on Carbon for the elastic and reaction<sup>2</sup> channels, and their sum [55].

---

2. This paper calls “inelastic interaction” what we refer as to “reaction channel”.

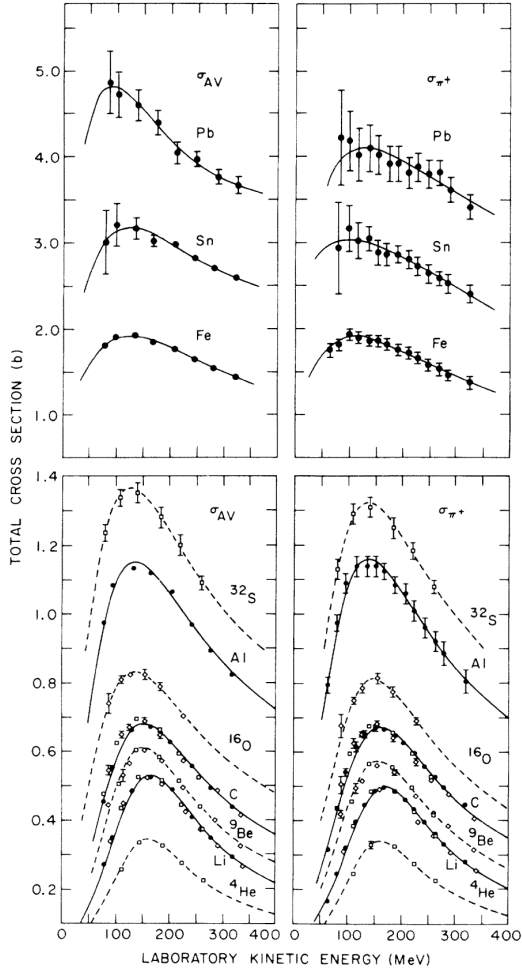


Figure 1.3: Pion-nucleus total cross sections:  $\sigma_{\pi^+}$  for positive pions (right) and  $\sigma_{AV}$  (left) for the average between positive and negative pions  $\sigma_{AV} = \frac{\sigma_{\pi^+} + \sigma_{\pi^-}}{2}$  in the  $\Delta$  resonance region. The error bars include estimates of systematic uncertainties. The curves are the results of fits to the data assuming a Breit-Wigner shape. This summary plot is reported in [36] and uses data from [52, 117].

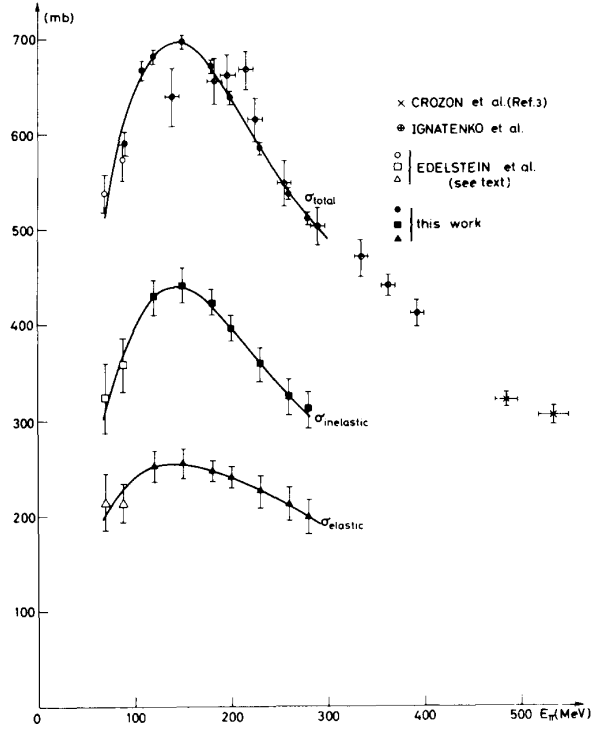


Figure 1.4: Negative pion nucleus total, elastic and reaction cross sections on  $^{12}\text{C}$  as from [55].

## 690 Negative Pion Interaction Cross Section in Simulation Packages

691 LArIAT uses Geant4 as the default simulation package. In particular, pions (and  
 692 kaons) transportation is achieved through the Geant4 FTFP\_BERT physics list. In  
 693 this physics list, Geant4 uses the Bertini cascade model [118] to simulate the products  
 694 of the pion-nucleus interaction as well as secondary hadronic re-interactions inside  
 695 the target nucleus (intra-nuclear cascade). The target nucleus is represented as a  
 696 continuous gas where the nuclear potential follows concentrical shells whose depths  
 697 approximate the Woods-Saxon shape. The CERN-HERA compilations [114, 115] of  
 698 hadron-nucleon interaction data is the data base used for the decision making process  
 699 after the cascade is invoked. The cross section model determines if the pion inter-  
 700 acts, the eventual type of interaction and the interaction multiplicity. For hadron  
 701 projectiles with energy less than 20 GeV, Geant4 reports the uncertainty on the cross

702 section model to be about the size of the error bars on the data used, or about 10%,  
703 increasing to 20-30% in energy regions where data is sparse.

704 The relevance of the GENIE generator for neutrino physics and its basic working  
705 principles have been outlined earlier in this section. Given GENIE’s modularity,  
706 information on hadron-nucleus interactions can be extracted from the INTRANUKE  
707 module and directly compared against the Geant4 predictions. The work in [98]  
708 reviews the current status of negative and positive pion simulation in Geant4 and  
709 GENIE for  $^{12}\text{C}$ ,  $^{56}\text{Fe}$ , and  $^{40}\text{Ca}$ . From that work, we report the results for  $^{12}\text{C}$  in  
710 Figure 1.5 as it allows a direct comparison between Geant4, GENIE and and pion  
711 re-scattering data. Geant4 predictions for  $\pi^-$  on Carbon are in good agreement with  
712 data over the entire spectrum spectrum, while GENIE predictions seem to show some  
713 features at around 500 MeV and 900 MeV, maybe due to higher resonances in the hA  
714 model. From the same work, we also report the negative pion cross section on  $^{40}\text{Ca}$   
715 in Figure 1.6, since this is the nuclear medium closest to argon. The predictions from  
716 both Geant4 and GENIE agree with data in the high energy region; the Geant4 and  
717 GENIE predictions diverge in the resonance region, where data is not available. These  
718 few examples highlight how cross section data for the specific nucleus considered in  
719 the neutrino experiments is fundamental to inform the Monte Carlo simulation.

720 For the LArIAT simulation of the MC sample used in the  $\pi^-$  argon total hadronic  
721 cross section measurement we use the Geant4 Bertini Cascade model, whose predic-  
722 tions for the total, elastic and reaction hadronic cross sections are show in Figure  
723 1.7.

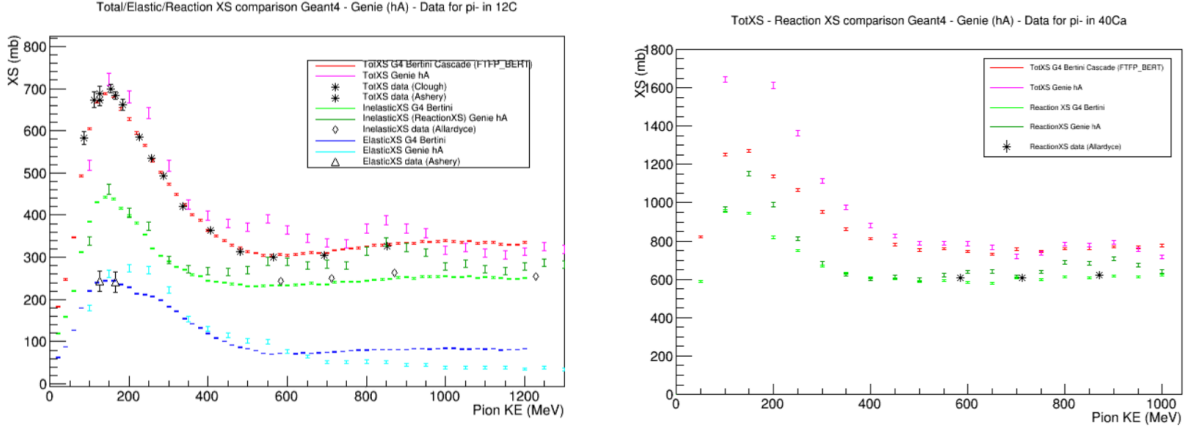


Figure 1.5: Total, elastic and reaction cross section for  $\pi^-$  on  $^{12}\text{C}$ . Comparison between results from Geant4 simulation (Bertini cascade model), Genie simulation (hA model), and experimental data [22, 52, 53, 109].

Figure 1.6: Total, elastic and reaction cross section for  $\pi^-$  on  $^{40}\text{Ca}$ . Comparison between results from Geant4 simulation (Bertini cascade model), Genie simulation (hA model), and experimental data [53].

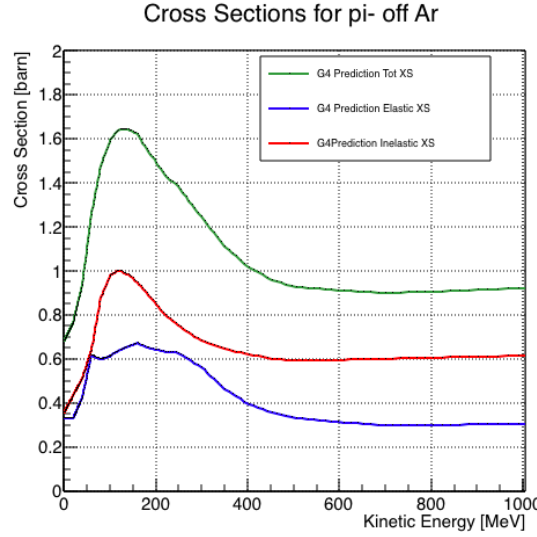


Figure 1.7: Total, elastic and reaction hadronic cross section for  $\pi^-$ -argon implemented in Geant4 10.01.p3.

Resonance	Decay Mode	Lifetime (s)
$\Delta$ (1232) $3/2^+$	$\Delta^{++}(\text{uuu}) \rightarrow p\pi^+$ $\Delta^+(\text{uud}) \rightarrow n\pi^+$ $\Delta^+(\text{uud}) \rightarrow p\pi^0$ $\Delta^0(\text{udd}) \rightarrow n\pi^0$ $\Delta^0(\text{udd}) \rightarrow p\pi^-$ $\Delta^-(\text{ddd}) \rightarrow n\pi^-$	$\sim 5.6 \times 10^{-24}$
$N^*$ (1440) $1/2^+$	$N^* \rightarrow N\pi$ $N^* \rightarrow N\pi\pi$	$\sim 2.2 \times 10^{-24}$

Table 1.3: Main decay modes of the lightest Delta resonance and Nucleon excited state.

N $\pi$ in FS	Channel Name	Reaction	Notes
0	Pion Absorption, $\sigma_{abs}$	$\pi^-(np) \rightarrow nn$ (2-body abs) $\pi^-(nnp) \rightarrow nnn$ (3-body abs) $\pi^-(npp) \rightarrow pnn$ (3-body abs) $\pi^-(nnpp) \rightarrow pmn$ (Multi-body abs)	Suppressed on single nucleon by energy conservation: the process occurs on at least two nucleons system.
1	Elastic Scattering, $\sigma_{el}$	$\pi^- + N \rightarrow \pi^- + N$	Scattering on nucleon or nucleus, the target is left in ground state
1	Charge Exchange, $\sigma_{chea}$	$\pi^- + p \rightarrow \Delta^0 \rightarrow \pi^0 + n$ $\pi^- + N \rightarrow \pi^+ + \text{nucleons}$	Single charge exchange: charged pion converts into neutral pion Double charge exchange: charged pion converts into opposite charge pion
1	Inelastic Scattering, $\sigma_{inel}$	$\pi^- + p \rightarrow \Delta^0 \rightarrow \pi^- + p$ (knock-out) $\pi^- + n \rightarrow \Delta^- \rightarrow \pi^- + n$ (knock-out)	Other possible reactions: Pure Inelastic scattering: population of low energy bound excited states Nuclear break-up with nucleons or fragments knock-out
2+	Pion Production, $\sigma_{\pi prod}$	$\pi^- + N \rightarrow \geq 2\pi + \text{nucleons}$	Possible if pion K.E $\geq 500$ MeV/c

Table 1.4: Summary of negative pion hadronic interactions of the reaction channel as a function of the pion multiplicity in the final state in the energy range [100-1200] MeV.

724 **1.4.2 Kaon-Argon Total Hadronic Cross Section**

725 This section outlines the importance of the kaon-argon total hadronic cross section.  
726 We start by discussing the measurement in the context of nucleon decay searches. We  
727 then describe the signal signature and historical measurements of kaon-nucleus cross  
728 section, as well as the implementation of this cross sections in the current version of  
729 the simulation package used by LArIAT.

730 **K<sup>+</sup>Ar Cross section in the Context of Nucleon Decay Searches**

731 Baryon number is accidentally conserved in the Standard Model. Even though no  
732 baryon number violation has been experimentally observed thus far, no underlying  
733 symmetry in line with the Noether paradigm [97] explains its conservation. As shown  
734 in section 1.3.2, almost all Grand Unified Theories predict at some level baryon num-  
735 ber violation in the form of nucleon decay on long time-scales. Given the impossibil-  
736 ity to reach grand unification energy scales with collider experiments (Energy Scale  
737 > 10<sup>15</sup> GeV), an indirect proof of GUTs is needed. The experimental observation of  
738 nucleon decay may be the only viable way to explore these theories.

739 In case of nucleon decay discovery, the dominant decay mode may uncover addi-  
740 tional information about the GUT type. Supersymmetric GUTs [24, 46] prefer the  
741 presence of kaons in the products of the decay, e.g.  $p \rightarrow K^+ \bar{\nu}$  (see fig 1.8, left).  
742 Gauge mediated GUTs, in which new gauge bosons are introduced that allow for the  
743 transformation of quarks into leptons, and vice versa, prefer the mode  $p \rightarrow e^+ \pi^0$  (see  
744 fig 1.8, right).

745 LArIAT tiny active volume makes it impossible for the experiment to place com-  
746 petitive limits on nucleon decay searches. However, LArIAT provides excellent data  
747 to characterize kaons in liquid argon for the “LAr golden mode”,  $p \rightarrow K^+ \bar{\nu}$ . The  
748 result of these studies will affect future proton decay searches in LArTPCs. Previous  
749 work has been done to assess the potential identification efficiency for different decay

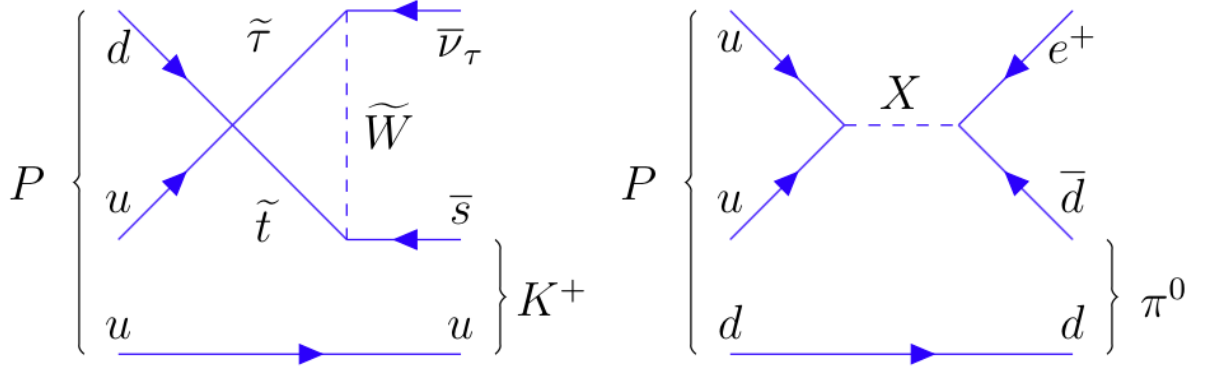


Figure 1.8: Feynman diagrams for proton decay “golden modes”:  $p \rightarrow K^+\bar{\nu}$  for supersymmetric GUTs on the left and  $p \rightarrow e^+\pi^0$  for gauge-mediated GUTs on the right.

750 modes in a LArTPC [51], but, as the time of this writing, no study of kaon selection  
 751 efficiency in LArTPCs has been performed on data. The  $K^+$ -Ar interaction cross  
 752 section has never been measured before and can affect the possibility of detecting  
 753 and measuring kaons when produced in a proton decay event. Kaon interactions with  
 754 argon can distort the kaon energy spectrum as well as change the topology of single  
 755 kaon events. In a LArTPC, non-interacting kaons appear as straight tracks with a  
 756 high ionization depositions at the end (Bragg peak). The topology of interacting  
 757 kaons can be quite different. In case of elastic scattering, a distinct kink will be  
 758 present in the track. In case of inelastic scattering the Bragg peak will not be present  
 759 and additional tracks will populate the event. Performing the total hadronic  $K^+$ -Ar  
 760 cross section measurement on data serves the double purpose of identifying the rate  
 761 of “unusual” topologies (kinks and additional tracks) and of developing tools for kaon  
 762 tracking in LAr.

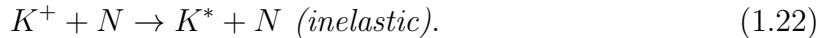
### 763 **$K^+$ Ar Hadronic Interaction: Signal Signatures**

The interaction of a mildly relativistic charged kaon with an argon nucleus is determined largely by the strong force. The total hadronic  $K^+$ -Ar interaction cross section

is defined as the one related to the single (hadronic) process driven only by the strong interaction. In this case, “total” indicates all strong interactions regardless of the final state. This condition purposefully includes both elastic and inelastic (reaction) channels. Indeed, the total cross section section can be then decomposed into

$$\sigma_{Tot} = \sigma_{Elastic} + \sigma_{Reaction}.$$

764 For the LArIAT cross section analysis, the kaons considered span a momentum  
765 inside the TPC from 100 MeV/c to 800 MeV/c. In this energy range, the relevant  
766 K-Nucleon interactions are according to [63]:



767 **Previous Measurements: Lighter and Heavier Nuclei**

768 In general, measurements on kaon cross sections are extremely scarce. The mea-  
769 surement of the kaon interaction cross section would bring the additional benefit  
770 of reducing the uncertainties associated with hadron interaction models adopted in  
771 MC simulations for argon targets, beneficial for both proton decay studies and kaon  
772 production from neutrino interaction studies, where the uncertainties for final state  
773 interaction models are big [47].

774 Figure 1.9 shows a 1997 measurement on several elements as performed by Fried-  
775 mann et al. [65]. As a reference, this paper measures a  $\sigma_{Tot}$  for Si of  $366.5 \pm 4.8$   
776 mb and a  $\sigma_{Tot}$  for Ca of  $494.6 \pm 7.7$  mb at 488 MeV/c. The cross section for argon

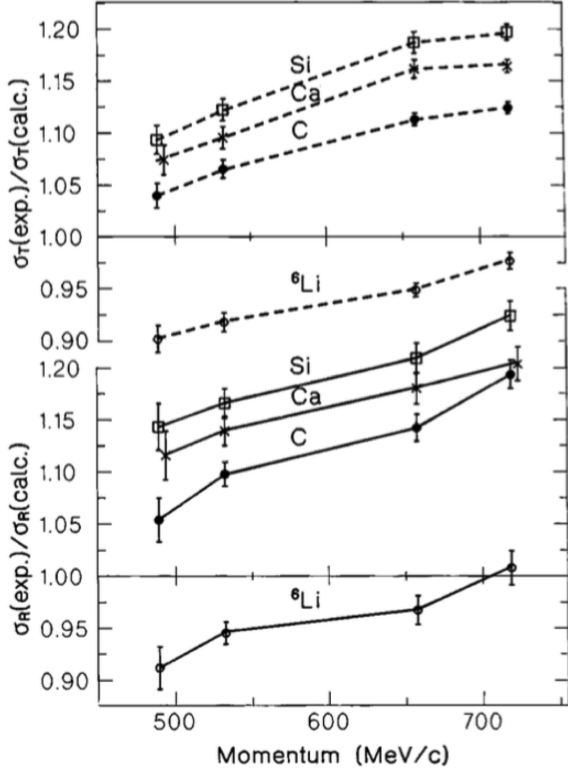


Figure 1.9: Ratios between experimental and calculated cross sections as from [65].  
Top: Total cross sections.  
Bottom: reaction cross sections.

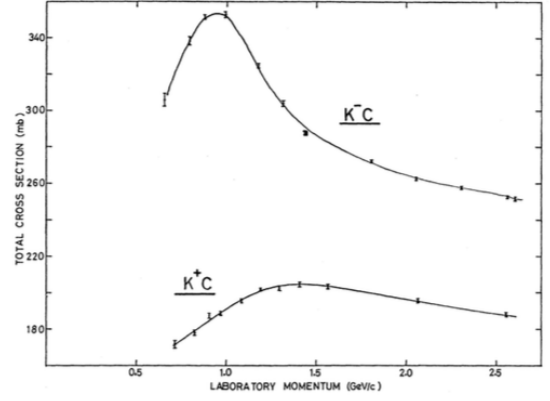


Figure 1.10: Total  $K^+$  and  $K^-$  cross sections on carbon as from [32].

is expected to lie in between these two measurements. Additional data on the kaon cross section are provided by Bugg et al. [32]. Bugg performs a measurement of the total  $K^+$  and  $K^-$  cross sections on protons and deuterons over the range of 0.6-2.65 GeV/c, as well as a measurement of the total  $K^+$  and  $K^-$  cross sections on carbon for a number of momenta; the results of this paper on carbon are reported in Figure 1.10.

### 783 Kaon Interaction Cross Section for thin target in Geant4

Since the kaon cross section in argon has never been measured before, simulation packages tune kaon transportation in argon by extrapolation from lighter and heavier nuclei. LArIAT uses the Geant4 suite for particle transportation. Since kaon data on

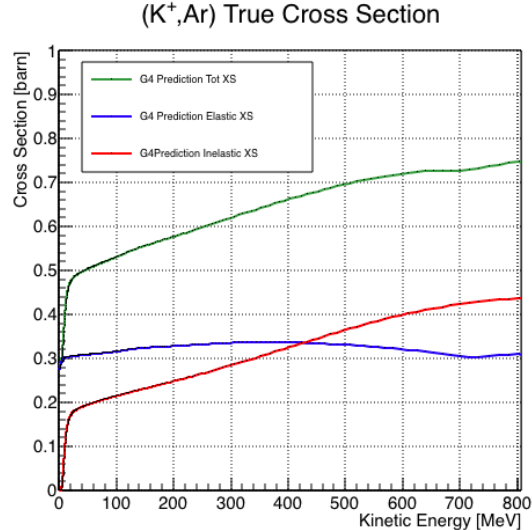
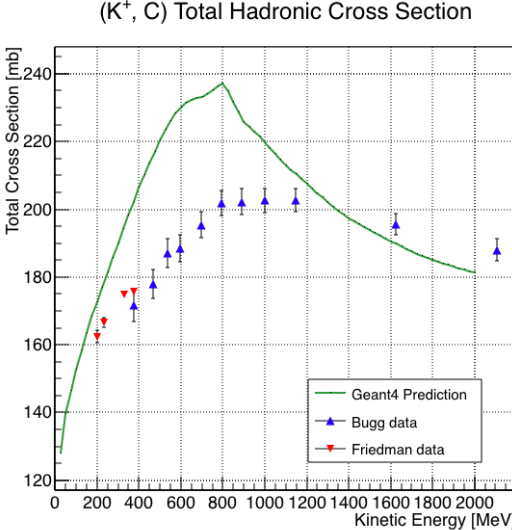


Figure 1.11: Total hadronic cross section for carbon implemented in Geant4 10.01.p3 with overlaid with the Bugg and Friedman data.

Figure 1.12: Total, elastic and reaction hadronic cross section for  $K^+$ -argon implemented in Geant4 10.01.p3.

787 carbon are available, we used it as a metric to evaluate the Geant4 prediction perfor-  
 788 mances. Figure 1.11 shows the total hadronic cross section for carbon implemented in  
 789 Geant4 10.01.p3 overlaid with the Bugg and Friedman data. Unfortunately, version  
 790 10.01.p3<sup>3</sup> of Geant4, which is the version used for the simulation in this work, does  
 791 not reproduce the data for carbon closely. On one hand, this evidence makes us even  
 792 more wary when using the Monte Carlo in simulating the kaon-argon interactions.  
 793 On the other, it further highlights the importance of the kaon measurement. For  
 794 the LArIAT simulation of the MC sample used in the  $K^+$  argon total hadronic cross  
 795 section measurement we use the Geant4 Bertini Cascade model, whose predictions  
 796 for the total, elastic and reaction hadronic cross sections are show in Figure 1.12.

---

3. It should be noted that the latest Geant4 version, 10.03.p3, uses a different parametrization for the kaon cross section and retrieves a better agreement with data.

797 **Chapter 2**

798 **Liquid Argon Detectors at the**  
799 **Intensity Frontier**

800 “*Don’t you know, honey,*  
801 *Ain’t nobody ever gonna love you, the way I try to do?*”  
802 – Janis Joplin, 1971 –

803 In the next few years, LArTPCs will be the tools to answer some of the burning  
804 questions in neutrino physics today. This chapter illustrates the operational principles  
805 of this detector technology, as well as the scope of the key detectors in the US liquid  
806 argon program – SBN, DUNE and LArIAT.

807 **2.1 The Liquid Argon Time Projection Chamber**  
808 **Technology**

809 In this section, we outline an extremely brief history of Time Projection Chambers  
810 as particle detectors, focusing on their incarnation as Argon detectors for neutrino  
811 physics. We further describe the working principles of Liquid Argon Time Projection

812 Chambers, leading to the description of the event reconstruction in LArTPC.

### 813 2.1.1 TPCs, Neutrinos & Argon

814 David Nygren designed the first Time Projection Chamber (TPC) in the late 1970s [99]  
815 for the PEP-4 experiment, a detector apt to study electron-positron collisions at the  
816 PEP storage ring at the SLAC National Accelerator Laboratory. From the original  
817 design in the seventies – a cylindrical chamber filled with methane gas – the TPC  
818 detector concept has seen many incarnations, the employment of several different  
819 active media and a variety of different particle physics applications, including, but  
820 not limited to the study of electron/positron storage rings (e.g. PEP4, TOPAZ,  
821 ALEPH and DELPHI), heavy ions collisions in fixed target and collider experiments  
822 (e.g. EOS/HISSL and ALICE ), dark matter (ArDM), rare decays and capture (e.g.  
823 TRIUMF, MuCap), neutrino detectors and nucleon decay (ICARUS, SBN, DUNE),  
824 and neutrino less double beta decay (Next). A nice review of the history of TPCs  
825 and working principles is provided in [78].

826 Several features of the TPC technology make these detectors a more versatile tool  
827 compared to other ionization detectors and explain such a wide popularity. TPCs are  
828 the only electronically read detector which deliver simultaneous three-dimensional  
829 track information and a measurement of the particle energy loss. Leveraging on both  
830 tracking and calorimetry, particle identification (PID) capabilities are enhanced over  
831 a wide momentum range.

832 Historically, the active medium in ionization detectors has been in the gaseous  
833 form. Carlo Rubbia first proposed the use of a Liquid Argon TPC for a neutrino  
834 experiment, ICARUS [108], in 1977. Using nobles elements in the liquid form for  
835 neutrino detectors is advantageous for several reasons. The density of liquids is  $\sim$ 1000  
836 times greater than gases, augmenting the number of targets for neutrino's interaction  
837 in the same volume, in a effort to balance the smallness of neutrino cross section. Since

Element	LAr	LXe
Atomic Number	18	54
Atomic weight A	40	131
Boiling Point Tb at 1 atm	87.3 K	165.0 K
Density	1.4 g/cm <sup>3</sup>	3.0 g/cm <sup>3</sup>
Radiation length	14.0 cm	2.8 cm
Moliere Radius	10.0 cm	5.7 cm
Work function	23.6 eV	15.6 eV
Electron Mobility at $E_{field} = 10^4$ V/m	0.047 m <sup>2</sup> /Vs	0.22 m <sup>2</sup> /Vs
Average dE/dx MIP	2.1 MeV/cm	3.8 MeV/cm
Average Scintillation Light Yield	40000 $\gamma$ /MeV	42000 $\gamma$ /MeV
Scintillation $\lambda$	128 nm	175 nm

Table 2.1: LAr, LXe summary of properties relevant for neutrino detectors.

the energy loss of charged particle is proportional to the target material density, as shown in the Bethe-Block equation (eq. 2.1), the increased density reflects into a proportionally higher energy loss, enhancing the calorimetry capability of detectors with a liquid active medium. Additionally, the ionization energy of liquids is smaller than gasses by the order of tens of eV. Thus, at the passage of charged particles, liquids generally produce more ionization electrons than gases for the same deposited energy, forcing the particles to deposit more energy in a shorter range. The downside of using noble liquid elements in experiments is that they require expensive cryogenic systems to cool the gas until it transitions to its the liquid form. The properties of liquid argon in comparison liquid xenon – a popular choice for dark matter and neutrinoless double beta decay detectors – are summarized in table 2.1. Albeit xenon would be more desirable than argon given some superior properties such as lower ionization energy and higher density and light yield, argon relative abundance abates the cost of argon compared to xenon, making argon a more viable choice for the construction of ton (and kilo-ton) scale neutrino detectors.

LArTPCs are some times referred as to “electronic” bubble-chambers, for the similarity in the tracking and energy resolution which is coupled with an electronic readout of the imaging information in LArTPCs. Compared to these historic detectors

856 however, LArTPC bestow tridimensional tracking and a self triggering mechanism  
857 provided by the scintillation light in the liquid argon. An event display of a  $\nu_\mu$  CC  
858 interaction candidate in the MicroBooNE detector is shown in picture 2.1 to display  
859 the level of spatial details these detectors are capable of; the color scale of the image  
860 is proportional to the energy deposited, hinting to these calorimetry capabilities of  
the detectors.

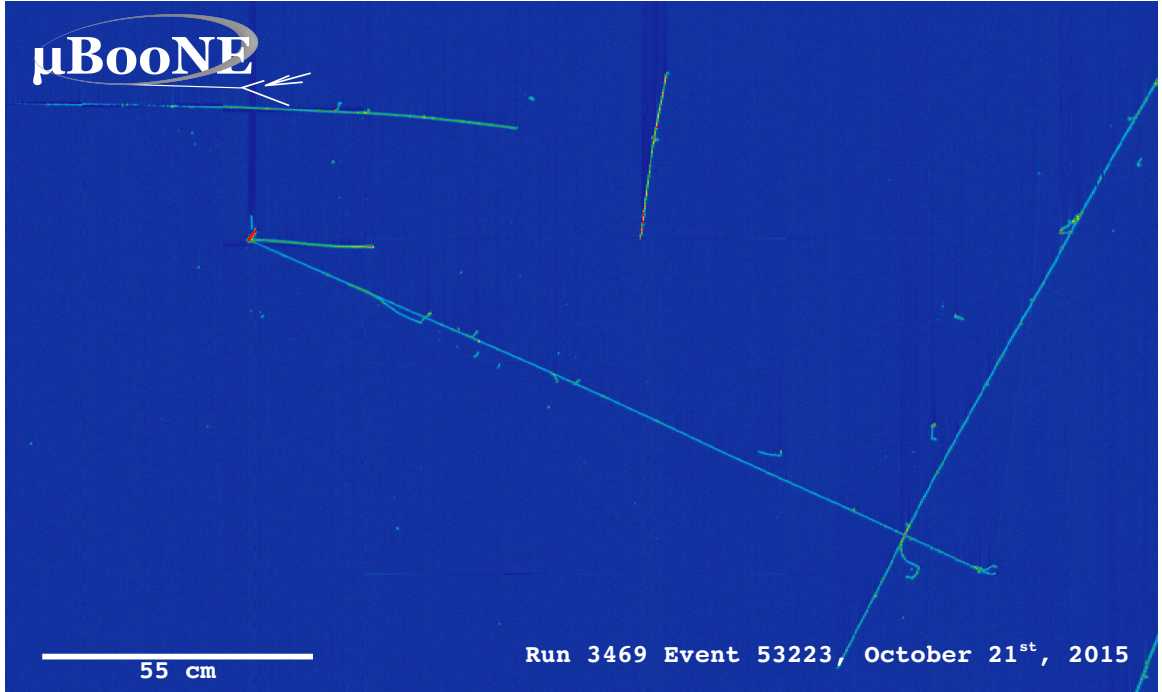


Figure 2.1: Event display of a  $\nu_\mu$  CC interaction candidate in the MicroBooNE detector.

861

### 862 2.1.2 LArTPC: Principles of Operation

863 To the bare bones, a LArTPC is a bulk of liquid argon sandwiched in a flat capacitor,  
864 equipped with a light collection system, as the cartoon in 2.2 shows. A uniform  
865 electric field of the order of 500 V/cm is maintained constant between the faces of the  
866 capacitor. The anode is sensitive to ionization charge and it is usually made of two  
867 or more planes segmented into several hundreds parallel sense wires a few millimeters  
868 apart; different geometries for the anode segmentation are under study [48].

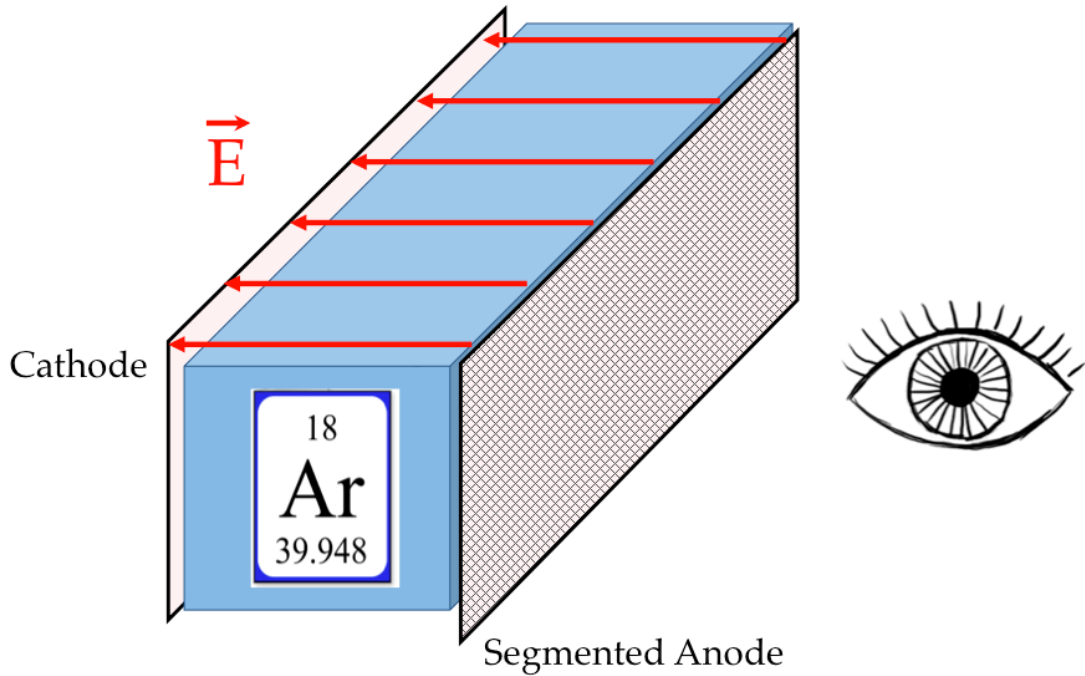


Figure 2.2: A cartoonish sketch of a LArTPC.

Argon ionization and scintillation are the processes leveraged to detect particles in the LArTPC active volume. When a ionizing radiation traverses the argon active volume it leaves a trail of ionization electrons along its trajectory and it excites the argon producing scintillation light – details on the production and detection of ionization charge and scintillation light are provided in 2.1.4 and 2.1.4 respectively. The optical detector sees the argon scintillation light in matters of nanoseconds. This flash of light determines the start time of an event in the chamber,  $t_0$ . The uniform electric field drifts the ionization electrons from the production point towards the anode in order of hundreds of microseconds or more depending on the chamber dimensions<sup>1</sup>. The anode sense wires see either an induced current by the drifting ionization charge (on induction planes) or an injection of such charge (collection

---

1. The ionized argon also drifts, but in the opposite directions compared to the electrons. Since the drift time is proportional to the particle mass, the ions' drift time is much longer than the electrons'. Ionized argon is collected on the cathode which is not instrumented, so it is not used to infer information about the interactions in the chamber.

880 plane). An appropriate choice of the voltage bias on each wire plane assures ideal  
881 charge transparency, so that all the ionization charge is collected on the collection  
882 plane and none on the induction planes.

883 The arrival time of the charge on the anode sense wires is used to measure the  
884 position of the original ionizing radiation in the drift direction. In fact, since the  
885 constant electric field implies that the drift velocity is also constant, the position of  
886 the original ionization is simply given by the multiplication of the drift velocity by the  
887 drift time, where the “drift time” is the difference between  $t_0$  and the charge arrival  
888 time on the wire planes. The spacial resolution on this dimension is limited by the  
889 time resolution of the electronics or by longitudinal diffusion of the electrons. The  
890 spatial information on the different wire planes maps a bi-dimensional projection of  
891 the interaction pattern in the plane perpendicular to the drift direction. The spacial  
892 resolution on this dimension is limited by the transverse electron diffusion in argon  
893 and by the grain of the anode segmentation, i.e. the spacing between the wires in  
894 the sense planes [45]. The off-line combination of the 2-D information on the wire  
895 planes with the timing information allows for the 3D reconstruction of the event in  
896 the chamber.

897 Since the charge deposited by the ionizing radiation is proportional to the de-  
898 posited energy and the charge collected on the sense plane is a function of the de-  
899 posited charge, LArTPCs allow the measurement of the energy deposit in the active  
900 volume. Effects due to the presence of free charge and impurities in the active vol-  
901 ume, such as a finite electron lifetime, recombination and space charge, complicate  
902 the relationship between deposited and collected charge affecting the measurement of  
903 the particle’s energy, as described in the next section.

904 **2.1.3 Liquid Argon: Ionization Charge**

905 The mean rate of energy loss by moderately relativistic elementary charge particles  
 906 heavier than electrons is well described by the modified Bethe-Bloch [102] equation

$$-\frac{dE}{dx} = K z^2 \frac{Z}{A} \varrho \frac{1}{\beta^2} \left[ \frac{1}{2} \ln \frac{2m_e c^2 \beta^2 \gamma^2 T_{max}}{I^2} - \beta^2 - \frac{\delta}{2} \right], \quad (2.1)$$

907 where  $z$  is the number of unit charge of the ionizing radiation,  $Z$ ,  $A$  and  $\varrho$  are the  
 908 atomic number, mass number and density of the medium,  $m_e$  is the electron mass,  
 909  $\gamma = \frac{\beta}{\sqrt{1-\beta^2}}$  is the Lorentz factor of the ionizing radiation,  $T_{max}$  is the maximum kinetic  
 910 energy which can be imparted to a free electron in a single collision,  $I$  is the mean  
 911 excitation energy on eV,  $\delta$  is the density correction and  $K = 0.307075 \text{ MeV g}^{-1} \text{ cm}^2$  is  
 912 a numerical conversion factor. The Bethe-Bloch treats the energy loss by an ionizing  
 913 radiation via quantum-mechanical collisions producing ionization or an excitation in  
 914 the medium as an uniform and continuous process. The density correction terms  
 915 becomes relevant for incident particle with high energy, where screening effects due  
 916 to the polarization of the medium by high energy particles occur.

917 Excitation and ionization of the detector medium occur in similar amounts. Since  
 918 the ionizing collisions occur randomly, we can parametrize their number  $k$  in a segment  
 919 of length  $s$  along the track with a Poissonian function

$$P(k) = \frac{s^k}{k! \lambda^k} e^{-s/\lambda}, \quad (2.2)$$

920 where  $\lambda = 1/N_e \sigma_i$ , with  $N_e$  being the electron density of  $\sigma_i$  the ionization cross-  
 921 section per electron. About 66% of the ionizing collisions in Argon produce only  
 922 a single electron/ion pair [78]; in the other cases, the transferred kinetic energy is  
 923 enough for the primary electron to liberate one or more secondary electrons, which  
 924 usually stay close to the original pair. Occasionally, electrons can receive enough

925 energy to be ejected with high energy, forming a so-called “ $\delta$ -ray”: a detectable short  
926 track off the particle trajectory, as shown in figure 2.3. The average number of  $\delta$ -ray  
927 with energy  $E > E_0$  per cm follows the empirical form

$$P(E > E_0) \sim \frac{y}{\beta^2 E_0}, \quad (2.3)$$

928 where  $y$  is an empirical factor depending on the medium (0.114 for gaseous Ar), and  
929  $\beta$  is  $v/c$ .

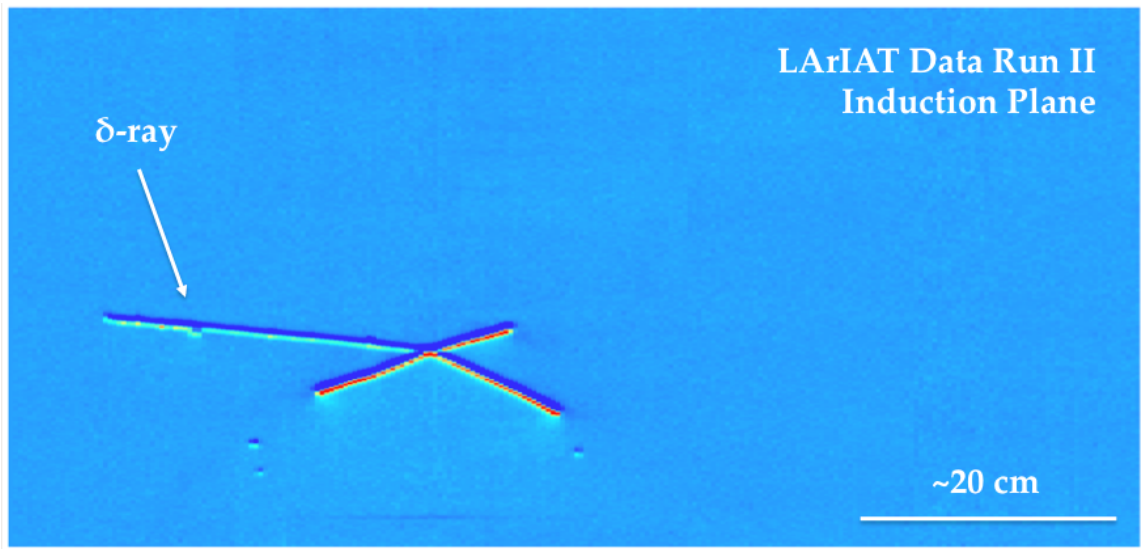


Figure 2.3: Events display for a LArIAT pion absorption candidate on the induction plane, with highlighted delta ray.

### 930 Purity & Electron Life Time

931 The presence of electronegative contaminants in liquid argon, such as oxygen  $O_2$   
932 and water  $H_2O$ , is particularly pernicious, since these molecules quench the charge  
933 produced by the ionizing radiation. Thus, amount of charge per unit of length  $dQ/dx$   
934 collected on the collection plane depends on the charge's production point in the  
935 detector: ionization produced close to the cathode will see more impurities along its  
936 journey to the collection plane than ionization produced close to the anode, resulting

937 in greater attenuation of its charge. As a result, the amount of charge collected on  
 938 the sense wires as a function of the traveled distance follows an exponential decay  
 939 trend. The traveled distance is generally measured in terms of drift time and the  
 940 characteristic time constant of the exponential decay is called electron lifetime  $\tau_e$ .  
 941 Figure 2.4 shows the typical life time for LArIAT data. The procedure to measure  
 942 the electron lifetime in LArIAT is outlined in [105]. LArIAT small drift distance (47  
 943 cm) allows for a relatively short electron life time. The life time for bigger detectors  
 944 such as MicroBooNE, whose drift distance is 2.6 m, needs to be of the order of  
 945 tens of milliseconds to allow a charge collection usable for physics analyses. Energy  
 946 reconstruction in LArTPC applies a correction for the finite lifetime to calibrate the  
 947 detector calorimetric response; details for LArIAT are provided in Section C.

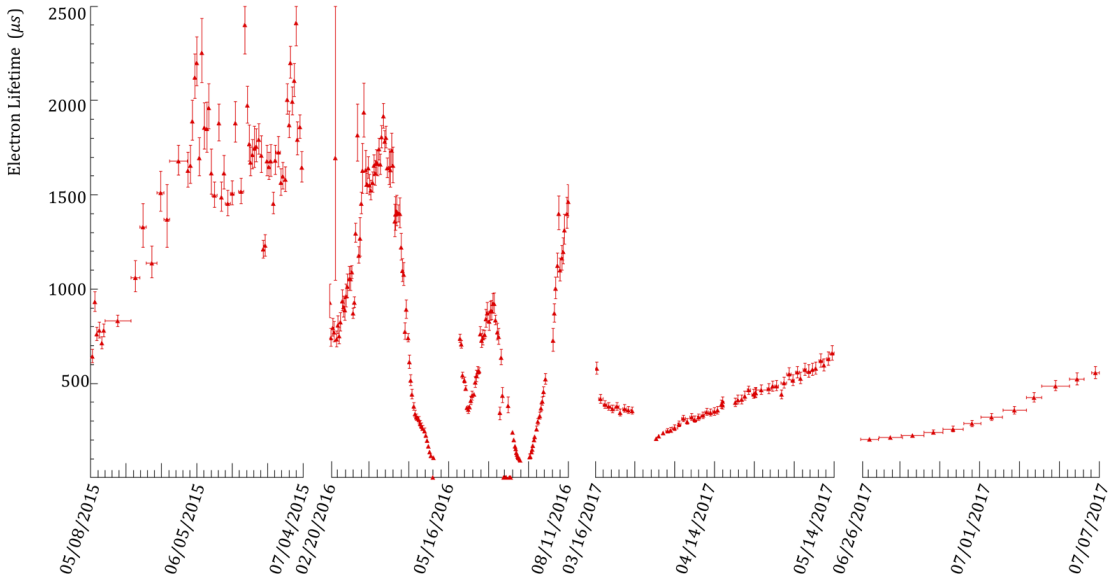


Figure 2.4: Electron lifetime during the LArIAT run period [43].

948 LArTPCs use hermetically sealed and leak-checked vessels to abate the leakage  
949 and diffusion of contaminants into the system. The liquid argon filling of the volume  
950 occurs after the vessel is evacuated or purged with gaseous argon [10] to reduce re-  
951 maining gases in the volume. Even so, the construction of a pure tank of argon is  
952 unviable, as several sources of impurity remain. In particular, impurities can come  
953 from the raw argon supply, the argon filtration system and from the outgassing from  
954 internal surfaces. Outgassing is a continuous diffusive process producing contami-  
955 nants, especially water, even after the vessel is sealed, particularly from materials in  
956 the ullage region<sup>2</sup>. Since research-grade argon comes from the industrial distillation  
957 of air, the impurities with the highest concentration are nitrogen, oxygen and water,  
958 generally maintained under the 1 part per million level by the vendor. Even so, a  
959 higher level of purity is necessary to achieve a free electron life time usable in meter  
960 scale detectors. Thus, argon is constantly filtered in the cryogenic system, which  
961 reduce the oxygen and water contamination to less than 100 parts per trillion. The  
962 filtration system depends on the size and drift distance of the experiment and, for  
963 experiments on several meters scale, it includes an argon recirculation system.

964 **Recombination Effect**

965 After production, ionization electrons thermalize with the surrounding medium and  
966 may recombine with nearby ions. Recombination might occur either between the  
967 electron and the parent ion through Coulomb attraction, as described in the geminate  
968 theory [100], or thanks to the collective charge density of electrons and ions from  
969 multiple ionizations in a cylindrical volume surrounding the particle trajectory, as  
970 described in the columnar model [81]. Consideration on the average electron-ion  
971 distance and the average ion-ion distance for argon show that the probability of

---

2. While the liquid argon low temperature reduces outgassing in the liquid, this process remains significant for absorptive material (such as plastic) above the surface of the liquid phase.

972 geminate recombination is low; thus recombination in argon is mainly due to collective  
973 effects [5]. Since protons, kaons and stopping particles present a higher ionization  
974 compared to MIPs, recombination effects are more prominent when considering the  
975 reconstruction of energy deposited by these particles.

976       Theoretical descriptions of recombination based on the Birks model and the Box  
977 model are provided in [29] and [113], respectively. The Birks model assumes a gaus-  
978 sian spatial distribution around the particle trajectory during the entire recombina-  
979 tion phase and identical charge mobility for ions and electrons. The Box model also  
980 assumes that electron diffusion and ion mobility are negligible in liquid argon during  
981 recombination. In these models, the fraction of ionization electrons surviving recom-  
982 bination is a function of the number of ion-electron pairs per unit length, the electric  
983 field, the average ion-electron separation distance after thermalization and the angle  
984 of the particle with respect to the direction of the electric field – plus the diffusion  
985 coefficient in the Birks model. Given the stringent assumptions, it is perhaps not sur-  
986 prising that these models are in accordance to data only in specific regimes: the Birks  
987 model is generally used to describe recombination for low  $dE/dx$ , the Box model for  
988 high  $dE/dX$ . In LArTPC, the ICARUS and ArgoNeut experiments have measured  
989 recombination in [16] and [5] respectively. Since LArIAT uses the refurbished Ar-  
990 goNeut TPC and cryostat at the same electric field, LArIAT currently corrects for  
991 recombination using the ArgoNeut measured recombination parameters in [5].

## 992 Space Charge Effect

993 Slow-moving positive argon ions created during ionization can build-up in LArTPC,  
994 causing the distortion of the electric field within the detector. This effect, called  
995 “space charge effect” leads to a displacement in the reconstructed position of the  
996 signal ionization electrons. In surface LArTPCs the space charge effect is primarily  
997 due to the rate of ionization produced by cosmic rays which is slowly drifting in the

998 chamber at all times. Surface LArTPC of the size of several meters are expected  
999 to be modestly impacted from the space charge effect, where charge build-up create  
1000 anisotropy of the electric field magnitude of the order of 5% at a drift field of 500  
1001 V/cm [94]. The smallness of the LArIAT drift volume and its relatively high electric  
1002 field are such that the effect of space charge is expected to be negligible.

### 1003 **2.1.4 Liquid Argon: Scintillation Light**

1004 Liquid argon emits scintillation light at the passage of charged particles. LArTPCs  
1005 leverage this property to determine when the ionization charge begins to drift towards  
1006 the anode plane.

#### 1007 **Scintillation Process**

1008 Scintillation light in argon peaks in the ultraviolet at a 128 nm, shown in comparison  
1009 to Xenon and Kypton in Figure 2.5, from [95]. The light yield collected by the optical  
1010 detector depends on the argon purity, the electric field, the dE/dx and particle type,  
1011 averaging at the tens of thousands of photons per MeV.

1012 The de-excitation of Rydberg dimers in the argon is responsible for the scintillation  
1013 light. Rydberg dimers exist in two states: singlets and a triplets. The time constant  
1014 for the singlet radiative decay is 6 ns, resulting in a prompt component for the scin-  
1015 tillation light. The decay of the triplet is delayed by intersystem crossing, producing  
1016 a slow component with a time constant of  $\sim$  1500 ns. “Self-trapped exciton lumines-  
1017 cence” and “recombination luminescence” are the two processes responsible for the  
1018 creation of the Rydberg dimers [84]. In the first process, a charged particle excites an  
1019 argon atom which becomes self-trapped in the surrounding bulk of argon, forming a  
1020 dimer; the dimer is in the singlet state 65% of the times and in the triplet state 35%  
1021 of the times. In case of recombination luminescence, the charged particle transfers  
1022 enough energy to ionize the argon. The argon ion forms a charged argon dimer state,

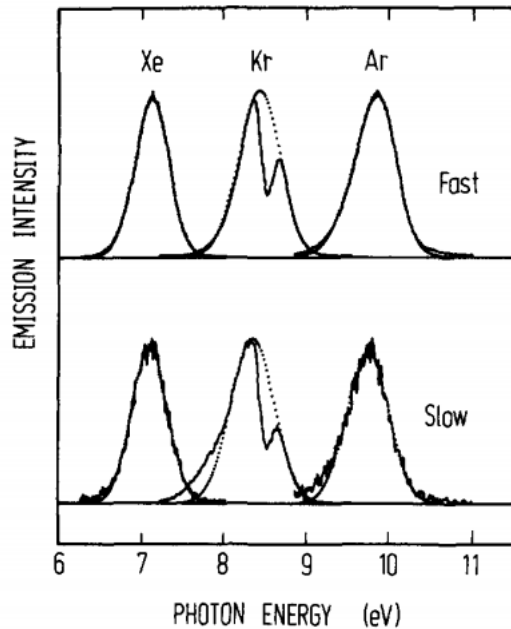


Figure 2.5: Emission spectra of the fast and slow emission components in Xenon, Krypton and Argon according to [95]. The dotted lines correspond to the Gaussian fits.

which quickly recombines with the thermalized free electron cloud. Excimer states are produced in the recombination, roughly half in the singlet and half in the triplet state. The light yield dependency on the electric field, on the  $dE/dx$  and particle type derives from the role of free charge in the recombination luminescence process. The spacial separation between the argon ions and the free electron cloud depends on the electric field. On one hand, a strong electric field diminishes the recombination probability, leading to a smaller light yield; on the other, it increases the free charge drifting towards the anode plane. Hence, the amount of measurable charge and light anti-correlates as a function of the electric field. Ionizing particles in the argon modify the local density of both free electrons and ions depending on their  $dE/dx$ . Since the recombination rate is proportional to the square of the local ionization density, highly ionizing particles boost recombination and the subsequent light yield compared to MIPs. The possibility to leverage this dependency for pulseshape-based particle identification has been shown in [31, 89].

1037 **Effects Modifying the Light Yield**

1038 The production mechanism through emission from bound excimer states implies that  
1039 argon is transparent to its own scintillation light. In fact, the photons emitted from  
1040 these metastable states are not energetic enough to re-excite the argon bulk, greatly  
1041 suppressing absorption mechanisms. In a LArTPC however, several processes modify  
1042 the light yield in between the location where light is produced and the optical detector.  
1043 In a hypothetical pure tank of argon, Rayleigh scattering would be the most important  
1044 processes modifying the light yield. Rayleigh scattering changes the path of light  
1045 propagation in argon, prolonging the time between light production and detection.  
1046 The scattering length has been measured to be 66 cm [79] , shorter than the theoretical  
1047 prediction of  $\sim 90$  cm [112]; this value is short enough to be relevant for the current  
1048 size of LArTPCs detectors. In fact, Rayleigh scattering worsen the resolution on  $t_0$ ,  
1049 the start time for charge drifting, and alters the light directionality, complicating the  
1050 matching between light and charge coming from the same object in case of multiple  
1051 charged particles in the detector.

1052 Traces of impurities in argon such as oxygen, water and nitrogen also affect the  
1053 light yield, mainly via absorption and quenching mechanisms. Absorption occurs as  
1054 the interaction of a 128 nm photon directly with the impurity dissolved in the liquid  
1055 argon. Differently, quenching occurs as the interaction of an argon excimer and an  
1056 impurity, where the excimer transfers its excitation to the impurity and dissociates  
1057 non-radiatively. Given this mechanism, it is evident how quenching is both a function  
1058 of the impurity concentrations and the excimer lifetime. Since the triplet states  
1059 live much longer than the singlet states, quenching occurs mainly on triplet states,  
1060 affecting primarily the slow component of the light, reducing the scintillation yield  
1061 and a shortening of the scintillation time constants.

1062 The stringent constraints for the electron life time limit the presence of oxygen and  
1063 water to such a low level that both absorption and quenching on these impurity is not

1064 expected to be significant. Contrarily, the nitrogen level is not bound by the electron  
1065 life time constraints – nitrogen being an inert gas, expensive to filter. Thus, nitrogen  
1066 is often present at the level provided by the vendor. The effects of nitrogen on argon  
1067 scintillation light have been studied in the WArP R&D program and at several test  
1068 stands. The quenching process induced by nitrogen in liquid Ar has been measured  
1069 to be proportional to the nitrogen concentration, with a rate constant of  $\sim 0.11$   
1070  $\mu\text{s}^{-1}$  ppm $^{-1}$ ; appreciable decreasing in lifetime and relative amplitude of the slow  
1071 component have been shown for contamination as high as a few ppm of nitrogen [6].  
1072 For a nitrogen concentration of 2 parts per million, typical of the current generation  
1073 of LArTPC, the attenuation length due to nitrogen has been measured to be  $\sim 30$   
1074 meters [83].

## 1075 **Wavelength Shifting of LAr Scintillation Light**

1076 Liquid argon scintillation light is invisible for most optical detectors deployed in a  
1077 LArTPC, such as cryogenic PMTs and SiPMs, since a wavelength of 128 nm is gen-  
1078 erally too short to be absorbed from most in glasses, polymers and semiconductor  
1079 materials. Research on prototype SiPMs absorbing directly VUV light and their  
1080 deployment in noble gasses experiment is ongoing but not mature [120]. Thus, ex-  
1081 periments need to shift the wavelength of scintillation light to be able to detect it.  
1082 Albeit deployed in different ways, neutrinos and dark matter experiments commonly  
1083 use 1,1,4,4-tetraphenyl-butadiene (TPB) to shift the scintillation light. TPB absorbs  
1084 the vacuum ultraviolet (VUV) light and emits in the visible at  $\sim 425$  nm [33], with  
1085 a ratio of visible photon emitted per VUV photon absorbed of  $\sim 1.2:1$  [66].

1086 Neutrino experiments typically coat their optical detector system evaporating a  
1087 layer of TPB either directly on the PMTs glass surface or on acrylic plates mounted in  
1088 front of the PMTs [60]; this technique allows the fast detection light coming directly  
1089 from the neutrino interaction. Dark matter experiments typically evaporate TPB on

1090 reflective foils mounted on the inside walls of the sensitive volume and detect the  
1091 light after it has been reflected; this technique leads to a higher and more uniform  
1092 light yield, though scattering effects for both the visible and VUV light augment  
1093 the propagation time and hinder directionality information [61]. In order to take  
1094 advantage of both these techniques, hybrid systems with PMT coating and foils are  
1095 being considered for the next generation of large neutrino detectors.

### 1096 2.1.5 Signal Processing and Event Reconstruction

1097 In this section we illustrate the processing and reconstruction chain of the TPC sig-  
1098 nals, from the pulses on the sense wire to the construction of three dimensional objects  
1099 with associated calorimetry. Different experiments can chose different software pack-  
1100 ages for their off line signal processing and event reconstruction, but a popular choice  
1101 for US based LArTPCs is LArSoft [40]. Based on the Art framework [73], LArSoft is  
1102 an event-based toolkit to perform simulation, analysis and reconstruction of LArT-  
1103 PCs events.

1104

1105 LArTPC signal processing develops in several consecutive stages that we summa-  
1106 rize here in the following categories: *Deconvolution, Hit Reconstruction, 2D Cluster-*  
1107 *ing, 3D Tracking, Calorimetry Reconstruction*. A visualization of the signal processing  
1108 workflow is shown in figure 2.6.

1109

1110 **Deconvolution.** Induction and collection planes have different field responses,  
1111 given the different nature of the signals on these planes: the wires on the induction  
1112 planes see the inductive signal of the drifting charge, while the wires on the collection  
1113 planes see the current derived from the charge entering the conductor. Thus, signals  
1114 on the induction plane are bi-polar pulse and signal on the collection plane are unipo-  
1115 lar pulses, see Figure 2.6 panel a). The first step in signal processing is deconvolution,

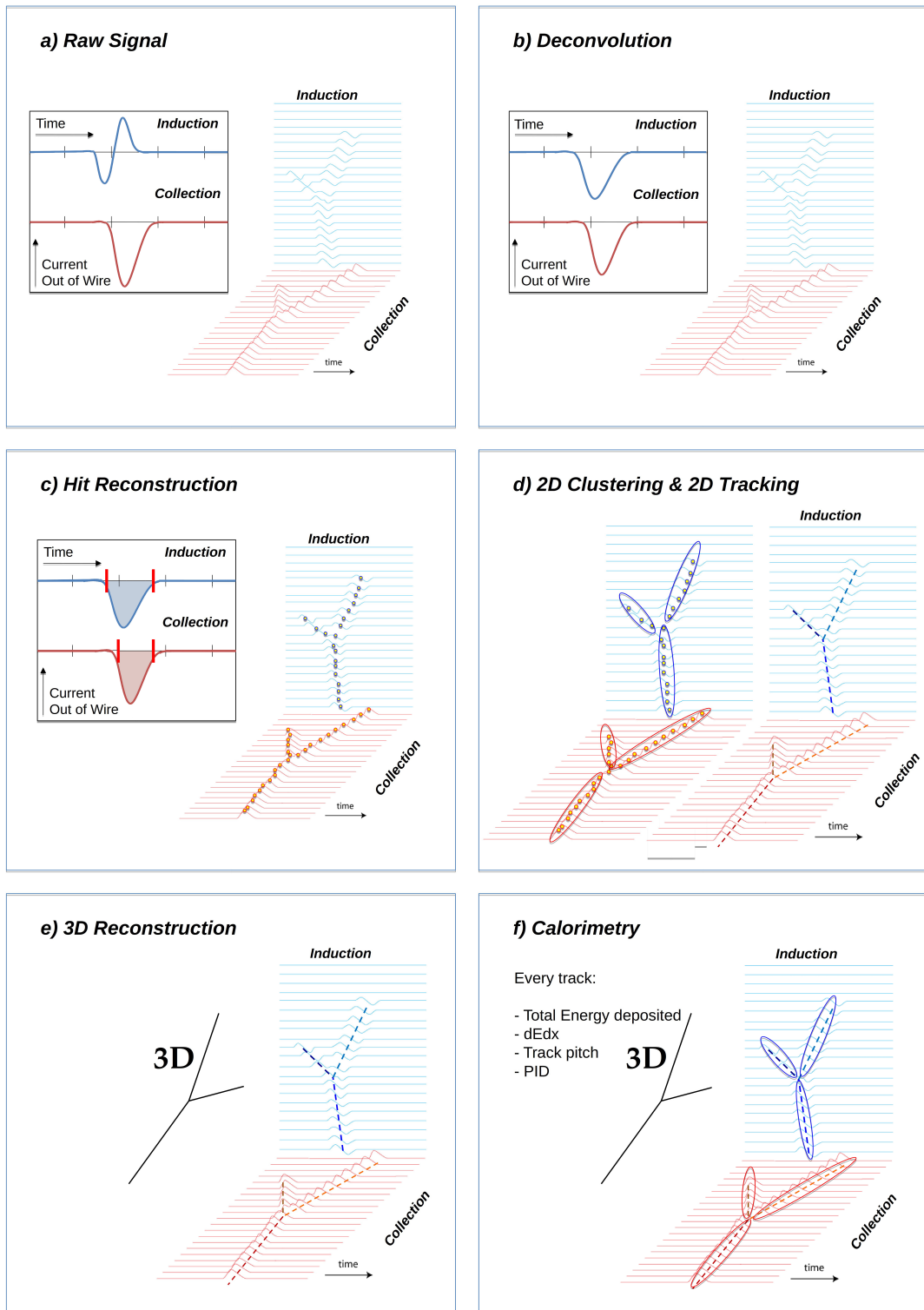


Figure 2.6: A scheme of a typical signal processing workflow in LArSoft.

1116 that is a series of off-line algorithms geared towards undoing the detector effects. The  
1117 result of the deconvolution step is the production of a comparable set waveforms on  
1118 all planes presenting unipolar, approximately gaussian-like pulses (Figure 2.6 panel  
1119 b). Signal from all planes are treated on equal footage beyond this point. Some  
1120 LArTPC apply noise filtering in the frequency domain just after the deconvolution  
1121 to clean up wire cross talk. Since signals from the LArIAT TPC are extremely clean,  
1122 noise filtering is not necessary.

1123

1124 **Hit Reconstruction.** The second stage of the signal processing is the recon-  
1125 struction of hits, indicating an energy deposition in the detector. A peak finder scans  
1126 the deconvolved TPC waveforms for each wire on the whole readout time looking for  
1127 spikes above the waveform’s baseline. It then fits these peaks with gaussian shapes  
1128 and stores the fit parameters such as the quality of the fit, the peak time, height and  
1129 area under the gaussian fit. The information resulting from this process on a single  
1130 spike form a single reconstructed “hit”, see Figure 2.6 panel c). The next steps in  
1131 the event reconstruction chain will then decide if rejecting hits with poor fits. It is  
1132 important to notice how the height and width of the hit depend on the topology of  
1133 the event: for example, a particle running parallel to the wire planes will leave a series  
1134 of sharp hits on many consecutive wires, while a particle traveling towards the planes  
1135 will leave a long, wide hit on very few wires. The height of the hits and their integral  
1136 is proportional to the charge collected on the wire, so it depends on the particle type.

1137

1138 The event reconstruction chain uses collection of hits to form more complex objects  
1139 associated with the particles in the detector. The development of different approaches  
1140 to accomplish this task is an extremely hot topic in LArTPC event reconstruction  
1141 which spans from more traditional approaches such as line-clustering [26] to the use of  
1142 machine learning tools [59]. Generally speaking, the scope of hit clustering and event

1143 reconstruction to provide shower-like or track like-objects with an associated energy  
1144 reconstruction. This is because different particles have different topology in the de-  
1145 tector – electrons and photon create electromagnetic showers, resulting in shower-like  
1146 topologies, while muons and hadrons leave track-like signals. For the scope of these  
1147 thesis, we will describe only LArIAT’s approach to track reconstruction even if we  
1148 recognize the breath of LArTPC event reconstruction is much wider. We are inter-  
1149 ested in the reconstruction of pions and kaons in the active volume, whose topology  
1150 is track-like.

1151

1152 **2D Clustering Reconstruction.** The LArIAT reconstruction of track-like ob-  
1153 jects starts by clustering hits on the collection and induction planes separately with  
1154 the use of the TrajCluster clustering package [25]. TrajCluster looks for a collection  
1155 of hits in the wire-time 2D space which can be described with a line-like 2D trajec-  
1156 tory. TrajCluster reconstructs trajectories by adding trajectory points to the leading  
1157 edge of the trajectory while stepping through the 2D space of hits. Several factors  
1158 determine whether a hit is added to the trajectory, including but not limited to

- 1159 1. the goodness of the fit of the single hit,
- 1160 2. the charge of the hit compared to the average charge and RMS of the hits  
1161 already forming the trajectory,
- 1162 3. the goodness of trajectory fit with and without the hit addition,
- 1163 4. the angle between the two lines formed by the collection of hits before and after  
1164 the considered hit in the trajectory.

1165 The final product of this reconstruction stage is the collection of bidimensional clusters  
1166 on each wire plane, see Figure 2.6 panel d).

1167 **3D Tracking.** The 3D tracking set of algorithms uses clusters close in time on  
1168 the induction and collection planes as starting point to form a 3D track. Firstly, it

1169 construct a tentative 3D trajectory using the edges of the clusters. Then, it projected  
1170 back the tentative trajectory on to the planes and adjusts the parameters of the 3D  
1171 track fit such that they minimize the distance between the fit projections and the  
1172 track hits in all wire planes simultaneously. Tridimensional tracking can use multiple  
1173 clusters in one plane, but it can never break them in smaller groups of hits. This  
1174 algorithm was first developed for the ICARUS collaboration [20]. The final product  
1175 of this reconstruction stage is the formation of tridimensional objects in the TPC  
1176 active volume, see Figure 2.6 panel e).

1177

1178 **Calorimetry.** The last step in the event reconstruction chain is to assign calorimetric  
1179 information to the track (or shower) objects. Calorimetry is performed separately  
1180 on the different planes. A multi-step procedure is needed to retrieve the energy  
1181 deposited in the TPC from the charge seen by the wires. For each hit associated with  
1182 the track object, the calorimetry algorithms calculate the charge seen on every wire  
1183 using the area underneath the gaussian fit; then, they correct this raw charge by the  
1184 electron life time, the electronic noise on the considered wire and the recombination  
1185 effect. Lastly an overall calibration of the energy, explained in detail in section C,  
1186 is applied and the calorimetric information for the given track is assigned. Even if  
1187 calorimetry is done in 2D, it benefits from the 3D tracking information; typical information  
1188 available after the calorimetric reconstruction are the total energy deposited  
1189 by the particle and its stopping power  $dE/dx$  at each “track pitch”, i.e. at each 2D  
1190 projection on the wire plane of the 3D trajectory.

## 1191 2.2 The Intensity Frontier Program

1192 This section highlights the role of Liquid Argon Time Projection Chambers at the  
1193 Intensity frontier. In particular, we show the prospects for the exploration of neutrino

1194 physics (Section 2.2.1) and GUT models (Section 2.2.2) in current and forthcoming  
1195 LAr experiments. In Section , we introduce LArIAT and its role in the Intensity  
1196 Frontier panorama.

1197 **2.2.1 Prospects for LArTPCs in Neutrino Physics: SBN and**  
1198 **DUNE**

1199 The ArgoNeut experiment [17] together the LAr R&D experiments TallBo and the  
1200 Yale TPC initiated the US LArTPC neutrino program. Following the success of the  
1201 ArgoNeut small TPC on the NuMI beam, a wide program of LArTPCs on neutrino  
1202 beams has flourished. The construction of LArTPCs as near and far detectors at  
1203 different baseline allows for the exploration of some of the fundamental questions in  
1204 neutrino physics today illustrated in section 1.3.1.

1205 The Short-Baseline Neutrino (SBN) [21] program at Fermilab is tasked with con-  
1206 clusively assess the nature of the “LSND and MiniBooNE anomalies” [14, 15, 23],  
1207 resolving the mystery of sterile neutrinos at the eV<sup>2</sup> scale. The SBN program entails  
1208 three surface LArTPCs positioned on the Booster Neutrino Beam at different dis-  
1209 tances from the neutrino production in oder to fully exploit the L/E dependence of  
1210 the oscillation pattern: SBND (100 m from the decay pipe), MicroBooNE (450 m),  
1211 and ICARUS (600 m). Within the oscillation context, the choice of the LArTPC tech-  
1212 nology for the SBN detectors changes the set of systematics with respect to LSND  
1213 and MiniBooNE, whose detection techniques were both based on Cherenkov light.  
1214 In particular, LArTPCs provide excellent electron/photon separation [9] lacking in  
1215 Cherenkov detectors which can be leveraged to abate the photon background from  
1216 neutral current interactions in  $\nu_e$  searches. MicroBooNE [8], the first detector of the  
1217 SBN program to be fully operational, started its first neutrino run in October 2015.  
1218 MicroBooNE is a 89 ton active volume LArTPC, single drift chamber with TPC di-  
1219 mensions of 2.6 m (drift) x 2.3 m (heigh) x 10.4 m (depth). MicroBooNE is positioned

at a very similar L/E on the Booster neutrino beam as MiniBooNE has the scope to directly cross check the MiniBooNE oscillation measurement. In case MicroBooNE confirms the presence of the “low energy excess” anomaly, SBND and ICARUS will provide the full measurement of the oscillation parameters. SBND and ICARUS are both dual drift chambers, whose active volume is respectively 112 ton and 600 ton. ICARUS is scheduled to become operational by the end of 2018 and SBND shortly after. Besides the oscillation analysis, the second main goals of SBN is to perform an extensive campaign of neutrino cross section measurements in argon. Given the importance of nuclear effects in (relatively) heavy materials, as discussed in section 1.2.3, both the oscillation analysis of the SBN program and the measurements of neutrino properties in DUNE will benefit from such a campaign.

On a different neutrino beam and baseline, the DUNE experiment, née LBNE [11], is the flagship experiment on the medium-long term of US-based neutrino physics, scheduled to start data taking in 2026. Shooting neutrinos from Fermilab for 800 miles to the SURF laboratory in South Dakota, DUNE is tasked with performing conclusive measurements of CP violation in the lepton sector, the neutrino mass ordering and the  $\theta_{23}$  octant. The DUNE far detector will count four 10 kton LArTPCs, roughly of dimensions of 19 m (horizontally) x 18 m (vertically) x 66 m (depth).

## 2.2.2 Prospects for LArTPCs in GUT Physics: DUNE

The experimental exploration of a manifestation of Grand Unified Theory is possible in DUNE thanks to its sheer mass. In particular, proton decay searches are a capital topic of DUNE’s wide non-accelerator physics program. The key elements for a rare decay experiment are: massive active volume, long exposure, high identification efficiency and low background. Figure 2.7 shows the current best experimental limits on nucleon decay lifetime over branching ratio (dots). Historically, the dominant technology used in these searches has been water Cherenkov detectors: all the best

1246 experimental limits on every decay mode are indeed set by Super-Kamiokande [?, ?].  
 1247 As shown in section 1.3.2, different family of GUTs predict the proton to decay in  
 1248 different modes. In particular, SUSY flavored GUTs prefer the presence of kaons  
 1249 in the decay products, e.g.  $p \rightarrow K^+ \bar{\nu}$ . It is particularly important to notice that  
 1250 the kaon energy for the proton decay mode  $p \rightarrow K^+ \bar{\nu}$  is under Cherenkov threshold  
 1251 in water. Thus, Super-Kamiokande set the limit on the lifetime for the  $p \rightarrow K^+ \bar{\nu}$   
 1252 mode by relying on photons from nuclear de-excitation and on the muon tagging in  
 1253 the kaon decay leptonic mode. For this reason, an attractive alternative approach to  
 1254 identifying nucleon decay is the use of a LArTPCs, where the kaon is directly visible  
 1255 in the detector. According to [11], DUNE will have an active volume large enough,  
 1256 have sufficient shielding from the surface, and will run for lengths of time sufficient  
 1257 to compete with Hyper-K, opening up the opportunity for the discovery of nucleon  
 1258 decay.

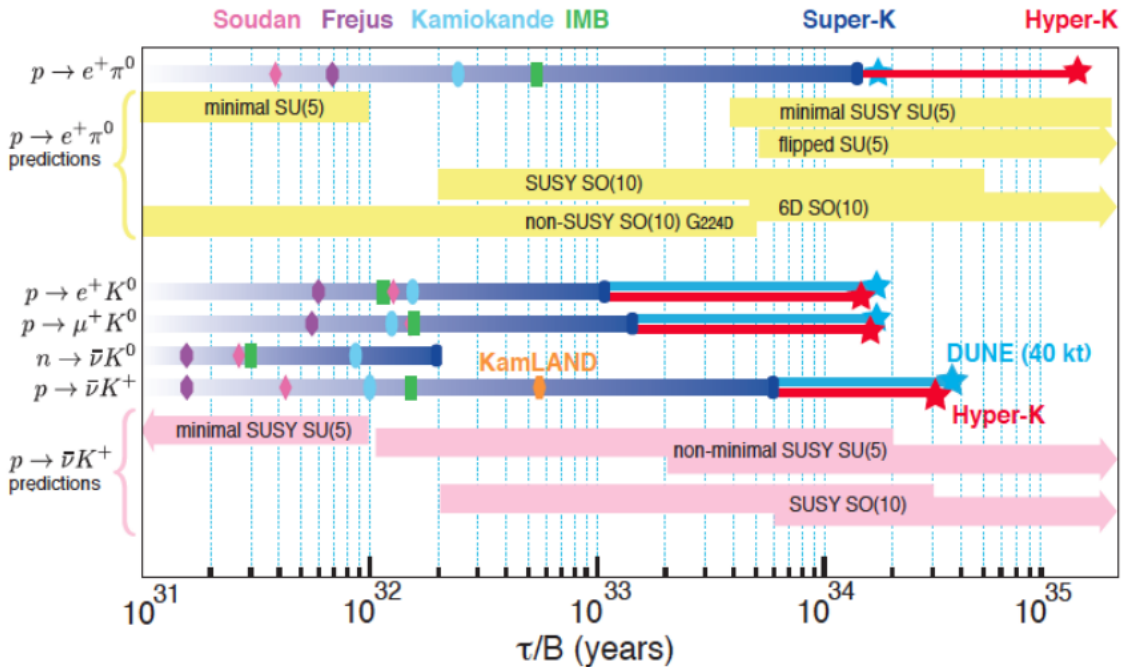


Figure 2.7: Proton decay lifetime limits from passed and future experiments.

1259 **2.2.3 Enabling the next generation of discoveries: LArIAT**

1260 LArIAT, a small LArTPC in a test beam, is designed to perform an extensive physics  
1261 campaign centered on charged particle cross section measurements while characteriz-  
1262 ing the detector performance for future LArTPCs. Since LArTPCs represent the most  
1263 advanced experiments for physics at the Intensity Frontier, their complex technology  
1264 needs a thorough calibration and dedicated measurements of some key quantities to  
1265 achieve the precision required for the next generation of discoveries. LArIAT’s goal  
1266 is to provide such calibration and dedicated measurements. The LArIAT LArTPC is  
1267 deployed in a dedicated calibration test beamline at Fermilab. We use the LArIAT  
1268 beamline to characterize the charge particles before they enter the TPC: the particle  
1269 type and initial momentum is known from beamline information. The precise calori-  
1270 metric energy reconstruction of the LArTPC technology enables the measurement of  
1271 the total differential cross section for tagged hadrons. The Pion-Nucleus and Kaon-  
1272 Nucleus total hadronic interaction cross section have never been measured before in  
1273 argon and they are a fundamental step to shed light on light meson interaction in nu-  
1274 clei per se, while providing a key input to neutrino physics and proton decay studies  
1275 in future LArTPC experiments like SBN and DUNE.

1276 In order to showcase LArIAT’s utility to SBN and DUNE, we illustrate briefly  
1277 two comparisons as examples: one regarding neutrino interactions and the second  
1278 regarding proton decay studies.

1279 The left side of figure 2.8 shows the distribution of products in momentum spectrum  
1280 and particle type as simulated in a  $\nu_e$  CC interaction in DUNE (according to [88]);  
1281 the range of these distribution is to compare with the momentum distribution of  
1282 light particles in the LArIAT beamline – shown on the right side of figure 2.8. The  
1283 momentum spectrum in the LArIAT beamline for electrons, muons and pions – the  
1284 most abundant particles produced in a  $\nu_e$  CC interaction – covers a wide range of the  
1285 expected momentum distribution in a neutrino event.

1286        The signature of a proton decay event in the “LAr golden mode” is the presence of  
 1287        a single kaon of about 400 MeV in the detector; the momentum spectrum of the kaon  
 1288        pre and post FSI in such an event as simulated by GENIE is shown on the left side  
 1289        of figure 2.9. The right side of figure 2.9 shows the momentum spectrum of kaons in  
 1290        the LArIAT beamline. Kaons arriving to the LArIAT TPC are ideal for proton decay  
 1291        studies, since their momentum in the beamline is just above the typical momentum  
 1292        for kaons in a proton decay event: the majority of LArIAT kaons slow down in the  
 1293        TPC enough to enter the desired momentum window.

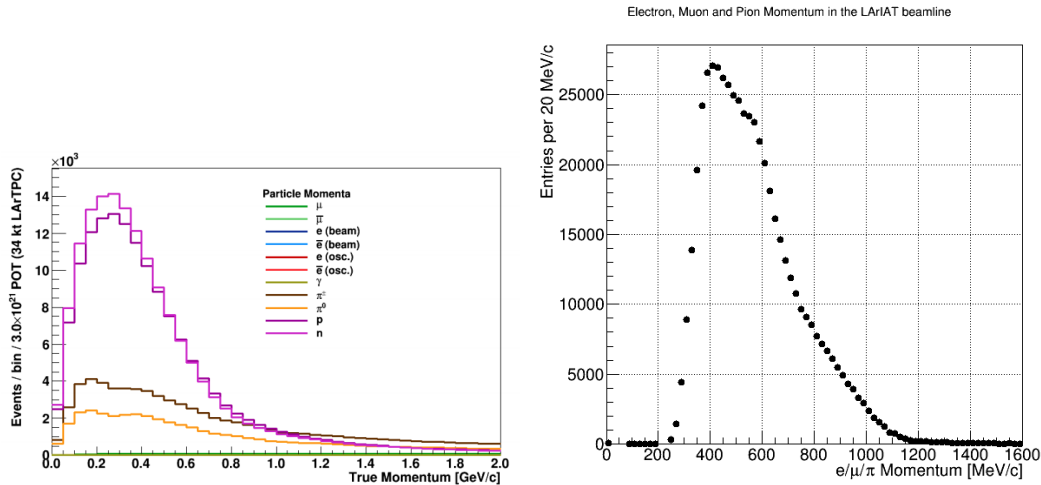


Figure 2.8: *Left.* Simulation of the products of a  $\nu_e$  CC interaction in DUNE, both in particles type and momentum.  
*Right.* Momentum spectrum for low mass particles ( $e, \mu, \pi$ ) in the LArIAT beamline, negative tune, Run II, Picky Tracks see section 3.2.2.

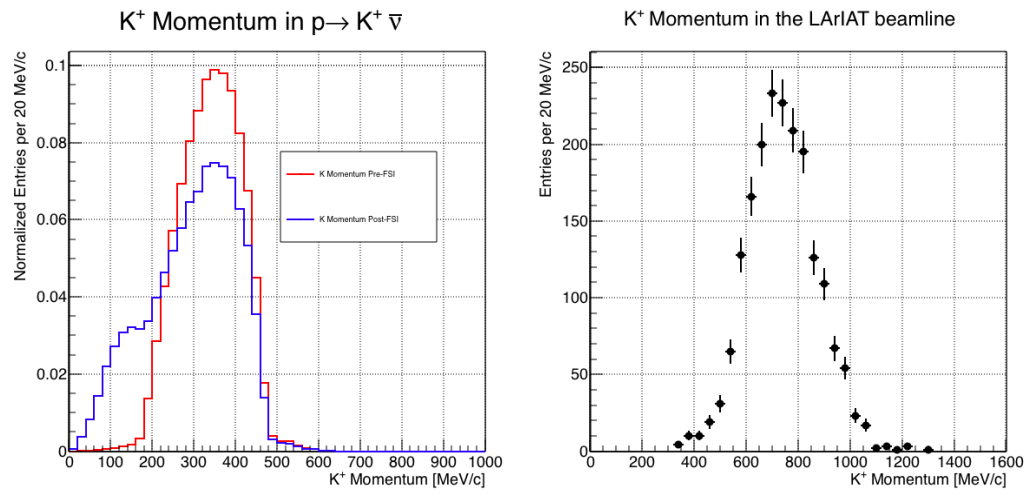


Figure 2.9: *Left.* Momentum of the kaon outgoing a proton decay  $p \rightarrow K^+ \bar{\nu}$  event as simulated by the Genie 2.8.10 event generator in argon. The red line represents the kaon momentum distribution before undergoing the simulated final state interaction inside the argon nucleus, while the blue line represents the momentum distribution after FSI.

*Right.* Positive Kaon momentum spectrum in the LArIAT beamline, positive tune, Run II, Picky Tracks see section 3.2.2.

<sub>1294</sub> **Chapter 3**

<sub>1295</sub> **LArIAT: Liquid Argon In A**

<sub>1296</sub> **Testbeam**

<sub>1297</sub> “*But, hey we need to be somewhat foolish...*”

<sub>1298</sub> – Agnes Obel, 2010 –

<sub>1299</sub> In this chapter, we describe the LArIAT experimental setup. We start by illus-  
<sub>1300</sub> trating the journey of the charged particles in the Fermilab accelerator complex, from  
<sub>1301</sub> the gaseous thermal hydrogen at the Fermilab ion source to the delivery of the LAr-  
<sub>1302</sub> IAT tertiary beam at MC7. We then describe the LArIAT beamline detectors, the  
<sub>1303</sub> LArTPC, the DAQ and the monitoring system.

<sub>1304</sub> **3.1 The Particles’ Path to LArIAT**

<sub>1305</sub> LArIAT’s particle history begins in the Fermilab accelerator complex with a beam of  
<sub>1306</sub> protons. The process of proton acceleration develops in gradual stages (see picture  
<sub>1307</sub> 3.1): gaseous hydrogen is ionized in order to form H<sup>-</sup> ions; these ions are boosted  
<sub>1308</sub> to 750 keV by a Cockcroft-Walton accelerator and injected into the linear accelerator  
<sub>1309</sub> (Linac) that increases their energy up to 400 MeV; then, H<sup>-</sup> ions pass through a

1310 carbon foil and lose the two electrons; the resulting protons are then injected into a  
1311 rapid cycling synchrotron, called the Booster; at this stage, protons reach 8 GeV of  
1312 energy and are compacted into bunches; the next stage of acceleration is the Main  
1313 Injector, a synchrotron which accelerates the bunches up to 120 GeV; in the Main  
1314 Injector, several bunches are merged into one and are ready for delivery.

1315 The Fermilab accelerator complex works in supercycles of 60 seconds in duration.  
1316 A 120 GeV primary proton beam with variable intensity is extracted in four-second  
1317 “spills” and sent to the Meson Center beam line.

1318 LArIAT’s home at Fermilab is the Fermilab Test Beam Facility (FTBF), where  
1319 the experiment characterizes a beam of charged particles in the Meson Center beam  
1320 line. At FTBF, the primary beam is focused onto a tungsten target to create LAr-  
1321 IAT’s secondary beam. The secondary beamline is set such that the composition of  
1322 the secondary particle beam is mainly positive pions. The momentum peak of the  
1323 secondary beam was fixed at 64 GeV/c for the LArIAT data considered in this work,  
1324 although the beam is tunable in momentum between 8-80 GeV/c; this configuration  
1325 of the secondary beamline assured a stable beam delivery at the LArIAT experimental  
1326 hall.

1327 The secondary beam impinges then on a copper target within a steel collimator  
1328 inside the LArIAT experimental hall (MC7) to create the LArIAT tertiary beam,  
1329 (shown in Fig. 3.2). The steel collimator selects particles produced with a 13° pro-  
1330 duction angle. The particles are then bent by roughly 10° through a pair of dipole  
1331 magnets. By configuring the field intensity of the magnets we allow the particles of  
1332 LArIAT’s tertiary beam to span a momentum range from 0.2 to 1.4 GeV/c. The  
1333 polarity of the magnet is also configurable and determines the sign of the beamline  
1334 particles which are focused on the LArTPC. If the magnet polarity is positive the  
1335 tertiary beam composition is mostly pions and protons with a small fraction of elec-  
1336 trons, muons, and kaons. It is the job of the LArIAT beamline equipment to select the

## Fermilab Accelerator Complex

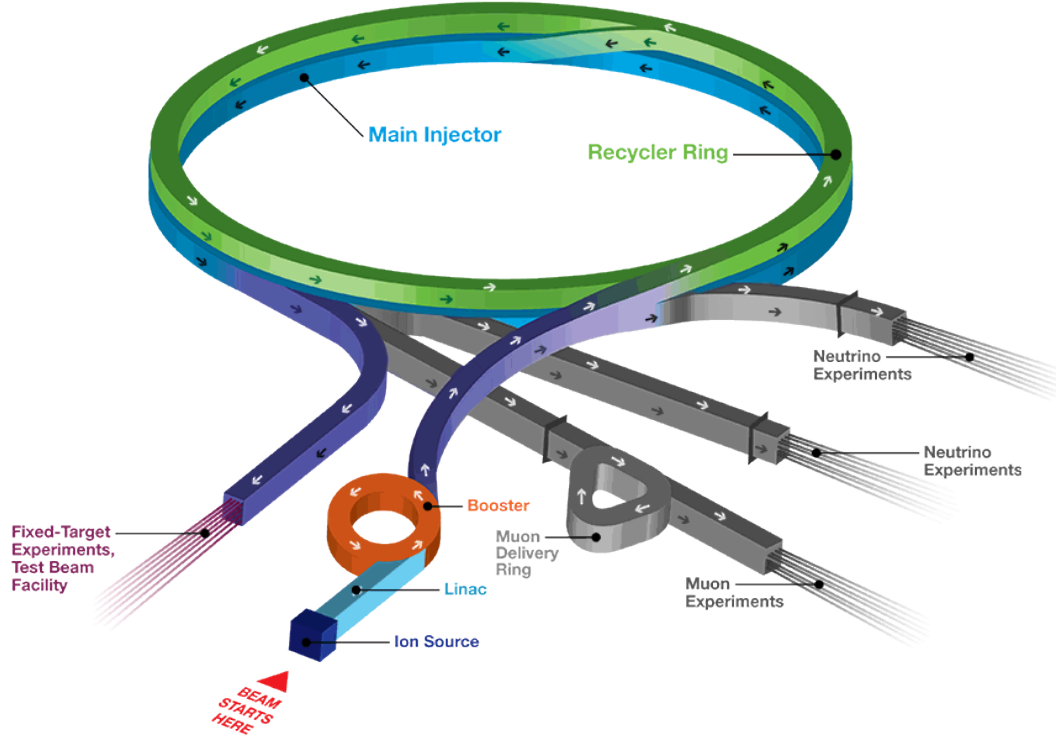


Figure 3.1: Layout of Fermilab Accelerator complex.

1337 particles polarity, to perform particle identification in the beamline and to measure  
1338 the momentum of the tertiary beam particles before they get to the LArTPC. The  
1339 LArIAT detectors are described in the following paragraphs.

### 1340 3.2 LArIAT Tertiary Beam Instrumentation

1341 The instrumentation of LArIAT tertiary beam and the TPC components have changed  
1342 several times during the three years of LArIAT data taking. The following paragraphs  
1343 describe the components operational during “Run II”, the data taking period relevant  
1344 to the hadron cross section measurements considered in this thesis.

1345 The key components of the tertiary beamline instrumentation for the hadron cross  
1346 section analyses are the two bending magnets, a set of four wire chambers (WCs)

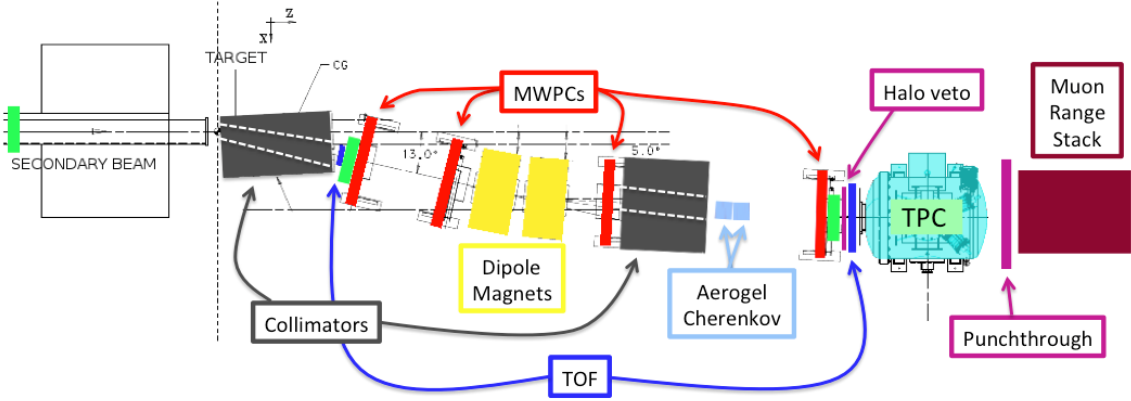


Figure 3.2: Bird’s eye view of the LArIAT tertiary beamline. In grey: upstream and downstream collimators; in yellow: bending magnets; in red: multi wire proportional chambers; in blue: time of flight; in green: liquid argon TPC volume; in maroon: muon range stack.

and two time-of-flight scintillating paddles (TOF) and, of course, the LArTPC. The magnets determine the polarity of the particles in the tertiary beam; the combination of magnets and wire chambers determines the particles’ momenta, which is used to determine the particle species in conjunction with the TOF. A muon range stack downstream from the TPC and two sets of cosmic paddles configured as a telescope surrounding the TPC are also used for calibration purposes. A couple of Aerogel Cherenkov counters, which we will not describe here as they are not used in the hadron cross section measurements, completes the beamline instrumentation.

### 3.2.1 Bending Magnets

LArIAT uses a pair of identical Fermilab type “NDB” electromagnets, recycled from the Tevatron’s anti-proton ring, in a similar configuration used for the MINERvA T-977 test beam calibration [56]. The magnets are a fundamental piece of the LArIAT beamline equipment, as they are used for the selection of the particle polarity and for the momentum measurement before the LArTPC. The sign of the current in the magnets allows us to select either positively or negatively charged particles; the value

1362 of the magnetic field is used in the momentum determination and in the subsequent  
1363 particle identification.

1364 We describe here the characteristics and response of one magnet, as the second one  
1365 has a similar response, given its identical shape and history. Each magnet is a box with  
1366 a rectangular aperture gap in the center to allow for the particle passage. The magnet  
1367 aperture measures 14.22 cm in height, 31.75 cm in width, and 46.67 cm in length.  
1368 Since the wire chambers aperture ( $\sim 12.8 \text{ cm}^2$ ) is smaller than the magnet aperture,  
1369 only the central part of the magnet gap is utilized. The field is extremely uniform  
1370 over this limited aperture and was measured with two hall probes, both calibrated  
1371 with nuclear magnetic resonance probes. The probes measured the excitation curve  
1372 shown in Figure 3.3.

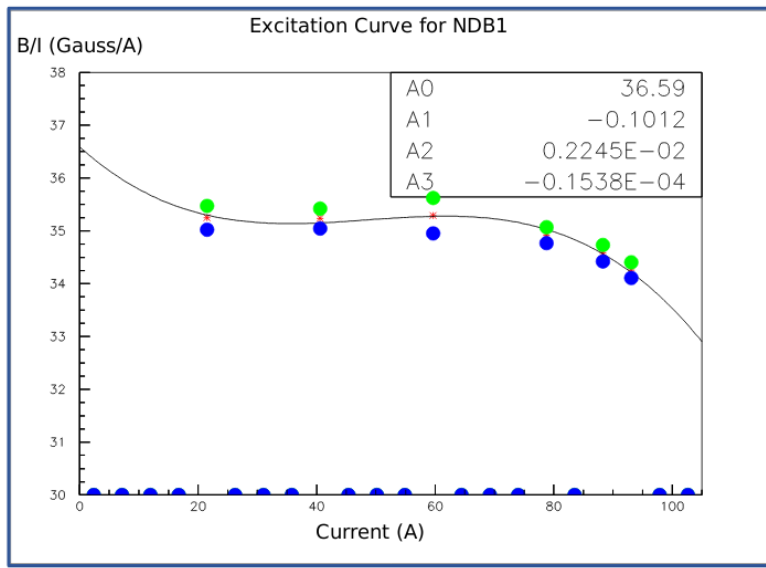


Figure 3.3: Magnetic field over current as a function of the current, for one NDB magnet (excitation curve). The data was collected using two hall probes (blue and green). We fit the readings with a cubic function (black) to average of measurements (red) given in the legend [43].

1373 The current through the magnets at a given time is identical in both magnets.  
1374 For the Run II data taking period, the current settings explored were 60A ( $B \sim 0.21$   
1375 T) and 100A ( $B \sim 0.35$  T) in both polarities. Albeit advantageous to enrich the  
1376 tertiary beam composition with high mass particles such as kaons, we never pushed

1377 the magnets current over 100 A, not to incur in overheating. During operation, we  
1378 operated an air and water cooling system on the magnets and we remotely monitored  
1379 the magnet temperatures.

1380 **3.2.2 Multi-Wire Proportional Chambers**



Figure 3.4: One of the four Multi Wire Proportional Chambers (WC) used in the LArIAT tertiary beamline and related read-out electronics.

1381 LArIAT uses four multi-wire proportional chambers, or wire chambers (WC) for  
1382 short, two upstream and two downstream from the bending magnets. The geometry of  
1383 one chamber is shown in Figure 3.4: the WC effective aperture is a square of 12.8 cm  
1384 perpendicular to the beam direction. Inside the chamber, the 128 horizontal and 128  
1385 vertical wires strung at a distance of 1 mm from each other in a mixture of 85% Argon  
1386 and 15% isobutane gas. The WC operating voltage is between 2400 V and 2500 V.  
1387 The LArIAT wire chambers are an upgraded version of the Fenker Chambers [62],  
1388 where an extra grounding improves the signal to noise ratio of the electronic readout.

1389 Two ASDQ chips [96] mounted on a mother board plugged into the chamber serve  
1390 as front end amplifier/discriminator. The chips are connected to a multi-hit TDC [74]  
1391 which provides a fast OR output used as first level trigger. The TDC time resolution  
1392 is 1.18 ns/bin and can accept 2 edges per 9 ns. The maximum event rate acceptable  
1393 by the chamber system is 1 MHz: this rate is not a limiting factor considering that

1394 the rate of the tertiary particle beam at the first wire chamber is estimated to be less  
1395 than 15 kHz. A full spill of data occurring once per supercycle is stored on the TDC  
1396 board memory at once and read out by a specially designed controller. We use LVDS  
1397 cables to carry both power and data between the controller and the TDCs and from  
1398 the controller to the rest of the DAQ.

### 1399 Multi-Wire Proportional Chambers functionality

1400 We use the wire chamber system together with the bending magnets to measure the  
1401 particle's momentum.

1402 In the simplest scenario, only one hit on each and every of the four wire chambers  
1403 is recorded during a single readout of the detector systems. Thus, we use the hit  
1404 positions in the two wire chambers upstream of the magnets to form a trajectory  
1405 before the bend, and the hit positions in the two wire chambers downstream of the  
1406 magnets to form a trajectory after the bend. We use the angles in the XZ plane  
1407 between the upstream and downstream trajectories to calculate the  $Z$  component of  
1408 the momentum as follows:

$$P_z = \frac{B_{eff}L_{eff}}{3.3(\sin(\theta_{DS}) - \sin(\theta_{US}))}, \quad (3.1)$$

1409 where  $B_{eff}$  is the effective maximum field in a square field approximation,  $L_{eff}$   
1410 is the effective length of both magnets (twice the effective length of one magnet),  
1411  $\theta_{US}$  is the angle off the  $z$  axis of the upstream trajectory,  $\theta_{DS}$  is the angle off the  
1412  $z$  axis of the downstream trajectory and  $3.3 c^{-1}$  is the conversion factor from [T·m]  
1413 to [MeV/c]. By using the hit positions on the third and fourth wire chamber, we  
1414 estimate the azimuthal and polar angles of the particle trajectory, and we are able to  
1415 calculate the other components of the momentum.

1416 The presence of multiple hits in a single wire chamber or the absence of hits in one  
1417 (or more) wire chambers can complicate this simple scenario. The first complication

is due to beam pile up, while the latter is due to wire chamber inefficiency. In the case of multiple hits on a single WC, at most one wire chamber track is reconstructed per event. Since the magnets bend particles only in the X direction, we assume the particle trajectory to be roughly constant in the YZ plane, thus we keep the combination of hits which fit best with a straight line. It is still possible to reconstruct the particle’s momentum even if the information is missing in either of the two middle wire chambers (WC2 or WC3), by constraining the particle trajectory to cross the plane in between the magnets.

Events satisfying the simplest scenario of one single hit in each of the four wire chambers form the “Picky Track” sample. We construct another, higher statistics sample, where we loosen the requirements on single hit and wire chamber efficiency: the “High Yield” sample. For LArIAT Run II, the High Yield sample is about three times the Picky Tracks statistics. We assume an uncertainty of 2% for four-point WC track, momentum uncertainty as reported for the same beamline in [56].

### 3.2.3 Time-of-Flight System

Two scintillator paddles, one upstream of the first set of WCs and one downstream of the second set of WCs form LArIAT time-of-flight (TOF) detector system.

The upstream paddle is made of a 10 x 6 x 1 cm scintillator piece, read out by two PMTs mounted on the beam left side which collect the light from light guides mounted on all four edges of the scintillator. The downstream paddle is a 14 x 14 x 1 cm scintillator piece read out by two PMTs on the opposite ends of the scintillator, as shown in figure 3.5. The relatively thin width in the beamline direction minimizes energy loss of beam particles traveling through the scintillator material.

The CAEN 1751 digitizer is used to digitize the TOF PMTs signals at a sampling rate of 1 GHz. The 12 bit samples are stored in a circular memory buffer. At trigger time, data from the TOF PMTs are recorded to output in a 28.7  $\mu$ s windows starting

1444 approximately 8.4  $\mu$ s before the trigger time.

1445 **TOF functionality**

1446 The TOF signals rise time (10-90%) is 4 ns and a full width, half-maximum of 9 ns  
1447 consistent in time. The signal amplitudes from the upstream TOF and downstream  
1448 TOF are slightly different: 200 mV for the upstream PMTs but only 50 mV for  
1449 downstream PMTs. The time of the pulses was calculated utilizing an oversampled  
1450 template derived from the data itself. We take the pulse pedestal from samples  
1451 far from the pulse and subtract it from the pulse amplitude. We then vertically  
1452 stretch a template to match the pedestal-subtracted pulse amplitude and we move  
1453 it horizontally to find the time. With this technique, we find a pulse time-pickoff  
1454 resolution better than 100 ps. The pulse pile up is not a significant problem given  
1455 the TOF timing resolution and the rate of the particle beam. Leveraging on the  
1456 pulses width uniformity of any given PMT, we flag events where two pulses overlap  
1457 as closely in time as 4 ns with a 90% efficiency according to simulation.

1458 We combine the pulses from the two PMTs on each paddle to determine the  
1459 particles' arrival time by averaging the time measured from the single PMT, so to  
1460 minimize errors due to optical path differences in the scintillator. However, a time  
1461 spread of approximately 300 ps is present in both the upstream and downstream  
1462 detectors, likely due to transit time jitter in the PMTs themselves.

1463 **3.2.4 Punch-Through and Muon Range Stack Instruments**

1464 The punch-through and the muon range stack (MuRS) detectors are located down-  
1465 stream of the TPC. These detectors provide a sample of TPC crossing tracks without  
1466 relying on TPC information and can be used to improve particle ID for muons and  
1467 pions with momentum higher than 450 MeV/c.

1468 The punch-through is simple sheet of scintillator material, read out by two PMTs.



Figure 3.5: Image of the down stream time of flight paddle, PMTs and relative support structure before mounting.

1469 The MuRS is a segmented block of steel with four slots instrumented with scintillation  
1470 bars. The four steel layers in front of each instrumented slot are 2 cm, 2 cm, 14 cm  
1471 and 16 cm deep in the beam direction. Each instrumented slot is equipped with  
1472 four scintillation bars each, positioned horizontally in the direction orthogonal to the  
1473 beam. Each scintillator bar measures  $\textcolor{red}{? \times ? \times 2}$  cm and it is read out by one PMT.

1474 The signals from both the punch-thorough and the MuRS PMTs are sent to a  
1475 NIM discriminator. If the signal crosses the discriminator threshold, it is digitized in  
1476 the CAEN V1740, same as the TPC. The sampling time of the CAEN V1740 is slow  
1477 (of the order of 128 ns) and that the pulse shape information from the PMT is lost.  
1478 A Punch-thorough and MuRS signal will then be simply a “hit” at a given time in  
1479 the beamline event.

1480 It is worth mentioning here the presence of an additional scintillation paddle  
1481 between WC4 and the downstream paddle of the TOF system, called halo. The  
1482 halo is a  $39 \times 38 \times 1$  cm $^3$  paddle with a 6.5 cm radius hole in the center, whose original  
1483 function was to reject beam particles slightly offset from the beamline center. Data

1484 from this paddle turned out to be unusable, so our data events include both particle  
1485 going through the halo scintillation material or through the halo hole.

### 1486 3.2.5 LArIAT Cosmic Ray Paddle Detectors

1487 LArIAT triggers both on beam events and on cosmic rays events. We perform this  
1488 latter trigger by using two sets of cosmic ray paddle detectors (a.k.a. “cosmic towers”.)  
1489 The cosmic towers frame the LArIAT cryostat, as one sits in the downstream left  
1490 corner and the other sits in the upstream right corner of the cryostat. Two paddle  
1491 sets of four scintillators pieces each make up each cosmic tower, an upper set and a  
1492 lower set per tower. Of the four paddles, a couple of two matched paddles stands  
1493 upright while the a second matched pair lies across the top of the assembly in the top  
1494 sets (or across the bottom of the assembly in the bottom sets). The horizontal couple  
1495 is used as a veto for particles traveling from inside the TPC out. The four signals  
1496 from the vertical paddles along one of the body diagonals of the TPC are combined  
1497 in a logical “AND”. This allows to select track due to cosmic muons at the ground  
1498 level crossing the TPC along one of its diagonals. Cosmic ray muons whose average  
1499 energy is in the few GeV range crossing both anode and cathode populate the events  
1500 triggered this way. This particularly useful sample of tracks is associated can be used  
1501 for many tasks; for example, we use anode-cathode piercing tracks to cross check  
1502 the TPC electric field on data (see Appendix A), to calibrate the charge response of  
1503 the TPC wires for the full TPC volume and to measure the electron lifetime in the  
1504 chamber [105].

1505 We retrieved the scintillation paddles from the decommissioning of the CDF de-  
1506 tector at Fermilab and we used only the paddles with a counting efficiency greater  
1507 than 95% and low noise at working voltage. The measured trigger rate of the whole  
1508 system is 0.032 Hz, corresponding to  $\sim 2$  muons per minute.



Figure 3.6: Photograph of one of the scintillation counters used in the cosmic towers.

### **1509 3.3 In the Cryostat**

**1510** The heart of the LArIAT experiment lives in the LArIAT cryostat. In this section,  
**1511** we describe the cryogenic system and the argon purity (Section 3.3.1), the LArIAT  
**1512** TPC (Section 3.3.2) and light collection system (3.3.3).

#### **1513 3.3.1 Cryogenics and Argon Purity**

**1514** LArIAT repurposed the ArgoNeuT cryostat [17] in order to use it in a beam of charged  
**1515** particles, and added a new process piping and a new liquid argon filtration system in  
**1516** FTBF. Inside the LArIAT experimental hall, the cryostat sits in the beam of charged  
**1517** particles with its horizontal main axis oriented parallel to the secondary beam,  $3^\circ$   
**1518** off axis from the tertiary beam

**1519** Two volumes make up LArIAT cryostat, shown in Figure 3.7: the inner vessel and  
**1520** the outer vessel. Purified liquid argon fills the inner vessel, while the outer volume  
**1521** provides insulation through a vacuum jacket equipped with layers of aluminized mylar  
**1522** superinsulation. The inner vessel is a cylinder of 130 cm length and 76.2 cm diameter,  
**1523** containing about 550 L of LAr, corresponding to a mass of 0.77 ton. We run the signal  
**1524** cables for the LArTPC and the high voltage feedthrough through a “chimney” at the  
**1525** top and mid-length of the cryostat.

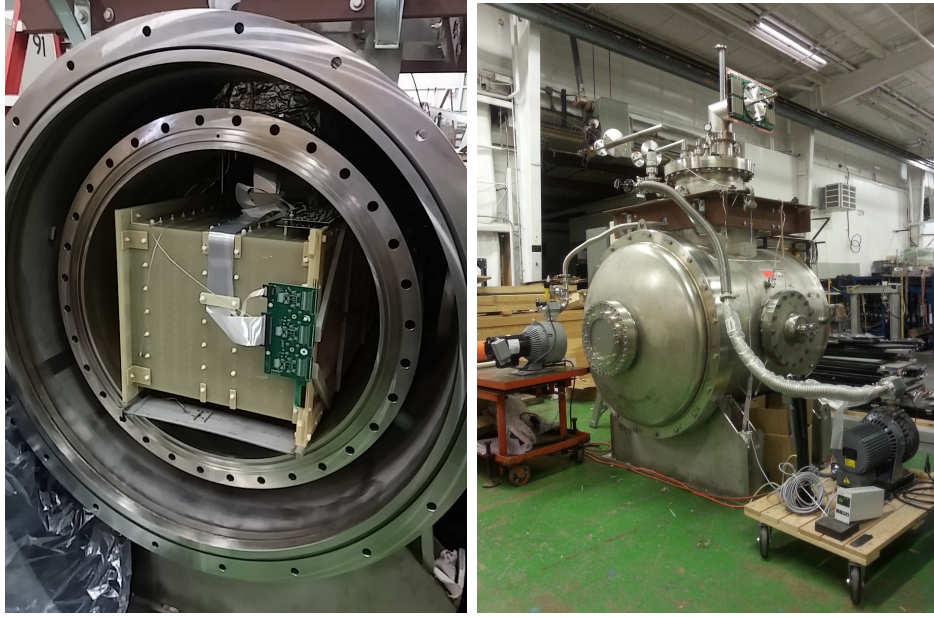


Figure 3.7: Left: the LArIAT TPC in the inner volume of the open cryostat. Right: cryostat fully sealed ready to be transported to FTBF.

Given the different scopes of the ArgoNeuT and LArIAT detectors, we made several modifications to the ArgoNeuT cryostat in order to use it in LArIAT. In particular, the modifications shown in Figure 3.8 were necessary to account for the beam of charged particles entering the TPC and to employ the new FTBF liquid argon purification system. We added a “beam window” on the front outer end cap and an “excluder” on the inner endcap, with the purpose of minimizing the amount of non-instrumented material upstream of the TPC’s active volume. The amount of non-instrumented material in front of the TPC for LArIAT corresponds to  $\sim 0.3$  electron radiation lengths ( $X_0$ ), to compare against the  $\sim 1.6X_0$  of ArgoNeuT. To allow studies of the scintillation light, we added a side port feedthrough which enables the mounting of the light collection system, as well as the connections for the corresponding signal and high-voltage cables (see Section 3.3.3). We modified the bottom of the cryostat adding Conflat and ISO flange sealing to connect the liquid argon transfer line to the new argon cooling and purification system.

As in any other LArTPC, argon purity is a crucial parameter for LArIAT. Indeed,



Figure 3.8: Main modifications to the ArgoNeuT cryostat: 1) outlet for connection to the purification system at the bottom of the cryostat; 2) the “beam-window” on the outer endcap and “excluder” which reduces the amount of non-instrumented material before the TPC; 3) the side port to host the light collection system.

1541 the presence of contaminants affects both the basic working principles of a LArTPC,  
 1542 as shown in section 2.1.2: electronegative contaminants such as oxygen and water de-  
 1543 crease the number of ionization electrons collected on the wires after drifting through  
 1544 the volume. In addition, contaminants such as Nitrogen decrease the light yield  
 1545 from scintillation light, especially in its slow component. In LArIAT, contaminations  
 1546 should not exceed the level of 0.2 parts per billion (ppb). We achieve this level of  
 1547 purity in several stages. The specifics required for the commercial argon bought for  
 1548 LArIAT are 2 parts per million (ppm) oxygen, 3.5 ppm water, and 10 ppm nitrogen.  
 1549 This argon is monitored with the use of commercial gas analyzer. Argon is stored in  
 1550 a dewar external to LArIAT hall and filtered before filling the TPC. LArIAT uses a  
 1551 filtration system designed for the Liquid Argon Purity Demonstrator (LAPD) [57]:  
 1552 half of a 77 liter filter contains a 4A molecular sieve (Sigma-Aldrich [111]) able to re-  
 1553 move mainly water, while the other half contains BASF CU-0226 S, a highly dispersed  
 1554 copper oxide impregnated on a high surface area alumina, apt to remove mainly oxy-

1555 gen [27]. A single pass of argon in the filter is sufficient to achieve the necessary  
1556 purity, unless the filter is saturated. In case the filter saturates, the media needs to  
1557 be regenerated by using heated gas; this happened twice during the Run II period<sup>1</sup>.  
1558 The electron lifetime during the full LArIAT data taking are shown in Figure 2.4.  
1559 The filtered argon reaches the inner vessel via a liquid feedthrough which is routed to  
1560 the bottom of the cryostat. Argon is not recirculated in the system; rather, it boils  
1561 off and vents to the atmosphere. During data taking, we replenish the argon in the  
1562 cryostat every 6 hours to keep the TPC high voltage feedthrough and cold electronics  
1563 always submerged. In fact, we constantly monitor the level, temperature, and pres-  
1564 sure of the argon both in the commercial dewar and inside the cryostat during data  
1565 taking.

### 1566 **3.3.2 LArTPC: Charge Collection**

1567 The LArIAT Liquid Argon Time Projection Chamber is a rectangular box of dimen-  
1568 sions 47 cm (drift) x 40 cm (height) x 90 cm (length), containing 170 liters of Liquid  
1569 Argon. The LArTPC three major subcomponents are

- 1570 1) the cathode and field cage,
- 1571 2) the wire planes,
- 1572 3) the read-out electronics.

#### 1573 **Cathode and field cage**

1574 A G10 plain sheet with copper metallization on one of the 40 x 90 cm inner surfaces  
1575 forms the cathode. A high-voltage feedthrough on the top of the LArIAT cryostat  
1576 delivers the high voltage to the cathode; the purpose of the high voltage system

---

1. We deemed the filter regeneration necessary every time the electron lifetime dropped under 100  $\mu\text{s}$ .

1577 (Figure 3.9) is to drift ionization electrons from the interaction of charged particles  
 1578 in the liquid argon to the wire planes. The power supply used in this system is a  
 1579 Glassman LX125N16 [71] capable of generating up to -125 kV and 16 mA of current,  
 1580 but operated at -23.5kV during LArIAT Run-II. The power supply is connected via  
 1581 high voltage cables to a series of filter pots before finally reaching the cathode.

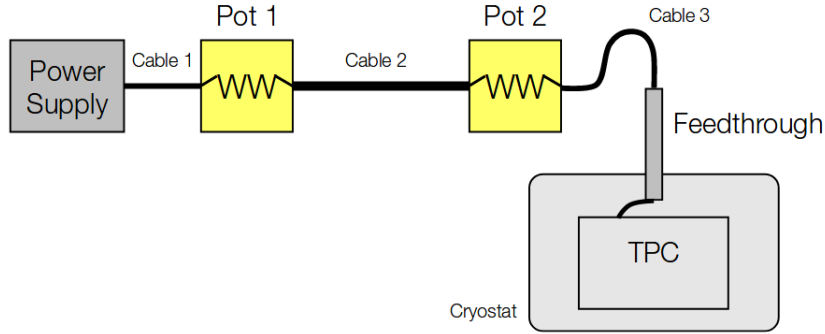


Figure 3.9: Schematic of the LArIAT high voltage system.

1582 The field cage is made of twenty-three parallel copper rings framing the inner walls  
 1583 of the G10 TPC structure. A network of voltage-dividing resistors connected to the  
 1584 field cage rings steps down the high voltage from the cathode to form a uniform electric  
 1585 field. The electric field over the entire TPC drift volume is 486 V/cm, as measured  
 1586 in appendix A. The maximum drift length, i.e. the distance between cathode and  
 1587 anode planes, is 47 cm.

### 1588 Wire planes

1589 LArIAT Run-II has three wire planes separated by 4 mm spaces: in order of increasing  
 1590 distance from the cathode, they are the shield, the induction and the collection plane.  
 1591 The “wire pitch”, i.e., the distance between two adjacent wires in a given plane, is  
 1592 4 mm. The shield plane counts 225 parallel wires of equal length oriented vertically.  
 1593 This plane is not connected with the read-out electronics; rather it shields the outer  
 1594 planes from extremely long induction signals due to the ionization in the whole drift

volume. As the shield plane acts almost like a Faraday cage, the resulting shape of signals in the first instrumented plane (induction) is easier to reconstruct. Both the induction and collection planes count 240 parallel wires of different length oriented at  $60^\circ$  from the vertical with opposite signs. Electrons moving past the induction plane will induce a bipolar pulse on its wires; the drifting electrons will be then collected on the collection plane's wires, forming a unipolar pulse.

The three wire planes and the cathode form three drift volumes, as shown in Figure 3.10. The main drift volume is defined as the region between the cathode plane and the shield plane (C-S). The other two drift regions are those between the shield plane and the induction plane (S-I), and between the induction plane and the collection plane (I-C). The electric field in these regions is chosen to satisfy the charge transparency condition and allow for 100% transmission of the drifting electrons through the shield and the induction planes.

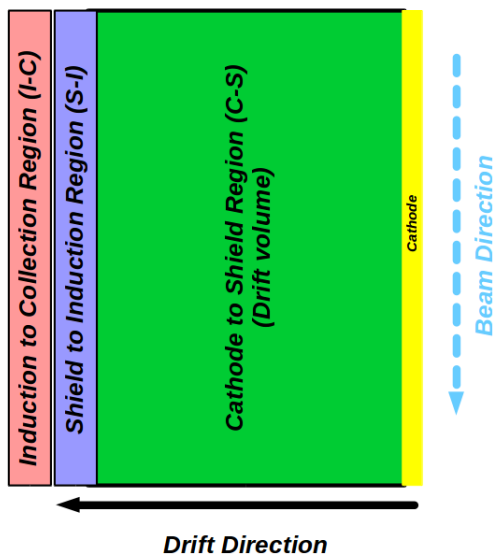


Figure 3.10: Schematic of the three drift regions inside the LArIAT TPC: the main drift volume between the cathode and the shield plane (C-S) in green, the region between the shield plane and the induction plane (S-I) in purple, and the region between the induction plane and the collection plane (I-C) in pink.

Table 3.1 provides the default voltages applied to the cathode and the shield,

1609 induction, and collection plane.

Table 3.1: Cathode and anode planes default voltages

Cathode	Shield	Induction	Collection
-23.17 kV	-298.8 V	-18.5 V	338.5 V

## 1610 **Electronics**

1611 Dedicated electronics read the induction and collection plane wires, for a total of  
1612 480-channel analog signal path from the TPC wires to the signal digitizers. A digital  
1613 control system for the TPC-mounted electronics, a power supply, and a distribution  
1614 system complete the front-end system. Figure 3.11 shows a block diagram of the  
1615 overall system. The direct readout of the ionization electrons in liquid argon forms  
1616 typically small signals on the wires, which need amplification in oder to be processed.  
1617 LArIAT performs the amplification stage directly in cold with amplifiers mounted  
1618 on the TPC frame inside the liquid argon. The BNL ASICs adopted in LArIAT are  
1619 designated as LArASIC, version 4-star and are the same used by the MicroBooNE  
1620 experiment [60]. The signal from the ASICs are driven to the other end of the readout  
1621 chain, to the CAEN V1740 digitizers [35]. The CAEN V1740 has a 12 bit resolution  
1622 and a maximum input range of 2 VDC, resulting in about 180 ADC count for a  
1623 crossing MIP.

### 1624 **3.3.3 LArTPC: Light Collection System**

1625 The collection of scintillation photons is the second mechanism of particle detection  
1626 in argon other than the ionization electrons. Over the course of LArIAT's three years  
1627 of data taking, the light collection system changed several times. We describe here  
1628 the light collection system for Run II. Two PMTs, a 3-inch diameter Hamamatsu  
1629 R-11065 and 2-inch diameter ETL D757KFL [7], as well as three SiPMs arrays (two  
1630 Hamamatsu S11828-3344M 4x4 arrays and one single-channel SensL MicroFB-60035)

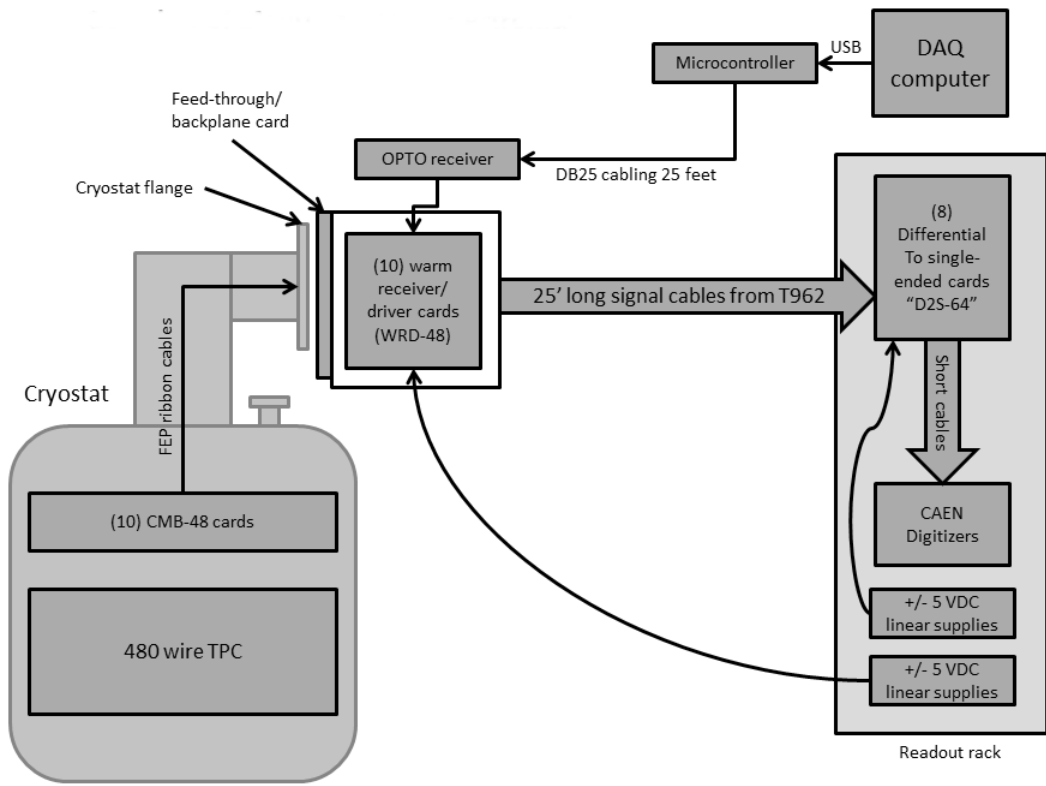


Figure 3.11: Overview of LArIAT Front End electronics.

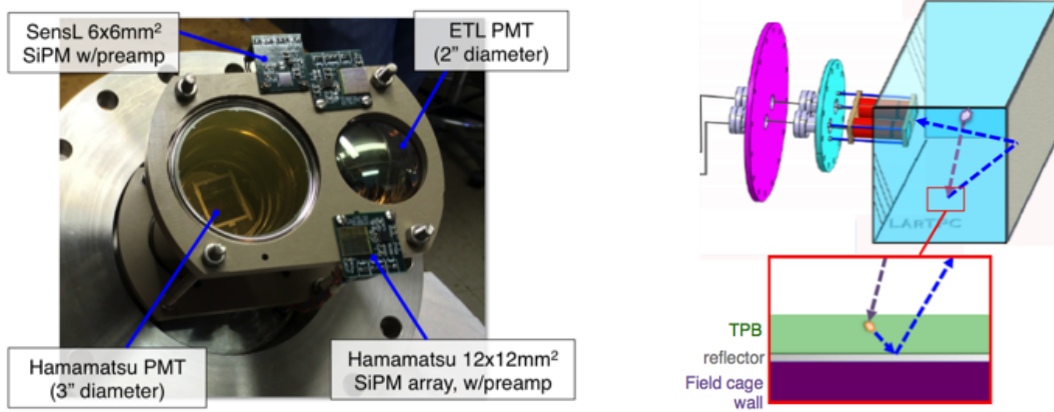


Figure 3.12: LArIAT’s photodetector system for observing LAr scintillation light inside the TPC (left), and a simplified schematic of VUV light being wavelength-shifting along the TPB-coated reflecting foils (right).

1631 are mounted on the PEEK support structure. PEEK screws into an access flange  
 1632 as shown in Figure 3.12, on the anode side, leaving approximately 5 cm of clearance  
 1633 from the collection plane.

1634 Liquid argon scintillates in vacuum-ultraviolet (VUV) range at 128 nm; since  
 1635 cryogenic PMTs are not sensitive to VUV wavelengths, we need to shift the light to a  
 1636 range that is visible to the PMTs. In LArIAT, the wavelength shifting is achieved by  
 1637 installing highly-reflective 3M VIKUITI dielectric substrate foils coated with a thin  
 1638 layer of tetraphenyl-butadiene (TPB) on the four unbiased walls of the TPC. The  
 1639 scintillation light interaction with the TPB emits one or more visible photons, which  
 1640 are then reflected into the chamber. Thus, the light yield increases and results in  
 1641 higher uniformity of light across the TPC active volume, allowing the possibility of  
 1642 light-based calorimetry, currently under study.

1643 For Run II, we coated the windows of the ETL PMT and the SensL SiPM with  
 1644 a thin layer of TPB. In doing so, some of the VUV scintillation light converts into  
 1645 visible right at the sensor faces, keeping information on the direction of the light  
 1646 source. Information about the light directionality is hindered for the light reflected  
 1647 on foils, as the reflection is uniform in angle.

## 1648 3.4 Trigger and DAQ

1649 The LArIAT DAQ and trigger system governs the read out of all the many subsystems  
1650 forming LArIAT. The CAEN V1495 module [34] and its user-programmable FPGA  
1651 are the core of this system. Every 10 ns, this module checks for matches between  
1652 sixteen logical inputs and user-defined patterns in the trigger menu; if it finds a match  
1653 for two consecutive clock ticks, that trigger fires.

1654 LArIAT receives three logic signals from the Fermilab accelerator complex related  
1655 to the beam timing which we use as input triggers: a pulse just before the beam, a  
1656 pulse indicating beam-on, and a beam-off pulse.

1657 The beam instruments, the cosmic ray taggers, and the light collection system  
1658 provide the other NIM-standard logic pulse inputs to the trigger decision. We auto-  
1659 matically log the trigger inputs configuration with the rest of the DAQ configuration  
1660 at the beginning of each run.

1661 Fundamental inputs to the trigger card come from the TOF (see section 3.2.3)  
1662 and the wire chambers (see section 3.2.2), as activity in these systems points to the  
1663 presence of a charged particle in tertiary beam line. In particular, the discriminated  
1664 pulses from the TOF PMTs form a NIM logic pulse for the trigger logic. We ask  
1665 for a coincidence within a 20 ns window for all the pulses from the PMTs looking at  
1666 the same scintillator block and use a delayed coincidence between the upstream and  
1667 downstream paddle to inform the trigger decision. In order to form a coincidence  
1668 between the upstream and downstream paddles, we delay the upstream paddle coin-  
1669 cidence by 20 ns and widen it by 100 ns. The delay and widening are necessary to  
1670 account for both lightspeed particles and slower particles (high-mass) to travel the  
1671 6.5 m between the upstream and the downstream paddles. For the read out of the  
1672 wire chambers, we use a total of sixteen multi-hit TDCs [74], four per chamber: two  
1673 TDC per plane (horizontal and vertical), sixty-four wires per TDC. In each TDC, we  
1674 keep the logical “OR” for any signal over threshold from the sixty-four wires. We

1675 then require a coincidence between the “OR” for the horizontal TDCs and the “OR”  
1676 for the vertical TDCs: with this logic we make sure that at least one horizontal wire  
1677 and one vertical wire saw significant signal in one wire chamber. The single logical  
1678 pulse from each of the four wire chambers feeds into the first four inputs to the V1495  
1679 trigger card. We require a coincidence within 20 ns of at least three logical inputs to  
1680 form a trigger.

1681 The cosmic towers (see Section 3.2.5) provide another primary input to the trigger,  
1682 in order to capture long tracks from cosmic muons crossing the TPC. We use NIM  
1683 modules to require coincidences between one upper and one lower paddle set of any  
1684 opposite cosmic towers. The OR all the opposite towers’ coincidences is fed as an  
1685 input to the trigger card.

1686 We use the signal from the cryogenic PMTs (see Section 3.3.3) to form several  
1687 interesting triggers. The coincidence of signals from all the PMT pulses within  $\sim$ 20 ns  
1688 is an indication of ionizing radiation in the TPC and forms a trigger input. The  
1689 coincidence of two subsequent scintillation logic pulses delayed by a maximum of  $7 \mu\text{s}$   
1690 forms the Michel electron trigger.

## 1691 **3.5 Control Systems**

1692 LArIAT is a complex ensemble of systems which needed to be monitored simultane-  
1693 ously during data taking. We performed the monitoring of the systems operations  
1694 with a slow control system, a DAQ monitoring system and a low level data quality  
1695 monitoring described in the following sections.

### 1696 **Slow Control**

1697 We used the Synoptic Java Web Start framework [19] as a real-time display of subsys-  
1698 tem conditions. Synoptic provides a Graphical User Interface that talks to the Fer-

milab Accelerator Control System via the ACNET protocol. Its simple GUI allowed us to change the operating parameters and to graph the trends of several variables of interest for all of the tertiary beam detectors. Among the most important quantities monitored by Synoptic there are the level of argon in both the inner vessel and the external dewar, the operating voltages of cathode and wire planes, of the PMTs and SiPMs, and of the four wire chambers, as well as the magnet temperatures. Figure 3.13 shows an example of the monitoring system. LArIAT uses the Accelerator Control NETwork system (ACNET) to monitor the beam conditions of the MCcenter beamline. For example, the horizontal and vertical position of the beam at the first two wire chambers (WC1 and WC2) are shown in 3.14 as seen by the shifter during data taking.

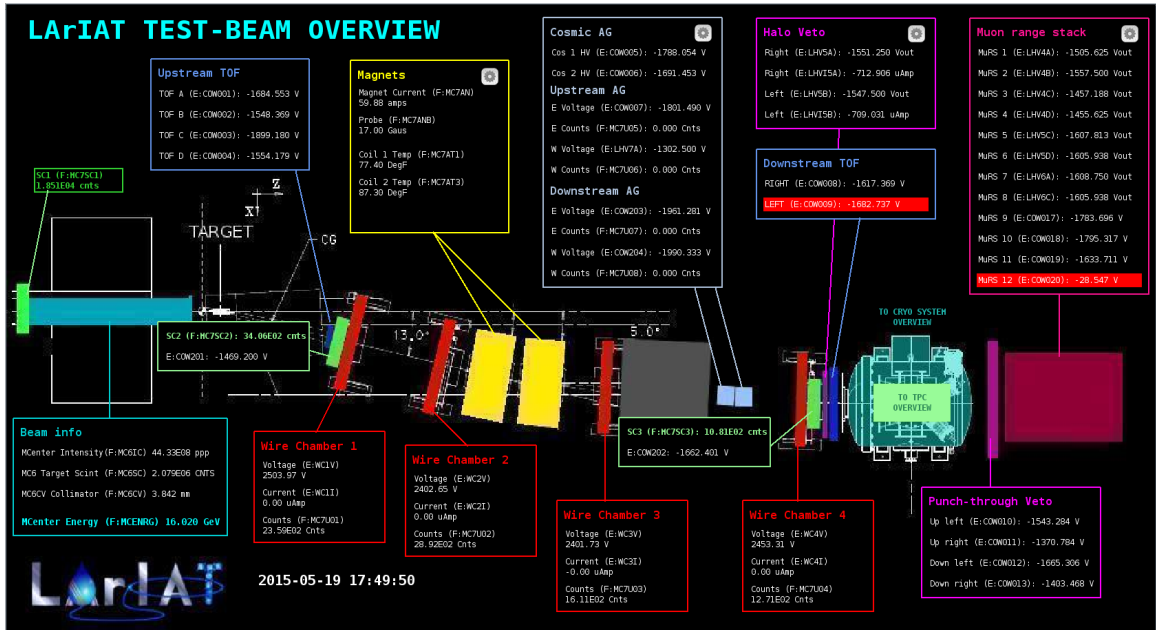


Figure 3.13: Interface of the Synoptic slow control system

## 1710 DAQ Monitoring

1711 We monitor the data taking and the run time evolution with the Run Status Webpage  
 1712 (<http://lariat-wbm.fnal.gov/lariat/run.html>), a webpage updated in real-time. The

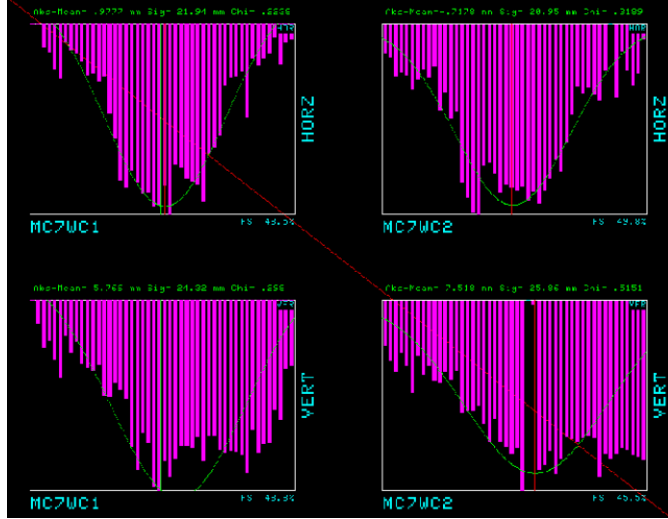


Figure 3.14: Beam position at the upstream wire chambers monitored with ACNET.

1713 page displays, among other information, the total number of triggers in the event,  
 1714 the total number of detectors triggered during a beam spill, the trigger patterns, the  
 1715 number of times a particular trigger pattern was satisfied during a beam spill, and  
 1716 the current time relative to the Fermilab accelerator complex supercycle. A screen  
 1717 shot of the page is show in figure 3.15.

### 1718 Data Quality Monitoring

1719 We employ two systems to ensure the quality of our data during data taking: the  
 1720 Near-Real-Time Data Quality Monitoring and the Event Viewer.

1721 The Near-Real-Time Data Quality Monitoring (DQM) is a webpage which receives  
 1722 updates from all the VME boards in the trigger system and displays the results of  
 1723 a quick analysis of the DAQ stream of raw data on a spill-by-spill basis. The DQM  
 1724 allows the shifter to monitor almost in real time (typically with a 2-minute delay)  
 1725 a series of low level-quantities and compare them to past collections of beam spills.  
 1726 Some of the variables monitored in the DQM are the pedestal mean and RMS on  
 1727 CAEN digitizer boards of the TPC wires and PMTs of the beamline detectors, the  
 1728 hit occupancy and timing plots on the wire chambers, and number of data fragments

1729 recorded that are used to build a TPC event. Abnormal values for low-level quantity  
1730 in the data activates a series of alarms in the DQM; this quick feedback on the DAQ  
1731 and beam conditions is fundamental to assure a fast debugging of the detector and a  
1732 very efficient data taking during beam uptime.

1733 The online Event Viewer displays a two dimensional representation (Wire vs Time)  
1734 of LArIAT TPC events on both the Induction and the Collection planes in near real  
1735 time. The raw pulses collected by the DAQ on each wire are plotted as a function  
1736 of drift time, resulting in an image of the TPC event easily readable by the shifter.  
1737 This tool guarantees a particularly good check of the TPC operation which activate  
1738 an immediate feedback for troubleshooting a number of issues. For example, it is  
1739 easy for the shifter to spot high occupancy events and request a reduction of the  
1740 primary beam intensity, or to spot a decrease of the argon purity which requires the  
1741 regeneration of filters, or to catch the presence of electronic noise and reboot the  
1742 ASICs. An example of high occupancy event is shown in 3.16.

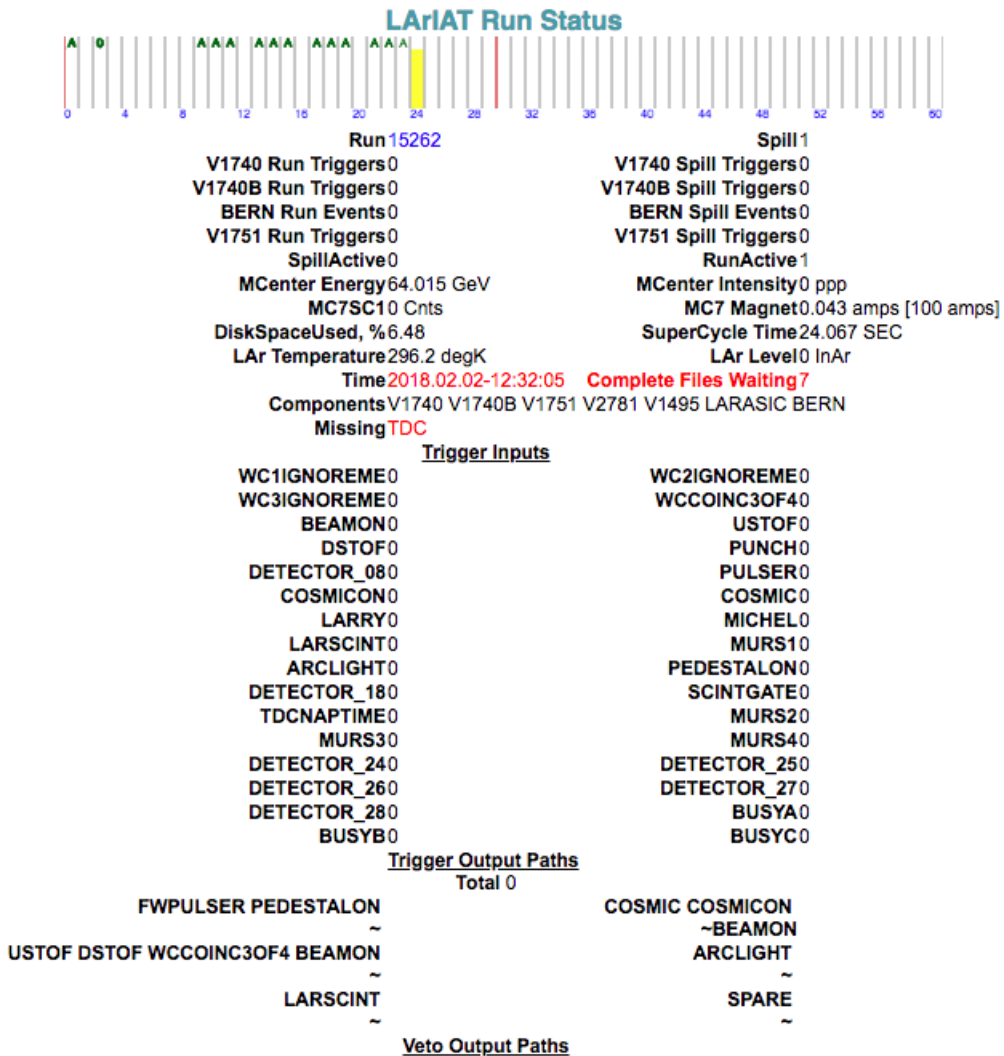


Figure 3.15: Run Status page at LArIAT downtime. At the top the yellow bar displays the current position in the Fermilab supercycle. Interesting information to be monitored by the shifter were the run number and number of spills, time elapsed from data taking (here in red), the energy of the secondary beam and the trigger paths.

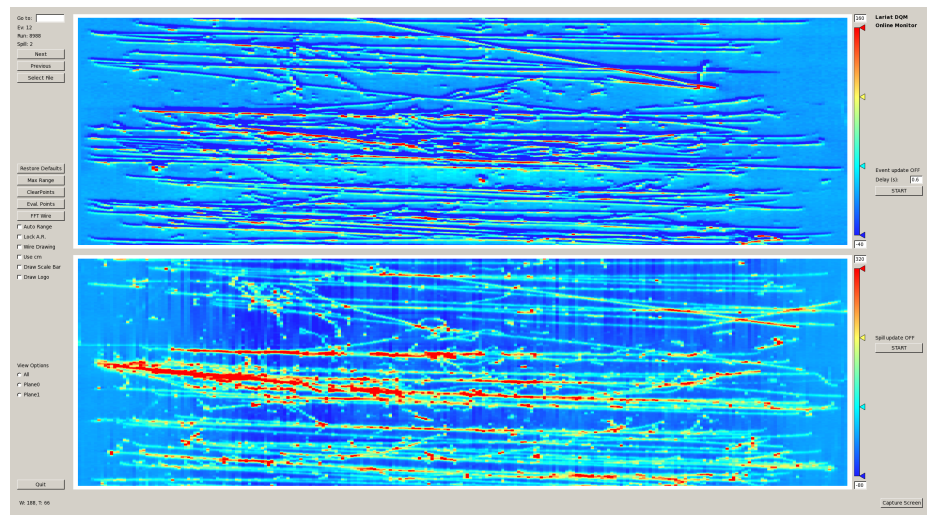


Figure 3.16: High occupancy event display: induction plane (top) and collection plane (bottom).

<sup>1743</sup> **Chapter 4**

<sup>1744</sup> **Total Hadronic Cross Section**

<sup>1745</sup> **Measurement Methodology**

<sup>1746</sup> “Like a lemon to the lime and the bubble to the bee”

<sup>1747</sup> – Eazy-E, 1993 –

<sup>1748</sup> This chapter describes the general procedure employed to measure a total hadronic  
<sup>1749</sup> differential cross section in LArIAT. Albeit with small differences, both the ( $\pi^-$ ,Ar)  
<sup>1750</sup> and ( $K^+$ ,Ar) total hadronic cross section measurements rely on the same procedure.  
<sup>1751</sup> We start by selecting the particle of interest using a combination of beamline detectors  
<sup>1752</sup> and TPC information (Section 4.1). We then perform a handshake between the  
<sup>1753</sup> beamline information and the TPC tracking to assure the selection of the correct  
<sup>1754</sup> TPC track (Section 4.2). Finally, we apply the “thin slice” method and measure the  
<sup>1755</sup> “raw” hadronic cross section (Section 4.3). A series of corrections are then evaluated  
<sup>1756</sup> to obtain the “true” cross section (Section 4.3.3).

<sup>1757</sup> At the end of this chapter, we show a sanity check of the methodology by applying  
<sup>1758</sup> the thin slice method employing only MC truth information and retrieving the Geant4  
<sup>1759</sup> tabulated cross section for pions and kaons (Section 4.4).

## **4.1 Event Selection**

The measurement of the ( $\pi^-$ ,Ar) and ( $K^+$ ,Ar) total hadronic cross section in LArIAT starts by selecting the pool of pion or kaon candidates and measuring their momentum. This is done through the series of selections on beamline and TPC information described in the next sections. The summary of the event selection in data is reported in Table 4.1.

### **4.1.1 Selection of Beamline Events**

As shown in equation 4.5, we leverage the beamline particle identification and momentum measurement before entering the TPC as an input to evaluate the kinetic energy for the hadrons used in the cross sections measurements. Thus, we select the LArIAT data to keep only events whose wire chamber and time of flight information is registered (line 1 in Table 4.1). Additionally, we perform a check of the plausibility of the trajectory inside the beamline detectors: given the position of the hits in the four wire chambers, we make sure the particle's trajectory does not cross any impenetrable material such as the collimator and the magnets steel (line 2 in Table 4.1).

	Run-II Neg Pol	Run-II Pos Pol
1. Events Reconstructed in Beamline	158396	260810
2. Events with Plausible Trajectory	147468	240954
3. Beamline $\pi^-/\mu^-/e^-$ Candidate	138481	N.A.
4. Beamline $K^+$ Candidate	N.A	2837
5. Events Surviving Pile Up Filter	108929	2389
6. Events with WC2TPC Match	41757	1081
7. Events Surviving Shower Filter	40841	N.A.
8. Available Events For Cross Section	40841	1081

Table 4.1: Number of data events for Run-II Negative and Positive polarity

1776 **4.1.2 Particle Identification in the Beamline**

1777 In data, the main tool to establish the identity of the hadron of interest is the LArIAT  
1778 tertiary beamline, in its function of mass spectrometer. We combine the measurement  
1779 of the time of flight,  $TOF$ , and the beamline momentum,  $p_{Beam}$ , to reconstruct the  
1780 invariant mass of the particles in the beamline,  $m_{Beam}$ , as follows

$$m_{Beam} = \frac{p_{Beam}}{c} \sqrt{\left(\frac{TOF * c}{l}\right)^2 - 1}, \quad (4.1)$$

1781 where  $c$  is the speed of light and  $l$  is the length of the particle's trajectory between  
1782 the time of flight paddles.

1783 Figure 4.1 shows the mass distribution for the Run II negative polarity runs on  
1784 the left and positive polarity runs on the right. We perform the classification of events  
1785 into the different samples as follows:

- 1786 •  $\pi/\mu/e$ : mass  $< 350 \text{ MeV}/c^2$   
1787 • kaon:  $350 \text{ MeV} < \text{mass} < 650 \text{ MeV}/c^2$   
1788 • proton:  $650 \text{ MeV} < \text{mass} < 3000 \text{ MeV}/c^2$ .

1789 Lines 3 and 4 in Table 4.1 show the number of negative  $\pi/\mu/e$  and positive  $K$   
1790 candidates which pass the mass selection for LArIAT Run-II data.

1791 **4.1.3 TPC Selection: Halo Mitigation**

1792 The secondary beam impinging on LArIAT secondary target produces a plethora of  
1793 particles which propagates downstream. The presence of upstream and downstream  
1794 collimators greatly abates the number of particles tracing down the LArIAT tertiary  
1795 beamline. However, it is possible that more than one particle sneaks into the LArTPC  
1796 during its readout time: the TPC readout is triggered by the particle firing the

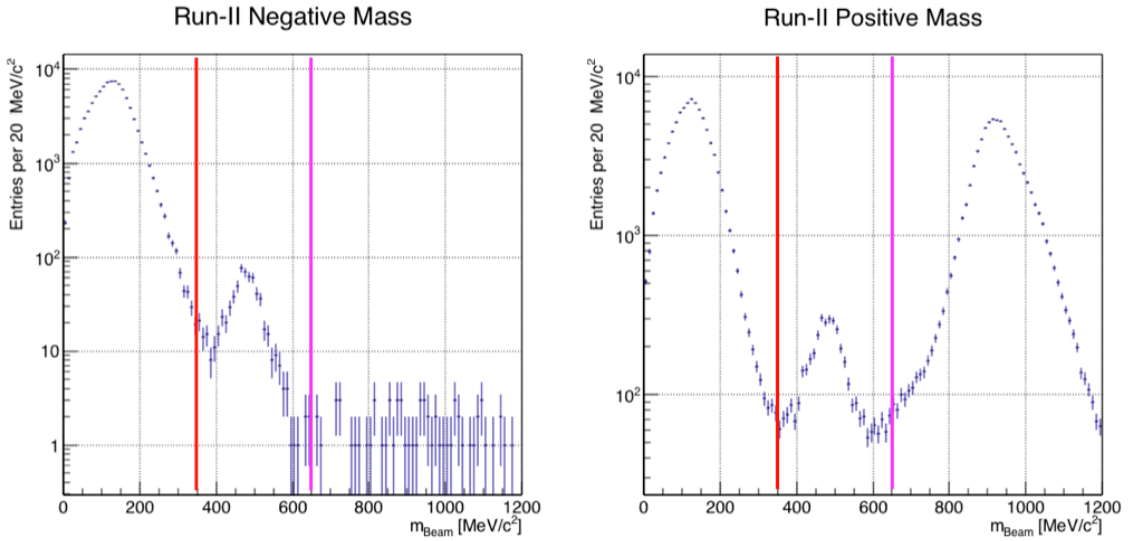


Figure 4.1: Distribution of the beamline mass as calculated according to equation 4.1 for the Run-II events reconstructed in the beamline, negative polarity runs on the left and positive polarity runs on the right. The classification of the events into  $\pi^\pm/\mu^\pm/e^\pm$ ,  $K^\pm$ , or (anti)proton is based on these distributions, whose selection cut are represented by the vertical colored lines.

beamline detectors, but particles from the beam halo might be present in the TPC at the same time. We call “pile up” the additional traces in the TPC. We adjusted the primary beam intensity between LArIAT Run I and Run II to reduce the presence of events with high pile up particles in the data sample. For the cross section analyses, we remove events with more than 4 tracks in the first 14 cm upstream portion of the TPC from the sample (line 5 in Table 4.1).

#### 4.1.4 TPC Selection: Shower Removal

In the case of the  $(\pi^-, \text{Ar})$  cross section, the resolution of beamline mass spectrometer is not sufficient to select a beam of pure pions. In fact, muons and electrons survive the selection on the beamline mass. It is important to notice that the composition of the negative polarity beam is mostly pions, as will be discussed in section 5.2.1. Still, we devise a selection on the TPC information to mitigate the presence of electrons

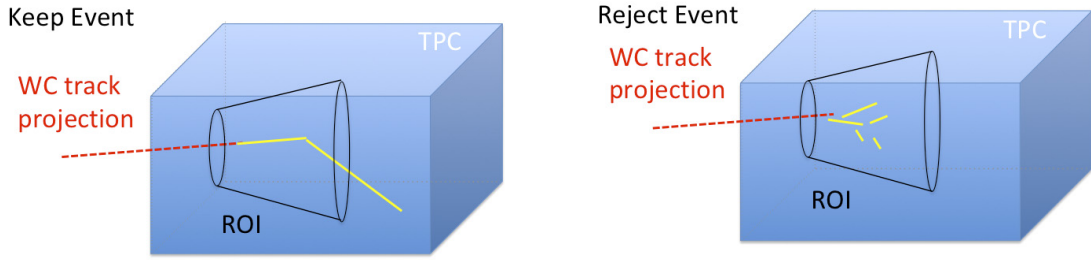


Figure 4.2: Visual rendering of the shower filter. The ROI is a cut cone, with a small radius of 4 cm, a big radius of 10 cm and an height of 42 cm (corresponding to 3 radiation lengths for electrons in Argon).

in the sample used for the pion cross section. The selection relies on the different topologies of a pion and an electron event in the argon: while the former will trace a track inside the TPC active volume, the latter will tend to “shower”, i.e. interact with the medium, producing bremsstrahlung photons which pair convert into several short tracks. In order to remove the shower topology, we create a region of interest (ROI) around the TPC track corresponding to the beamline particle. We look for short tracks contained in the ROI, as depicted in figure 4.4: if more than 5 tracks shorter than 10 cm are in the ROI, we reject the event. Line 7 in Table 4.1 shows the number of events surviving this selection.

## 4.2 Beamline and TPC Handshake: the Wire Chamber to TPC Match

For each event passing the selection on its beamline information, we need to identify the track inside the TPC corresponding to the particle which triggered the beamline detectors, a procedure we refer to as “WC to TPC match” (WC2TPC for short). In general, the TPC tracking algorithm will reconstruct more than one track in the event, partially due to the fact that hadrons interact in the chamber and partially because of pile up particles during the triggered TPC readout time, as shown in

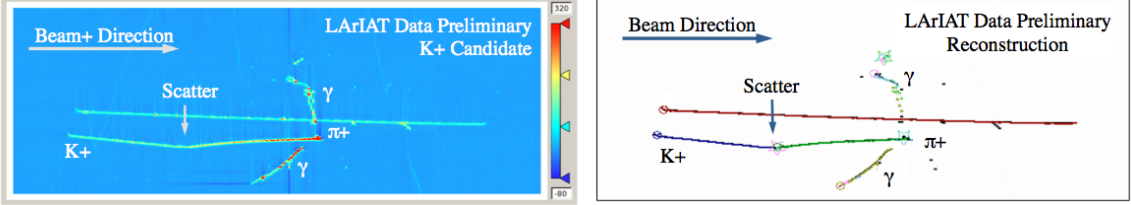


Figure 4.3: Kaon candidate event: on the right, event display showing raw quantities; on the left, event display showing reconstructed tracks. In the reconstructed event display, different colors represent different track objects. A kink is visible in the kaon ionization, signature of a hadronic interaction: the tracking correctly stops at the kink position and two tracks are formed. An additional pile-up track is so present in the event (top track in red).

1826 figure 4.3.

1827 We attempt to uniquely match one wire chamber track to one and only one recon-  
 1828 structed TPC track. In order to determine if a match is present, we apply a geomet-  
 1829 rical selection on the relative the position of the wire chamber and TPC tracks. We  
 1830 start by considering only TPC tracks whose first point is in the first 2 cm upstream  
 1831 portion of the TPC for the match. We project the wire chamber track to the TPC  
 1832 front face where we define the coordinates of the projected point as  $x_{FF}$  and  $y_{FF}$ . For  
 1833 each considered TPC track, we define  $\Delta X$  as the difference between the  $x$  position of  
 1834 the most upstream point of the TPC track and  $x_{FF}$ .  $\Delta Y$  is defined analogously. We  
 1835 define the radius difference,  $\Delta R$ , as  $\Delta R = \sqrt{\Delta X^2 + \Delta Y^2}$ . We define as  $\alpha$  the angle  
 1836 between the incident WC track and the TPC track in the plane that contains them.  
 1837 If  $\Delta R < 4$  cm,  $\alpha < 8^\circ$ , a match between WC-track and TPC track is found. We  
 1838 describe how we determine the value for the radius and angular selection in Section  
 1839 B.0.1. We discard events with multiple WC2TPC matches. We use only those TPC  
 1840 tracks that are matched to WC tracks in the cross section calculation. Line 6 in Table  
 1841 4.1 shows the number of events where a unique WC2TPC match was found.

1842 In MC, we mimic the matching between the WC and the TPC track by construct-  
 1843 ing a fake WC track using truth information at wire chamber four. We then apply  
 1844 the same WC to TPC matching algorithm as in data.

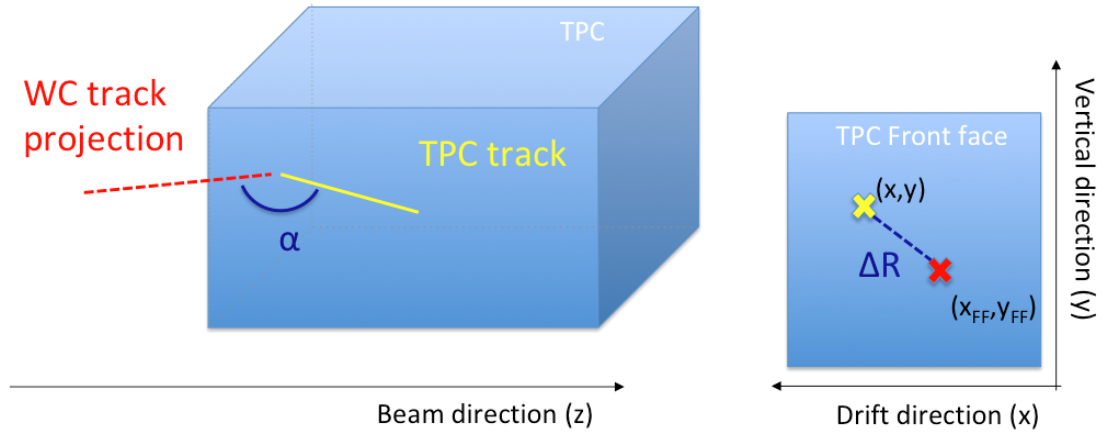


Figure 4.4: Visual rendering of the wire chamber to TPC match.

## 1845 4.3 The Thin Slice Method

1846 Once we have selected the pool of hadron candidates and we have identified the TPC  
1847 track corresponding to the beamline event, we apply the thin slice method to measure  
1848 the cross section, as the following sections describe.

### 1849 4.3.1 Cross Sections on Thin Target

1850 Cross section measurements on a thin target have been the bread and butter of  
1851 nuclear and particle experimentalists since the Geiger-Marsden experiments [67]. At  
1852 their core, this type of experiments consists in shooting a beam of particles with a  
1853 known flux on a thin slab of material and recording the outgoing flux.

1854 In general even in the case of thin target, the target is not a single particle,  
1855 but rather a slab of material containing many diffusion centers. The so-called “thin  
1856 target” approximation assumes that the target centers are uniformly distributed in  
1857 the material and that the target is thin compared to the projectile interaction length,  
1858 so that no center of interaction sits in front of another. In this approximation, the  
1859 ratio between the number of particles interacting in the target  $N_{\text{Int}}$  and the number of  
1860 incident particles  $N_{\text{Inc}}$  on the target determines the interaction probability  $P_{\text{Interacting}}$ ,

1861 which is the complementary to one of the survival probability  $P_{Survival}$ . Equation 4.2

$$P_{Survival} = 1 - P_{Interacting} = 1 - \frac{N_{Int}}{N_{Inc}} = e^{-\sigma_{TOT} n \delta X} \quad (4.2)$$

1862 describes the probability for a particle to survive the thin target. This formula relates  
1863 the interaction probability to the total hadronic cross section ( $\sigma_{TOT}$ ), the density of  
1864 the target centers ( $n$ )<sup>1</sup> and the thickness of the target along the incident hadron  
1865 direction ( $\delta X$ ). If the target is thin compared to the interaction length of the process  
1866 considered, we can Taylor expand the exponential function in equation 4.2 and find  
1867 a simple proportionality relationship between the cross section and the number of  
1868 incident and interacting particles, as shown in equation 4.3:

$$1 - \frac{N_{Int}}{N_{Inc}} = 1 - \sigma_{TOT} n \delta X + O(\delta X^2). \quad (4.3)$$

1869 Solving for the cross section, we find:

$$\sigma_{TOT} = \frac{1}{n \delta X} \frac{N_{Int}}{N_{Inc}}. \quad (4.4)$$

### 1870 4.3.2 Not-so-Thin Target: Slicing the Argon

1871 The interaction length of pions and kaons in argon is expected to be of the order  
1872 of 50 cm for pions and 100 cm for kaons. Thus, the LArIAT TPC, with its 90 cm  
1873 of length, is not a thin target. However, the fine-grained tracking of the LArIAT  
1874 LArTPC allows us to treat the argon volume as a sequence of many adjacent thin  
1875 targets.

1876 As described in Chapter 3, LArIAT wire planes consist of 240 wires each. The  
1877 wires are oriented at +/- 60° from the vertical direction at 4 mm spacing, while the

---

1. The scattering center density in the target,  $n$ , relates to the argon density  $\rho$ , the Avogadro number  $N_A$  and the argon molar mass  $m_A$  as  $n = \frac{\rho N_A}{m_A}$ .

beam direction is oriented 3 degrees off the  $z$  axis in the  $XZ$  plane. The wires collect  
 signals proportional to the energy loss of the hadron along its path in a  $\delta X = 4$   
 $\text{mm}/(\sin(60^\circ)\cos(3^\circ)) \approx 4.7$  mm slab of liquid argon. Thus, one can think to slice  
 the TPC into many thin targets of  $\delta X = 4.7$  mm thickness along the direction of the  
 incident particle, making a measurement at each wire along the path.

Considering each slice  $j$  a “thin target”, we can apply the cross section calculation  
 from Equation 4.4 iteratively, evaluating the kinetic energy of the hadron as it enters  
 each slice,  $E_j^{kin}$ . For each WC2TPC matched particle, the energy of the hadron  
 entering the TPC is known thanks to the momentum and mass determination by the  
 tertiary beamline,

$$E_{FrontFace}^{kin} = \sqrt{p_{Beam}^2 - m_{Beam}^2} - m_{Beam} - E_{loss}, \quad (4.5)$$

where  $E_{loss}$  is a correction for the energy loss in the uninstrumented material between  
 the beamline and the TPC front face. The energy of the hadron at each slab is  
 determined by subtracting the energy released by the particle in the previous slabs.  
 For example, at the  $j^{th}$  point of a track, the kinetic energy will be

$$E_j^{kin} = E_{FrontFace}^{kin} - \sum_{i < j} E_{Dep,i}, \quad (4.6)$$

where  $E_{Dep,i}$  is the energy deposited at each argon slice before the  $j^{th}$  point as measured  
 by the calorimetry associated with the tracking.

If the particle enters a slice, it contributes to  $N_{Inc}(E^{kin})$  in the energy bin corresponding  
 to its kinetic energy in that slice. If it interacts in the slice, it also contributes  
 to  $N_{Int}(E^{kin})$  in the appropriate energy bin. The cross section as a function of kinetic  
 energy,  $\sigma_{TOT}(E^{kin})$  will then be proportional to the ratio  $\frac{N_{Int}(E^{kin})}{N_{Inc}(E^{kin})}$ .

Our goal is to measure the total interaction cross section, independently from the  
 topology of the interaction. Thus, we determine that a hadron interacted simply by

	min	max
X	1 cm	46 cm
Y	-15 cm	15 cm
Z	0 cm	86 cm

Table 4.2: Fiducial volume boundaries used to determine cross section interaction point.

requiring that the last point of the WC2TPC matched track lies inside the fiducial volume, whose boundaries are defined in Table 4.2. If the TPC track stops within the fiducial volume, its last point will be the interaction point; if the track crosses the boundaries of the fiducial volume, the track will be considered “through going” and no interaction point will be found. The only points of the hadronic candidate track considered to fill the  $N_{\text{Inc}}$ ) and  $N_{\text{Inc}}$  plots are the ones contained in the fiducial volume.

### 4.3.3 Corrections to the Raw Cross Section

Equation 4.4 is a prescription for measuring the cross section in case of a pure beam of the hadron of interest and 100% efficiency in the determination of the interaction point. For example, if LArIAT had a beam of pure pions and were 100% efficient in determining the interaction point within the TPC, the pion cross section in each energy bin would be given by

$$\sigma_{TOT}^{\pi^-}(E_i) = \frac{1}{n\delta X} \frac{N_{\text{Int}}^{\pi^-}(E_i)}{N_{\text{Inc}}^{\pi^-}(E_i)}. \quad (4.7)$$

Unfortunately, this is not the case. In fact, the selection used to isolate pions in the LArIAT beam allows for the presence of some muons and electrons as background, while the kaon selection allows for a small percentage of protons (see Section 5.2.1). Also, the LArIAT TPC is not 100% efficient in determining the interaction point. Therefore we need to apply two corrections evaluated on the MC in order to

1918 extract the true cross section from LArIAT data: the background subtraction and  
 1919 the efficiency correction. Still using the pion case as example, we estimate the pion  
 1920 cross section in each energy bin changing Equation 4.7 into

$$\sigma_{TOT}^{\pi^-}(E_i) = \frac{1}{n\delta X} \frac{N_{Int}^{\pi^-}(E_i)}{N_{Inc}^{\pi^-}(E_i)} = \frac{1}{n\delta X} \frac{\epsilon^{Inc}(E_i)[N_{Int}^{TOT}(E_i) - B_{Int}(E_i)]}{\epsilon^{Int}(E_i)[N_{Inc}^{TOT}(E_i) - B_{Inc}(E_i)]}, \quad (4.8)$$

1921 where  $N_{Int}^{TOT}(E_i)$  and  $N_{Inc}^{TOT}(E_i)$  is the measured content of the interacting and  
 1922 incident histograms for events that pass the event selection,  $B_{Int}(E_i)$  and  $B_{Inc}(E_i)$   
 1923 represent the contributions from the background to the interacting and incident his-  
 1924 tograms respectively, and  $\epsilon^{Int}(E_i)$  and  $\epsilon^{Inc}(E_i)$  are the efficiency corrections for said  
 1925 histograms.

1926 As we will show in section 5.3, the background subtraction for the interacting  
 1927 and incident histograms can be translated into a corresponding relative pion content  
 1928  $C_{Interacting}^{\pi MC}(E_i)$  and  $C_{Incident}^{\pi MC}(E_i)$  and the cross section re-written as follows

$$\sigma_{TOT}^{\pi^-}(E_i) = \frac{1}{n\delta X} \frac{\epsilon^{Inc}(E_i)}{\epsilon^{Int}(E_i)} \frac{C_{Int}^{\pi MC}(E_i)}{C_{Inc}^{\pi MC}(E_i)} \frac{N_{Int}^{TOT}(E_i)}{N_{Inc}^{TOT}(E_i)}. \quad (4.9)$$

## 1929 4.4 Procedure testing with truth quantities

1930 The  $(\pi^-, \text{Ar})$  and  $(K^+, \text{Ar})$  total hadronic cross section implemented in Geant4 can be  
 1931 used as a tool to validate the measurement methodology. We describe here a closure  
 1932 test done on Monte Carlo to prove that the methodology of slicing the TPC retrieves  
 1933 the underlying cross section distribution implemented in Geant4 within the statistical  
 1934 uncertainty.

1935 For pions and kaons in the considered energy range, the Geant4 inelastic model  
 1936 adopted is “BertiniCascade”; the pion elastic cross sections are tabulated from on  
 1937 Chips, while the kaon elastic cross sections are tabulated on Gheisha and Chips.

1938 For the validation test, we fire a sample of pions and a sample of kaons inside the

1939 LArIAT TPC active volume using the Data Driven Monte Carlo (see section 5.2.2).  
1940 We apply the thin-sliced method using only true quantities to calculate the hadron  
1941 kinetic energy at each slab in order to decouple reconstruction effects from possible  
1942 issues with the methodology. For each slab of 4.7 mm length along the path of the  
1943 hadron, we integrate the true energy deposition as given by the Geant4 transportation  
1944 model. Then, we recursively subtracted it from the hadron kinetic energy at the TPC  
1945 front face to evaluate the kinetic energy at each slab until the true interaction point is  
1946 reached. Since the MC is a pure beam of the hadron of interest and truth information  
1947 is used to retrieve the interaction point, no correction is applied. Doing so, we obtain  
1948 the true interacting and incident distributions for the considered hadron, from which  
1949 we derive the true MC cross section as a function of the hadron true kinetic energy.

1950 Figure 4.5 shows the total hadronic cross section for argon implemented in Geant4  
1951 10.03.p1 (solid lines) overlaid with the true MC cross section as obtained with the  
1952 sliced TPC method (markers) for pions on the left and kaons on the right; the total  
1953 cross section is shown in green, the elastic cross section in blue and the inelastic  
1954 cross section in red. The nice agreement with the Geant4 distribution and the cross  
1955 section obtained with the sliced TPC method gives us confidence in the validity of  
1956 the methodology.

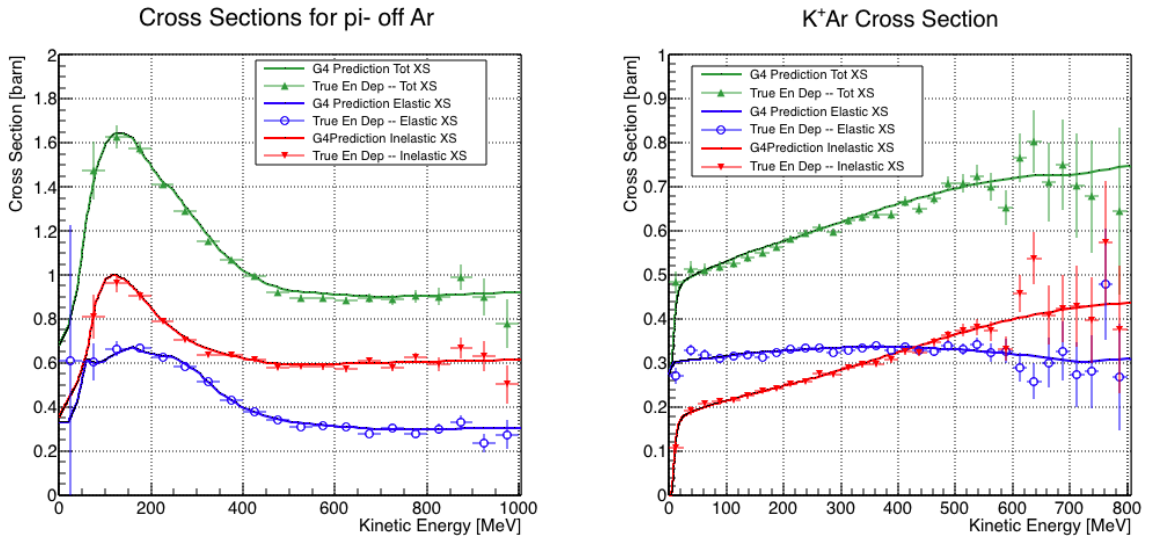


Figure 4.5: Hadronic cross sections for ( $\pi^-$ ,Ar) on the left and ( $K^+$ ,Ar) on the right as implemented in Geant4 10.03.p1 (solid lines) overlaid the true MC cross section as obtained with the sliced TPC method (markers). The total cross section is shown in green, the elastic cross section in blue and the inelastic cross section in red.

# <sup>1957</sup> Chapter 5

## <sup>1958</sup> Data and MC preparation for the <sup>1959</sup> Cross Section Measurements

<sup>1960</sup> “*Il dolce non lo mangi mai, ma qualche volta ti rifai.*  
<sup>1961</sup> *Abbracciami*”  
<sup>1962</sup> – Pietro Ciampi, 1971 –

<sup>1963</sup> This chapter describes the work done on the data and Monte Carlo samples in  
<sup>1964</sup> preparation for the cross section analyses. This entails the choice of the datasets  
<sup>1965</sup> and the production of the information needed to construct the Monte Carlo Simula-  
<sup>1966</sup> tion (Section 5.1), the construction and use of said Monte Carlo simulation (section  
<sup>1967</sup> 5.2), the study of backgrounds for the pion cross section (Section 5.3), the study of  
<sup>1968</sup> the energy loss between WC4 and TPC (Section 5.4), the study of the tracking in the  
<sup>1969</sup> TPC (Section 5.5), and study of the calorimetry response (Section 5.6).

### <sup>1970</sup> 5.1 Cross Section Analyses Data Sets

<sup>1971</sup> We choose LArIAT Run-II as the data period for the ( $\pi^-$ ,Ar) and ( $K^+$ ,Ar) total  
<sup>1972</sup> hadronic cross section analyses. Data taking for the this period started on 03/15/2016

1973 and ended on 07/31/2016. Since we are interested in beamline and TPC information,  
1974 we ask basic requirements on the operational status of the time of flight, wire chambers  
1975 and TPC to form the good run list for this period, which we informally call “lovely  
1976 runs”.

1977 The subset of lovely runs chosen for the  $(\pi^-, \text{Ar})$  total hadronic cross section  
1978 analysis includes only the -60A and -100A magnet configurations in negative polarity,  
1979 even if LArIAT explored several other beamline configurations during Run-II. The -  
1980 60A and -100A combined data set accounts for approximately 90% of the total Run-II  
1981 negative polarity runs. The choice of the main two beamline settings limits the need  
1982 for the production of many different MC sets and related corrections, still maintaining  
1983 a high number of events.

1984 Similarly, the subset of lovely runs chosen for the  $(K^+, \text{Ar})$  total hadronic cross  
1985 section analysis includes only the +60A and +100A magnet configurations in positive  
1986 polarity. It should be noted that kaons are extremely rare in the +60A sample, thus  
1987 the data sample for the  $(K^+, \text{Ar})$  cross section after the mass selection is about 90%  
1988 +100A runs, as shown in Table 5.1.

1989 For the first measurements in LArIAT that uses both beamline and TPC infor-  
1990 mation, we choose strict requirements on the reconstruction of the WC tracks, the  
1991 so-called “Picky Track” sample (see Section 3.2.2). This choice presents two ad-  
1992 vantages: the uncertainty on the momentum reconstruction for the “Picky Tracks”  
1993 sample is smaller compared to the “High Yield” sample, and the comparison with  
1994 the beamline MC results is straightforward. A possible future update and cross check  
1995 of these analysis would be the use of the High Yield sample, where the statistics is  
1996 about three times higher.

1997 The breakdown of beamline events as a function of the magnets settings is shown  
1998 in Table 5.1. The choice of the data sets determines the production of beamline MC  
1999 and serves as basis for the production of Data Driven MC, as shown in the next

2000 sections.

## 2001 5.2 Construction of a Monte Carlo Simulation for 2002 LArIAT

2003 For the simulation of LArIAT events and for the simulation of the datasets' particle  
2004 make up, we use a combination of two MC generators: the G4Beamline Monte Carlo  
2005 and the Data Driven single particle Monte Carlo (DDMC). We use the G4Beamline  
2006 MC to simulate the particle transportation in the beamline and calculate the particle  
2007 composition of the beam just after the fourth Wire Chamber (WC4). In order to  
2008 simulate the beamline particles after WC4 and in the TPC, we use the DDMC.

### 2009 5.2.1 G4Beamline

2010 G4Beamline simulates the beam collision with the LArIAT secondary target, the  
2011 energy deposited by the particles in the LArIAT beamline detectors, and the action  
2012 of the LArIAT magnets, effectively accounting for particle transportation through the  
2013 beamline from the LArIAT target until “Big Disk”, a fictional, void detector located  
2014 just before the LArIAT cryostat. At the moment of this writing, G4Beamline does  
2015 not simulated the responses of the beamline detectors. It is possible to interrogate the  
2016 truth level information of the simulated particles in several points of the geometry.  
2017 In order to ease the handshake between G4Beamline and the DDMC, we ask for  
2018 the beam composition just after WC4. Since LArIAT data are taken under different

	I = 60 A	I = 100 A	Total
Data Events after $\pi/\mu/e$ Mass Selection	67068	71413	138481
Data Events after $K$ Mass Selection	274	2563	2837

Table 5.1: Number of data events which fit the  $\pi/\mu/e$  or  $K$  mass hypothesis as a function of magnet settings.

beam conditions, we need to simulate separately the beam composition according to the magnets' settings and the secondary beam intensity with G4Beamline. For the pion cross section analysis the relevant beam conditions are secondary beam energy of 64 GeV, negative polarity magnet with current of 100 A and 60 A. For the kaon cross section analysis the relevant beam conditions is a secondary beam energy of 64 GeV, positive polarity magnet with current of 100 A.

## Beam Composition for Negative Pion Cross Section

Even if pions are by far the biggest beam component in negative polarity runs, the LArIAT tertiary beam is not a pure pion beam. While useful to discriminate between pions, kaons, and protons, the beamline detectors are not sensitive enough to discriminate among the lighter particles in the beam: electrons, muons and pions fall under the same mass hypothesis. Thus, we need to assess the contamination from beamline particles other than pions in the event selections used for the pion cross section analysis and correct for its effects. The first step of this process is assessing the percentage of electrons and muons in the  $\pi/\mu/e$  beamline candidates via the G4Beamline MC. Since the beamline composition is a function of the magnet settings, we simulate separately events for magnet current of -60A and -100A. Figure 5.1 shows the momentum predictions from G4Beamline overlaid with data for the 60A runs (left) and for the 100A runs (right). The predictions for electrons, muons and pions have been staggered and their sum is area normalized to data. Albeit not perfect, these plots show a reasonable agreement between the momentum shapes in data and MC. We attribute the difference in shape to a two approximations performed in the MC. Firstly, G4Beamline lacks the simulation of the WC efficiency which is momentum dependent and leads to enhance the number events in the center of the momentum distribution. Secondly, G4Beamline stop tracking pions and their products if they decay in after WC1; in data, pion decays in flight can still create a

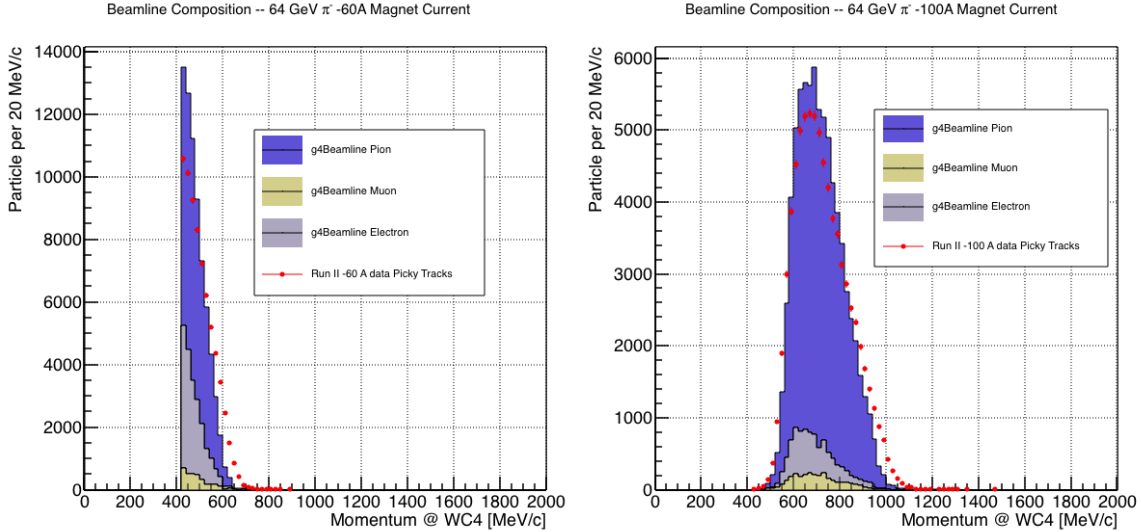


Figure 5.1: Beam composition for the -60A runs (left) and -100A runs (right). The solid blue plot represents the simulated pion content, the yellow plot represents the simulated muon content and the grey plot represents the simulated electron content. The plots are area normalized to the number of data events, shown in red.

	I = -60 A	I = -100 A
G4Pions	68.8 %	87.4 %
G4Muons	4.6 %	3.7 %
G4Electrons	26.6 %	8.9 %

Table 5.2: Simulated beamline composition per magnet settings

2045 trigger if the produced muon travels thought the beamline detectors. In the pion cross  
 2046 section analysis, these differences between data and G4Beamline are accounted for as  
 2047 a systematic uncertainty related to the beam composition (see Section 6.2.1).

2048 Table 5.2 shows the beam composition per magnet setting after the mass selection  
 2049 according to the G4Beamline simulation.

2050 The estimated beam composition is used as a basis to estimate the background  
 2051 contamination in the  $(\pi^-, \text{Ar})$  cross section measurement, whose full treatment is  
 2052 described in section 5.3.

2053 **Beam Composition for Positive Kaon Cross Section**

2054 In the positive polarity runs, the tertiary beam composition is mainly pions and  
2055 protons. The left side of Figure 5.2 shows the predictions for the momentum spectra  
2056 for the 100A positive runs according to G4Beamline (solid colors) overlaid with data  
2057 (black points). Since the LArIAT beamline detectors can discriminate between kaons  
2058 and other particles, we do not rely on the G4Beamline simulation to estimate the  
2059 beamline contamination in the pool of kaon candidates (as in the case of the pion  
2060 cross section), but rather we use a data driven approach. The basic idea of this data  
2061 driven approach is to estimate the bleed over from high and low mass peaks under  
2062 the kaon peak by fitting the tails of the  $\pi/\mu/e$  and proton mass distributions, as  
2063 shown in Figure 5.2 right side. Since the shape of the tails is unknown, the estimate  
2064 is done multiple times varying the range and shape for reasonable functions. For  
2065 example, to estimate the proton content under the kaon peak, we start by fitting the  
2066 left tail of the proton mass distribution with a gaussian function between  $650 \text{ MeV}/c^2$   
2067 and  $750 \text{ MeV}/c^2$ . We extend the fit function under the kaon peak and integrate the  
2068 extended fit function between  $350-650 \text{ MeV}/c^2$ . We integrate the mass histogram  
2069 in the same range and calculate the proton contamination as the ratio between the  
2070 two integrals. We repeat this procedure for several fit shapes (gaussian, linear and  
2071 exponential functions) and tail ranges. Finally, we calculate the contamination as  
2072 the weighted average of single estimates, where the weights are calculated to be the  
2073  $1./|1 - \chi^2|$  of the tail fits. The procedure is repeated for lighter particles mass peak  
2074 independently. With 12 iterations of this method we find a proton contamination of  
2075  $5.0 \pm 2.0 \%$  and a contamination from the lighter particles of  $0.2 \pm 0.5 \%$ . The  
2076 estimate of the proton background is currently not used in the kaon cross section  
2077 analysis, but it is a fundamental step to retrieve the true kaon cross section which  
2078 will be implemented in the further development of the analysis.

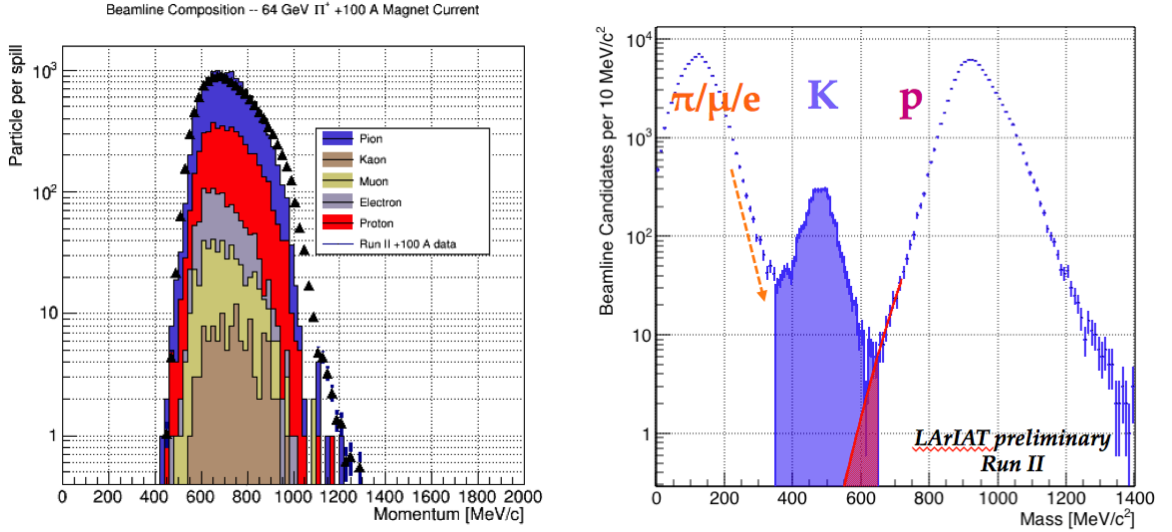


Figure 5.2: *Left:* Beam composition for the +100A runs after WC4 (no mass selection applied). The solid colors represent the contributions from the G4Beamline simulated particles: blue plot represents the simulated pion content, the yellow plot represents the simulated muon content and the grey plot represents the simulated positron content, the red the proton content and the mustard the kaon content. The plots are area normalized to the number of data events, shown in black. *Right:* Mass distribution for the Run-II positive runs, where the area under the kaon mass peak is highlighted in purple. The area under the extension of a possible fit for the proton tail is highlighted in red.

2079 **5.2.2 Data Driven MC**

2080 The Data Driven single particle Monte Carlo (DDMC) is a single particle gun which  
2081 simulates the particle transportation from WC4 into the TPC leveraging on the beam-  
2082 line data information. The DDMC uses the data momentum and position at WC4  
2083 to derive the event generation: a general sketch of the DDMC workflow is shown in  
2084 Figure 5.3.

2085 When producing a DDMC sample, beamline data from a particular running pe-  
2086 riod and/or running condition are selected first. For example, data for the negative  
2087 60A runs and for the negative 100A runs inform the event generation stage of two  
2088 different DDMC samples. Figure 5.4 schematically shows the data quantities of in-  
2089 terest leveraged from data: the momentum ( $P_x, P_y, P_z$ ) and position ( $X, Y$ ) at WC4.  
2090 For each data event, we obtain the particle position ( $X, Y$ ) at WC4 directly from the  
2091 data measurement; we calculate the components of the momentum using the beam-  
2092 line measurement of the momentum magnitude in conjunction with the hits on WC3  
2093 and WC4 to determine the direction of the momentum vector, as described in section  
2094 3.2.2. The momentum and position of the selected data form a 5-dimensional tuple,  
2095 which we sample thousands of times through a 5-dimensional hit-or-miss sampling  
2096 procedure to generate the MC events. This sampling generates MC events with the  
2097 same momentum and position distributions as data, with the additional benefit of  
2098 accounting for the correlations between the  $P_x, P_y, P_z, X, Y$  variables. As an example,  
2099 the results of the DDMC generation compared to data for the kaon +100A sample  
2100 are shown in figure 5.5 for the  $P_z, X$  and  $Y$  distributions; as expected, MC and data  
2101 agree within the statistical uncertainty by construction. A LArSoft simulation mod-  
2102 ule then launches single particle MC from  $z = -100$  cm (the location of the WC4)  
2103 using the generated events. The particles are free to decay and interact in their path  
2104 from WC4 to the TPC according to the Geant4 simulation.

2105 Using the DDMC technique ensures that the MC and data particles have very

2106 similar momentum, position and angular distributions at WC4 and allows us to use  
 2107 the MC sample in several occasions: to estimate the background contamination to  
 2108 the pion cross section (see Section 5.3), to calibrate the energy loss upstream of the  
 2109 TPC (see Section 5.4), or to study the tracking and the calorimetric performance  
 2110 (sections 5.5 and 5.6). A small caveat is in order here: the DDMC is a single particle  
 2111 Monte Carlo, which means that the beam pile-up is not simulated.

2112 We generate six samples for the pion cross section measurement: three samples  
 2113 of  $\sim 330000$  pions, muons and electrons to simulate the negative 60A runs, and three  
 2114 samples of  $\sim 340000$  pions, muons and electrons for the negative 100A runs. We  
 2115 generate a sample of 195000 kaons for the kaon cross section analysis.

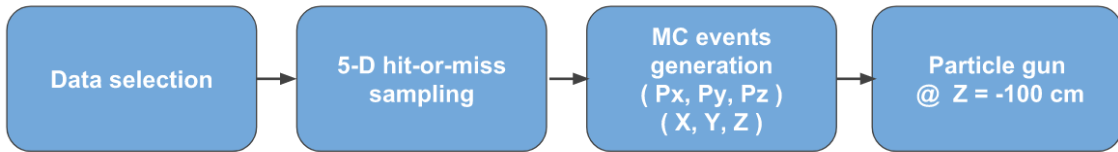


Figure 5.3: Workflow for Data Driven single particle Monte Carlo production.

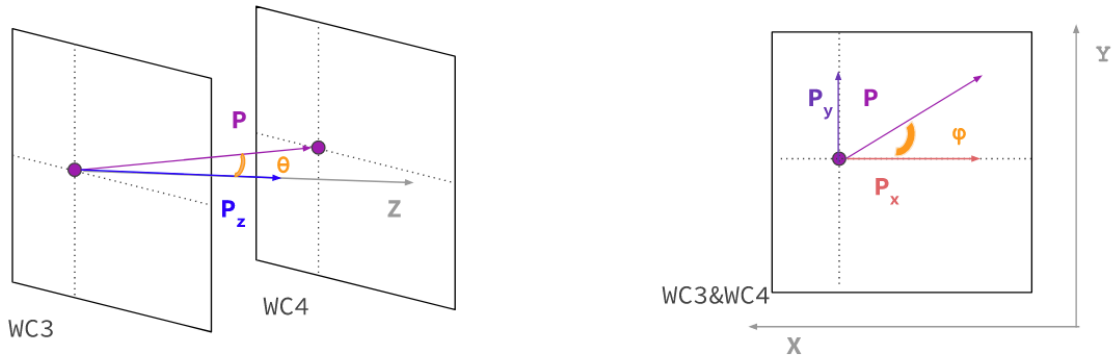


Figure 5.4: Scheme of the quantities of interest for the DDMC event generation:  
 $P_x, P_y, P_z, X, Y$  at WC4.

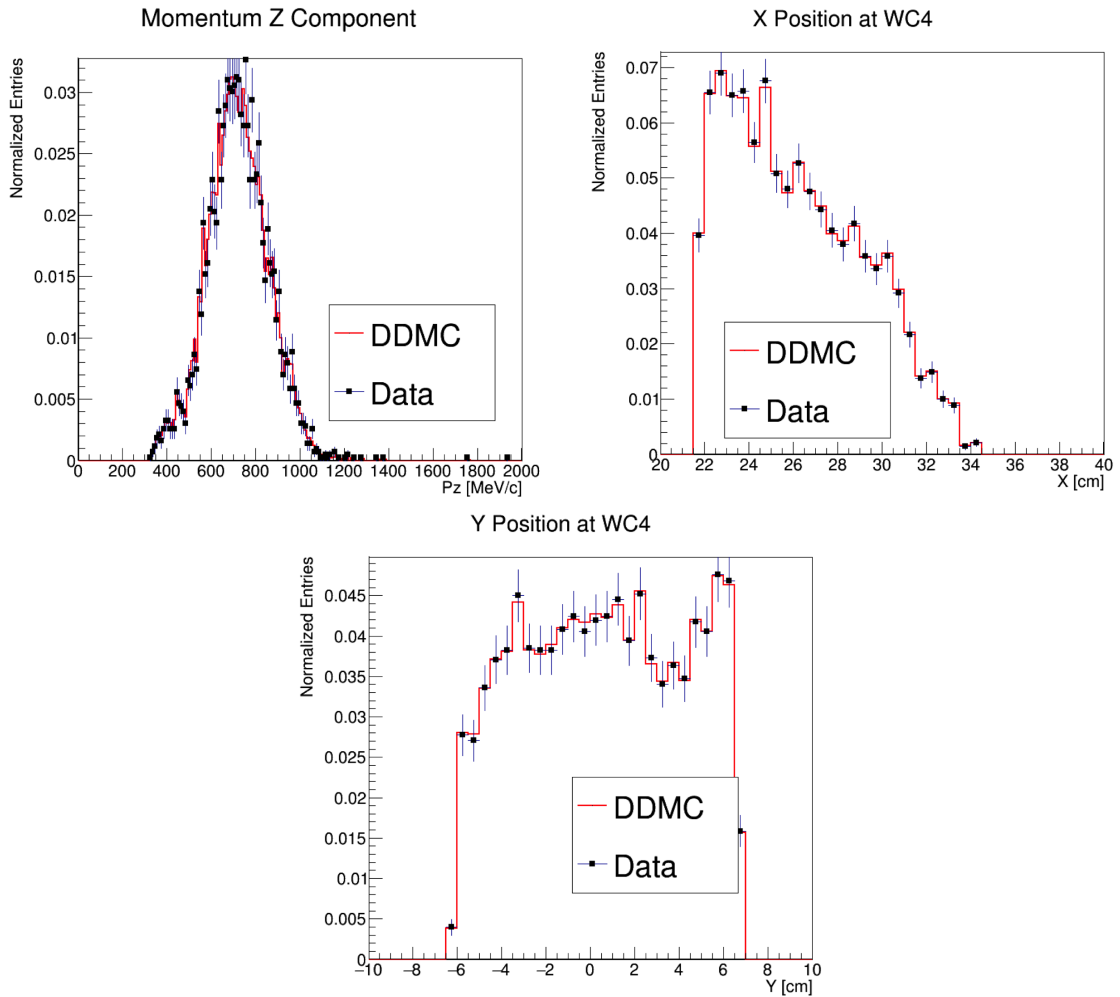


Figure 5.5: Comparison between generated quantities and data distributions for the 100A kaon sample: Z component of the momentum at WC4 (top left), X position at Wire Chamber 4 (top right), Y position at Wire Chamber 4 (bottom).

2116 **5.3 Estimate of Backgrounds in the Pion Cross  
2117      Section**

2118 We use the beamline simulation and the DDMC simulation to estimate the back-  
2119 ground in the total hadronic pion cross section. Two categories of background exists  
2120 for the negative pion cross section measurement: the one related to the pion interac-  
2121 tion in the chamber, discussed in Section 5.3.1 and the one related to the beamline  
2122 contamination, discussed in Section 5.3.2.

2123 **5.3.1 Background from Pion Capture and Decay**

2124 Our goal is to measure the total hadronic cross section for negative pions in argon.  
2125 Since pion capture can be classified as an electromagnetic process and pion decay is a  
2126 weak process, capture and decay represent unwanted interactions. We present here a  
2127 study of capture and decay in Monte Carlo and the solution we adopted to mitigate  
2128 their occurrence in the data sample.

2129 For this MC study, we use a sample of MC pions generated according to the  
2130 –60A beam profile with the DDMC (see Section 5.2.2). It is important to notice  
2131 that capture occurs predominantly at rest, while decay may occur both in flight and  
2132 at rest. Thus, we can highly mitigate capture and decay at rest by removing pions  
2133 which would release all their energy in the TPC and stop. This translates into a  
2134 momentum selection, where we keep only events whose WC momentum is above a  
2135 certain threshold. Figure 5.6 shows the true momentum distribution for the primary  
2136 pions<sup>1</sup> that arrive to the TPC (pink), that capture (green) or decay (blue) inside the  
2137 TPC, on a linear scale (left) and on a log scale (right) vertical axis.

---

2138 1. We use here the Geant4 denomination “primary” to indicate that the pion considered does not undergo interactions modifying its energy before getting to the TPC. In fact, not every pion shot from wire chamber four will arrive to the TPC as primary, some will decay or interact before the TPC.

2138 In order to choose the selection value for the wire chamber momentum, it is  
2139 beneficial to estimate the ratio of events which capture or decay that survive the  
2140 selection in MC as a function of the momentum threshold, and compare it with the  
2141 survival ratio for all the 60A events. This is done in figure 5.7. We define the survival  
2142 ratio simply as the number of events surviving the true momentum selection divided  
2143 by the number of events of that category. We calculate the survival ratio separately  
2144 for the three event categories explained above: total (pink), capture (green) and decay  
2145 (blue). Selecting pions with momentum greater than 420 MeV/c reduces the capture  
2146 events by 99% while maintaining about 80% of the 60A data sample and almost  
2147 the entire 100A sample. Figure 5.8 shows the ratio of events which end their life in  
2148 capture (green) or decay (blue) over the total number of events as a as a function of  
2149 the true momentum at wire chamber four. This ratio is slightly dependent on the  
2150 inelastic cross section implemented in Geant4, as we are able to register a pion capture  
2151 (or decay) only if it did not interact inelastically in the TPC. We choose a momentum  
2152 threshold of 420 MeV/c because the percentage of capture events drops below 1% and  
2153 the percentage of decays is never above 2% for momenta greater than 420 MeV/c.  
2154 After the momentum selection, we evaluate the contribution of capture and decay to  
2155 be a negligibly small background to the cross section measurement compared to the  
2156 background related to the beamline which we will address in the next section.

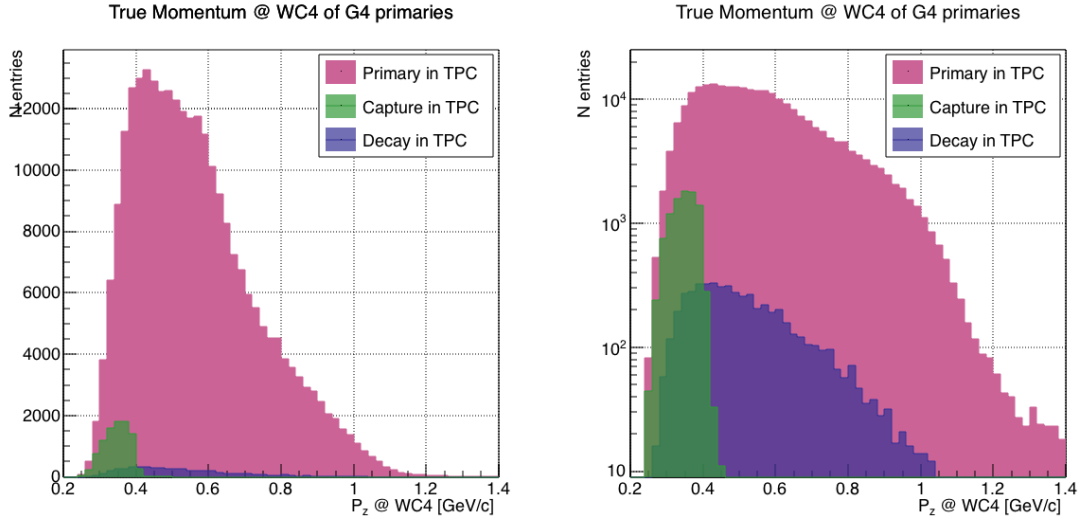


Figure 5.6: True momentum distribution at wire chamber 4 for every simulated pion arriving in the TPC (pink), ending its life in capture (green) or in decay (blue) in the TPC, linear vertical axis on the left, logarithmic on the right.

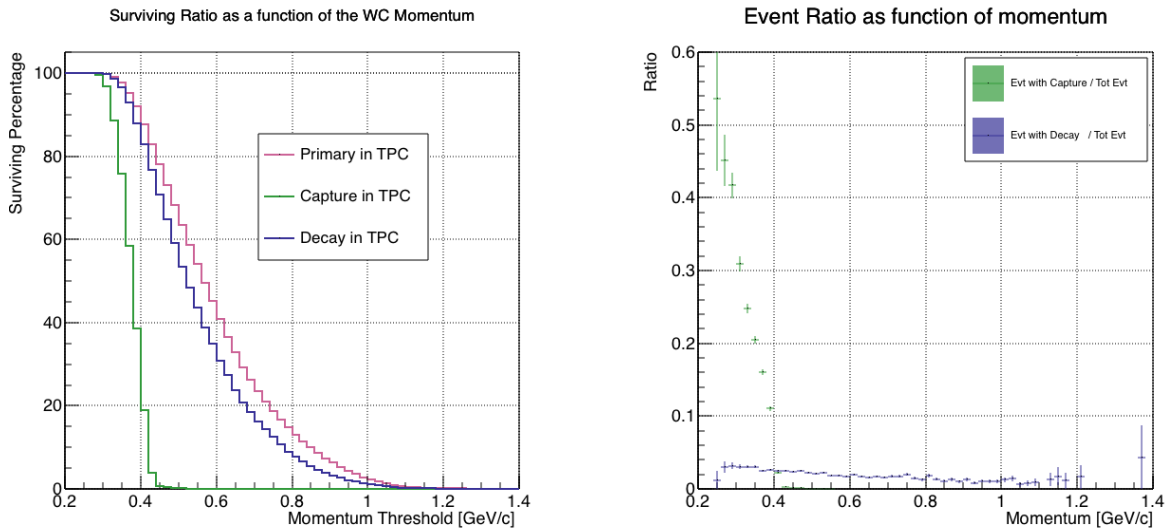


Figure 5.7: Survival ratio as a function of selection threshold on true momentum at wire chamber four for every simulated pion arriving in the TPC (pink), capture (green) or in decay (blue).

Figure 5.8: Ratio between the capture (green) and decay (blue) events over the total number of events as a function of the true momentum at wire chamber four.

2157 **5.3.2 Contributions from the Beamline Background**

2158 We define beamline background every TPC track matched to the WC track which is  
2159 not a primary pion. Potentially, there are 4 different types of beamline background:

2160 1) electrons,

2161 2) muons,

2162 3) secondaries from pion events,

2163 4) matched pile up events.

2164 The first step to quantify the effect of the beamline background on the pion cross  
2165 section is to estimate what percentage of events used in the cross section calculation  
2166 is not a primary pion. We start by noting that the last type of background, the  
2167 “matched pile up” events, is a negligible fraction, because of the definition of the  
2168 WC2TPC match: we deem the probability of a single match with a halo particle in  
2169 the absence of a beamline particle<sup>2</sup> negligibly small. As shown in Section 5.2.1, we  
2170 use G4Beamline to estimate the percentage of pions, muons and electrons at WC4,  
2171 obtaining the composition shown in Table 5.2. The next step is to simulate those  
2172 pions, muons and electrons from WC4 to the TPC with the DDMC and evaluate their  
2173 contribution to the cross section. To do so, we start by simulating the same number  
2174 of electrons, muons and pions with the DDMC and we apply the same selection chain  
2175 (i.e. track multiplicity rejection, WC2TPC acceptance and shower rejection) on the  
2176 three samples. The number of events per particle species surviving this selection is  
2177 shown on table 5.3. In order to reproduce the closest make up of the beam to data,  
2178 we weight each event of a given particle species according to the estimated beam  
2179 composition. In case of 60A runs, for example, the weights are 0.688 for pions, 0.046  
2180 for muons and 0.266 for electrons.

---

2. Events with multiple WC2TPC matches are always rejected.

	Magnet Current -60A			Magnet Current -100 A		
	MC $\pi^-$	MC $\mu^-$	MC $e^-$	MC $\pi^-$	MC $\mu^-$	MC $e^-$
Total Initial events	334500	334500	334500	344500	344500	344500
After Multiplicity Rejection	330668	333420	198065	326576	344208	201380
After WC2TPC Selection	218239	296333	91139	230418	300228	98834
Evts After Shower Rejection	208063	288914	20293	219882	293585	17780
Selection Survival Rate	62.3%	86.6%	6.1%	63.8%	85.5%	5.2%
Beam Composition @WC4	68.8%	4.6 %	26.6 %	87.4 %	3.7 %	8.9 %
Beam Composition @TPC FF	88.5%	8.2%	3.3 %	94.0%	5.3%	0.7%

Table 5.3: MC selection flow per particle species.

2181 It should be noted that pions may interact hadronically in the steel or in the  
 2182 non-instrumented argon upstream to the TPC front face while travelling the length  
 2183 of between WC4 and the TPC. Or, they could decay in flight between WC4 and the  
 2184 TPC. One of the interaction products can leak into the TPC and be matched with the  
 2185 WC track, contributing to the pool of events used for the cross section calculation. We  
 2186 call this type of particles “secondaries” from pion events, with a terminology inspired  
 2187 by Geant4. We estimate the number of secondaries using the DDMC pion sample.  
 2188 The percentage of secondaries is given by the number of matched WC2TPC tracks  
 2189 whose corresponding particle is not flagged as primary by Geant4. The secondary to  
 2190 pion ratio is 4.9% in the 60A sample and 4.3% in the 100A sample.

2191 We evaluate the beamline background contribution to the cross section by pro-  
 2192 ducing the interacting and incident histograms for the events surviving the selection,  
 2193 staggering the contributions for each particle species, as shown in Figure 5.9. From  
 2194 those histograms, we are able to evaluate the contribution of pions and beamline  
 2195 backgrounds to each bin of the interacting and incident histograms separately and  
 2196 obtain the relative pion content. The relative pion content in each bin for the inter-  
 2197 acting and incident histograms represents the correction applied to data. We take

here the interacting histogram as example, noting that the derivation of the correction for the incident histogram is identical. The number of entries in each bin of the interacting plot (Figure 5.9 left) is  $N_{\text{Int}}^{\text{TOT}}(E_i)$ , equal to the sum of the pions and beamline backgrounds in that bin, namely

$$N_{\text{Int}}^{\text{TOT}}(E_i) = N_{\text{Int}}^{\pi}(E_i) + \underbrace{N_{\text{Int}}^{\mu}(E_i) + N_{\text{Int}}^e(E_i) + N_{\text{Int}}^{\text{Secondary}}(E_i)}_{B_{\text{Int}}(E_i)}. \quad (5.1)$$

Thus, the relative pion content to each bin in MC can be calculated as follows

$$C_{\text{Int}}^{\pi MC}(E_i) = \frac{N_{\text{Int}}^{\pi MC}}{N_{\text{Int}}^{\text{TOTMC}}(E_i)} = \frac{N_{\text{Int}}^{\text{TOTMC}}(E_i) - B_{\text{Int}}^{MC}(E_i)}{N_{\text{Int}}^{\text{TOTMC}}(E_i)}. \quad (5.2)$$

In order to evaluate the pion content of each bin in data, we scale the measured bin by the corresponding relative pion content found in MC, as follows

$$N_{\text{Int}}^{\pi RecoData} = N_{\text{Int}}^{\text{TOTData}}(E_i) - B_{\text{Int}}^{\text{Data}}(E_i) = C_{\text{Int}}^{\pi MC}(E_i)N_{\text{Int}}^{\text{TOTData}}(E_i). \quad (5.3)$$

The pion content is evaluated separately in the interacting and incident histograms. Their ratio determines a correction to the measured raw cross section. For example, the measured raw cross section of a sample with enhanced muons content will tend to be lower than the raw cross section of a muon free sample. This is because most of the muons will cross the TPC without stopping, thus contributing almost exclusively to the incident histogram, forcing the pion content to be lower in the incident histogram than in the interacting; thus, the correction will tend to enhance the cross section.

## 2213 5.4 Estimate of Energy Loss before the TPC

2214 The beamline particles travel a path from where their momentum is measured in  
2215 the beamline until they are tracked again inside the TPC. In the LArIAT geometry,  
2216 a particle leaving the WC4 will encounter the materials listed in Table 5.4 before  
2217 being registered again. The energy lost by the particle in this non-instrumented  
2218 material modifies the particle's kinetic energy and directly affects the cross section  
2219 measurement, as shown in equation 4.5.

Material	density [g/cm <sup>3</sup> ]	width [cm]
Fiberglass laminate (G10)	1.7	1.28
Liquid Argon	1.4	3.20
Stainless Steel	7.7	0.23
Titanium	4.5	0.04
Air	$1.2 \cdot 10^{-3}$	89.43
Plastic Scintillator	1.03	1.20 (+ 1.30)

Table 5.4: LArIAT material budget from WC4 to the TPC Front Face.

We derive an estimate of the energy loss between the beamline momentum measurement and the TPC ( $E_{loss}$ ) from the pion and kaon DDMC samples, since this quantity is not measurable directly on data. The  $E_{loss}$  distribution for the 60A and 100A pion sample is shown in figure 5.10, left and right respectively. The  $E_{loss}$  distribution for the whole kaon sample is shown in figure 5.11. A clear double peaked structure is visible, which is due to the particles either missing or hitting the HALO paddle: a schematic rendering of this occurrence is shown in figure 5.12. The kinematic at WC4 determines the trajectory of a particle and whether or not it will hit the halo paddle. In figure 5.13 , we plot the true horizontal component of the momentum  $P_x$  versus the true  $X$  position at WC4 for pions missing the halo paddle (left) and for pions hitting the halo paddle (right) for the -60A MC simulation runs – analogous plots are obtained with the -100A pion simulation and with the kaon simulation. These distributions can be separated drawing a line in this position-momentum space.

We use a logistic regression [13] as a classifier to find the best separating line, shown in both plots as the red line. We classify as “hitting the halo paddle” all pions whose  $P_x$  and  $X$  are such that

$$P_x + 0.02 * X - 0.4 < 0$$

and as “missing the halo paddle” all pions whose  $P_x$  and  $X$  are such that

$$P_x + 0.02 * X - 0.4 > 0,$$

where the coefficients of the line are empirically found by the logistic regression estimation. Overall, this simple method classifies in the right category (hit or miss) about 86% of the pion events. In MC, we assign  $E_{loss} = 32 \pm 4$  MeV for pion events classified as “hitting the halo paddle”; we assign  $E_{loss} = 24 \pm 3$  MeV for pion events classified as “missing the halo paddle”. We apply the same classifier on data.

A scan of the simulated geometry showed an excess of 3 cm of uninstrumented argon compared with the surveyed detector geometry. We account for this difference by assigning in data  $E_{loss} = 24 \pm 6$  MeV for pion events classified as “hitting the halo paddle” and  $E_{loss} = 17 \pm 6$  MeV for pion events classified as “missing the halo paddle”, where the uncertainty is derived as the standard deviation of the double peaked distribution.

The summary of the values for used for  $E_{Loss}$  for the pion sample is listed in table 5.5 with the analogous results for the study on the kaon case.

	$E_{loss}$ [MeV]	
	Hitting Halo	Missing Halo
Pion MC	$32 \pm 4$	$24 \pm 3$
Pion Data	$25 \pm 6$	$17 \pm 6$
Kaon MC	$38 \pm 6$	$31 \pm 5$
Kaon Data	$26 \pm 7$	$22 \pm 7$

Table 5.5: Energy loss for pions and kaons.

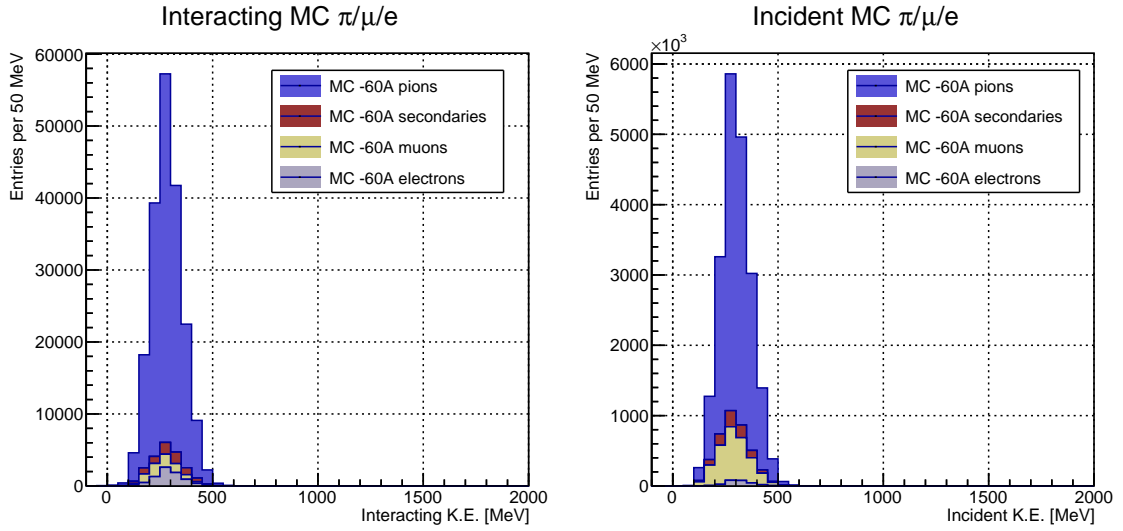


Figure 5.9: Left: staggered contributions to the interacting kinetic energy distribution for electron (grey), muons (yellow) and pion (blue) in the 60A simulation sample. Right: staggered contributions to the incident kinetic energy distribution for electron (grey), muons (yellow) and pion (blue) in the 60A simulation sample.

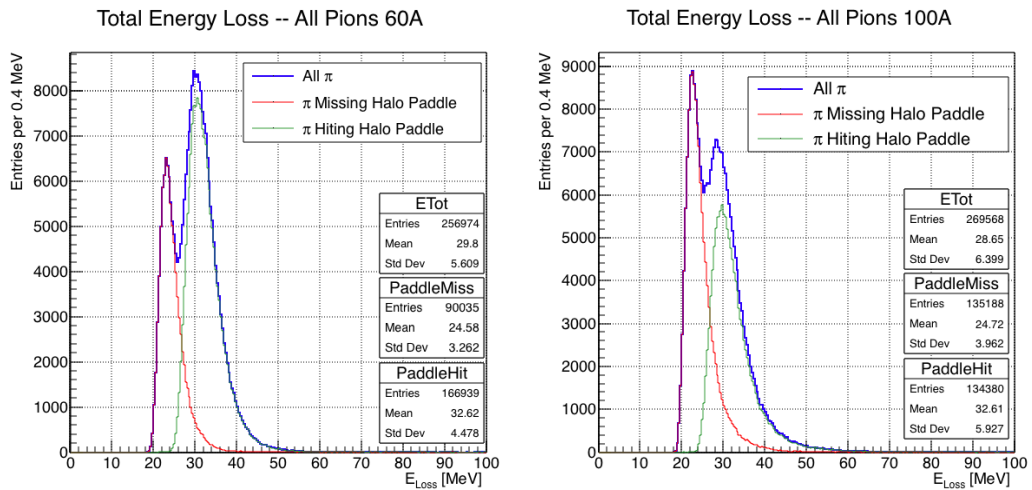


Figure 5.10: True energy loss between WC4 and the TPC front face according to the MC simulation of negative pions of the 60A runs (left) and of the 100A runs (right). The distribution for the whole data sample is shown in blue, the distribution for the pions missing the halo is shown in red, and the distribution for the pions hitting the halo is shown in green.

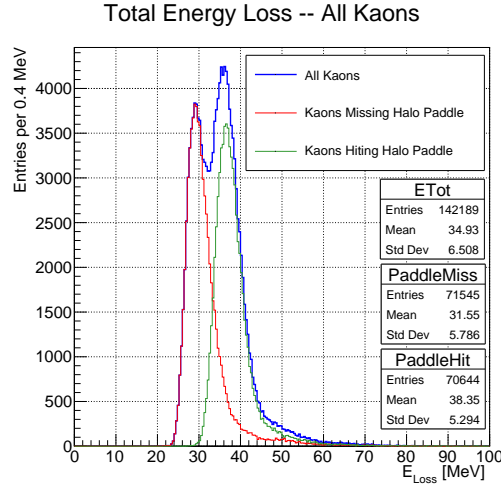


Figure 5.11: True energy loss between WC4 and the TPC front face according to the MC simulation of positive kaons in the 60A and 100A combined sample. The distribution for the whole data sample is shown in blue, the distribution for the kaons missing the halo is shown in red, and the distribution for the kaons hitting the halo is shown in green.

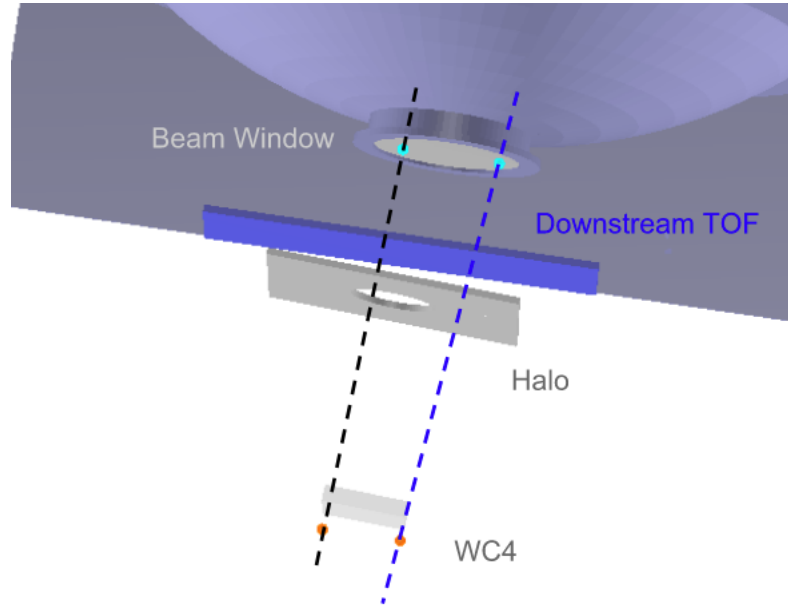


Figure 5.12: Schematic rendering of the particle path between WC4 and the TPC front face. The paddle with the hollow central circle represents the Halo paddle. We illustrate two possible trajectories: in black, a trajectory that miss the paddle and goes through the hole in the Halo, in blue a trajectory that hits the Halo paddle and goes through the scintillation material.

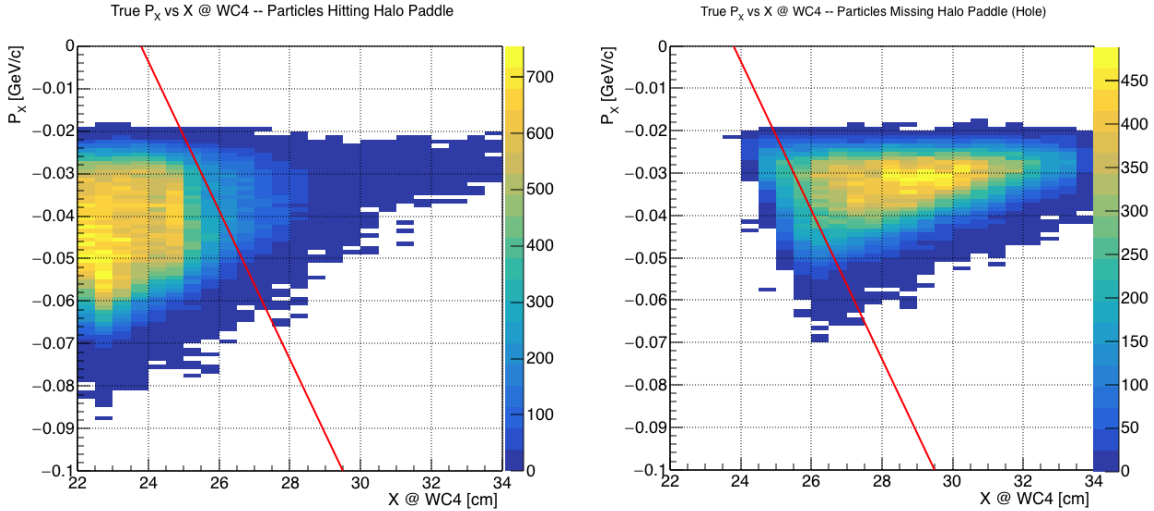


Figure 5.13: Horizontal component of the true momentum vs the horizontal position at WC4 for MC simulated pions of the 60A runs. The plot on the left shows the distribution for pion that miss the halo paddle and the plot on the right shows the distributions for pions that hit the halo. The form of the classifier is overlaid to both plots (red line).

## 2233 5.5 Tracking Studies

2234 The tracking of hadrons in the TPC determines both the beamline to TPC hand-  
2235 shake and the identification of the interaction point within the TPC. Thus, it plays  
2236 a fundamental role in the cross section measurements. We performed several studies  
2237 geared towards the optimization of the package for tracking in the TPC. In particular,  
2238 we studied a suitable set of parameters for the WC2TPC match and we optimized  
2239 the clustering algorithm to maximize the efficiency of finding the interaction point on  
2240 MC. Given the technical nature of these studies, we report them in Appendix B. We  
2241 report here the evaluation of the angular resolution of the tracking algorithm in data  
2242 and MC, due to its implication on the physics measurement.

### 2243 5.5.1 Angular Resolution

2244 Scope of this study is to understand and compare the tracking performances and  
2245 angular resolution of the TPC tracking on data and MC. We use the angular resolution

2246 of the tracking to determine the value of smallest angle that we can reconstruct with  
2247 a non-zero efficiency, effectively determining a selection on the angular distribution  
2248 of the cross section measurement due to the tracking performance.

2249 We start by selecting all the WC2TPC matched tracks used for the cross section  
2250 analysis. These tracks can contain from a minimum of 3 3D-space points to a maxi-  
2251 mum of 240 3D-space points. We fit a line to all the 3D-space points associated with  
2252 the track. For each track we calculate the average distance between each point in  
2253 space and the fit line as follows

$$\bar{d} = \frac{\sum_i^N d_i}{N}, \quad (5.4)$$

2254 where  $N$  is the number of 3D-space points of the track and  $d_i$  is the distance of the  
2255  $i$ -th space point to the line fit. Several tests to compare the goodness of fit between  
2256 data and MC have been considered. We decided to use  $\bar{d}$  for its straightforward  
2257 interpretation. The  $\bar{d}$  distribution for data and MC is shown in Figure 5.16 for pions  
2258 and in Figure 5.18 for kaons and shows a relatively good agreement between data and  
2259 MC.

2260 A visual representation of the procedure used to evaluate the angular resolution  
2261 is shown in Figure 5.14. For each track, we order the space points according to their  
2262 Z position along the positive beam direction (panel a) and we split them in two sets:  
2263 the first set contains all the points belonging to the first half of the track and the  
2264 second set contains all the points belonging the second half of the track. We remove  
2265 the last four points in the first set and the first four points in the second set, so to  
2266 have a gap in the middle of the original track (panel b). We fit the first and the second  
2267 set of points with two lines (panel c). We then calculate the angle between the fit of  
2268 the first and second half  $\alpha$  (panel d). The angle  $\alpha$  determines the spatial resolution  
2269 of the tracking. The distributions for data and MC for  $\alpha$  are given in Figure 5.17 for  
2270 pions and in Figure 5.19 for kaons. The mean of the data and MC angular resolution  
2271 are reported in Table tab:AngRes for pions and kaons in data and MC.

2272     Interaction angles smaller than the angle resolution are indistinguishable for the  
 2273     reconstruction. Therefore, we assess our ability to measure the cross section to be  
 2274     limited to interaction angles greater than 5.0 deg. More accurate studies of the angular  
 2275     resolution as a function of the kinetic energy and track length, albeit interesting, are  
 2276     left for an improvement of the analysis.

2277     It is beneficial to take a moment to describe the definition of interaction angle.  
 2278     In case of elastic scattering, the definition is straightforward: the interaction angle is  
 2279     the angle between the incoming and outgoing hadron, i.e.

$$\theta = \cos^{-1} \left( \frac{\vec{p}_{\text{incoming}} \cdot \vec{p}_{\text{outgoing}}}{|\vec{p}_{\text{incoming}}| |\vec{p}_{\text{outgoing}}|} \right). \quad (5.5)$$

2280     In case of inelastic scattering, the presence of several topologies requires a more  
 2281     complex definition, as shown in figure 5.15. We define the scattering angle as the  
 2282     biggest of the angles between the incoming hadron and the visible daughters, where  
 2283     the visible daughters are charged particles that travel more than 0.47 cm in the  
 2284     detector (see panel a); in case all the daughters are invisible, the angle is assigned  
 2285     to be 90 deg (see panel b). We chose this working definition of scattering angle  
 2286     for inelastic scattering keeping in mind how our tracking reconstruction works: the  
 2287     tracking will stop correctly non of the daughters are is visible in the detector and it  
 2288     is likely to stop correctly if multiple daughters form an interaction vertex. The only  
 2289     “dangerous” case is the production of one charged daughter plus neutrals, which we  
 2290     can study with this working definition of scattering angle (see panel c).

2291     We can see the effects of the angular resolution on the cross section by plotting the  
 2292     true Geant4 cross section for interaction angles greater than a minimum interaction

	Data	MC
Pions	$\bar{\alpha}_{Data} = (5.0 \pm 4.5) \text{ deg}$	$\bar{\alpha}_{MC} = (4.5 \pm 3.9) \text{ deg}$
Kaons	$\bar{\alpha}_{Data} = (4.3 \pm 3.7) \text{ deg}$	$\bar{\alpha}_{MC} = (4.4 \pm 3.6) \text{ deg}$

Table 5.6: Angular resolution for Pion and Kaon tracking in both data and MC.

angle. Figure 5.20 shows the true Geant4 cross section for interaction angles greater than 0 deg (green), 4.5 deg (red), 5.0 deg (blue) and 9.0 deg (yellow). A small 0.5 deg systematic shift between the mean of the data and MC angular resolution is present.

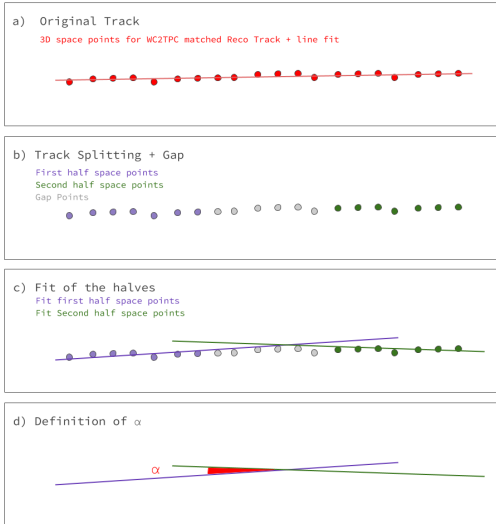


Figure 5.14: A visual representation of the procedure used to evaluate the angular resolution.

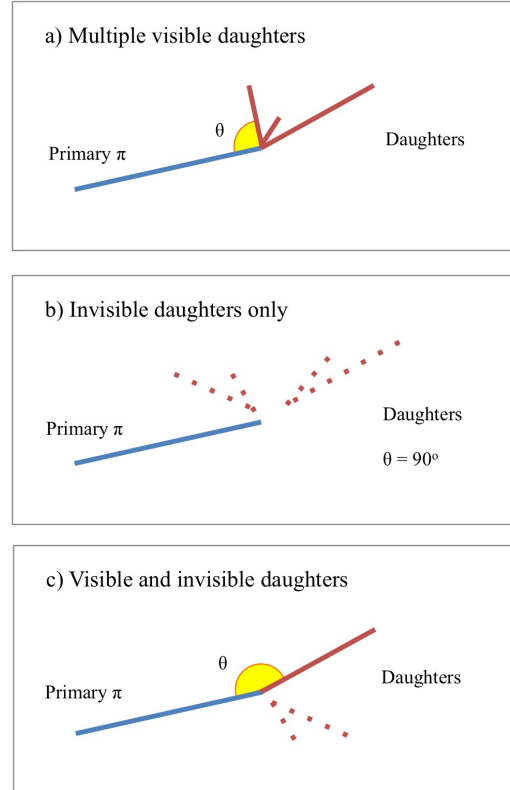


Figure 5.15: A visual representation of the scattering angle definition in case of inelastic scattering.

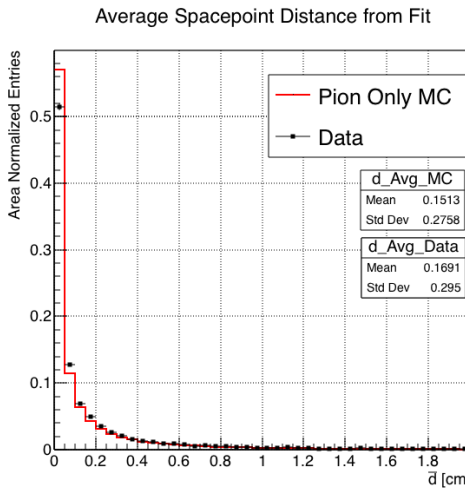


Figure 5.16: Distributions of the average distance between each 3D point in space and the fit line,  $\bar{d}$  for the data used in the pion cross section analysis and the pion only DDMC. The distributions are area normalized.

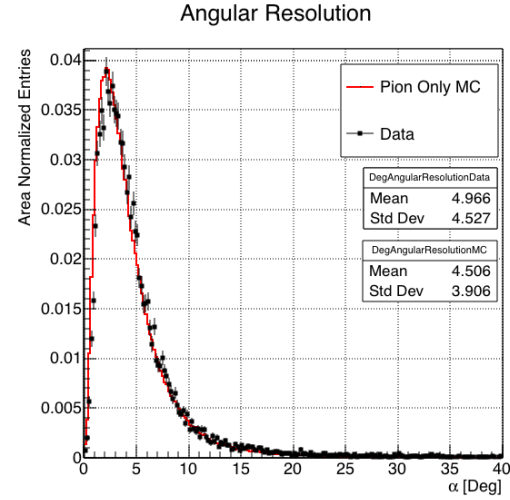


Figure 5.17: Distributions of angular resolution  $\alpha$  for data used in the pion cross section analysis and pion only DDMC. The distributions are area normalized.

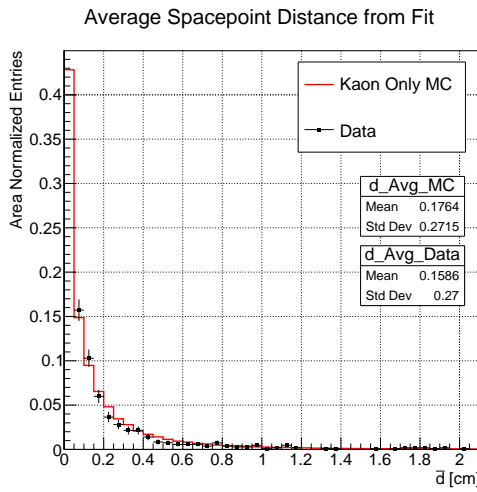


Figure 5.18: Distributions of the average distance between each 3D point in space and the fit line,  $\bar{d}$  for the data used in the kaon cross section analysis and the kaon only DDMC. The distributions are area normalized.

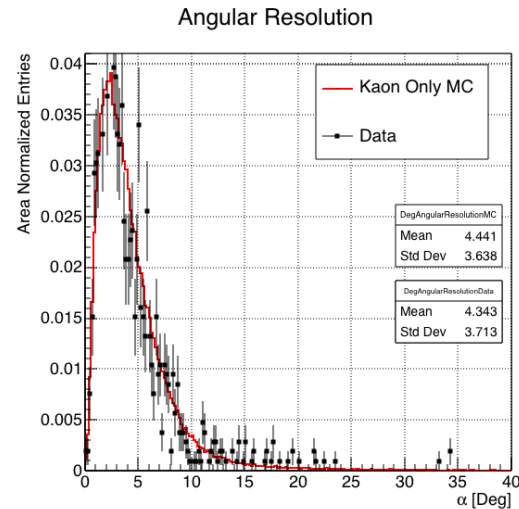


Figure 5.19: Distributions of angular resolution  $\alpha$  for data used in the kaon cross section analysis and kaon only DDMC. The distributions are area normalized.

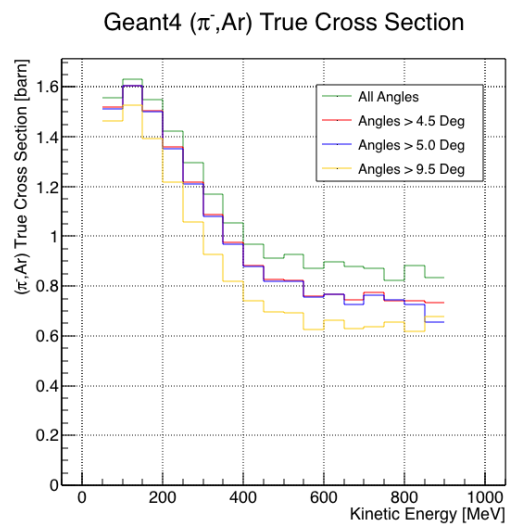


Figure 5.20: True ( $\pi^-$ , Ar) cross section for interaction angles greater than 0 deg (green), 4.5 deg (red), 5.0 deg (blue) and 9.0 deg (yellow).

2296 **5.6 Calorimetry Studies**

2297 The measured kinetic energy of a hadron candidate at each argon slab determines  
2298 which bins of the interacting and incident histograms a selected event is going to fill.  
2299 Thus, the energy measurement provided by the LArTPC is fundamental for the cross  
2300 section analysis. In Appendix C, we describe how we calibrate the TPC calorimetric  
2301 response. In the following section, we describe how we measure the kinetic energy of  
2302 the hadrons in the TPC.

2303 **5.6.1 Kinetic Energy Measurement**

2304 In this section, we define the measurement on the kinetic energy and determine the  
2305 related uncertainty. We will propagate this uncertainty into the cross section mea-  
2306 surement, as discussed in Section 6.1.2 for the pion cross section and in Section ??  
2307 for the kaon cross section.

2308 The kinetic energy of a hadron at the  $j^{\text{th}}$  slice of argon in the TPC is given by

$$KE_j = \sqrt{p_{\text{Beam}}^2 + m_{\text{Beam}}^2} - m_{\text{Beam}} - E_{\text{Loss}} - E_{\text{FF-j}}, \quad (5.6)$$

2309 where  $p_{\text{Beam}}$  is the momentum measured by the beamline detectors,  $m_{\text{Beam}}$  is the  
2310 mass of the hadron as reported in the PDG,  $E_{\text{Loss}}$  is the energy loss between the  
2311 beamline and the TPC, and  $E_{\text{FF-j}}$  is the energy that the hadron deposited from the  
2312 TPC front face until the  $j^{\text{th}}$  slice. The uncertainty on  $KE_j$  is then given by

$$\delta KE_j = \sqrt{\delta p_{\text{Beam}}^2 + \delta E_{\text{Loss}}^2 + \delta E_{\text{dep FF-j}}^2}, \quad (5.7)$$

2313 where we have dropped the uncertainty on the mass, since it is orders of magnitude  
2314 smaller than the other uncertainties. We assume the relative uncertainty on  $p_{\text{Beam}}$  to  
2315 be 2%, and the uncertainty on the energy loss upstream to be 7 MeV, as calculated

2316 in Section 5.4. We describe the estimate of the uncertainty on  $E_{\text{FF-j}}$  in the rest of  
2317 this section.

2318 The energy deposited by the hadron from the TPC front face until the  $j^{\text{th}}$  slice is  
2319 the sum of the measured energy deposited in each previous slabs  $E_i$ , i.e.

$$E_{\text{FF-j}} = \sum_{i < j} E_i, \quad (5.8)$$

2320 where  $E_i$  is measured in each slab as the product of the stopping power,  $dE/dX_i$ ,  
2321 and the track pitch,  $\text{Pitch}_i$ , for that point. If we assume conservatively that the  
2322 measurements of  $E_i$  are not independent from one another, the uncertainty on  $E_{\text{FF-j}}$   
2323 becomes

$$\delta E_{\text{FF-j}} = (j - 1)\delta E_i, \quad (5.9)$$

2324 where  $\delta E_i$  is the uncertainty on the energy loss in one slab of argon.

2325 The left side of Figure 5.21 shows the distribution of the energy deposited in each  
2326 slab of argon, for the 60A negative pion dataset in black and for the pion only MC  
2327 in blue. The analogous plot for the -100A negative pion data set is show on the right  
2328 side of Figure 5.21. The distributions are fitted with a landau displayed in red for  
2329 data and in teal for MC. The uncertainty on  $E_i$  is given by the width of the Landau  
2330 fit to the data. A small systematic uncertainty is given by a 1.0% difference between  
2331 the most probable value of the landau fits in data and MC.

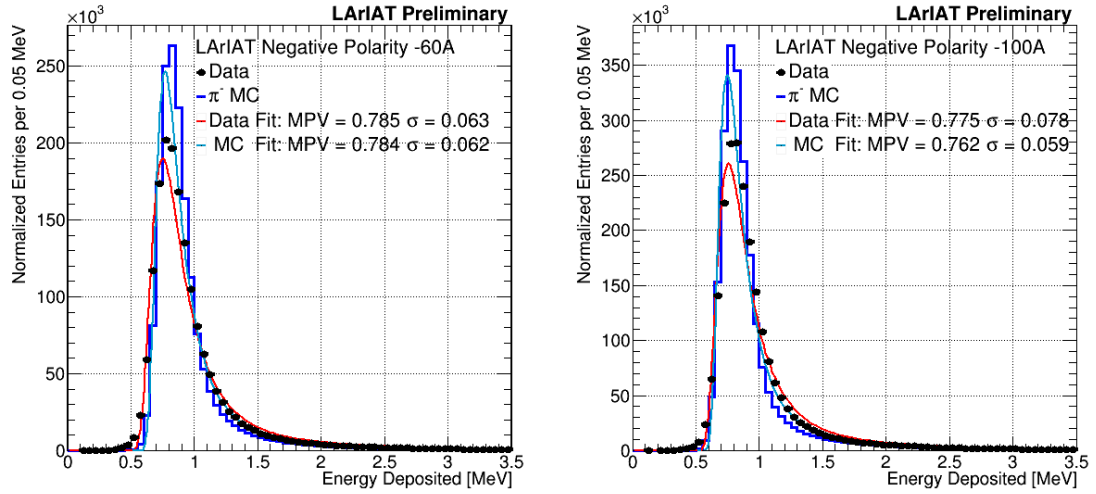


Figure 5.21: Energy deposited  $E_i$  in a single slab of argon for the pion -60A runs (left) and -100A runs (right). The data is shown in black, the MC in blue. The distributions are fitted with a landau displayed in red for data and in teal for MC.

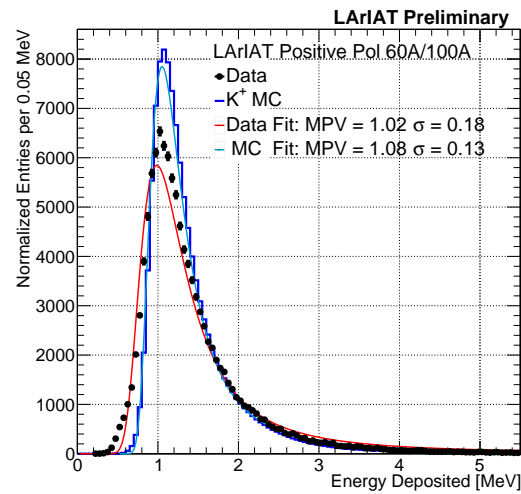


Figure 5.22: Energy deposited  $E_i$  in a single slab of argon for the kaons of the +60A runs and +100A runs. The data is shown in black, the MC in blue. The distributions are fitted with a landau displayed in red for data and in teal for MC.

2332 **Chapter 6**

2333 **Negative Pion Cross Section**

2334 **Measurement**

2335 “*Y ella es flama que se eleva, Y es un pájaro a volar.*

2336 *En la noche que se incendia, estrella de oscuridad*  
2337 *que busca entre la tiniebla, la dulce hoguera del beso.”*

2338 – Lila Downs, 2002 –

2339 In this chapter, we show the result of the thin slice method to measure the ( $\pi^-$ -  
2340 Ar) total hadronic cross section. In Section 6.1, we start by measuring the raw  
2341 cross section, i.e. the cross section obtained exclusively using data reconstruction,  
2342 without any additional corrections. In Section 6.2, we apply a statistical subtraction  
2343 of the background contributions based on simulation and a correction for detection  
2344 inefficiency. The final results are presented in Section 6.3.

2345 **6.1 Raw Cross Section**

2346 We measure the raw ( $\pi^-$ -Ar) total hadronic cross section as a function of the kinetic  
2347 energy in the two chosen data sets, the -60A and -100A negative runs. As we will

clarify in Section 6.2, the corrections to the raw cross section depend on the beam conditions and need to be calculated independently for the two datasets. Thus, we present here the measurement of the raw cross section on the two datasets separately.

As stated in section 4.3.2, the raw cross section is given by the equation 4.4

$$\sigma_{TOT}(E_i) = \frac{1}{n\delta X} \frac{N_{Int}^{TOT}(E_i)}{N_{Inc}^{TOT}(E_i)}, \quad (6.1)$$

where  $N_{Int}^{TOT}$  is the measured number of particles interacting at kinetic energy  $E_i$ ,  $N_{Inc}^{TOT}$  is the measured number of particles incident on an argon slice at kinetic energy  $E_i$ ,  $n$  is the density of the target centers and  $\delta X$  is the thickness of the argon slice. The density of the target centers and the slab thickness are  $n = 0.021 \cdot 10^{24} \text{ cm}^{-3}$  and  $\delta X = 0.47 \text{ cm}$ , respectively.

Figure 6.1 shows the distribution of  $N_{Int}^{TOT}$  as a function of the kinetic energy for the 60A dataset on the left and for the 100A dataset on the right. The data central points are represented by black dots, the statistical uncertainty is shown in black, while the systematic uncertainty is shown in red. Data is displayed over the  $N_{Int}^{TOT}$  distribution obtained with a MC mixed sample of pions, muon and electrons (additional details on the composition will be provided in Section ??). The contribution from the simulated pions is shown in blue, the one from secondaries in red, the one from muons in yellow and the ones from electrons in gray. The simulated pion's and backgrounds' contributions are stacked; the sum of the integrals from each particle species is normalized to the integral of the data.

Figure 6.2 shows the distribution of  $N_{Inc}^{TOT}$  for the 60A dataset on the left and for the 100A dataset on the right. Data is displayed over the MC. The same color scheme and normalization procedure is used for both the interacting and incident histograms.

Figure 6.3 shows the raw cross section for the 60A dataset on the left and for the 100A dataset on the right, statistical uncertainty in black and systematic uncertainty

2372 in red. The raw data cross section is overlaid to the reconstructed cross section for  
 2373 the MC mixed sample, displayed in azure. Since the background contributions and  
 2374 the detector effects for the 60A and 100A sample are different, it is premature to  
 2375 compare the raw cross sections obtained from the two samples at this point.

2376 We describe the calculation of the statistical uncertainty for the interacting, in-  
 2377 cident and cross section distributions in Section 6.1.1; we describe the procedure to  
 2378 calculate the corresponding systematics uncertainty on Section 6.1.2.

### 2379 6.1.1 Statistical Uncertainty

2380 The statistical uncertainty for a given kinetic energy bin of the cross section is cal-  
 2381 culated by error propagation from the statistical uncertainty on  $N_{\text{Inc}}^{\text{TOT}}$  and  $N_{\text{Int}}^{\text{TOT}}$   
 2382 correspondent bin. Since the number of incident particles in each energy bin is given  
 2383 by a simple counting, we assume that  $N_{\text{Inc}}^{\text{TOT}}$  is distributed as a poissonian with mean  
 2384 and variance equal to  $N_{\text{Inc}}^{\text{TOT}}$  in each bin. On the other hand,  $N_{\text{Int}}^{\text{TOT}}$  follows a bino-  
 2385 mial distribution: a particle in a given energy bin might or might not interact. The  
 2386 variance for the binomial is given by

$$\text{Var}[N_{\text{Int}}^{\text{TOT}}] = \mathcal{N}P_{\text{Interacting}}(1 - P_{\text{Interacting}}). \quad (6.2)$$

2387 Since the interaction probability  $P_{\text{Interacting}}$  is  $\frac{N_{\text{Int}}^{\text{TOT}}}{N_{\text{Inc}}^{\text{TOT}}}$  and the number of tries  $\mathcal{N}$  is  
 2388  $N_{\text{Inc}}^{\text{TOT}}$ , equation 6.2 translates into

$$\text{Var}[N_{\text{Int}}^{\text{TOT}}] = N_{\text{Inc}}^{\text{TOT}} \frac{N_{\text{Int}}^{\text{TOT}}}{N_{\text{Inc}}^{\text{TOT}}} \left(1 - \frac{N_{\text{Int}}^{\text{TOT}}}{N_{\text{Inc}}^{\text{TOT}}}\right) = N_{\text{Int}}^{\text{TOT}} \left(1 - \frac{N_{\text{Int}}^{\text{TOT}}}{N_{\text{Inc}}^{\text{TOT}}}\right). \quad (6.3)$$

2389  $N_{\text{Inc}}^{\text{TOT}}$  and  $N_{\text{Int}}^{\text{TOT}}$  are not independent. The statistical uncertainty on the cross  
 2390 section is thus calculated as

$$\delta\sigma_{\text{TOT}}(E) = \sigma_{\text{TOT}}(E) \left( \frac{\delta N_{\text{Int}}^{\text{TOT}}}{N_{\text{Int}}^{\text{TOT}}} + \frac{\delta N_{\text{Inc}}^{\text{TOT}}}{N_{\text{Inc}}^{\text{TOT}}} \right) \quad (6.4)$$

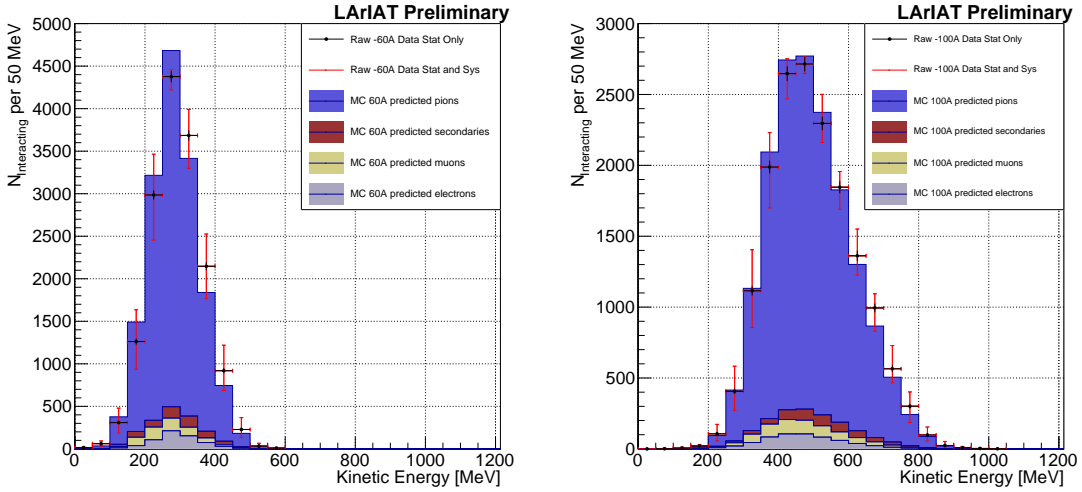


Figure 6.1: Raw number of interacting pion candidates as a function of the reconstructed kinetic energy for the 60A runs (left) and for the 100A runs (right). The statistical uncertainties are shown in black, the systematic uncertainties in red.

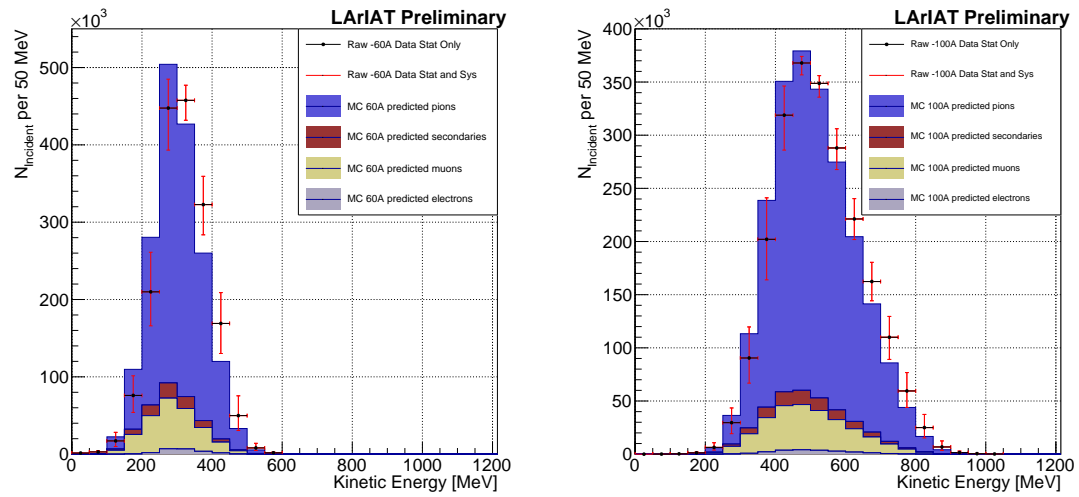


Figure 6.2: Raw number of incident pion candidates as a function of the reconstructed kinetic energy for the 60A runs (left) and for the 100A runs (right). The statistical uncertainty is shown in black, the systematic uncertainties in red.

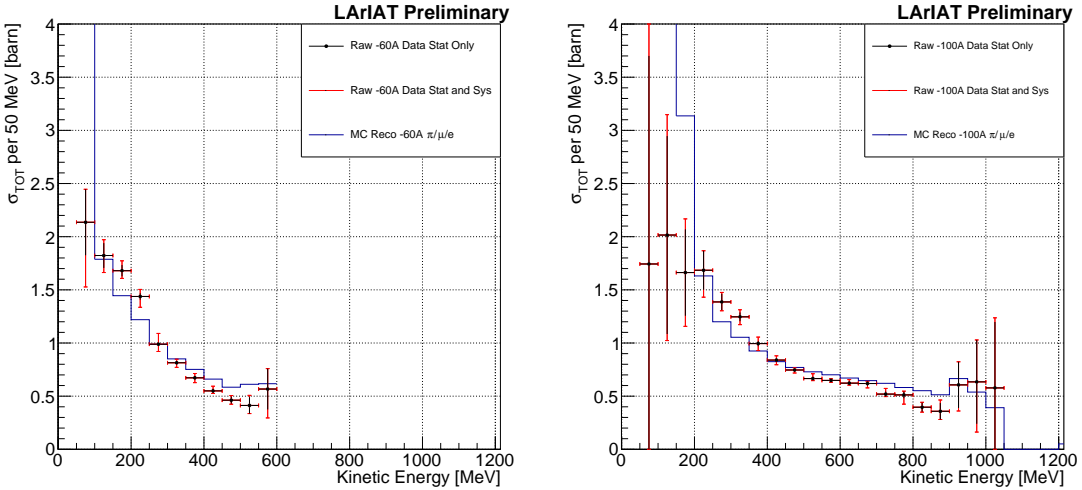


Figure 6.3: Raw ( $\pi^-$ -Ar) total hadronic cross section for the 60A runs (left) and for the 100A runs (right). The statistical uncertainty is shown in black, the systematic uncertainties in red. The raw cross section obtained with a MC mixed sample of pions, muon and electrons in the percentage predicted by G4Beamline is shown in azure.

2391 where:

$$\delta N_{\text{Inc}}^{\text{TOT}} = \sqrt{N_{\text{Inc}}^{\text{TOT}}} \quad (6.5)$$

$$\delta N_{\text{Int}}^{\text{TOT}} = \sqrt{N_{\text{Int}}^{\text{TOT}} \left(1 - \frac{N_{\text{Int}}^{\text{TOT}}}{N_{\text{Inc}}^{\text{TOT}}}\right)}. \quad (6.6)$$

### 2392 6.1.2 Treatment of Systematics

2393 The only systematic effect considered in the measurement of the raw cross section  
 2394 results from the propagation of the uncertainty associate with the measurement of  
 2395 the kinetic energy at each argon slab. As shown in Section 5.6.1, the uncertainty on  
 2396 the kinetic energy of a pion candidate at the  $j^{\text{th}}$  slab of argon is given by

$$\delta KE_j = \sqrt{\delta p_{\text{Beam}}^2 + \delta E_{\text{Loss}}^2 + \delta E_{\text{dep FF-j}}^2} \quad (6.7)$$

$$= \sqrt{(2\% p_{\text{Beam}})^2 + (6 \text{ [MeV]})^2 + (j - 1)^2 (\sim 0.08 \text{ [MeV]})^2}. \quad (6.8)$$

2397 We propagate this uncertainty by varying the energy measurement  $KE_j$  at each  
 2398 argon slab. We measure  $N_{\text{Inc}}^{\text{TOT}}$ ,  $N_{\text{Int}}^{\text{TOT}}$  and the cross section in three cases: first  
 2399 assigning the measured  $KE_j$  at each kinetic energy sampling, then assigning  $KE_j +$   
 2400  $\delta KE_j$ , and finally assigning  $KE_j - \delta KE_j$ . The difference between the values obtained  
 2401 using the  $KE_j$  sampling and the maximum and minimum values in each kinetic energy  
 2402 bin determines the systematic uncertainty.

## 2403 **6.2 Corrections to the Raw Cross Section**

2404 As described in section 4.3.3, we need to apply a background correction and an  
 2405 efficiency correction in order to derive the true pion cross section from the raw cross  
 2406 section. The true cross section is given in equation 4.9,

$$\sigma_{\text{TOT}}^{\pi^-}(E_i) = \frac{1}{n\delta X} \frac{\epsilon^{\text{Inc}}(E_i)}{\epsilon^{\text{Int}}(E_i)} \frac{C_{\text{Int}}^{\pi MC}(E_i)}{C_{\text{Inc}}^{\pi MC}(E_i)} \frac{N_{\text{Int}}^{\text{TOT}}(E_i)}{N_{\text{Inc}}^{\text{TOT}}(E_i)}. \quad (4.9)$$

2407 Section 6.2.1 describes the evaluation of pion content in the interacting and inci-  
 2408 dent histograms, ( $C_{\text{Int}}^{\pi MC}(E_i)$  and  $C_{\text{Inc}}^{\pi MC}(E_i)$ ) and the propagation to the cross section  
 2409 measurement of the relative systematic uncertainties.

2410 Section 6.2.2 describes the procedure employed to obtain the efficiency corrections  
 2411  $\epsilon^{\text{Int}}(E_i)$  and  $\epsilon^{\text{Inc}}(E_i)$  and the propagation to the cross section measurement of the  
 2412 relative uncertainties.

### 2413 **6.2.1 Background subtraction**

2414 We use the procedure described in 5.3.2 to evaluate the relative pion content in  
 2415 the interacting histogram  $C_{\text{Int}}^{\pi MC}(E_i)$  and the relative pion content in the incident  
 2416  $C_{\text{Inc}}^{\pi MC}(E_i)$ . We start by evaluating the relative pion content assuming the beamline  
 2417 composition simulated by G4Beamline, whose pion, muon and electron percentages  
 2418 per beam condition are reported again in the first line of Table 6.1. The left side of

2419 Figure 6.4 shows the MC estimated relative pion content for the interacting histogram  
2420 as function of kinetic energy for the 60A runs (top) and 100A runs (bottom). The  
2421 right side of the same figure shows the MC estimated relative pion content for the  
2422 incident histogram as function of kinetic energy for the 60A runs (top) and 100A  
2423 runs (bottom). In Figure 6.4 the central curves displayed in light blue are obtained  
2424 using the beamline composition as predicted by G4Beamline: these are the correction  
2425 curves for the relative pion content applied to data.

2426 So, the question now becomes: how well do we know the beamline composition?  
2427 In absence of additional data constraints, we take a 100% systematic uncertainty on  
2428 the electron content, reported in lines 3 and 4 of Table 6.1. The effect of doubling or  
2429 halving the electron percentage in the beam on the pion relative content is displayed  
2430 in red in Figure 6.4. We reserve a slightly different treatment for the muon content.  
2431 Since G4Beamline tracks only particles which cross all the wire chambers, pion events  
2432 that decay in flight from WC1 to WC4 are not recorded by G4Beamline. Pion decays  
2433 in the beamline could be trigger the beamline detectors in data, if the produced muon  
2434 proceeds in the beamline. Thus, we take the G4Beamline prediction for muons as a  
2435 lower bound in the composition: the effect of doubling the muon content (line 2 in  
2436 Table 6.1) is shown in blue on Figure 6.4. A future study of data from additional  
2437 beamline detectors such as the Aerogel Chernkov detectors [43] or the muon range  
2438 stack (see Section 3.2.4) has the potential of a narrowing the systematics uncertainty  
2439 coming from the beamline composition.

2440 We propagate the uncertainty on the beamline composition as a systematic un-  
2441 certainty to the cross section by varying the beam composition for all the cases listed  
2442 in Table 6.1 and evaluating variation of obtained data cross sections in each bin. This  
2443 systematic uncertainty is summed in quadrature with the statistical uncertainty and  
2444 the systematic uncertainty related to the kinetic energy measurement.

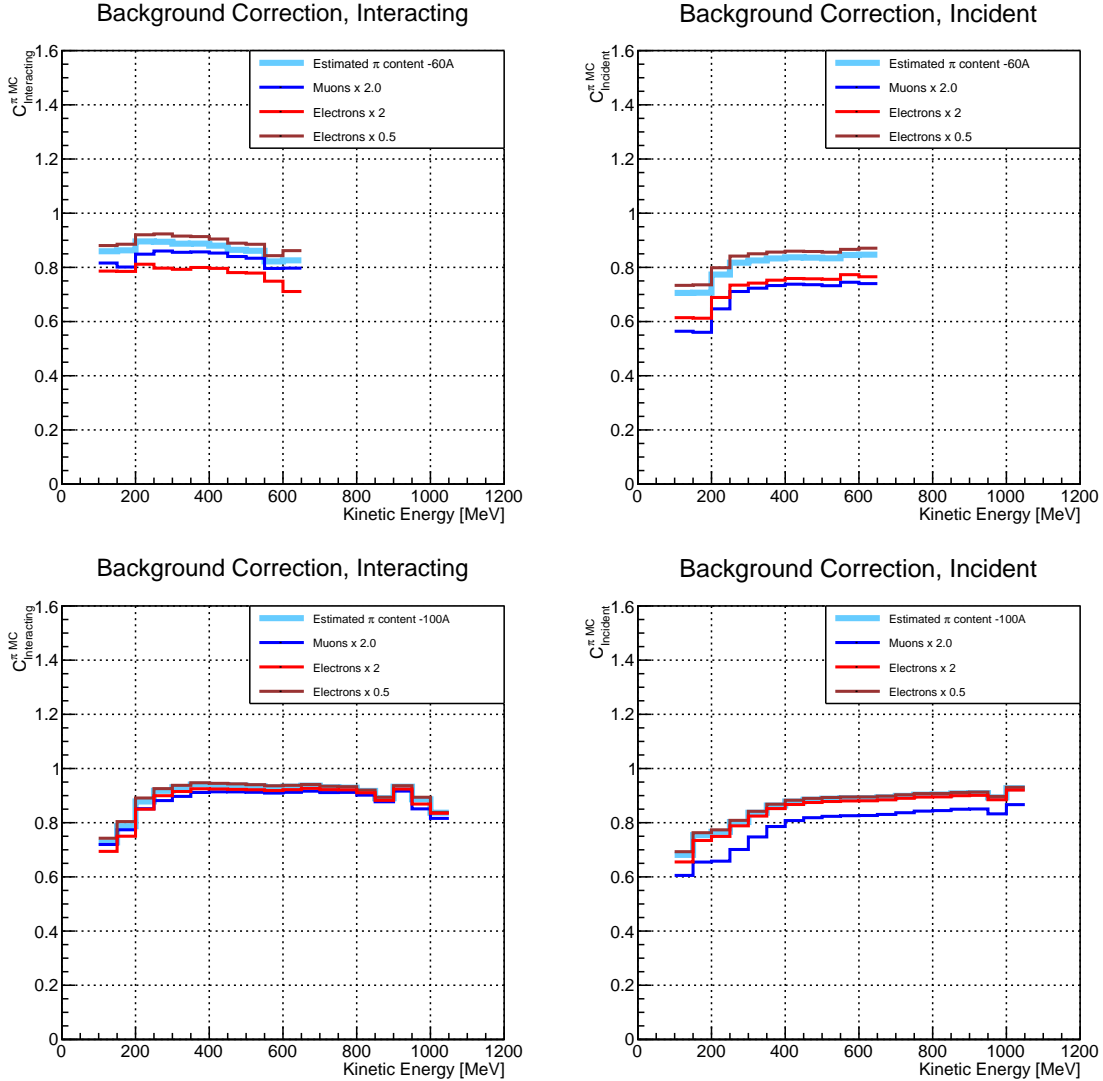


Figure 6.4: *Left:* MC estimated relative pion content for interacting histogram a function of kinetic energy for the 60A runs (top) and 100A runs (bottom), predicted background content in azure and muon and electron content variation in blue and red. *Right:* MC estimated relative pion content for incident histogram a function of kinetic energy for the 60A runs (top) and 100A (bottom), predicted background content in azure and muon and electron content variation in blue and red

## 2445 6.2.2 Efficiency Correction

2446 The interaction point for a track used in the total hadronic cross section analysis  
2447 is defined to be the last point of the WC2TPC matched track which lies inside the  
2448 fiducial volume. This definition is independent from the topology of the interaction.  
2449 If the TPC track stops within the fiducial volume, its last point will be the interaction  
2450 point, no matter what the products of the interaction look like; if the track crosses the  
2451 boundaries of the fiducial volume, the track will be considered “through going” and no  
2452 interaction point will be found. Given this definition, it is evident that we rely on the  
2453 tracking algorithm to discern where the interaction occurred in the TPC and correctly  
2454 stop the tracking. The tracking algorithm has an intrinsic angle resolution as shown  
2455 in section 5.5.1, which limits its efficiency, especially in the case of elastic scattering  
2456 occurring at low angles. Thus, we need to apply an efficiency correction to data in order  
2457 to retrieve the true cross section. The efficiency correction is evaluated separately for  
2458 the interacting and incident histograms, namely  $\epsilon_i^{\text{int}}$  and  $\epsilon_i^{\text{inc}}$ , and propagated to the  
2459 cross section as shown in equation 4.9.

### 2460 Efficiency Correction: Procedure

2461 We describe here the procedure to calculate the efficiency correction taking the in-  
2462 teracting histogram as example and noting that the procedure is identical for the  
2463 incident histogram.

2464 We derive the correction on a set of pure pion MC, calculating its value bin by  
2465 bin as the ratio between the true bin content and the correspondent reconstructed  
2466 bin content. The correction is then applied to the relevant bin in data. In formulae,  
2467 the efficiency correction is calculated to be

$$\epsilon^{\text{Int}}(E_i) = \frac{N_{\text{Interacting}}^{\pi \text{ Reco MC}}(E_i)}{N_{\text{Interacting}}^{\pi \text{ True MC}}(E_i)}, \quad (6.9)$$

2468 where  $N_{\text{Int}}^{\pi \text{ True MC}}(E_i)$  is the content of the  $i$ -th bin in for the true interacting  
 2469 histogram, and  $N_{\text{Int}}^{\pi \text{ Reco MC}}(E_i)$  is the content of the  $i$ -th bin in for the reconstructed  
 2470 interacting histogram. The correction is applied to data as follows

$$N_{\text{Int}}^{\pi \text{ True Data}}(E_i) = \frac{N_{\text{Int}}^{\pi \text{ Reco Data}}(E_i)}{\epsilon^{\text{Int}}(E_i)} = N_{\text{Int}}^{\pi \text{ Reco Data}}(E_i) \frac{N_{\text{Int}}^{\pi \text{ True MC}}(E_i)}{N_{\text{Int}}^{\pi \text{ Reco MC}}(E_i)}. \quad (6.10)$$

2471 where  $N_{\text{Int}}^{\pi \text{ Reco Data}}(E_i)$  is the background subtracted bin content of the  $i$ -th bin in  
 2472 for the reconstructed interacting histogram for data, i.e.

$$N_{\text{Int}}^{\pi \text{ Reco Data}}(E_i) = N_{\text{Int}}^{\text{TOT Data}}(E_i) - B_{\text{Int}}^{\text{Data}}(E_i) = C_{\text{Int}}^{\pi \text{ MC}}(E_i) N_{\text{Int}}^{\text{TOT Data}}(E_i). \quad (6.11)$$

2473 In section 5.5.1, we estimated the angular resolution for data and MC to be  
 2474  $\bar{\alpha}_{\text{Data}} = (5.0 \pm 4.5)$  deg and  $\bar{\alpha}_{\text{MC}} = (4.5 \pm 3.9)$  deg, respectively. Most interaction  
 2475 angles smaller than the angular resolution will thus be indistinguishable for the re-  
 2476 construction. Thus, we claim we are able to measure the cross section for interaction  
 2477 angles greater than 5.0 deg. Geant4 simulates interactions at all angles, as shown in  
 2478 figure 6.7. In order to calculate the efficiency correction, we select events which have  
 2479 an interaction angle greater than a given  $\alpha_{\text{res}}$  to construct the true interacting and  
 2480 incident histograms (the denominator of the efficiency correction). The systematics  
 2481 on the efficiency correction is estimated by varying the value of  $\alpha_{\text{res}}$  between 0 deg  
 2482 and 4.5 deg and propagating the uncertainty on the cross section.

2483 Figure 6.5 shows  $\epsilon^{\text{Int}}(E_i)$  in the left side and  $\epsilon^{\text{Inc}}(E_i)$  on the right as a function of  
 2484 the kinetic energy for the 60A runs and their systematic uncertainty. Similarly, figure  
 2485 6.6 shows  $\epsilon^{\text{Int}}(E_i)$  in the left side and  $\epsilon^{\text{Inc}}(E_i)$  on the right as a function of the kinetic  
 2486 energy for the 100A runs and their systematic uncertainty.

	Magnet Current -60A			Magnet Current -100 A		
	MC $\pi^-$	MC $\mu^-$	MC $e^-$	MC $\pi^-$	MC $\mu^-$	MC $e^-$
Expected Composition	68.8 %	4.6 %	26.6 %	87.4 %	3.7 %	8.9 %
Composition 2x Muons	64.2 %	9.2 %	26.6 %	83.7 %	7.4 %	8.9 %
Composition 2x Electrons	42.2 %	4.6 %	53.2 %	78.5 %	3.7 %	17.8 %
Composition 0.5x Electrons	82.1 %	4.6 %	13.3 %	91.9 %	3.7 %	4.4 %

Table 6.1: Beam composition variation for the study of systematics due to beam contamination.

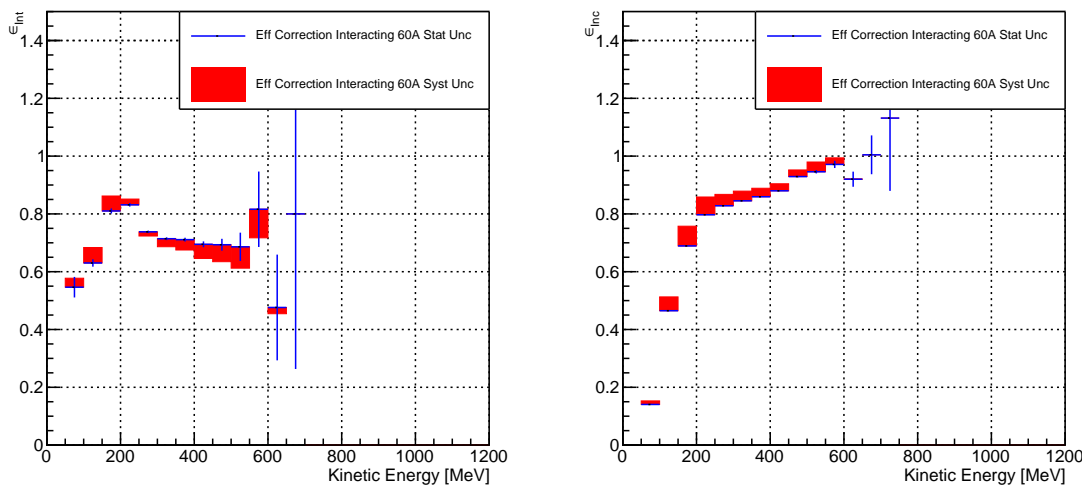


Figure 6.5: *Left:* Efficiency correction on the 60A interacting histogram, statistical uncertainty in blue, systematic uncertainty in red. *Right:* Efficiency correction on the 60A incident histogram, statistical uncertainty in blue, systematic uncertainty in red.

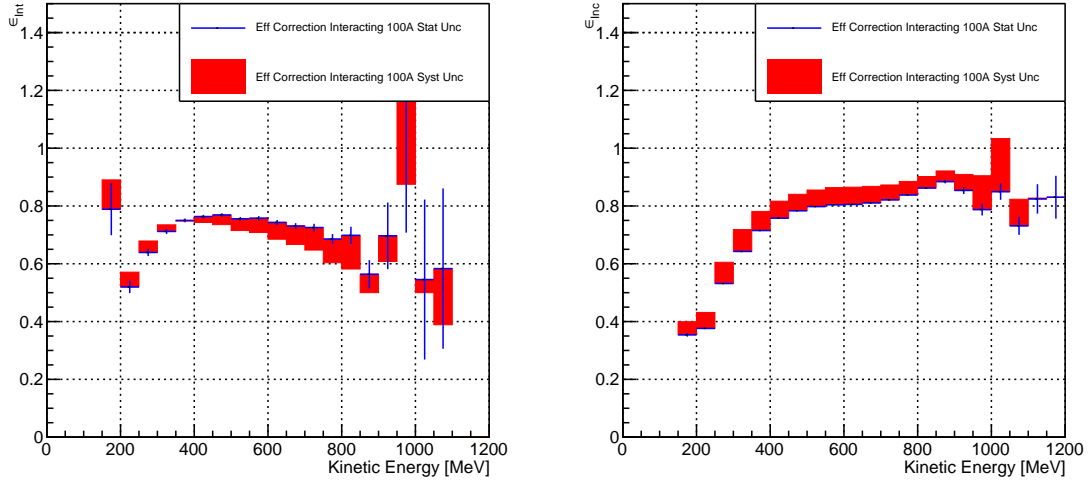


Figure 6.6: *Left*: Efficiency correction on the 100A interacting histogram, statistical uncertainty in blue, systematic uncertainty in red. *Right*: Efficiency correction on the 100A incident histogram, statistical uncertainty in blue, systematic uncertainty in red.

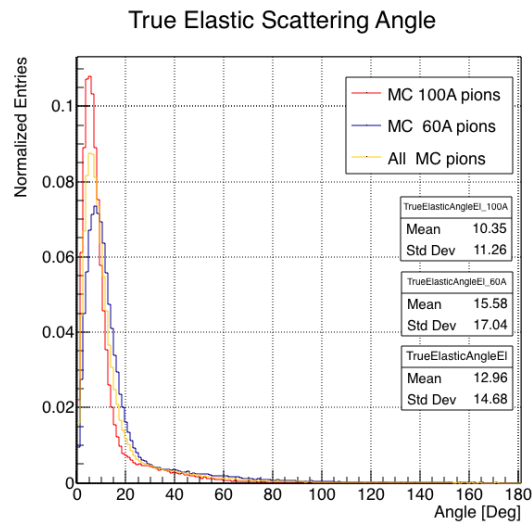


Figure 6.7: Distribution of the true scattering angle for a pion elastic scattering off the argon nucleus as simulated by Geant4.

2487 **6.3 Results**

2488 Figure 6.8 show the measurement of the ( $\pi^-$ -Ar) total hadronic cross section for  
2489 scattering angles greater than  $5^\circ$ , as the result of the background subtraction and  
2490 efficiency correction to the raw cross section. The top left plot is the measurement  
2491 obtained on the 60A data, statistical uncertainty in black and systematic uncertainty  
2492 in red. The top right plot is the measurement obtained on the 100A data, statistical  
2493 uncertainty in black and systematic uncertainty in blue. The bottom plot shows the  
2494 two measurements overlaid. In all three plot, the Geant4 prediction for the total  
2495 hadronic cross section for angle scattering greater than  $5^\circ$  is displayed in green.

2496 The systematic uncertainty on the cross section is the sum in quadrature of the  
2497 statistical uncertainty, the systematic uncertainty related to the kinetic energy mea-  
2498 surement, the systematic uncertainty related to the beam composition and the sys-  
2499 tematic uncertainty related to the efficiency correction.

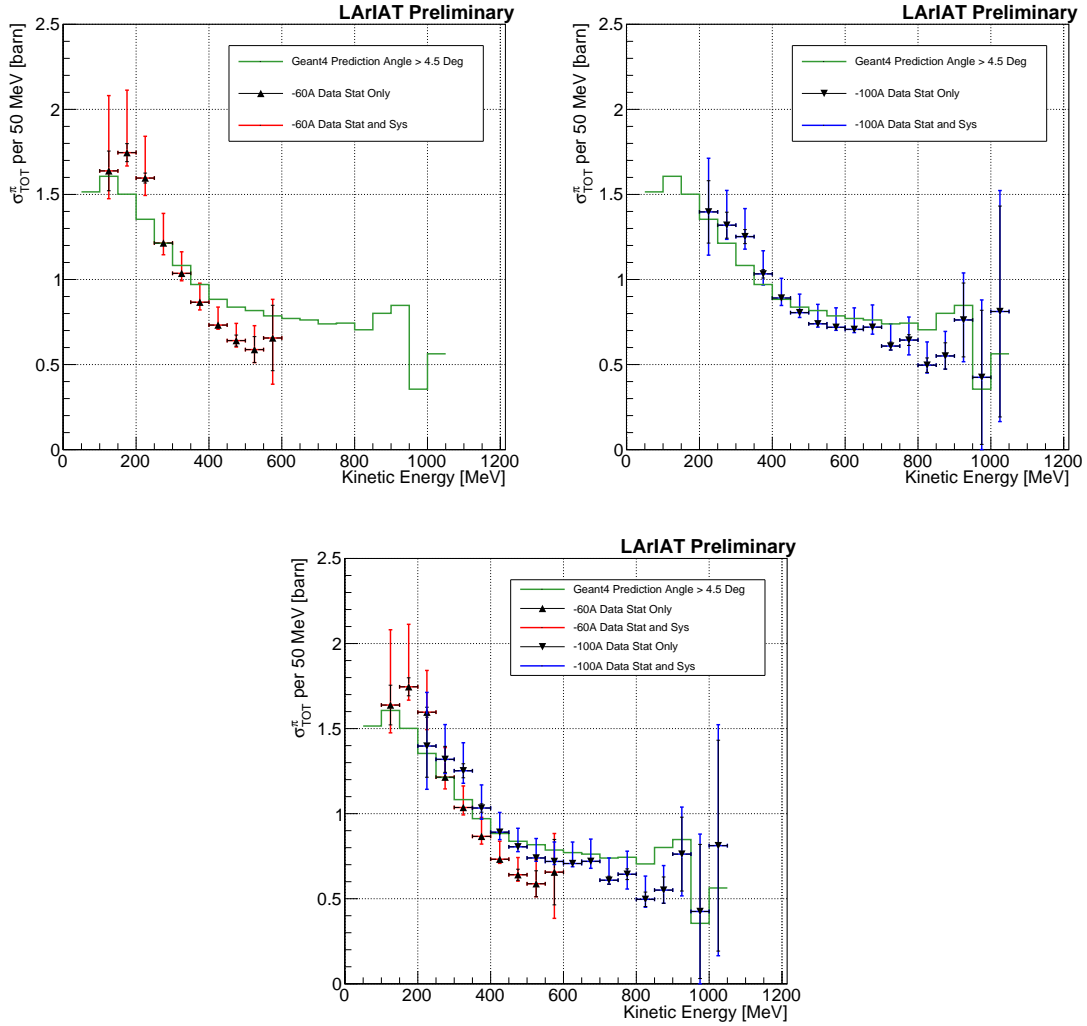


Figure 6.8: *Top Left:* ( $\pi^-$ -Ar) total hadronic cross section for scattering angles greater than  $5^\circ$  measured in the 60A sample, statistical uncertainty in black and systematic uncertainty in red. The Geant4 prediction for the total hadronic cross section for angle scattering greater than  $5^\circ$  is displayed in green.

*Top Right:* ( $\pi^-$ -Ar) total hadronic cross section for scattering angles greater than  $5^\circ$  measured in the 100A sample, statistical uncertainty in black and systematic uncertainty in blue. The Geant4 prediction for the total hadronic cross section for angle scattering greater than  $5^\circ$  is displayed in green.

*Bottom:* ( $\pi^-$ -Ar) total hadronic cross section measurements in the 60A and 100A samples overlaid with the Geant4 prediction (green).

2500 **Chapter 7**

2501 **Positive Kaon Cross Section**  
2502 **Measurement**

2503 “Beat-up little seagull, on a marble stair  
2504 Tryin’ to find the ocean, lookin’ everywhere.”  
2505 – Nina Simone, 1978 –

2506 In this chapter, we show the result of the thin slice method to measure the ( $K^+$ -  
2507 Ar) total hadronic cross section. In Section 7.1, we start by measuring the raw  
2508 cross section. In Section 7.2, we apply a statistical subtraction of the background  
2509 contributions based on simulation and a correction for detection inefficiency. The  
2510 final results are presented in Section 7.3.

2511 **7.1 Raw Cross Section**

2512 We measure the raw ( $K^+$ -Ar) total hadronic cross section as a function of the kinetic  
2513 energy in the combined +60A and +100A dataset.

2514 Similar to the pion case, the raw cross section is given by the equation 4.4

$$\sigma_{TOT}(E_i) = \frac{1}{n\delta X} \frac{N_{Int}^{TOT}(E_i)}{N_{Inc}^{TOT}(E_i)}, \quad (7.1)$$

2515 where  $N_{Int}^{TOT}$  is the measured number of particles interacting at kinetic energy  $E_i$ ,  
2516  $N_{Inc}^{TOT}$  is the measured number of particles incident on an argon slice at kinetic energy  
2517  $E_i$ ,  $n$  is the density of the target centers and  $\delta X$  is the thickness of the argon slice.  
2518 The density of the target centers and the slab thickness are  $n = 0.021 \cdot 10^{24} \text{ cm}^{-3}$  and  
2519  $\delta X = 0.47 \text{ cm}$ , respectively.

2520 As in the case of pions, kaons might decay or interact between WC4 and the TPC  
2521 front face. Some of the interaction products may be wrongly matched to the WC  
2522 track, forming the “secondary” particle’s background in the kaon sample. We estimate  
2523 the effect of the contamination of secondaries through the DDMC kaon sample. Figure  
2524 7.1 shows the distribution of  $N_{Int}^{TOT}$  as a function of the kinetic energy. The data  
2525 central points are represented by black dots, the statistical uncertainty is shown in  
2526 black, while the systematic uncertainty is shown in red. Data is displayed over the  
2527  $N_{Int}^{TOT}$  distribution obtained with a DDMC sample of kaons shot from WC4. The  
2528 contribution from the simulated kaons which interact hadronically is shown in pink,  
2529 the contributions from kaon decay is shown in orange and the one from secondaries  
2530 in red. The simulated kaon’s and secondaries’ contributions are stacked; the sum of  
2531 their integrals is normalized to the integral of the data.

2532 Figure 7.2 shows the distribution of  $N_{Inc}^{TOT}$ . Data is displayed over the MC. For the  
2533  $N_{Inc}^{TOT}$  distribution we do not make a distinction between kaons that decay or interact  
2534 hadronically because any kaon independently from its final interaction contributes  
2535 to the flux of incident particles at given kinetic energy. The same normalization  
2536 procedure is used for both the interacting and incident histograms.

2537 Figure 7.3 shows the raw cross section, statistical uncertainty in black and system-

atic uncertainty in red. The raw data cross section is overlaid to the reconstructed cross section for the MC mixed sample, displayed in azure. We calculate the statistical uncertainty for the interacting, incident and cross section distributions in a similar fashion to the pion case as described in Section 6.1.1.

As in the pion case, the only systematic effect considered in the measurement of the raw cross section results from the propagation of the uncertainty associate with the measurement of the kinetic energy at each argon slab. For kaons, the uncertainty on the kinetic energy of a candidate at the  $j^{th}$  slab of argon is given by

$$\delta KE_j = \sqrt{\delta p_{Beam}^2 + \delta E_{Loss}^2 + \delta E_{dep\ FF-j}^2} \quad (7.2)$$

$$= \sqrt{(2\% p_{Beam})^2 + (7\text{ [MeV]})^2 + (j - 1)^2(\sim 0.18\text{ [MeV]})^2}. \quad (7.3)$$

We propagate this uncertainty by varying the energy measurement  $KE_j$  at each argon slab. We measure  $N_{Inc}^{TOT}$ ,  $N_{Int}^{TOT}$  and the cross section in three cases: first assigning the measured  $KE_j$  at each kinetic energy sampling, then assigning  $KE_j + \delta KE_j$ , and finally assigning  $KE_j - \delta KE_j$ . The difference between the values obtained using the  $KE_j$  sampling and the maximum and minimum values in each kinetic energy bin determines the systematic uncertainty.

## 7.2 Corrections to the Raw Cross Section

As described in section 4.3.3, we need to apply a background correction and an efficiency correction in order to derive the true Kaon cross section from the raw cross section. The true cross section is given in equation 4.9,

$$\sigma_{TOT}^{K^+}(E_i) = \frac{1}{n\delta X} \frac{\epsilon^{Inc}(E_i)}{\epsilon^{Int}(E_i)} \frac{C_{Int}^{KMC}(E_i)}{C_{Inc}^{KMC}(E_i)} \frac{N_{Int}^{TOT}(E_i)}{N_{Inc}^{TOT}(E_i)}. \quad (4.9)$$

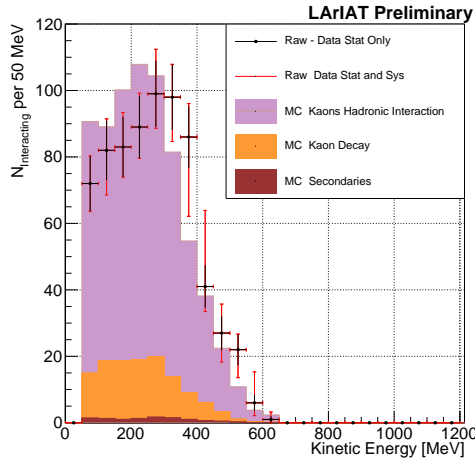


Figure 7.1: Raw number of interacting kaon candidates as a function of the reconstructed kinetic energy. The statistical uncertainties are shown in black, the systematic uncertainties in red.

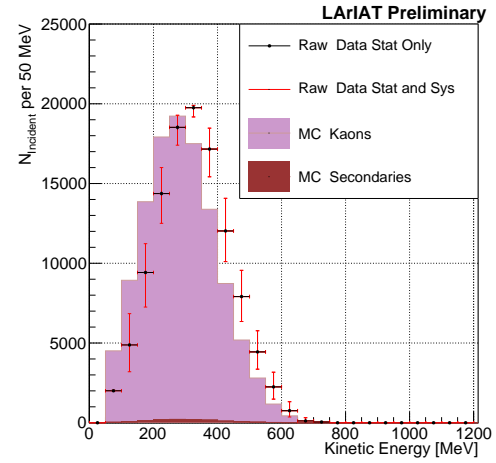


Figure 7.2: Raw number of incident kaon candidates as a function of the reconstructed kinetic energy. The statistical uncertainty is shown in black, the systematic uncertainties in red.

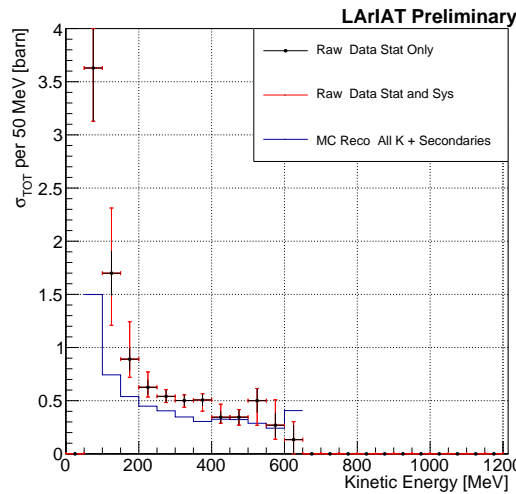


Figure 7.3: Raw ( $K^+$ -Ar) total hadronic cross section. The statistical uncertainty is shown in black, the systematic uncertainties in red. The raw cross section obtained with a MC sample of kaons is shown in blue. For the MC cross section, we include the contributions from secondaries.

2556 Currently, the only background considered for the kaon hadronic cross section  
2557 comes from the presence of secondaries. A further development of the analysis will  
2558 need to account for the presence of a small proton contamination. Figure 7.4 shows  
2559 the relative kaon content for the interacting and incident histograms.

2560 As described in 6.2.2 for the pion case, we derive the correction on a set of pure  
2561 kaon MC, calculating its value bin by bin as the ratio between the true bin content  
2562 and the correspondent reconstructed bin content. The correction is then applied to  
2563 the relevant bin in data. The efficiency correction is evaluated separately for the  
2564 interacting and incident histograms, namely  $\epsilon_i^{\text{int}}$  and  $\epsilon_i^{\text{inc}}$ , and propagated to the cross  
2565 section as shown in equation 4.9.

2566 In section 5.5.1, we estimated the angular resolution for data and MC to be  
2567  $\bar{\alpha}_{\text{Data}} = (4.3 \pm 3.7)$  deg and  $\bar{\alpha}_{\text{MC}} = (4.4 \pm 3.6)$  deg, respectively. Most interaction  
2568 angles smaller than the angular resolution will thus be indistinguishable for the re-  
2569 construction. Thus, we claim we are able to measure the cross section for interaction  
2570 angles greater than 4.5 deg. Geant4 simulates interactions at all angles: in order to  
2571 calculate the efficiency correction, we select events which have an interaction angle  
2572 greater than a  $\alpha_{\text{res}}$  to construct the true interacting and incident histograms (the de-  
2573 nominator of the efficiency correction). The systematics on the efficiency correction  
2574 is estimated by varying the value of  $\alpha_{\text{res}}$  between 0 deg and 4.5 deg and propagating  
2575 the uncertainty on the cross section.

2576 Figure 7.5 shows  $\epsilon^{\text{Int}}(E_i)$  in the left side and  $\epsilon^{\text{Inc}}(E_i)$  on the right as a function of  
2577 the kinetic energy for the kaon sample and their systematic uncertainty.

## 2578 7.3 Results

2579 Figure 7.6 show the measurement of the ( $K^+$ -Ar) total hadronic cross section for  
2580 scattering angles greater than  $5^\circ$ , as the result of the background subtraction and

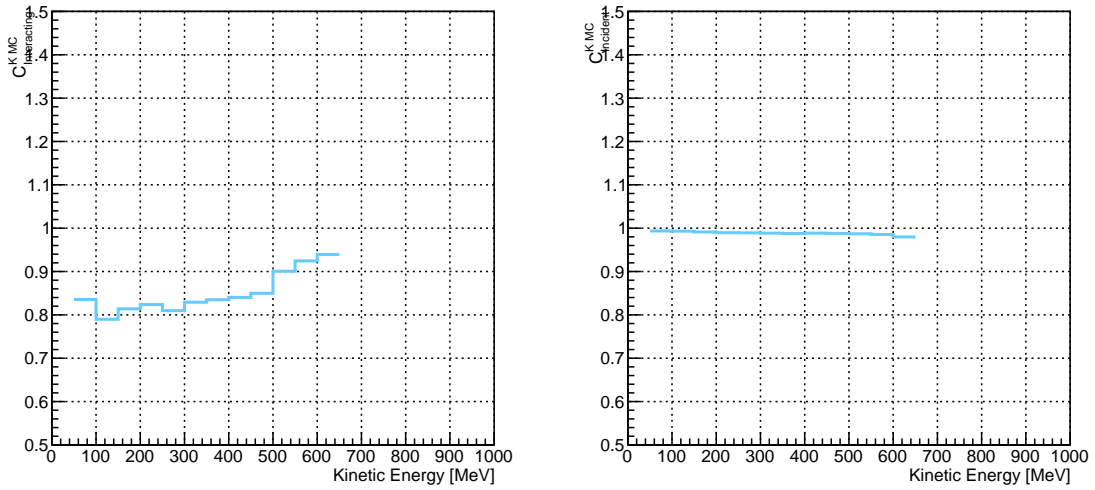


Figure 7.4: *Left:* MC estimated relative kaon content for kaons interacting hadronically as function of kinetic energy. *Right:* MC estimated relative kaon content for incident histogram a function of kinetic energy.

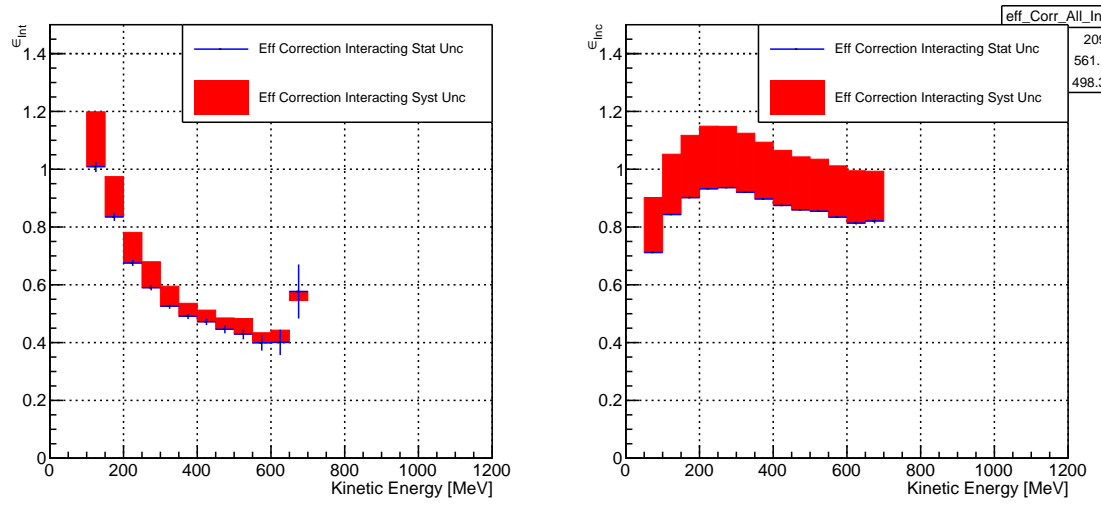


Figure 7.5: *Left:* Efficiency correction on the interacting histogram, statistical uncertainty in blue, systematic uncertainty in red. *Right:* Efficiency correction on the incident histogram, statistical uncertainty in blue, systematic uncertainty in red.

2581 efficiency correction to the raw cross section. The plot shows the measurement ob-  
 2582 tained on the full dataset, statistical uncertainty in black and systematic uncertainty  
 2583 in red. The Geant4 prediction for the total hadronic cross section for angle scattering  
 2584 greater than  $5^\circ$  is displayed in green.

2585 The systematic uncertainty on the cross section is the sum in quadrature of the  
 2586 statistical uncertainty, the systematic uncertainty related to the kinetic energy mea-  
 2587 surement and the systematic uncertainty related to the efficiency correction.

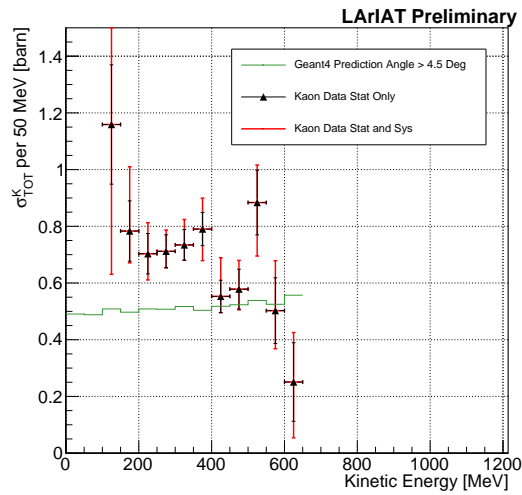


Figure 7.6: ( $K^+$ -Ar) total hadronic cross section for scattering angles greater than  $5^\circ$  measured in the 60A sample, statistical uncertainty in black and systematic uncertainty in red. The Geant4 prediction for the total hadronic cross section for angle scattering greater than  $5^\circ$  is displayed in green.

2588 **Chapter 8**

2589 **Conclusions**

2590 In the era of neutrino precision measurements, of huge liquid argon detectors and  
2591 of massive amount of information from LArTPCs, a renew interest for an ancient  
2592 measurement arises: the measurement of hadronic interactions with matter. With  
2593 this work, we presented the first ever ( $\pi^-$ -Ar) and ( $K^+$ -Ar) total hadronic cross  
2594 section measurements as a function of the hadron kinetic energy. These analyses are  
2595 the first physics analyses developed by the LArIAT experiment. Both the analysis  
2596 follow a similar workflow and they rely on beam line detector information as well as  
2597 both calorimetry and tracking in the TPC.

2598 In order to measure ( $\pi^-$ -Ar) total hadronic argon cross sections, we start by  
2599 selecting pion beamline candidates through a series of selections on the beamline  
2600 and TPC information apt to maximize the number of pions in the selection over the  
2601 number of muons and electrons. We use the LArIAT beamline MC to estimate the  
2602 beam composition of the selected beamline candidate and we propagate the particle  
2603 species to the LArIAT TPC constructing a properly weighted sample with the DDMC.

2604 The analyses start by identifying a sample of the hadron of interest in the beam  
2605 line and assessing the beam line contaminations. It proceeds with tracking the hadron  
2606 candidates in the TPC and measuring their kinetic energy at each point in the track-

2607 ing: the fine sampling of an hadron in the TPC forms the set of “incident” hadrons.  
2608 Then, the hadronic interaction point is identified and the raw cross section is cal-  
2609 culated. Two corrections are then applied to the raw cross section – a background  
2610 subtractions and a correction for detector effects – to obtain the true cross section  
2611 measurement.

2612

2613 These analyses’ work flow will serve as a basis for the future cross section mea-  
2614 surements of pions and kaons in the exclusive channels.

2615 **Appendix A**

2616 **Measurement of LArIAT Electric  
2617 Field**

2618 The electric field of a LArTPC in the drift volume is a fundamental quantity for  
2619 the proper functionality of this technology, as it affects almost every reconstructed  
2620 quantity such as the position of hits or their collected charge. Given its importance,  
2621 we calculate the electric field for LArIAT with a single line diagram from our HV  
2622 circuit and we cross check the obtained value with a measurement relying only on  
2623 TPC data.

2624 Before getting into the details of the measurement procedures, it is important to  
2625 explicit the relationship between some quantities in play. The electric field and the  
2626 drift velocity ( $v_{drift}$ ) are related as follows

$$v_{drift} = \mu(E_{field}, T)E_{field}, \quad (\text{A.1})$$

2627 where  $\mu$  is the electron mobility, which depends on the electric field and on the  
2628 temperature (T). The empirical formula for this dependency is described in [?] and  
2629 shown in Figure A.1 for several argon temperatures.

2630 The relationship between the drift time ( $t_{drift}$ ) and the drift velocity is trivially

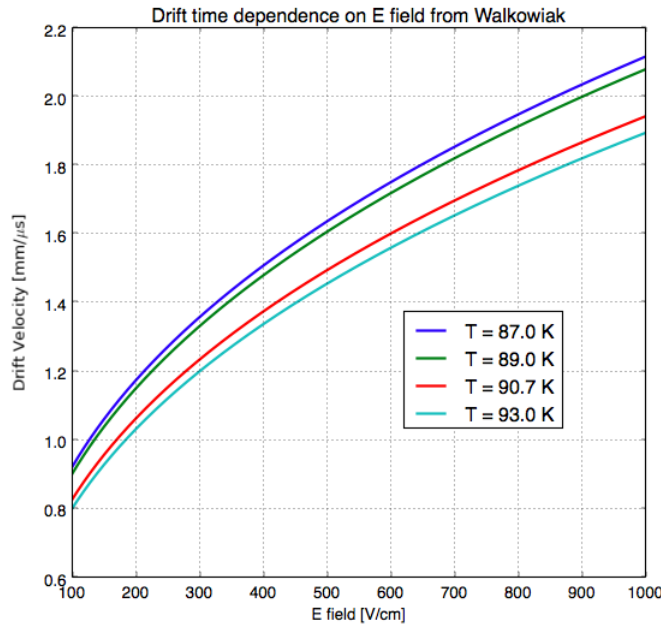


Figure A.1: Drift velocity dependence on electric field for several temperatures. The slope of the line at any one point represents the electron mobility for that given temperature and electric field.

Table A.1: Electric field and drift velocities in LArIAT smaller drift volumes

	Shield-Induction	Induction-Collection
$E_{field}$	700.63 V/cm	892.5 V/cm
$v_{drift}$	1.73 mm/μs	1.90 mm/μs
$t_{drift}$	2.31 μs	2.11 μs

2631 given by

$$t_{drift} = \Delta x / v_{drift}, \quad (\text{A.2})$$

2632 where  $\Delta x$  is the distance between the edges of the drift region. Table A.1 reports the  
2633 values of the electric field, drift velocity, and drift times for the smaller drift volumes.

2634 With these basic parameters established, we can now move on to calculating the  
2635 electric field in the main drift region (between the cathode and the shield plane).

## 2636 Single line diagram method

2637 The electric field strength in the LArIAT main drift volume can be determined know-  
 2638 ing the voltage applied to the cathode, the voltage applied at the shield plane, and the  
 2639 distance between them. We assume the distance between the cathode and the shield  
 2640 plane to be 470 mm and any length contraction due to the liquid argon is negligibly  
 2641 small ( $\sim 2$  mm).

2642 The voltage applied to the cathode can be calculated using Ohm's law and the  
 2643 single line diagram shown in Figure A.2. A set of two of filter pots for emergency  
 2644 power dissipation are positioned between the Glassman power supply and the cathode,  
 2645 one at each end of the feeder cable, each with an internal resistance of  $40 \text{ M}\Omega$ .

2646 Given the TPC resistor chain, the total TPC impedance is  $6 \text{ G}\Omega$ . Since the total  
 2647 resistance on the circuit is driven by the TPC impedance, we expect the resulting  
 2648 current to be

$$I = V_{PS}/R_{tot} = -23.5 \text{ kV}/6 \text{ G}\Omega \sim 4 \mu\text{A}, \quad (\text{A.3})$$

2649 which we measure with the Glassman power supply, shown in Figure A.3.

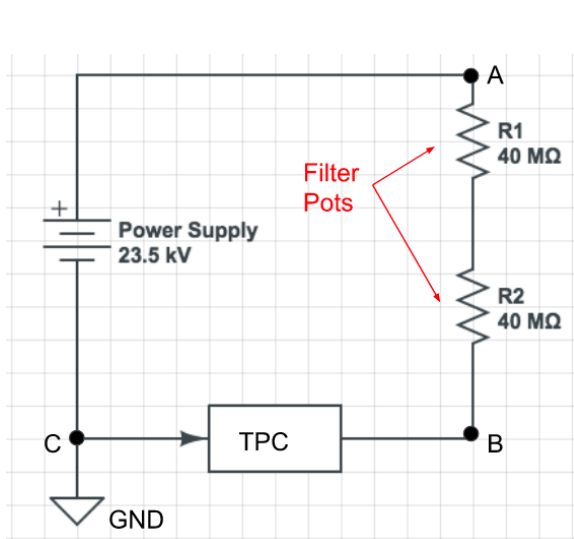


Figure A.2: LArIAT HV simple schematics.

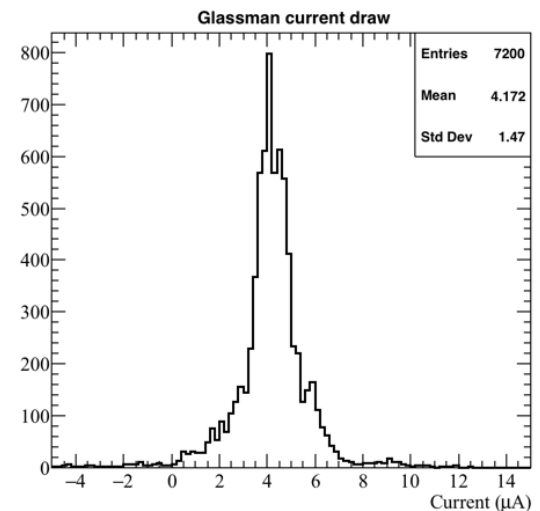


Figure A.3: Current reading from the Glassman between May 25th and May 30th, 2016 (typical Run-II conditions).

2650 Using this current, the voltage at the cathode is calculated as

$$V_{BC} = V_{PS} - (I \times R_{eq}) = -23.5 \text{ kV} + (0.00417 \text{ mA} \times 80 \text{ M}\Omega) = -23.17 \text{ kV}, \quad (\text{A.4})$$

2651 where  $I$  is the current and  $R_{eq}$  is the equivalent resistor representing the two filter  
2652 pots. The electric field is then calculated to be

$$E_{\text{field}} = \frac{V_{BC} - V_{\text{shield}}}{\Delta x} = 486.54 \text{ V/cm}. \quad (\text{A.5})$$

2653 **E field using cathode-anode piercing tracks**

2654 We devise an independent method to measure the drift time (and consequently drift  
2655 velocity and electric field) using TPC cathode to anode piercing tracks. We use this  
2656 method as a cross check to the single line method. The basic idea is simple:

- 2657 0. Select cosmic ray events with only 1 reconstructed track
- 2658 1. Reduce the events to the one containing tracks that cross both anode and cath-
- 2659 ode
- 2660 2. Identify the first and last hit of the track
- 2661 3. Measure the time difference between these two hits ( $\Delta t$ ).

2662 This method works under the assumptions that the time it takes for a cosmic particle  
2663 to cross the chamber ( $\sim \text{ns}$ ) is small compared to the charge drift time ( $\sim \text{hundreds}$   
2664 of  $\mu\text{s}$ ).

2665 We choose cosmic events to allow for a high number of anode to cathode piercing  
2666 tracks (ACP tracks), rejecting beam events where the particles travel almost perpen-  
2667 dicularly to drift direction. We select events with only one reconstructed track to  
2668 maximize the chance of selecting a single crossing muon (no-michel electron). We  
2669 utilize ACP tracks because their hits span the full drift length of the TPC, see figure

2670 A.4, allowing us to define where the first and last hit of the tracks are located in space  
2671 regardless of our assumption of the electric field.

2672 One of the main features of this method is that it doesn't rely on the measurement  
2673 of the trigger time. Since  $\Delta t$  is the time difference between the first and last hit of a  
2674 track and we assume the charge started drifting at the same time for both hits, the  
2675 measurement of the absolute beginning of drift time  $t_0$  is unnecessary. We boost the  
2676 presence of ACP tracks in the cosmic sample by imposing the following requirements  
2677 on tracks:

- 2678     • vertical position (Y) of first and last hits within  $\pm 18$  cm from TPC center  
2679         (avoid Top-Bottom tracks)
- 2680     • horizontal position (Z) of first and last hits within 2 and 86 cm from TPC front  
2681         face (avoid through going tracks)
- 2682     • track length greater than 48 cm (more likely to be crossing)
- 2683     • angle from the drift direction (phi in figure A.5) smaller than 50 deg (more  
2684         reliable tracking)
- 2685     • angle from the beam direction (theta in figure A.5) greater than 50 deg (more  
2686         reliable tracking)

2687 Tracks passing all these selection requirements are used for the  $\Delta t$  calculation.

2688 For each track passing our selection, we loop through the associated hits to retrieve  
2689 the timing information. The analysis is performed separately on hits on the collection  
2690 plane and induction plane, but lead to consistent results. As an example of the time  
2691 difference, figures A.6 and A.7 represent the difference in time between the last and  
2692 first hit of the selected tracks for Run-II Positive Polarity sample on the collection  
2693 and induction plane respectively. We fit with a Gaussian to the peak of the  $\Delta t$   
2694 distributions to extract the mean drift time and the uncertainty associated with it.

2695 The long tail at low  $\Delta t$  represents contamination of non-ACP tracks in the track  
2696 selection. We apply the same procedure to Run-I and Run-II, positive and negative  
2697 polarity alike.

2698 To convert  $\Delta t$  recorded for the hits on the induction plane to the drift time we  
2699 employ the formula

$$t_{drift} = \Delta t - t_{S-I} \quad (\text{A.6})$$

2700 where  $t_{drift}$  is the time the charge takes to drift in the main volume between the  
2701 cathode and the shield plane and  $t_{S-I}$  is the time it takes for the charge to drift from  
2702 the shield plane to the induction plane. In Table A.1 we calculated the drift velocity  
2703 in the S-I region, thus we can calculate  $t_{S-I}$  as

$$t_{S-I} = \frac{l_{S-I}}{v_{S-I}} = \frac{4mm}{1.73mm/\mu s} \quad (\text{A.7})$$

2704 where  $l_{S-I}$  is the distance between the shield and induction plane and  $v_{S-I}$  is the drift  
2705 velocity in the same region. A completely analogous procedure is followed for the hits  
2706 on the collection plane, taking into account the time the charge spent in drifting from  
2707 shield to induction as well as between the induction and collection plane. The value  
2708 for  $\Delta t_{drift}$ , the calculated drift velocity ( $v_{drift}$ ), and corresponding drift electric field  
2709 for the various run periods is given in Table A.2 and are consistent with the electric  
2710 field value calculated with the single line diagram method.

### Delta $t_{drift}$ , drift v and E field with ACP tracks

Data Period	$\Delta t_{Drift}$ [ $\mu s$ ]	Drift velocity [mm/ $\mu s$ ]	E field [V/cm]
RunI Positive Polarity Induction	$311.1 \pm 2.4$	$1.51 \pm 0.01$	$486.6 \pm 21$
RunI Positive Polarity Collection	$310.9 \pm 2.6$	$1.51 \pm 0.01$	$487.2 \pm 21$
RunII Positive Polarity Induction	$315.7 \pm 2.8$	$1.49 \pm 0.01$	$467.9 \pm 21$
RunII Positive Polarity Collection	$315.7 \pm 2.7$	$1.49 \pm 0.01$	$467.9 \pm 21$
RunII Negative Polarity Induction	$315.9 \pm 2.6$	$1.49 \pm 0.01$	$467.1 \pm 21$
RunII Negative Polarity Collection	$315.1 \pm 2.8$	$1.49 \pm 0.01$	$470.3 \pm 21$
Average Values	314.1	$1.50 \pm 0.01$	$474.3 \pm 21$

Table A.2:  $\Delta t$  for the different data samples used for the Anode-Cathode Piercing tracks study.

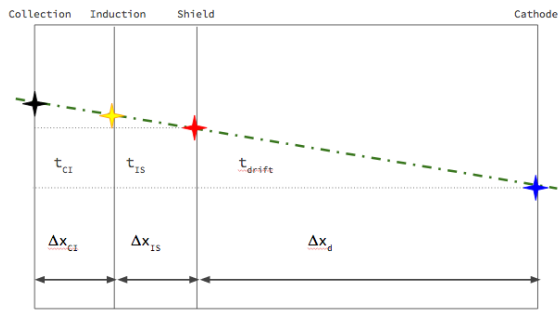


Figure A.4: Pictorial representation of the YX view of the TPC. The distance within the anode planes and between the shield plane and the cathode is purposely out of proportion to illustrate the time difference between hits on collection and induction. An ACP track is shown as an example.

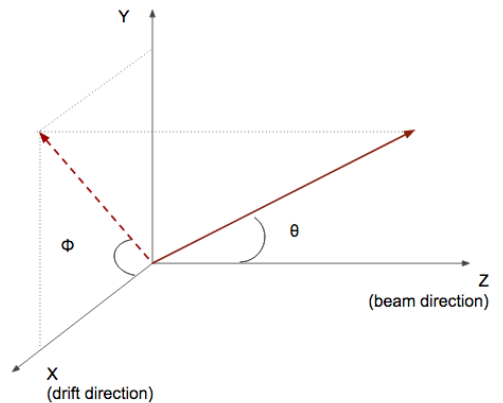


Figure A.5: Angle definition in the context of LArIAT coordinate system.

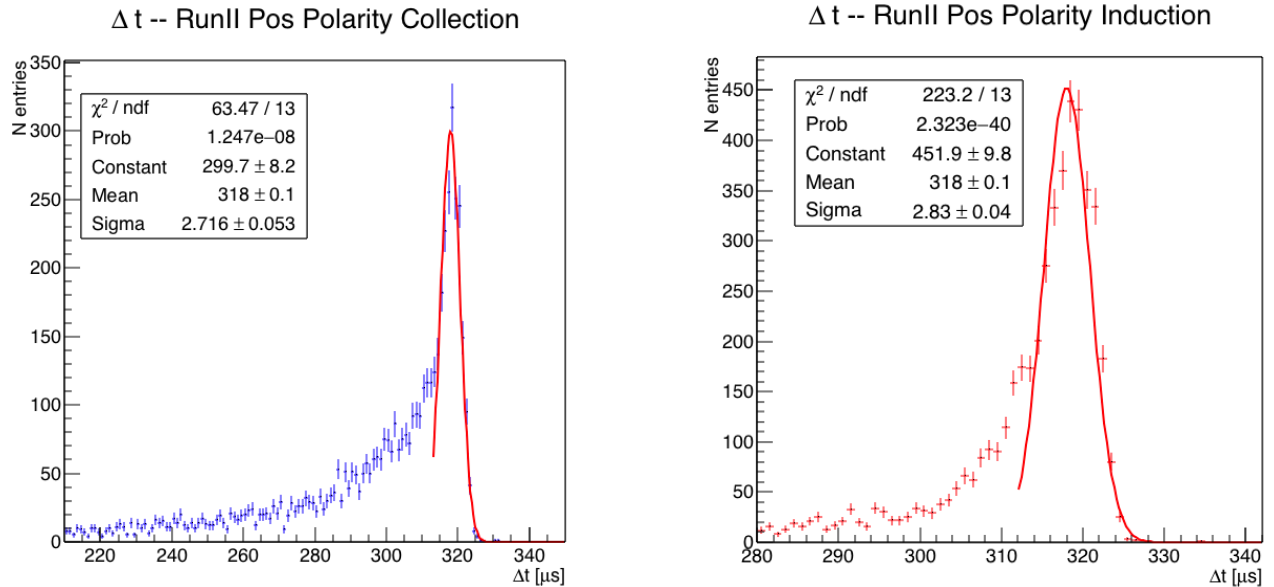


Figure A.6: Collection plane  $\Delta t$  fit for Run II positive polarity ACP data selected tracks.

Figure A.7: Induction plane  $\Delta t$  fit for Run II positive polarity ACP data selected tracks.

<sup>2711</sup> **Appendix B**

<sup>2712</sup> **Additional Tracking Studies for**  
<sup>2713</sup> **LArIAT Cross Section Analyses**

<sup>2714</sup> In this section, we describe two studies. The first is a justification of the selection  
<sup>2715</sup> criteria for the beamline handshake with the TPC information. We perform this  
<sup>2716</sup> study to boost the correct identification of the particles in the TPC associated with  
<sup>2717</sup> the beamline information, while maintaining sufficient statistics for the cross section  
<sup>2718</sup> measurement. The second study is an optimization of the tracking algorithm, with  
<sup>2719</sup> the scope of maximizing the identification of the hadronic interaction point inside the  
<sup>2720</sup> TPC. These two studies are related, since the optimization of the tracking is per-  
<sup>2721</sup> formed on TPC tracks which have been matched to the wire chamber track; in turn,  
<sup>2722</sup> the tracking algorithm for TPC tracks determines the number of reconstructed tracks  
<sup>2723</sup> in each event used to try the matching with the wire chamber track. Starting with  
<sup>2724</sup> a sensible tracking reconstruction, we perform the WC2TPC matching optimization  
<sup>2725</sup> first, then the tracking optimization. The WC2TPC match purity and efficiency are  
<sup>2726</sup> then calculated again with the optimized tracking.

2727    **B.0.1   Study of WC to TPC Match**

2728    Plots I want in this section:

2729        1. WC2TPC MC DeltaX, DeltaY and  $\alpha$

2730        Scope of this study is assessing the goodness of the wire chamber to TPC match  
2731        on Monte Carlo and decide the selection values we will use on data. A word of caution  
2732        is necessary here. With this study, we want to minimize pathologies associated with  
2733        the presence of the primary hadron itself, e.g. the incorrect association between the  
2734        beamline hadron and its decay products inside the TPC. Assessing the contamination  
2735        from pile-up<sup>1</sup>, albeit related, is beyond the scope of this study.

2736        In MC, we are able to define a correct WC2TPC match using the Geant4 truth  
2737        information. We are thus able to count how many times the WC tracks is associated  
2738        with the wrong TPC reconstructed track.

2739        We define a correct match if the all following conditions are met:

- 2740            - the length of the true primary Geant4 track in the TPC is greater than 2 cm,
- 2741            - the length of the reconstructed track length is greater than 2 cm,
- 2742            - the Z position of the first reconstructed point is within 2 cm from the TPC  
2743              front face
- 2744            - the distance between the reconstructed track and the true entering point is the  
2745              minimum compared with all the other reconstructed tracks.

2746        In order to count the wrong matches, we consider all the reconstructed tracks  
2747        whose Z position of the first reconstructed point lies within 2 cm from the TPC front  
2748        face. Events with true length in TPC < 2 cm are included. Since hadrons are shot

---

1. We remind the reader that the DDMC is a single particle Monte Carlo, where the beam pile up is not simulated.

2749 100 cm upstream from the TPC front face, the following two scenarios are possible  
2750 from a truth standpoint:

2751 [Ta ] the primary hadron decays or interact strongly before getting to the TPC,

2752 [Tb ] the primary hadron enters the TPC.

2753 As described in Section 4.2, we define a WC2TPC match according to the relative  
2754 position of the WC and TPC track parametrized with  $\Delta R$  and the angle between  
2755 them, parametrized with  $\alpha$ . Once we choose the selection values  $r_T$  and  $\alpha_T$  to de-  
2756 termine a reconstructed WC2TPC match, the following five scenarios are possible in  
2757 the truth to reconstruction interplay :

2758 1) only the correct track is matched

2759 2) only one wrong track is matched

2760 3) the correct track and one (or more) wrong tracks are matched

2761 4) multiple wrong tracks matched.

2762 5) no reconstructed tracks are matched

2763 Since we keep only events with one and only one match, we discard cases 3), 4)  
2764 and 5) from the events used in the cross section measurement. For each set of  $r_T$  and  
2765  $\alpha_T$  selection value, we define purity and efficiency of the selection as follows:

$$\text{Efficiency} = \frac{\text{Number of events correctly matched}}{\text{Number of events with primary in TPC}}, \quad (\text{B.1})$$

$$\text{Purity} = \frac{\text{Number of events correctly matched}}{\text{Total number of matched events}}. \quad (\text{B.2})$$

2766 Figure B.1 shows the efficiency (left) and purity (right) for WC2TPC match as  
2767 a function of the radius,  $r_T$ , and angle,  $\alpha_T$ , selection value. It is apparent how both

efficiency and purity are fairly flat as a function of the radius selection value at a given angle. This is not surprising. Since we are studying a single particle gun Monte Carlo sample, the wrong matches can occur only for mis-tracking of the primary or for association with decay products; decay products will tend to be produced at large angles compared to the primary, but could be fairly close to the in  $x$  and  $y$  projection of the primary. The radius cut would play a key role in removing pile up events.

For LArIAT cross section measurements, we generally prefer purity over efficiency, since a sample of particles of a pure species will lead to a better measurement. Obviously, purity should be balanced with a sensible efficiency to avoid rejecting the whole sample.

We choose  $(\alpha_T, r_T) = (8 \text{ deg}, 4 \text{ cm})$  and get a MC 85% efficiency and 98% purity for the kaon sample and a MC 95% efficiency and 90% purity for the pion sample.

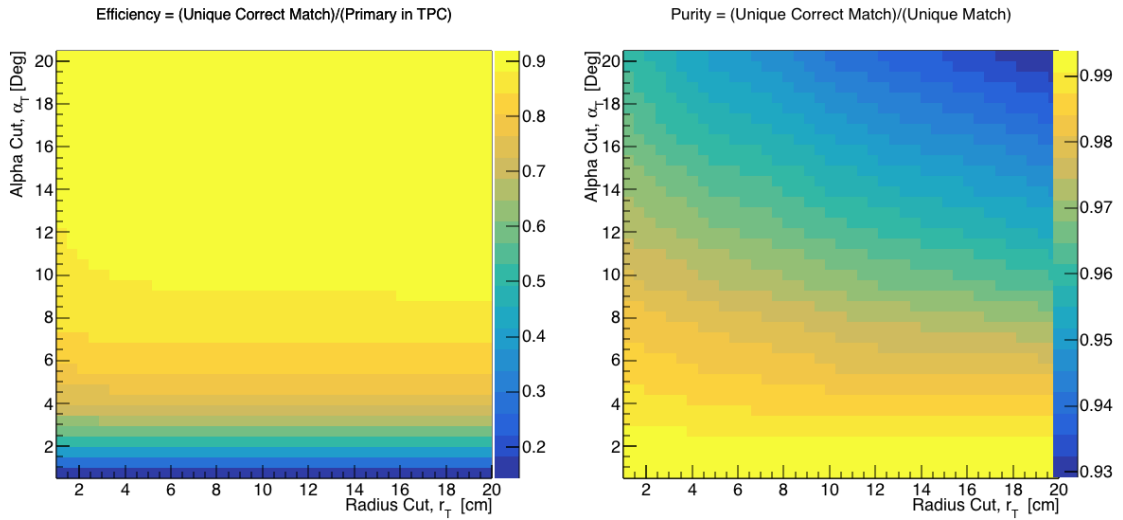


Figure B.1: Efficiency (left) and purity (right) for WC2TPC match as a function of the radius and angle selections for the kaon sample.

## B.0.2 Tracking Optimization

2781 **Appendix C**

2782 **Energy Calibration**

2783 Scope of the energy calibration is to identify the factors which convert the charge  
2784 collected ( $dQ$ ) to energy deposited in the chamber ( $dE$ ). As described in section  
2785 2.1.5, this is a multi-step procedure. In LArIAT, we first correct the raw charge by  
2786 the electronic noise on the considered wire [104], then by the electron lifetime [105],  
2787 and then by the recombination using the ArgoNeut recombination values. Lastly, we  
2788 apply overall calibration of the energy, i.e. we determine the “calorimetry constants”  
2789 using the procedure described in this section.

2790 We independently determine the calorimetry constants for Data and Monte Carlo  
2791 in the LArIAT Run-II Data samples using a parametrization of the stopping power  
2792 (a.k.a. energy deposited per unit length,  $dE/dX$ ) as a function of momentum. This is  
2793 done by comparing the stopping power measured on reconstructed quantities against  
2794 the Bethe-Bloch theoretical prediction for various particle species (see Equation 2.1).  
2795 We obtain the theoretical expectation for the  $dE/dX$  most probable value of pions  
2796 ( $\pi$ ), muons ( $\mu$ ), kaons ( $K$ ), and protons ( $p$ ) in the momentum range most relevant  
2797 for LArIAT (Figure C.1) using the tables provided by the Particle Data Group [102]  
2798 for liquid argon [1].

2799 The basic idea of this calibration technique is to utilize a sample of beamline

2800 events with known particle species and momentum to measure the  $dE/dX$  of the  
2801 corresponding tracks in the TPC. In particular, we decided to use positive pions as  
2802 calibration sample and samples from all the other particle species as cross check. Once  
2803 the  $dE/dX$  of the positive pion sample has been measured at various momenta, we  
2804 tune to calorimetry constants within the reconstruction software to align the measured  
2805 values to match the theoretical ones found in Figure C.1.

2806 In data, we start by selecting a sample of beamline positive pion beamline can-  
2807 didates without any restriction on their measured momentum<sup>1</sup>. We then apply the  
2808 WC2TPC match and subtract the energy loss upstream to the TPC front face, de-  
2809 termining the momentum at the TPC front face. For each surviving pion candidate,  
2810 we measure the  $dE/dx$  at each of the first 12 spacepoints associated the 3D recon-  
2811 structed track, corresponding to a  $\sim 5$  cm portion. These  $dE/dX$  measurements are  
2812 then put into a histogram that corresponds to measured momentum of the track.  
2813 The  $dE/dX$  histograms are sampled every 50 MeV/c in momentum (e.g. 150 MeV/c  
2814  $< P < 200$  MeV/c, 200 MeV/c  $< P < 250$ /c MeV, etc...). This process of selecting,  
2815 sampling, and recording the  $dE/dX$  for various momentum bins is repeated over the  
2816 entire sample of events, allowing us to collect sufficient statistic in most of the mo-  
2817 mentum bins between 150 MeV/c and 1100 MeV/c. On average, pions and muons  
2818 only lose  $\sim 10$  MeV in this 5 cm section of the track and protons lose  $\sim 20$  MeV. Thus  
2819 choosing 50 MeV/c size bins for our histograms covers the energy spread within those  
2820 bins due to energy loss from ionization for all the particle species identifiable in the  
2821 beamline. Each 50 MeV/c momentum binned  $dE/dX$  histogram is now fit with a  
2822 simple Landau function. The most probable value (MPV) and the associated error  
2823 on the MPV from the fit are extracted and plotted against the theoretical prediction  
2824 Figure C.1. Depending on the outcome of the data-prediction comparison, we modify  
2825 the calorimetry constants and we repeat the procedure until a qualitative agreement

---

1. it should be noted that some muon and position contamination is present in the  $\pi^+$  sample

2826 is achieved. We perform this tuning for the collection and induction plane separately.  
 2827 As a cross check to the calorimetry constants determined using the positive pions,  
 2828 we lock the constants and plot the  $dE/dx$  versus momentum distribution of all the  
 2829 other particle species identifiable in the beamline data ( $\pi/\mu/e$ , K , p, in both polarities)  
 2830 against the corresponding Beth-Bloch prediction. The agreement between data  
 2831 from the other particle species and the predictions is the expected result of this cross  
 2832 check. The results of the tuning and cross check for Run-II data on the collection  
 2833 plane is shown in Figure C.2 negative polarity data on top, positive polarity data on  
 2834 the bottom.

2835 In MC, we simulate the corresponding positive pion sample with the DDMC (see  
 2836 section 5.2.2) and follow the same steps as in data. More details on the calorimetry  
 2837 tuning can be found in [80].

2838 **Add agreement between data and MC for dedx for pions**

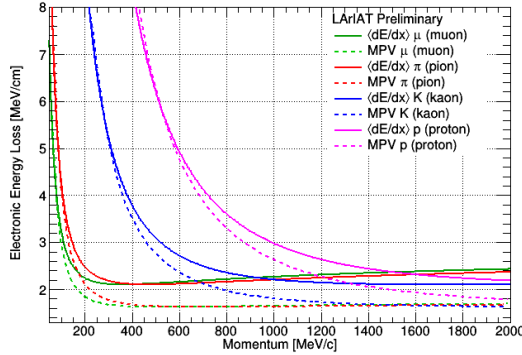


Figure C.1: Stopping power for pions, muons, kaons, and protons in liquid argon over the momentum range most relevant for LArIAT according to the Beth-Bloch equation. The solid lines represent the prediction for the mean energy  $dE/dX$ , while the dashed lines are the predictions for the MPV.

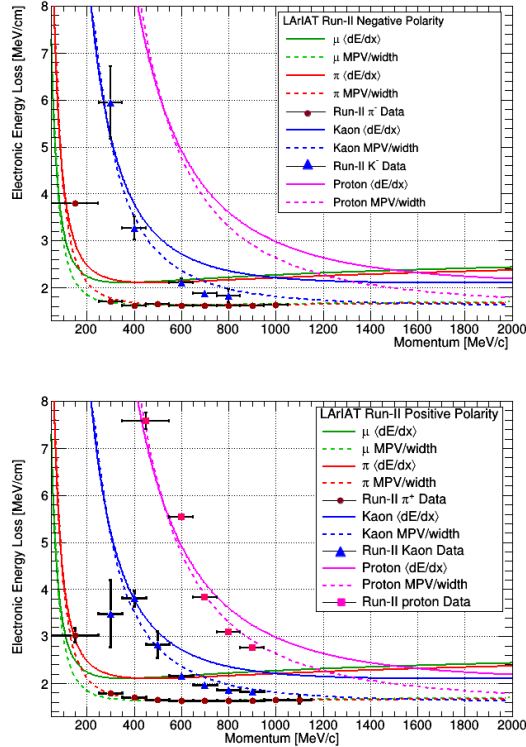


Figure C.2: Stopping power versus Momentum for Run-II negative (top) and positive (bottom) polarity data. We achieve the agreement between the Bethe-Bloch predictions and the distribution obtained with of the positive pions (top plot, red dots) by tuning the calorimetry constants. Once the calorimetry constants are locked in, the agreement between the other particle species and the Bethe-Bloch predictions follows naturally.

2839 **Bibliography**

- 2840 [1] PDG Tables for Liquid Argon. . Technical report.
- 2841 [2] Precision electroweak measurements on the  $Z$  resonance. *Physics Reports*,  
2842 427(5):257 – 454, 2006.
- 2843 [3] K. Abe, J. Amey, C. Andreopoulos, M. Antonova, S. Aoki, A. Ariga, D. Au-  
2844 tiero, S. Ban, M. Barbi, G. J. Barker, G. Barr, C. Barry, P. Bartet-Friburg,  
2845 M. Batkiewicz, V. Berardi, S. Berkman, S. Bhadra, S. Bienstock, A. Blondel,  
2846 S. Bolognesi, S. Bordoni, S. B. Boyd, D. Brailsford, A. Bravar, C. Bronner,  
2847 M. Buizza Avanzini, R. G. Calland, T. Campbell, S. Cao, S. L. Cartwright,  
2848 M. G. Catanesi, A. Cervera, C. Checchia, D. Cherdack, N. Chikuma,  
2849 G. Christodoulou, A. Clifton, J. Coleman, G. Collazuol, D. Coplowe, A. Cudd,  
2850 A. Dabrowska, G. De Rosa, T. Dealtry, P. F. Denner, S. R. Dennis, C. Densham,  
2851 D. Dewhurst, F. Di Lodovico, S. Di Luise, S. Dolan, O. Drapier, K. E. Duffy,  
2852 J. Dumarchez, M. Dziewiecki, S. Emery-Schrenk, A. Ereditato, T. Feusels,  
2853 A. J. Finch, G. A. Fiorentini, M. Friend, Y. Fujii, D. Fukuda, Y. Fukuda,  
2854 V. Galymov, A. Garcia, C. Giganti, F. Gizzarelli, T. Golan, M. Gonin, D. R.  
2855 Hadley, L. Haegel, M. D. Haigh, D. Hansen, J. Harada, M. Hartz, T. Hasegawa,  
2856 N. C. Hastings, T. Hayashino, Y. Hayato, R. L. Helmer, A. Hillairet, T. Hiraki,  
2857 A. Hiramoto, S. Hirota, M. Hogan, J. Holeczek, F. Hosomi, K. Huang, A. K.  
2858 Ichikawa, M. Ikeda, J. Imber, J. Insler, R. A. Intonti, T. Ishida, T. Ishii, E. Iwai,  
2859 K. Iwamoto, A. Izmaylov, B. Jamieson, M. Jiang, S. Johnson, P. Jonsson,

2860 C. K. Jung, M. Kabirnezhad, A. C. Kaboth, T. Kajita, H. Kakuno, J. Kameda,  
2861 D. Karlen, T. Katori, E. Kearns, M. Khabibullin, A. Khotjantsev, H. Kim,  
2862 J. Kim, S. King, J. Kisiel, A. Knight, A. Knox, T. Kobayashi, L. Koch, T. Koga,  
2863 A. Konaka, K. Kondo, L. L. Kormos, A. Korzenev, Y. Koshio, K. Kowalik,  
2864 W. Kropp, Y. Kudenko, R. Kurjata, T. Kutter, J. Lagoda, I. Lamont, M. Lam-  
2865 oureux, E. Larkin, P. Lasorak, M. Laveder, M. Lawe, M. Licciardi, T. Lindner,  
2866 Z. J. Liptak, R. P. Litchfield, X. Li, A. Longhin, J. P. Lopez, T. Lou, L. Ludovici,  
2867 X. Lu, L. Magaletti, K. Mahn, M. Malek, S. Manly, A. D. Marino, J. F. Martin,  
2868 P. Martins, S. Martynenko, T. Maruyama, V. Matveev, K. Mavrokordis, W. Y.  
2869 Ma, E. Mazzucato, M. McCarthy, N. McCauley, K. S. McFarland, C. McGrew,  
2870 A. Mefodiev, C. Metelko, M. Mezzetto, P. Mijakowski, A. Minamino, O. Mi-  
2871 neev, S. Mine, A. Missent, M. Miura, S. Moriyama, Th. A. Mueller, J. Myslik,  
2872 T. Nakadaira, M. Nakahata, K. G. Nakamura, K. Nakamura, K. D. Nakamura,  
2873 Y. Nakanishi, S. Nakayama, T. Nakaya, K. Nakayoshi, C. Nantais, C. Nielsen,  
2874 M. Nirko, K. Nishikawa, Y. Nishimura, P. Novella, J. Nowak, H. M. O'Keeffe,  
2875 K. Okumura, T. Okusawa, W. Oryszczak, S. M. Oser, T. Ovsyannikova, R. A.  
2876 Owen, Y. Oyama, V. Palladino, J. L. Palomino, V. Paolone, N. D. Patel,  
2877 P. Paudyal, M. Pavin, D. Payne, J. D. Perkin, Y. Petrov, L. Pickard, L. Pick-  
2878 ering, E. S. Pinzon Guerra, C. Pistillo, B. Popov, M. Posiadala-Zezula, J.-M.  
2879 Poutissou, R. Poutissou, P. Przewlocki, B. Quilain, T. Radermacher, E. Radi-  
2880 cioni, P. N. Ratoff, M. Ravonel, M. A. Rayner, A. Redij, E. Reinherz-Aronis,  
2881 C. Riccio, P. A. Rodrigues, E. Rondio, B. Rossi, S. Roth, A. Rubbia, A. Rychter,  
2882 K. Sakashita, F. Sánchez, E. Scantamburlo, K. Scholberg, J. Schwehr, M. Scott,  
2883 Y. Seiya, T. Sekiguchi, H. Sekiya, D. Sgalaberna, R. Shah, A. Shaikhiev,  
2884 F. Shaker, D. Shaw, M. Shiozawa, T. Shirahige, S. Short, M. Smy, J. T.  
2885 Sobczyk, H. Sobel, M. Sorel, L. Southwell, J. Steinmann, T. Stewart, P. Stowell,  
2886 Y. Suda, S. Suvorov, A. Suzuki, S. Y. Suzuki, Y. Suzuki, R. Tacik, M. Tada,

2887 A. Takeda, Y. Takeuchi, H. K. Tanaka, H. A. Tanaka, D. Terhorst, R. Terri,  
2888 T. Thakore, L. F. Thompson, S. Tobayama, W. Toki, T. Tomura, C. Touramani,  
2889 T. Tsukamoto, M. Tzanov, Y. Uchida, M. Vagins, Z. Vallari, G. Vasseur,  
2890 T. Vladislavljevic, T. Wachala, C. W. Walter, D. Wark, M. O. Wascko, A. We-  
2891 ber, R. Wendell, R. J. Wilkes, M. J. Wilking, C. Wilkinson, J. R. Wilson, R. J.  
2892 Wilson, C. Wret, Y. Yamada, K. Yamamoto, M. Yamamoto, C. Yanagisawa,  
2893 T. Yano, S. Yen, N. Yershov, M. Yokoyama, K. Yoshida, T. Yuan, M. Yu, A. Za-  
2894 lewska, J. Zalipska, L. Zambelli, K. Zaremba, M. Ziembicki, E. D. Zimmerman,  
2895 M. Zito, and J. Źmuda. Combined analysis of neutrino and antineutrino oscil-  
2896 lations at t2k. *Phys. Rev. Lett.*, 118:151801, Apr 2017.

2897 [4] K. Abe, Y. Haga, Y. Hayato, M. Ikeda, K. Iyogi, J. Kameda, Y. Kishimoto,  
2898 M. Miura, S. Moriyama, M. Nakahata, T. Nakajima, Y. Nakano, S. Nakayama,  
2899 A. Orii, H. Sekiya, M. Shiozawa, A. Takeda, H. Tanaka, T. Tomura, R. A. Wen-  
2900 drell, R. Akutsu, T. Irvine, T. Kajita, K. Kaneyuki, Y. Nishimura, E. Richard,  
2901 K. Okumura, L. Labarga, P. Fernandez, J. Gustafson, C. Kachulis, E. Kearns,  
2902 J. L. Raaf, J. L. Stone, L. R. Sulak, S. Berkman, C. M. Nantais, H. A.  
2903 Tanaka, S. Tobayama, M. Goldhaber, W. R. Kropp, S. Mine, P. Weatherly,  
2904 M. B. Smy, H. W. Sobel, V. Takhistov, K. S. Ganezer, B. L. Hartfiel, J. Hill,  
2905 N. Hong, J. Y. Kim, I. T. Lim, R. G. Park, A. Himmel, Z. Li, E. O’Sullivan,  
2906 K. Scholberg, C. W. Walter, T. Wongjirad, T. Ishizuka, S. Tasaka, J. S. Jang,  
2907 J. G. Learned, S. Matsuno, S. N. Smith, M. Friend, T. Hasegawa, T. Ishida,  
2908 T. Ishii, T. Kobayashi, T. Nakadaira, K. Nakamura, Y. Oyama, K. Sakashita,  
2909 T. Sekiguchi, T. Tsukamoto, A. T. Suzuki, Y. Takeuchi, T. Yano, S. V. Cao,  
2910 T. Hiraki, S. Hirota, K. Huang, T. Kikawa, A. Minamino, T. Nakaya, K. Suzuki,  
2911 Y. Fukuda, K. Choi, Y. Itow, T. Suzuki, P. Mijakowski, K. Frankiewicz, J. Hig-  
2912 night, J. Imber, C. K. Jung, X. Li, J. L. Palomino, M. J. Wilking, C. Yanag-  
2913 isawa, D. Fukuda, H. Ishino, T. Kayano, A. Kibayashi, Y. Koshio, T. Mori,

- 2914 M. Sakuda, C. Xu, Y. Kuno, R. Tacik, S. B. Kim, H. Okazawa, Y. Choi,  
2915 K. Nishijima, M. Koshiba, Y. Totsuka, Y. Suda, M. Yokoyama, C. Bronner,  
2916 M. Hartz, K. Martens, Ll. Marti, Y. Suzuki, M. R. Vagins, J. F. Martin, A. Kon-  
2917 aka, S. Chen, Y. Zhang, and R. J. Wilkes. Search for proton decay via  $p \rightarrow e^+ \pi^0$   
2918 and  $p \rightarrow \mu^+ \pi^0$  in 0.31 megaton · years exposure of the super-kamiokande water  
2919 cherenkov detector. *Phys. Rev. D*, 95:012004, Jan 2017.
- 2920 [5] R Acciarri, C Adams, J Asaadi, B Baller, T Bolton, C Bromberg, F Ca-  
2921 vanna, E Church, D Edmunds, A Ereditato, S Farooq, B Fleming, H Greenlee,  
2922 G Horton-Smith, C James, E Klein, K Lang, P Laurens, D McKee, R Mehdiyev,  
2923 B Page, O Palamara, K Partyka, G Rameika, B Rebel, M Soderberg, J Spitz,  
2924 A M Szelc, M Weber, M Wojcik, T Yang, and G P Zeller. A study of electron  
2925 recombination using highly ionizing particles in the argoneut liquid argon tpc.  
2926 *Journal of Instrumentation*, 8(08):P08005, 2013.
- 2927 [6] R Acciarri, M Antonello, B Baibussinov, M Baldo-Ceolin, P Benetti,  
2928 F Calaprice, E Calligarich, M Cambiaghi, N Canci, F Carbonara, F Cavanna,  
2929 S Centro, A G Cocco, F Di Pompeo, G Fiorillo, C Galbiati, V Gallo, L Grandi,  
2930 G Meng, I Modena, C Montanari, O Palamara, L Pandola, G B Piano Mortari,  
2931 F Pietropaolo, G L Raselli, M Roncadelli, M Rossella, C Rubbia, E Segreto,  
2932 A M Szelc, S Ventura, and C Vignoli. Effects of nitrogen contamination in  
2933 liquid argon. *Journal of Instrumentation*, 5(06):P06003, 2010.
- 2934 [7] R. Acciarri et al. Demonstration and Comparison of Operation of Photomulti-  
2935 plier Tubes at Liquid Argon Temperature. *JINST*, 7:P01016, 2012.
- 2936 [8] R. Acciarri et al. Design and Construction of the MicroBooNE Detector. *JINST*,  
2937 12(02):P02017, 2017.

- 2938 [9] R. Acciarri et al. First Observation of Low Energy Electron Neutrinos in a  
2939 Liquid Argon Time Projection Chamber. *Phys. Rev.*, D95(7):072005, 2017.  
2940 [*Phys. Rev.*D95,072005(2017)].
- 2941 [10] M Adamowski, B Carls, E Dvorak, A Hahn, W Jaskierny, C Johnson, H Jostlein,  
2942 C Kendziora, S Lockwitz, B Pahlka, R Plunkett, S Pordes, B Rebel, R Schmitt,  
2943 M Stancari, T Tope, E Voirin, and T Yang. The liquid argon purity demon-  
2944 strator. *Journal of Instrumentation*, 9(07):P07005, 2014.
- 2945 [11] C. Adams et al. The Long-Baseline Neutrino Experiment: Exploring Funda-  
2946 mental Symmetries of the Universe. 2013.
- 2947 [12] P. Adamson, L. Aliaga, D. Ambrose, N. Anfimov, A. Antoshkin, E. Arrieta-  
2948 Diaz, K. Augsten, A. Aurisano, C. Backhouse, M. Baird, B. A. Bambah,  
2949 K. Bays, B. Behera, S. Bending, R. Bernstein, V. Bhatnagar, B. Bhuyan,  
2950 J. Bian, T. Blackburn, A. Bolshakova, C. Bromberg, J. Brown, G. Brunetti,  
2951 N. Buchanan, A. Butkevich, V. Bychkov, M. Campbell, E. Catano-Mur, S. Chil-  
2952 dress, B. C. Choudhary, B. Chowdhury, T. E. Coan, J. A. B. Coelho, M. Colo,  
2953 J. Cooper, L. Corwin, L. Cremonesi, D. Cronin-Hennessy, G. S. Davies, J. P.  
2954 Davies, P. F. Derwent, R. Dharmapalan, P. Ding, Z. Djurcic, E. C. Dukes,  
2955 H. Duyang, S. Edayath, R. Ehrlich, G. J. Feldman, M. J. Frank, M. Gabrielyan,  
2956 H. R. Gallagher, S. Germani, T. Ghosh, A. Giri, R. A. Gomes, M. C. Goodman,  
2957 V. Grichine, R. Group, D. Grover, B. Guo, A. Habig, J. Hartnell, R. Hatcher,  
2958 A. Hatzikoutelis, K. Heller, A. Himmel, A. Holin, J. Hylen, F. Jediny, M. Judah,  
2959 G. K. Kafka, D. Kalra, S. M. S. Kasahara, S. Kasetti, R. Keloth, L. Kolupaeva,  
2960 S. Kotelnikov, I. Kourbanis, A. Kreymer, A. Kumar, S. Kurbanov, K. Lang,  
2961 W. M. Lee, S. Lin, J. Liu, M. Lokajicek, J. Lozier, S. Luchuk, K. Maan, S. Mag-  
2962 ill, W. A. Mann, M. L. Marshak, K. Matera, V. Matveev, D. P. Méndez, M. D.  
2963 Messier, H. Meyer, T. Miao, W. H. Miller, S. R. Mishra, R. Mohanta, A. Moren,

- 2964 L. Mualem, M. Muether, S. Mufson, R. Murphy, J. Musser, J. K. Nelson,  
2965 R. Nichol, E. Niner, A. Norman, T. Nosek, Y. Oksuzian, A. Olshevskiy, T. Ol-  
2966 son, J. Paley, P. Pandey, R. B. Patterson, G. Pawloski, D. Pershey, O. Petrova,  
2967 R. Petti, S. Phan-Budd, R. K. Plunkett, R. Poling, B. Potukuchi, C. Principato,  
2968 F. Psihas, A. Radovic, R. A. Rameika, B. Rebel, B. Reed, D. Rocco, P. Rojas,  
2969 V. Ryabov, K. Sachdev, P. Sail, O. Samoylov, M. C. Sanchez, R. Schroeter,  
2970 J. Sepulveda-Quiroz, P. Shanahan, A. Sheshukov, J. Singh, J. Singh, P. Singh,  
2971 V. Singh, J. Smolik, N. Solomey, E. Song, A. Sousa, K. Soustruznik, M. Strait,  
2972 L. Suter, R. L. Talaga, M. C. Tamsett, P. Tas, R. B. Thayyullathil, J. Thomas,  
2973 X. Tian, S. C. Tognini, J. Tripathi, A. Tsaris, J. Urheim, P. Vahle, J. Vasel,  
2974 L. Vinton, A. Vold, T. Vrba, B. Wang, M. Wetstein, D. Whittington, S. G. Wo-  
2975 jcicki, J. Wolcott, N. Yadav, S. Yang, J. Zalesak, B. Zamorano, and R. Zwaska.  
2976 Constraints on oscillation parameters from  $\nu_e$  appearance and  $\nu_\mu$  disappearance  
2977 in nova. *Phys. Rev. Lett.*, 118:231801, Jun 2017.
- 2978 [13] Alan Agresti. *Categorical Data Analysis*. Wiley Series in Probability and Statis-  
2979 tics. Wiley, 2013.
- 2980 [14] A. Aguilar-Arevalo et al. Evidence for neutrino oscillations from the observation  
2981 of anti-neutrino(electron) appearance in a anti-neutrino(muon) beam. *Phys.*  
2982 *Rev.*, D64:112007, 2001.
- 2983 [15] A. A. Aguilar-Arevalo et al. Improved Search for  $\bar{\nu}_\mu \rightarrow \bar{\nu}_e$  Oscillations in the  
2984 MiniBooNE Experiment. *Phys. Rev. Lett.*, 110:161801, 2013.
- 2985 [16] S. Amoruso et al. Study of electron recombination in liquid argon with the  
2986 ICARUS TPC. *Nucl. Instrum. Meth.*, A523:275–286, 2004.
- 2987 [17] C. Anderson et al. The ArgoNeuT Detector in the NuMI Low-Energy beam  
2988 line at Fermilab. *JINST*, 7:P10019, 2012.

- 2989 [18] C. Andreopoulos et al. The GENIE Neutrino Monte Carlo Generator. *Nucl.*  
2990 *Instrum. Meth.*, A614:87–104, 2010.
- 2991 [19] Timofei Bolshakov Andrey Petrov. Java synoptic toolkit. Technical report,  
2992 Sept 2010.
- 2993 [20] M. Antonello, B. Baibussinov, P. Benetti, E. Calligarich, N. Canci, S. Cen-  
2994 tro, A. Cesana, K. Cieslik, D. B. Cline, A. G. Cocco, A. Dabrowska, D. De-  
2995 qual, A. Dermenev, R. Dolfini, C. Farnese, A. Fava, A. Ferrari, G. Fiorillo,  
2996 D. Gibin, S. Gninenko, A. Guglielmi, M. Haranczyk, J. Holeczek, A. Ivashkin,  
2997 J. Kisiel, I. Kochanek, J. Lagoda, S. Mania, A. Menegolli, G. Meng, C. Monta-  
2998 nari, S. Otwinowski, A. Piazzoli, P. Picchi, F. Pietropaolo, P. Plonski, A. Rap-  
2999 poldi, G. L. Raselli, M. Rossella, C. Rubbia, P. Sala, A. Scaramelli, E. Seg-  
3000 reto, F. Sergiampietri, D. Stefan, J. Stepaniak, R. Sulej, M. Szarska, M. Ter-  
3001 rani, F. Varanini, S. Ventura, C. Vignoli, H. Wang, X. Yang, A. Zalewska,  
3002 and K. Zaremba. Precise 3d track reconstruction algorithm for the ICARUS  
3003 t600 liquid argon time projection chamber detector. *Advances in High Energy*  
3004 *Physics*, 2013:1–16, 2013.
- 3005 [21] M. Antonello et al. A Proposal for a Three Detector Short-Baseline Neutrino  
3006 Oscillation Program in the Fermilab Booster Neutrino Beam. 2015.
- 3007 [22] D. Ashery, I. Navon, G. Azuelos, H. K. Walter, H. J. Pfeiffer, and F. W.  
3008 Schlepütz. True absorption and scattering of pions on nuclei. *Phys. Rev. C*,  
3009 23:2173–2185, May 1981.
- 3010 [23] C. Athanassopoulos et al. Evidence for  $\nu(\mu) \rightarrow \nu(e)$  neutrino oscillations  
3011 from LSND. *Phys. Rev. Lett.*, 81:1774–1777, 1998.

- 3012 [24] Borut Bajc, Junji Hisano, Takumi Kuwahara, and Yuji Omura. Threshold  
3013 corrections to dimension-six proton decay operators in non-minimal {SUSY}  
3014  $\text{su}(5)$  {GUTs}. *Nuclear Physics B*, 910:1 – 22, 2016.
- 3015 [25] B. Baller. Trajcluster user guide. Technical report, apr 2016.
- 3016 [26] Gary Barker. Neutrino event reconstruction in a liquid argon TPC. *Journal of*  
3017 *Physics: Conference Series*, 308:012015, jul 2011.
- 3018 [27] BASF Corp. 100 Park Avenue, Florham Park, NJ 07932 USA.
- 3019 [28] R. Becker-Szendy, C. B. Bratton, D. R. Cady, D. Casper, R. Claus, M. Crouch,  
3020 S. T. Dye, W. Gajewski, M. Goldhaber, T. J. Haines, P. G. Halverson, T. W.  
3021 Jones, D. Kielczewska, W. R. Kropp, J. G. Learned, J. M. LoSecco, C. Mc-  
3022 Grew, S. Matsuno, J. Matthews, M. S. Mudah, L. Price, F. Reines, J. Schultz,  
3023 D. Sinclair, H. W. Sobel, J. L. Stone, L. R. Sulak, R. Svoboda, G. Thornton,  
3024 and J. C. van der Velde. Search for proton decay into  $e^+ + \pi^0$  in the imb-3  
3025 detector. *Phys. Rev. D*, 42:2974–2976, Nov 1990.
- 3026 [29] J B Birks. Scintillations from organic crystals: Specific fluorescence and relative  
3027 response to different radiations. *Proceedings of the Physical Society. Section A*,  
3028 64(10):874, 1951.
- 3029 [30] A. Bodek and J. L. Ritchie. Further studies of fermi-motion effects in lepton  
3030 scattering from nuclear targets. *Phys. Rev. D*, 24:1400–1402, Sep 1981.
- 3031 [31] Mark G. Boulay and A. Hime. Direct WIMP detection using scintillation time  
3032 discrimination in liquid argon. 2004.
- 3033 [32] D. V. Bugg, R. S. Gilmore, K. M. Knight, D. C. Salter, G. H. Stafford, E. J. N.  
3034 Wilson, J. D. Davies, J. D. Dowell, P. M. Hattersley, R. J. Homer, A. W. O'dell,

- 3035 A. A. Carter, R. J. Tapper, and K. F. Riley. Kaon-nucleon total cross sections  
3036 from 0.6 to 2.65 gev/ *c. Phys. Rev.*, 168:1466–1475, Apr 1968.
- 3037 [33] W. M. Burton and B. A. Powell. Fluorescence of tetraphenyl-butadiene in the  
3038 vacuum ultraviolet. *Applied Optics*, 12(1):87, jan 1973.
- 3039 [34] CAEN. Caen v1495 data sheet. Technical report, jan 2018.
- 3040 [35] CAEN. Caen v1740 data sheet. Technical report, jan 2018.
- 3041 [36] A. S. Carroll, I. H. Chiang, C. B. Dover, T. F. Kycia, K. K. Li, P. O. Mazur,  
3042 D. N. Michael, P. M. Mockett, D. C. Rahm, and R. Rubinstein. Pion-nucleus  
3043 total cross sections in the (3,3) resonance region. *Phys. Rev. C*, 14:635–638,  
3044 Aug 1976.
- 3045 [37] D. Casper. The nuance neutrino physics simulation, and the future. *Nuclear  
3046 Physics B - Proceedings Supplements*, 112(1-3):161–170, nov 2002.
- 3047 [38] F. Cavanna et al. LArIAT: Liquid Argon In A Testbeam. 2014.
- 3048 [39] A. Cervera, A. Donini, M.B. Gavela, J.J. Gomez Cádenas, P. Hernández,  
3049 O. Mena, and S. Rigolin. Golden measurements at a neutrino factory. *Nu-  
3050 clear Physics B*, 579(1-2):17–55, jul 2000.
- 3051 [40] E. Church. LArSoft: A Software Package for Liquid Argon Time Projection  
3052 Drift Chambers. 2013.
- 3053 [41] ATLAS Collaboration. Observation of a new particle in the search for the  
3054 standard model higgs boson with the ATLAS detector at the LHC. *Physics  
3055 Letters B*, 716(1):1–29, sep 2012.
- 3056 [42] CMS Collaboration. Observation of a new boson at a mass of 125 gev with the  
3057 cms experiment at the lhc. *Physics Letters B*, 716(1):30 – 61, 2012.

- 3058 [43] The LArIAT Collaboration. The liquid argon in a testbeam (lariat) experiment.  
3059 Technical report, In Preparation 2018.
- 3060 [44] Stefano Dell’Oro, Simone Marcocci, Matteo Viel, and Francesco Vissani. Neu-  
3061 trinoless double beta decay: 2015 review. *Advances in High Energy Physics*,  
3062 2016:1–37, 2016.
- 3063 [45] S.E. Derenzo, A.R. Kirschbaum, P.H. Eberhard, R.R. Ross, and F.T. Solmitz.  
3064 Test of a liquid argon chamber with 20 m rms resolution. *Nuclear Instruments  
3065 and Methods*, 122:319 – 327, 1974.
- 3066 [46] Savas Dimopoulos, Stuart Raby, and Frank Wilczek. Proton Decay in Super-  
3067 symmetric Models. *Phys. Lett.*, B112:133, 1982.
- 3068 [47] D. Drakoulakos et al. Proposal to perform a high-statistics neutrino scattering  
3069 experiment using a fine-grained detector in the NuMI beam. 2004.
- 3070 [48] A Ereditato, C C Hsu, S Janos, I Kreslo, M Messina, C Rudolf von Rohr,  
3071 B Rossi, T Strauss, M S Weber, and M Zeller. Design and operation of  
3072 argontube: a 5 m long drift liquid argon tpc. *Journal of Instrumentation*,  
3073 8(07):P07002, 2013.
- 3074 [49] Torleif Ericson and Wolfram Weise. *Pions and Nuclei (The International Series  
3075 of Monographs on Physics)*. Oxford University Press, 1988.
- 3076 [50] A.A. Aguilar-Arevalo et al. The miniboone detector. *Nuclear Instruments and  
3077 Methods in Physics Research Section A: Accelerators, Spectrometers, Detectors  
3078 and Associated Equipment*, 599(1):28 – 46, 2009.
- 3079 [51] Antonio Bueno et al. Nucleon decay searches with large liquid argon TPC de-  
3080 tectors at shallow depths: atmospheric neutrinos and cosmogenic backgrounds.  
3081 *Journal of High Energy Physics*, 2007(04):041–041, apr 2007.

- 3082 [52] A.S. Clough et al. Pion-nucleus total cross sections from 88 to 860 MeV. *Nuclear*  
3083 *Physics B*, 76(1):15–28, jul 1974.
- 3084 [53] B.W. Allardycce et al. Pion reaction cross sections and nuclear sizes. *Nuclear*  
3085 *Physics A*, 209(1):1 – 51, 1973.
- 3086 [54] C Athanassopoulos et al. The liquid scintillator neutrino detector and LAMPF  
3087 neutrino source. *Nuclear Instruments and Methods in Physics Research Section*  
3088 *A: Accelerators, Spectrometers, Detectors and Associated Equipment*, 388(1-  
3089 2):149–172, mar 1997.
- 3090 [55] F. Binon et al. Scattering of negative pions on carbon. *Nuclear Physics B*,  
3091 17(1):168 – 188, 1970.
- 3092 [56] L. Aliaga et al. Minerva neutrino detector response measured with test beam  
3093 data. *Nuclear Instruments and Methods in Physics Research Section A: Ac-*  
3094 *celerators, Spectrometers, Detectors and Associated Equipment*, 789:28 – 42,  
3095 2015.
- 3096 [57] M Adamowski et al. The liquid argon purity demonstrator. *Journal of Instru-*  
3097 *mentation*, 9(07):P07005, 2014.
- 3098 [58] P. Vilain et al. Coherent single charged pion production by neutrinos. *Physics*  
3099 *Letters B*, 313(1-2):267–275, aug 1993.
- 3100 [59] R. Acciarri et al. Convolutional neural networks applied to neutrino events  
3101 in a liquid argon time projection chamber. *Journal of Instrumentation*,  
3102 12(03):P03011, 2017.
- 3103 [60] R. Acciarri et al. Design and construction of the MicroBooNE detector. *Journal*  
3104 *of Instrumentation*, 12(02):P02017–P02017, feb 2017.

- 3105 [61] C. E. Aalseth et al.l. DarkSide-20k: A 20 tonne two-phase LAr TPC for direct  
3106 dark matter detection at LNGS. *The European Physical Journal Plus*, 133(3),  
3107 mar 2018.
- 3108 [62] H Fenker. Standard beam pwc for fermilab. Technical report, Fermi National  
3109 Accelerator Lab., Batavia, IL (USA), 1983.
- 3110 [63] H Fesbach. Theoretical nuclear physics: Nuclear reactions. 1992.
- 3111 [64] J. A. Formaggio and G. P. Zeller. From ev to eev: Neutrino cross sections across  
3112 energy scales. *Rev. Mod. Phys.*, 84:1307–1341, Sep 2012.
- 3113 [65] E. Friedman et al. K+ nucleus reaction and total cross-sections: New analysis  
3114 of transmission experiments. *Phys. Rev.*, C55:1304–1311, 1997.
- 3115 [66] V.M. Gehman, S.R. Seibert, K. Rielage, A. Hime, Y. Sun, D.-M. Mei,  
3116 J. Maassen, and D. Moore. Fluorescence efficiency and visible re-emission  
3117 spectrum of tetraphenyl butadiene films at extreme ultraviolet wavelengths.  
3118 *Nuclear Instruments and Methods in Physics Research Section A: Accelerators,*  
3119 *Spectrometers, Detectors and Associated Equipment*, 654(1):116 – 121, 2011.
- 3120 [67] H. Geiger and E. Marsden. On a diffuse reflection of the formula-particles.  
3121 *Proceedings of the Royal Society A: Mathematical, Physical and Engineering*  
3122 *Sciences*, 82(557):495–500, jul 1909.
- 3123 [68] Howard Georgi and S. L. Glashow. Unity of all elementary-particle forces. *Phys.*  
3124 *Rev. Lett.*, 32:438–441, Feb 1974.
- 3125 [69] G. Giacomelli. Introduction to the Workshop “30 years of bubble chamber  
3126 physics”. *ArXiv Physics e-prints*, April 2006.
- 3127 [70] D.Y. Wong (editor) G.L. Shaw (Editor). *Pion-nucleon Scattering*. John Wiley  
3128 & Sons Inc, 1969.

- 3129 [71] Glassman High Voltage, Inc., Precision Regulated High Voltage DC Power Sup-  
3130 ply.
- 3131 [72] D S Gorbunov. Sterile neutrinos and their role in particle physics and cosmology.  
3132 *Physics-Uspekhi*, 57(5):503, 2014.
- 3133 [73] C. Green, J. Kowalkowski, M. Paterno, M. Fischler, L. Garren, and Q. Lu. The  
3134 Art Framework. *J. Phys. Conf. Ser.*, 396:022020, 2012.
- 3135 [74] S. Hansen, D. Jensen, G. Savage, E. Skup, and A. Soha. Fermilab test beam  
3136 multi-wire proportional chamber tracking system upgrade. June 2014. Interna-  
3137 tional Conference on Technology and Instrumentation in Particle Physics (TIPP  
3138 2014).
- 3139 [75] J. Harada. Non-maximal  $\theta_{23}$ , large  $\theta_{13}$  and tri-bimaximal  $\theta_{12}$  via quark-  
3140 lepton complementarity at next-to-leading order. *EPL (Europhysics Letters)*,  
3141 103(2):21001, 2013.
- 3142 [76] Peter W. Higgs. Broken symmetries and the masses of gauge bosons. *Physical*  
3143 *Review Letters*, 13(16):508–509, oct 1964.
- 3144 [77] P.W. Higgs. Broken symmetries, massless particles and gauge fields. *Physics*  
3145 *Letters*, 12(2):132–133, sep 1964.
- 3146 [78] H J Hilke. Time projection chambers. *Reports on Progress in Physics*,  
3147 73(11):116201, 2010.
- 3148 [79] N. Ishida, M. Chen, T. Doke, K. Hasuike, A. Hitachi, M. Gaudreau, M. Kase,  
3149 Y. Kawada, J. Kikuchi, T. Komiyama, K. Kuwahara, K. Masuda, H. Okada,  
3150 Y.H. Qu, M. Suzuki, and T. Takahashi. Attenuation length measurements of  
3151 scintillation light in liquid rare gases and their mixtures using an improved  
3152 reflection suppresser. *Nuclear Instruments and Methods in Physics Research*

- 3153        *Section A: Accelerators, Spectrometers, Detectors and Associated Equipment*,  
3154        384(2-3):380–386, jan 1997.
- 3155        [80] G. Pulliam J. Asaadi, E. Gramellini. Determination of the electron lifetime in  
3156        lariat. Technical report, August 2017.
- 3157        [81] George Jaffé. Zur theorie der ionisation in kolonnen. *Annalen der Physik*,  
3158        347(12):303–344, 1913.
- 3159        [82] C. Jarlskog. A basis independent formulation of the connection between quark  
3160        mass matrices, CP violation and experiment. *Zeitschrift für Physik C Particles*  
3161        and Fields, 29(3):491–497, sep 1985.
- 3162        [83] B J P Jones, C S Chiu, J M Conrad, C M Ignarra, T Katori, and M Toups. A  
3163        measurement of the absorption of liquid argon scintillation light by dissolved ni-  
3164        trogen at the part-per-million level. *Journal of Instrumentation*, 8(07):P07011,  
3165        2013.
- 3166        [84] Benjamin J. P. Jones. *Sterile Neutrinos in Cold Climates*. PhD thesis, MIT,  
3167        2015.
- 3168        [85] Cezary Juszczak, Jarosław A. Nowak, and Jan T. Sobczyk. Simulations from  
3169        a new neutrino event generator. *Nuclear Physics B - Proceedings Supplements*,  
3170        159:211–216, sep 2006.
- 3171        [86] D. I. Kazakov. Beyond the standard model: In search of supersymmetry. In  
3172        *2000 European School of high-energy physics, Caramulo, Portugal, 20 Aug-2*  
3173        *Sep 2000: Proceedings*, pages 125–199, 2000.
- 3174        [87] Dae-Gyu Lee, R. N. Mohapatra, M. K. Parida, and Merostar Rani. Predic-  
3175        tions for the proton lifetime in minimal nonsupersymmetric  $so(10)$  models: An  
3176        update. *Phys. Rev. D*, 51:229–235, Jan 1995.

- 3177 [88] M A Leigui de Oliveira. Expression of Interest for a Full-Scale Detector Engi-  
3178 neering Test and Test Beam Calibration of a Single-Phase LAr TPC. Technical  
3179 Report CERN-SPSC-2014-027. SPSC-EOI-011, CERN, Geneva, Oct 2014.
- 3180 [89] W. H. Lippincott, K. J. Coakley, D. Gastler, A. Hime, E. Kearns, D. N. McK-  
3181 insey, J. A. Nikkel, and L. C. Stonehill. Scintillation time dependence and pulse  
3182 shape discrimination in liquid argon. *Phys. Rev. C*, 78:035801, Sep 2008.
- 3183 [90] Jorge L. Lopez and Dimitri V. Nanopoulos. Flipped SU(5): Origins and re-  
3184 cent developments. In *15th Johns Hopkins Workshop on Current Problems*  
3185 *in Particle Theory: Particle Physics from Underground to Heaven Baltimore,*  
3186 *Maryland, August 26-28, 1991*, pages 277–297, 1991.
- 3187 [91] Vincent Lucas and Stuart Raby. Nucleon decay in a realistic so(10) susy gut.  
3188 *Phys. Rev. D*, 55:6986–7009, Jun 1997.
- 3189 [92] Ettore Majorana. Teoria simmetrica dell'elettrone e del positrone. *Il Nuovo*  
3190 *Cimento*, 14(4):171–184, apr 1937.
- 3191 [93] Hisakazu Minakata and Alexei Yu. Smirnov. Neutrino mixing and quark-lepton  
3192 complementarity. *Phys. Rev. D*, 70:073009, Oct 2004.
- 3193 [94] M. Mooney. The microboone experiment and the impact of space charge effects.  
3194 2015.
- 3195 [95] E. Morikawa, R. Reininger, P. Gürtler, V. Saile, and P. Laporte. Argon, kryp-  
3196 ton, and xenon excimer luminescence: From the dilute gas to the condensed  
3197 phase. *The Journal of Chemical Physics*, 91(3):1469–1477, aug 1989.
- 3198 [96] FM Newcomer, S Tedja, R Van Berg, J Van der Spiegel, and HH Williams.  
3199 A fast, low power, amplifier-shaper-discriminator for high rate straw tracking  
3200 systems. *IEEE Transactions on Nuclear Science*, 40(4):630–636, 1993.

- 3201 [97] Emmy Noether. Invariant variation problems. *Transport Theory and Statistical*  
3202 *Physics*, 1(3):186–207, jan 1971.
- 3203 [98] I. Nutini. Study of charged particles interaction processes on ar in the 0.2 - 2.0  
3204 GeV energy range through combined information from ionization free charge  
3205 and scintillation light. Technical report, jan 2015.
- 3206 [99] D. R. Nygren. The time projection chamber: A new  $4\pi$  detector for charged  
3207 particles. Technical report, 1974.
- 3208 [100] L. Onsager. Initial recombination of ions. *Phys. Rev.*, 54:554–557, Oct 1938.
- 3209 [101] S. Pascoli, S.T. Petcov, and A. Riotto. Leptogenesis and low energy cp-violation  
3210 in neutrino physics. *Nuclear Physics B*, 774(1):1 – 52, 2007.
- 3211 [102] C. Patrignani et al. Review of Particle Physics. *Chin. Phys.*, C40(10):100001,  
3212 2016.
- 3213 [103] B. Pontecorvo. Neutrino Experiments and the Problem of Conservation of  
3214 Leptonic Charge. *Sov. Phys. JETP*, 26:984–988, 1968. [Zh. Eksp. Teor.  
3215 Fiz.53,1717(1967)].
- 3216 [104] T. Yang R. Acciarri. Investigation of the non-uniformity observed in the wire  
3217 response to charge in lariat run 1. Technical report, February 2017.
- 3218 [105] T. Yang R. Acciarri, M. Stancari. Determination of the electron lifetime in  
3219 lariat. Technical report, March 2016.
- 3220 [106] Martti Raidal. Relation between the neutrino and quark mixing angles and  
3221 grand unification. *Phys. Rev. Lett.*, 93:161801, Oct 2004.
- 3222 [107] Steve Ritz et al. Building for Discovery: Strategic Plan for U.S. Particle Physics  
3223 in the Global Context. 2014.

- 3224 [108] C. Rubbia. The Liquid Argon Time Projection Chamber: A New Concept for  
3225 Neutrino Detectors. 1977.
- 3226 [109] L.M. Saunders. Electromagnetic production of pions from nuclei. *Nucl. Phys.*,  
3227 *B7*: 293-310(1968).
- 3228 [110] Qaisar Shafi and Zurab Tavartkiladze. Neutrino democracy, fermion mass hier-  
3229 archies, and proton decay from 5d su(5). *Phys. Rev. D*, 67:075007, Apr 2003.
- 3230 [111] Sigma-Aldrich, P.O. Box 14508, St. Louis, MO 63178 USA.
- 3231 [112] R. K. Teague and C. J. Pings. Refractive index and the lorentz–lorenz function  
3232 for gaseous and liquid argon, including a study of the coexistence curve near the  
3233 critical state. *The Journal of Chemical Physics*, 48(11):4973–4984, jun 1968.
- 3234 [113] J. Thomas and D. A. Imel. Recombination of electron-ion pairs in liquid argon  
3235 and liquid xenon. *Phys. Rev. A*, 36:614–616, Jul 1987.
- 3236 [114] D.R.O. Morrison N. Rivoire V. Flaminio, W.G. Moorhead. Compilation of  
3237 Cross Sections I:  $\pi^+$  and  $\pi^-$  Induced Reactions. *CERN-HERA*, pages 83–01,  
3238 1983.
- 3239 [115] D.R.O. Morrison N. Rivoire V. Flaminio, W.G. Moorhead. Compilation of  
3240 Cross Sections II:  $K^+$  and  $K^-$  Induced Reactions. *CERN-HERA*, pages 83–02,  
3241 1983.
- 3242 [116] Hermann Weyl. Gravitation and the electron. *Proceedings of the National  
3243 Academy of Sciences of the United States of America*, 15(4):323–334, 1929.
- 3244 [117] Colin et al Wilkin. A comparison of pi+ and pi- total cross-sections of light  
3245 nuclei near the 3-3 resonance. *Nucl. Phys.*, B62:61–85, 1973.
- 3246 [118] D. H. Wright and M. H. Kelsey. The Geant4 Bertini Cascade. *Nucl. Instrum.  
3247 Meth.*, A804:175–188, 2015.

- 3248 [119] C. S. Wu, E. Ambler, R. W. Hayward, D. D. Hoppes, and R. P. Hudson.
- 3249        Experimental test of parity conservation in beta decay. *Phys. Rev.*, 105:1413–
- 3250        1415, Feb 1957.
- 3251 [120] N Yahlali, L M P Fernandes, K Gonzlez, A N C Garcia, and A Soriano. Imaging
- 3252        with sipms in noble-gas detectors. *Journal of Instrumentation*, 8(01):C01003,
- 3253        2013.
- 3254 [121] T. Yanagida. Horizontal symmetry and masses of neutrinos. *Progress of Theo-*
- 3255        *retical Physics*, 64(3):1103–1105, sep 1980.